Cavity Optomechanics for Hybrid Quantum Systems

Thesis by
Hengjiang Ren

In Partial Fulfillment of the Requirements for the
Degree of
Doctor of Philosophy

CALIFORNIA INSTITUTE OF TECHNOLOGY
Pasadena, California

2020
Defended January 16th, 2020

Hengjiang Ren
ORCID: 0000-0002-5612-8287

ACKNOWLEDGEMENTS

It has been an incredible journey in the last five years, I am grateful for the help and support I received from many individuals I have worked with during my time at Caltech.

Foremost I would like to thank Oskar Painter, my advisor, mentor and friend, for his extraordinary guidance and support throughout my graduate career. From the days and nights we were discussing and even tuning knobs together in the laboratories, I have learned a lot about the art of doing research from him, I hope I could have absorbed more.

This would not have been possible without the support and enduring encouragement of my family, especially my parents and my wife. My first bit of science and mathematics were learnt from both of my parents, at an age that I can no longer recall. They can not fully follow my PhD thesis defense presentation anymore, but I know that I would have never reached this milestone without them. For my wife, Yi, I would borrow and rephrase the sentence from her dissertation, which is also applicable for her: "great thanks to my wife, for her patience, endless love and encouragements."

During my Caltech days, I spent a significant amount of time in cleanroom and laboratory. And a large percent of it, is with my closest collaborator and friend in the group, Greg, who not only taught me all the nano-fabrication skills, but also together we spent thousands of hours tuning optical components, manipulating samples near absolute zero temperature, as well as remote-controlling data integration from beaches or mountains camps. It has been a great pleasure to work with you.

I also have to specially thank Roger, with whom I spent five years in the same office, thank you for your help in various research projects, as well as all the dinner talks and video games. My Caltech days have been much more fun and fruitful because of him, it is a pleasant journey to work on amazing things together.

Thanks to all the members of the Painter group, past, and current. My experimental setups are built based on Justin and Sean's hard work, Justin also mentored me during my initial months in the group. I would like to thank all the members who helped a great deal in making this thesis happen, Mohammad Mirhosseini, Alp Sipahigil, Matthew Matheny, Hannes Pfeifer and Hengyun Zhou. I benefited from many group members, on science, or on life, I owe special thanks to Barry Baker, Mahmoud Kalaee, Paul Dieterle, Michael Fang, Andrew Keller, Vinicius Ferreira, Eun Jong Kim, Steven Wood, Jash Banker, Sherry Zhang, Neil Sinclair, Srujan Meesala, Clai Owens, and others. To KNI staff, especially Guy DeRose, Nathan Lee, and Alex Wertheim. To collaborators in Max Plank Institute, Tirth Shah, Vittorio Peano, and especially Prof. Florian Marquardt, for your guidance. To Sameer Sonar and Utku Hatipoglu, who quickly came up to speed, who will (hopefully) continue this work into the near future.

To all my friends in Caltech, you have made it a wonderful journey for me.

ABSTRACT

Recent advances in optomechanical systems have led to a series of scientific and technical advances. In addition, they have demonstrated macroscopic quantum phenomena, including probabilistic preparation of quantum states, squeezed light, and coherent transduction between photons with different energies. There are advantages in using phonons within a quantum information network. Within the solid state, all optical and electronic phenomena strongly depend on the local distortions of the crystal lattice, i.e. mechanical phonons, hence could connect dissimilar degrees of freedom such as superconducting qubits operating at gigahertz frequencies with atomic/optical states. Also, unlike photons, phonons do not radiate into free space. Energy damping of phonon can occur through radiation into bulk structure which support the mechanical resonator, through impurities and defects in the material, and due to the inherent anharmonic motion of atoms within solid-state materials. In this thesis, we explore the limits of acoustic damping and coherence of a microwave-frequency acoustic nanocavity with a phononic crystal shield that possesses a wide bandgap for all polarizations of acoustic waves. The nanocavity is formed from an optomechanical crystal (OMC) nanobeam resonator. It supports an acoustic breathing mode at $\approx$ 5 GHz and a co-localized telecom optical resonant mode which allows us to excite and readout mechanical motion using radiation pressure from a pulsed laser source. This minimally invasive pulsed measurement technique avoids a slew of parasitic damping effects − typically associated with electrode materials and mechanical contact, or probe fields for continuous readout − and allows for the sensitive measurement of motion at the single phonon level. The results of acoustic ringdown measurements at millikelvin temperatures show that damping due to radiation is effectively suppressed by the phononic shield, with breathing mode quality factors reaching mechanical quality factor $Q = 4.9 \times 10^{10}$, corresponding to an unprecedented frequency-Q product of f-$Q = 2.6 \times 10^{20}$ and an effective phonon propagation length of several kilometers. Measurement of the frequency jitter of the acoustic resonance is also performed, indicating telegraph-like noise corresponding to a coherence time of $\approx$ 130 μs. The observed breathing mode behavior can be explained by TLS interactions when taking into account the highly modified density of phonon states in the shielded OMC cavity, which are most likely present in the amorphous etch-damaged region of the silicon surface. In particular, we find that damping due to nearly resonant TLS is suppressed due to

the bandgap of the phononic shield, and that relaxation damping from non-resonant TLS can explain the magnitude, low temperature dependence of the breathing mode damping, and lack of saturation of the damping with both temperature and acoustic amplitude. The extremely small motional mass and narrow linewidth of the OMC cavity make it ideal for precision mass sensing and in exploring limits to alternative quantum collapse models. Our mechanical modes exist in the same frequency range as common superconducting qubits, suggesting a possibility for creating a hybrid quantum architecture consisting of acoustic and superconducting quantum circuits, where the small scale, reduced cross-talk, and ultralong coherence time of quantum acoustic devices may provide significant improvements in connectivity and performance of current quantum hardware. A proposal of mechanical quantum memory based on ultra-high-Q mechanical model and piezo-electrical coupling is also discussed in this work.

One remaining roadblock, which significantly compromises the utility of OMCs integration with superconducting circuits, is the very weak, yet non-negligible parasitic optical absorption, which is thought to occur due to surface defect states, and together with inefficient thermalization can yield significant heating of the hypersonic mechanical mode of the device at ultralow temperatures, where microwave systems can be reliably operated as quantum devices. In 1D OMC experiments, the quantum cooperativity (C_{eff}), which corresponds to the standard photon-phonon cooperativity divided by the Bose factor of the thermal bath and is the most relevant figure-of-merit for operation of optomechanical systems at ultralow temperatures, was lower than unity for all but a microsecond around the time an optical pulse is applied. This limits quantum optomechanical experiments to schemes with short pulses. Increased C_{eff} can be achieved with improved thermalization, for example, by employing a two-dimensional (2D) OMC cavity. In this thesis, we demonstrate an improved silicon quasi-2D OMC with an over 50-fold improvement in back-action per photon over previous reports. We are able to measure the dynamics of the internal cavity acoustic modes of both 1D nanobeam and quasi-2D OMCs. Quasi-2D OMC shows much lower bath occupancy compared to 1D structures. Most importantly, quasi-2D OMCs demonstrated a C_{eff} greater than unity under steady-state optical pumping, a crucial threshold for realizing a variety of optomechanical applications. For example, bi-directional transduction or amplification of continuous quantum signals require the optomechanical device to be operated in a continuous mode. An analysis of piezo-optomechanical bi-directional microwave to optics transducer is also presented in this thesis.

TABLE OF CONTENTS

LIST OF ILLUSTRATIONS

LIST OF TABLES

PREFACE

After four years in college working on electromagnetics related projects, mostly in microwave domain, I decided to work on something with shorter wavelengths during my gap year before I started my graduate school, which were photovoltaics and plasmonics. At the time I joined the Painter group, my impression of the group was all about quantum optics, however, I realized there were on-going projects integrating mechanics and superconducting microwave circuits, and soon a significant portion of the group became superconducting qubits and related topics. I started my research in the Painter group on a project combining microwave and optics, a first attempt for a quantum microwave-to-optics transducer following Mahmoud and Paul, with some side projects on designs of on-chip microwave circuits and topological optomechanics. During the same time, Greg and I started initial numerical simulations of an optomechanics project using silicon nanobeams. Later, I realized my interest was still with those shorter wavelength projects, and settled on the silicon nanobeam project in Dilution Fridge with Greg, assisted heavily in the beginning by Roger and Justin. At that time a demonstration of phonon intensity interferometry at room temperature had already been achieve by Justin, Sean and Greg. The phonon-counting technique and pulsed excitation measurements have been mostly built in the lab. Greg and I were motivated to investigate high mechanical quality factors in a nanobeam OMC with acoustic shields. In order to do that, we started with a more careful numerical investigation of the acoustic shields. SEM image of fabricated devices were fitted and fed back to the next round of fabrication, and all the details in the fitted geometry were also considered in numerical simulation in order to know the real bandgap of the realized structure. In the first few fabrication iterations, even with the misalignment of the bandgap and the mechanical mode frequency due to subtleties of the lithography in fabrication, we observed a few devices with mechanical Q-factors above 1 billion. Knowing there was substantial room for improvement, more numerical optimization on the acoustic design, as well as iterations of lithography feedback were done. The acoustic bandgap size was further increased to the fabrication limitations and it was optimally centered around the mechanical resonance frequency.

After all these optimizations, later measurements of the mechanical lifetime showed a much clearer trend of mechanical-Q versus acoustic shield, and saturated to extremely large mechanical-Q factors on the order of 50 billion.

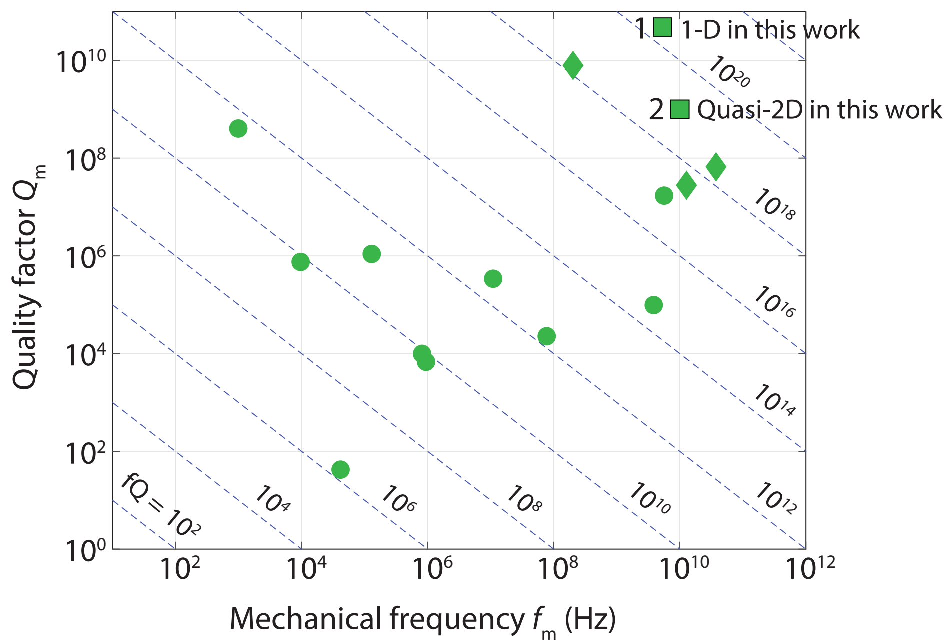

Figure 0.1: **Summary of fQ products for mechanical oscillators in cavity optomechanics and related systems**. Results in cavity optomechanics are represented by circles, with data adapted from Ref. [1]. Diamonds represent electromechanical/piezoelectric coupling to bulk acoustic modes, possessing some of the highest fQ products of any bulk material phonon modes prior to this work [2, 3]. Experiments presented in this work are represented by squares. Items (1) represent the 1D nanobeam OMC work presented in this thesis, and items (2) represent the quasi-2D OMC work presented in this thesis.

50 billion is a very encouraging number, and the corresponding fQ-product is an important figure of merit of a system protected from interactions with its thermal environment which causes decoherence. Figure 0.1 summarizes the fQ products realized for the mechanical element in various state-of-the-art optomechanical and electromechanical systems ([1, 2, 3]). The nanobeam devices with 5 GHz acoustic modes in our measurements reached an unprecedented energy coherence, reaching $f - Q = 2.6 \times 10^{20}$ and thermal decoherence times as large as $\tau_{\text{th}} = 1.5$ seconds, corresponding to an effective phonon propagation length of several kilometers.

On the other hand, we realized that the parasitic optical absorption in the silicon material can be a roadblock for further quantum applications. Due to the reduced thermal conductivity of silicon at low temperature and the 1D nature of nanobeam device, optical absorption on the surface of silicon can cause significant damping of the breathing mechanical mode. Around that time, we upgraded the optical setup capabilities such that we can use two pulsed lasers to probe the mechanical mode with large phonon amplitude, as well as using pump-probe techniques to perform fast spectral analyze. Measurements include the dependence of the mechanical linewidth and frequency upon laser power and temperature. Based on these spectral analyses together with energy decay temperature dependencies, we proposed that the mechanical dissipation and decoherence is mainly because of coupling to material defect two-level-systems residing in etch-damaged silicon surface layer.

In the meantime, a quasi-2D OMC design was investigated with the purpose of increased thermal conductance to the bulk substrate. Similar measurements were performed on these quasi-2D OMC devices, and significant improvement on quantum capabilities were observed in these devices, while still maintaining a relatively low intrinsic mechanical damping rate.

Similar nanobeam OMC devices combined with piezoelectric materials were also brought up for a new design of quantum microwave-to-optics transducer, which will be introduced in detail in this thesis, with the quasi-2D OMC design as a potentially better performance candidate. The ultra high-Q mechanical mode, combining with piezoelectric materials, is also a promising candidate in hybrid quantum systems together with GHz frequency superconducting qubits. These new hybrid platforms requires developing a new material system, which is Aluminum Nitride (AlN) in our choice. The efforts of growing and patterning AlN are detailed in Roger's thesis. A mechanical quantum memory proposal is also briefly introduced in this thesis and elaborated in Roger's thesis. These OMC platforms with high-Q, large quantum cooperativity, and ability to integrate with piezoelectric materials, which form the bulk of this thesis, show the possibility of creating hybrid quantum architectures, consisting of acoustic, optics and superconducting quantum circuits, where the small scale, reduced cross-talk, and ultralong coherence time of quantum acoustic devices may provide significant improvements in connectivity and performance of current quantum hardware.

On the way of developing these hybrid quantum systems, I also learned the nanofabrication method for superconducting qubits from Mohammad, Michael and Vinicius, which lead to an idea of hardware efficient programmable superconducting quantum logic circuit architecture with Roger, which is a promising platform for various research directions in quantum floquet engineering, topological photonic lattice, and even demonstration of small-size fault-tolerant protocols. Some initial results of a four-qubit device to create a synthetic quasi-3D tetrahedron interacting photonic lattice are shown in Roger's thesis.

Other collaborative projects I was involved in are mostly related to optomechanics, such as a collaboration with industry on optomechanical accelerometers and a project on acoustic topological insulators.

Chapter 1

CAVITY OPTOMECHANICS AND OPTOMECHANICAL CRYSTALS

In this chapter, an introduction to optomechanical resonators will be provided, focusing on optomechanical crystals and sideband-resolved cavity optomechanical systems, which is the platform for experiments in this thesis. Device design considerations, including optical coupling, optomechanical coupling rate optimization and impact of randomness in fabrication process on optical cavity and mechanical resonators, will be introduced in this chapter. A detailed design example on a quasi-2D Optomechanical Crystals (OMC) cavity based on these design principles will be discussed in Chapter 2. As the fundamental of optomechanics has already been presented in a previous thesis from the Painter group [4, 5, 6] and in review papers [7], this chapter will aim to present enough material to support the experimental work and new materials of latest design works, while avoiding redundant details.

1.1 Cavity Optomechanics

As shown in Figure 1.1, the canonical model of a cavity optomechanical system is modeled to be a Fabry-Perot cavity, with one end-mirror of the cavity is mechanically compliant. The optical cavity has resonance frequency ω_c. The moving end-mirror has mass m, mechanical resonance frequency ω_m, zero-point motion $x_{\text{zpf}} = \sqrt{\hbar/(2m\omega_m)}$, and position operator $\hat{x} = x_{\text{zpf}}(\hat{b}^\dagger + \hat{b})$. $\hat{b}$ ($\hat{b}^\dagger$) is the bosonic annihilation (creation) operator for the mechanical degree of freedom, and $\hat{a}$ ($\hat{a}^\dagger$) is the bosonic annihilation (creation) operator of optical mode. The bare Hamiltonian of the optomechanical system considering the absence of optomechincal or noise interaction is:

$$\hat{H} = \hbar\omega_c \hat{a}^\dagger \hat{a} + \hbar\omega_m \hat{b}^\dagger \hat{b}, \tag{1.1}$$

The Hamiltonian describing this system should also include optomechanical interaction, intrinsic losses to environment and coupling to an external optical pump. The

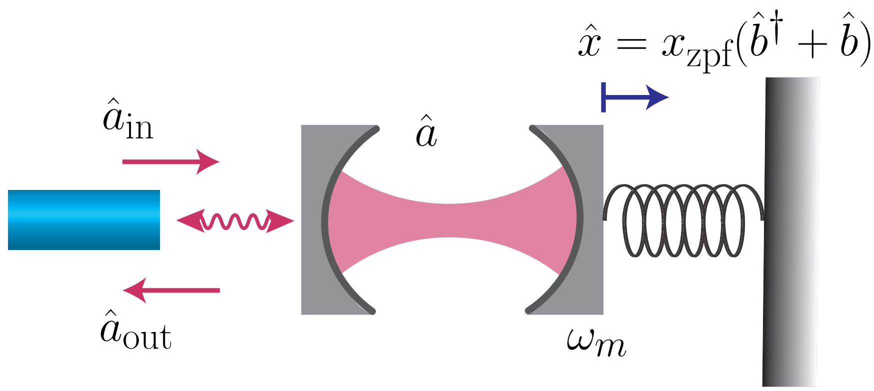

Figure 1.1: **Canonical cavity-optomechanical system.** An optomechanical system can be modeled by a Fabry-Perot cavity with two end-mirrors and coupling to optical waveguide, with one mirror being movable. The effective length of the Fabry-Perot cavity is L_{eff}, and the optical cavity frequency is ω_c. The moving mirror has mass m, mechanical resonance frequency ω_m, zero-point motion $x_{\mathrm{zpf}} = \sqrt{\hbar/(2m\omega_m)}$, and the position operator $\hat{x} = x_{\mathrm{zpf}}(\hat{b}^\dagger + \hat{b})$. $\hat{b}$ is the bosonic annihilation operator for the mechanical degree of freedom, and $\hat{a}$ is the bosonic annihilation operator of optical mode. $\hat{a}_{\mathrm{in}}$ and $\hat{a}_{\mathrm{out}}$ are used to describe optical input and output to the optomechanical system using the input-output formalism in open quantum systems.

optomechanical interaction part can be derived from modulation of cavity frequency ω_c by position of end-mirror $\hat{x}$. The optical resonance $\omega_c = nc/2L_{\mathrm{eff}}$, where n is an integer and c is the speed of light in vacuum. Upon the position of the end-mirror changing by a smaller amount $\hat{x} \ll L_{\mathrm{eff}}$, to the first order

$$\omega_c(\hat{x}) = \omega_0 + \frac{\omega_c}{L_{\mathrm{eff}}}\hat{x} \tag{1.2}$$

the Hamiltonian with the optomechinical interaction becomes

$$\hat{H} = \hbar\omega_c\hat{a}^\dagger\hat{a} + \hbar\omega_m\hat{b}^\dagger\hat{b} + \hbar g_0(\hat{b}^\dagger + \hat{b})\hat{a}^\dagger\hat{a}, \tag{1.3}$$

where we have used $g_0 \equiv \omega_c/L_{\mathrm{eff}}\hat{x}$, $\hat{x} = x_{\mathrm{zpf}}(\hat{b}^\dagger + \hat{b})$ and $x_{\mathrm{zpf}} = \sqrt{\hbar/(2m\omega_m)}$. Here, x_{zpf} is the zero-point fluctuation of the mechanical oscillator, and g_0 is defined as the vacuum optomechanical coupling rate of the system.

While Equation 1.3 is derived from a Fabry-Perot cavity model, in general, all optomechanical systems, where the motion of a mechanical oscillator changes the resonance frequency of an electromagnetic cavity, have interaction of this form to the lowest order [8], where g_0 needs to be replace by the general expression,

$$g_0 \equiv x_{\text{zpf}} \frac{\partial \omega_0}{\partial \hat{x}}. \tag{1.4}$$

Adding noise from the environment into consideration, the full Hamiltonian can be written as:

$$\begin{aligned} H = {} & \hbar\omega_c \hat{a}^\dagger \hat{a} + \hbar\omega_m \hat{b}^\dagger \hat{b} + \hbar g_0 (\hat{b}^\dagger + \hat{b}) \hat{a}^\dagger \hat{a} \\ & - \hbar \frac{\kappa}{2} i \hat{a}^\dagger \hat{a} - \hbar \frac{\gamma_{\text{i}}}{2} i \hat{b}^\dagger \hat{b} \\ & - \hbar \sqrt{\kappa_{\text{e}}} i (\hat{a}_{\text{in}} \hat{a}^\dagger + \hat{a}_{\text{in}}^\dagger \hat{a}) - \hbar \sqrt{\kappa_{\text{i}}} i (\hat{a}_i \hat{a}^\dagger + \hat{a}_{in}^\dagger \hat{a}) \\ & - \hbar \sqrt{\gamma_{\text{i}}} i (\hat{b}_i \hat{b}^\dagger + \hat{b}_i^\dagger \hat{b}). \end{aligned} \tag{1.5}$$

where $\kappa = \kappa_{\text{i}} + \kappa_{\text{e}}$ is the total optical loss rate (linewidth) of the optical mode, κ_{i} is the intrinsic optical cavity loss rate, and κ_{e} is the coupling rate to pump waveguide. γ_{i} is the intrinsic loss rate of the mechanical resonator into its environment.

In our experiment, we pump the optomechanical system with a pump laser at frequency ω_{L}, and we define the detuning of the pump laser to the cavity frequency by $\Delta = \omega_{\text{L}} - \omega_c$,

$$\begin{aligned} \hat{a} e^{-i\omega_{\text{L}} t} &= \hat{a} e^{-i(\omega_c - \Delta)t}, \\ \hat{b} e^{-i(\omega_{\text{L}} + \omega_{\text{m}})t} &= \hat{b} e^{-i(\omega_c - \Delta + \omega_{\text{m}})t}. \end{aligned} \tag{1.6}$$

Δ is chosen to be comparable to ω_m in our experiments. Some of the product terms in the Hamiltonian will be rapidly-varying at twice the optical frequency, while some will be slowly-varying on the scale of ω_m. We then make a rotating wave approximation by neglecting the rapidly-varying terms in the Hamiltonian. We also relabel some of the terms in the Equation 1.5 in the rotated frame, $e^{i\omega_{\text{L}} t} \hat{a}_{\text{in}} \longrightarrow \hat{a}_{\text{in}}^R$ and $e^{i\omega_{\text{L}} t} \hat{a}_i \longrightarrow \hat{a}_i^R$, the Hamiltonian in the rotated frame is

$$\begin{aligned}
H = &\hbar\Delta\hat{a}^\dagger\hat{a} + \hbar\omega_m\hat{b}^\dagger\hat{b} + \hbar g_0(\hat{b}^\dagger + \hat{b})\hat{a}^\dagger\hat{a} \\
&- \hbar\frac{\kappa}{2}i\hat{a}^\dagger\hat{a} - \hbar\frac{\gamma_\mathrm{i}}{2}i\hat{b}^\dagger\hat{b} \\
&- \hbar\sqrt{\kappa_\mathrm{e}}i({\hat{a}_\mathrm{in}}^R\hat{a}^\dagger + {\hat{a}_\mathrm{in}^\dagger}^R\hat{a}) - \hbar\sqrt{\kappa_\mathrm{i}}i({\hat{a}_i}^R\hat{a}^\dagger + {\hat{a}_{in}^\dagger}^R\hat{a}) \\
&- \hbar\sqrt{\gamma_\mathrm{i}}i(\hat{b}_i\hat{b}^\dagger + \hat{b}_i^\dagger\hat{b})
\end{aligned} \tag{1.7}$$

In the Heisenberg picture where the time evolution of an operator $\hat{A}$ is given by $\dot{\hat{A}} = -(i/\hbar)[\hat{A}, \hat{H}] + \partial\hat{A}/\partial t$, we arrive at the full Heisenberg-Langevin equations for the photon and phonon annihilation operators:

$$\dot{\hat{a}} = -i(\Delta - \frac{\kappa}{2}i)\hat{a} - ig_0(\hat{b} + \hat{b}^\dagger)\hat{a} + \sqrt{\kappa_\mathrm{e}}\hat{a}_\mathrm{in}^R + \sqrt{\kappa_\mathrm{i}}\hat{a}_i^R \tag{1.8}$$

$$\dot{\hat{b}} = -i(\omega_m - \frac{\gamma_\mathrm{i}}{2}i)\hat{b} - ig_0\hat{a}^\dagger\hat{a} + \sqrt{\gamma_\mathrm{i}}\hat{b}_i \tag{1.9}$$

For an optiomechanical system like ours (and all current realizations of the optomechnical systems), we are working in the vacuum weak coupling regime, where g_0 is smaller than optical damping. The optical field composes a large coherent amplitude and a small fluctuating part, such that the mechanical oscillator experiences a static radiation pressure force. Since the fluctuations of the field are comparably smaller compared to the coherent terms, we make the substitutions to linearize 1.8

$$\begin{aligned}
\hat{a} &\longrightarrow \alpha + \hat{a} \\
\hat{b} &\longrightarrow \beta + \hat{b}.
\end{aligned} \tag{1.10}$$

α and β are the classical coherent parts of the optical field and the mechanical field where

$$\alpha = \frac{\sqrt{\kappa_\mathrm{e}}\alpha_\mathrm{in}}{i\Delta + \frac{\kappa}{2}i} \tag{1.11}$$

$$\hat{b} = \frac{g_0|\alpha|^2}{\omega_\mathrm{m} - \frac{\gamma_\mathrm{i}}{2}i}. \tag{1.12}$$

Ignoring the terms corresponding to the product of quantum noise operators ($\hat{a}^2$, $\hat{a}^{\dagger 2}$ and $\hat{a}^\dagger\hat{a}$ in Hamiltonian), the linearized Heisenberg-Langevin equations are

$$\dot{\hat{a}} = -i(\Delta - \frac{\kappa}{2}i)\hat{a} - ig_0\alpha(\hat{b} + \hat{b}^\dagger) + \sqrt{\kappa_\mathrm{e}}\hat{a}_\mathrm{in}^R + \sqrt{\kappa_\mathrm{i}}\hat{a}_i^R \tag{1.13}$$

$$\dot{\hat{b}} = -i(\omega_\mathrm{m} - \frac{\gamma_\mathrm{i}}{2}i)\hat{b} - ig_0(\alpha^*\hat{a} + \alpha\hat{a}^\dagger) + \sqrt{\gamma_\mathrm{i}}\hat{b}_i. \tag{1.14}$$

Taking the Fourier Transform of the above equations, we can solve for the field amplitudes in the frequency domain

$$\hat{a}(\omega) = \frac{-iG(\hat{b}^\dagger(\omega) + \hat{b}(\omega)) + \sqrt{\kappa_\mathrm{e}}\hat{a}_\mathrm{in}(\omega) + \sqrt{\kappa_\mathrm{i}}\hat{a}_i(\omega)}{i(\Delta - \omega) + \kappa/2}, \tag{1.15}$$

$$\hat{b}(\omega) = \frac{\sqrt{\gamma_\mathrm{i}}\hat{b}_\mathrm{in}(\omega) - iG(\hat{a}(\omega) + \hat{a}^\dagger(\omega))}{i(\omega_m - \omega) + \gamma_i/2} \tag{1.16}$$

where we have used $G = g_0\alpha$ as the parametrically-enhanced optomechanical coupling rate. We can further obtain the expression for the mechanical fluctuations in terms of optical inputs by inserting Eqnation 1.15 into Eqnation 1.16,

$$\begin{aligned}\hat{b}(\omega) = \frac{1}{i(\omega_m - \omega) + \gamma_i/2}\Bigg(&\sqrt{\gamma_i}\hat{b}_\mathrm{in}(\omega) \\ &- iG\Bigg[\frac{-iG(\hat{b}^\dagger(\omega) + \hat{b}(\omega)) + \sqrt{\kappa_\mathrm{e}}\hat{a}_\mathrm{in}(\omega) + \sqrt{\kappa_\mathrm{i}}\hat{a}_i(\omega)}{i(\Delta - \omega) + \kappa/2} \\ &+ \frac{iG(\hat{b}^\dagger(\omega) + \hat{b}(\omega)) + \sqrt{\kappa_\mathrm{e}}\hat{a}_\mathrm{in}^\dagger(-\omega) + \sqrt{\kappa_\mathrm{i}}\hat{a}_i^\dagger(-\omega)}{-i(\Delta - \omega) + \kappa/2}\Bigg]\Bigg).\end{aligned} \tag{1.17}$$

Regrouping of the terms in Equation 1.17 gives renormalized mechanical frequency $\omega_m' \equiv \omega_m + \delta\omega_m$, where mechanical fluctuations are peaked, as well as the loss rate $\gamma = \gamma_\mathrm{i} + \gamma_\mathrm{OM}$ with

$$\delta\omega_m(\Delta) = G^2\mathrm{Im}\left\{\frac{1}{i(\Delta - \omega_m) + \kappa/2} - \frac{1}{-i(\Delta + \omega_m) + \kappa/2}\right\}, \tag{1.18}$$

$$\gamma_\mathrm{OM}(\Delta) = 2G^2\mathrm{Re}\left\{\frac{1}{i(\Delta - \omega_m) + \kappa/2} - \frac{1}{-i(\Delta + \omega_m) + \kappa/2}\right\}. \tag{1.19}$$

1.1.1 Sideband Resolved Regime

The sideband resolved (unresolved) regime corresponds to the case that $\kappa \gg \omega_\mathrm{m}$ ($\kappa \ll \omega_\mathrm{m}$). The OMC devices we used here have microwave frequency mechanical resonances (typically 5 - 10 GHz) with *sideband resolution ratio* of $\kappa/(2\omega_m) < 10\%$, placing us in the resolved sideband regime. In later experiments, we are most interested in two detuning scenarios, which we will refer to as red- and blue-detuned, $\Delta = \pm\omega_m$. The optomechanical coupling rate in these two cases are

$$\gamma_\mathrm{OM}(\Delta = \pm\omega_m) = \pm\frac{4G^2}{\kappa}. \tag{1.20}$$

Similar to Raman scattering, in cavity optomechanics incident photons are scattered by optomechanical interaction and generate Stokes and anti-Stokes motional optical sidebands. In the red-detuned (blue-detuned) case, the Stokes-like (anti-Stokes-like) sideband will be suppressed by the reduced cavity susceptibility. Pump photons will absorb a phonon and scatter into the cavity frequency ω_c, cooling and damping the mechanical resonator for red-detuned pump, while blue-detuned pump photons emit a phonon and scatter into the cavity frequency, amplifying and heating the mechanical resonator. The interaction Hamiltonian can be expressed as,

$$\hat{H}_\mathrm{int} = \begin{cases} \hbar G(\hat{a}^\dagger\hat{b}^\dagger + \hat{a}\hat{b}) & \text{if } \Delta = -\omega_m \\ \hbar G(\hat{a}^\dagger\hat{b} + \hat{a}\hat{b}^\dagger) & \text{if } \Delta = +\omega_m \end{cases}.$$

The average phonon occupancy $\langle n\rangle = \langle\hat{b}^\dagger\hat{b}\rangle$ is a very importance aspect of the optomechanical system, and $\langle n\rangle$ below unity is an important prerequisite of utilizing optomechanical resonators in quantum experiments [9, 10, 11, 12, 13, 14, 15, 16, 17, 18, 19]. Cooling of $\langle n\rangle$ with red-detuned pump in continuous wave (CW) has been of a great interest [20, 21, 22]. Phonon occupancy as well as effective quantum cooperativity of the OMC system will be analyzed in detail in later chapters.

1.2 Optomechanical Crystals

The physics of cavity optomechanics applies to any mechanical motion couples to the electromagnetic field in a cavity. Different systems have been explored across a large range of mass scales, as small as cold atomic traps, as large as reflective micromechanical membranes, microdisks and superconducting microwave circuits. According to the expression of g_0, in the case of a simple Fabry-Perot cavity,

$$g_0 \equiv \omega_c / L_{\text{eff}} \hat{x}, \tag{1.21}$$

we can see that the smaller the size of optical cavity and the smaller motional mass, the larger the vacuum optomechanical coupling rate. And this is in general true for all systems where mechanical motion couples to the frequency of an electromagnetic cavity. Here comes the benefit of Optomechanical Crystals (OMCs) cavities, where effective cavity volumes can be miniaturized to close to the theoretical minimum value of $\lambda/2n$. Here λ is the wavelength of electromagnetic wave and n is the effective dielectric constant of the electromagnetic cavity. In addition, a simultaneous phononic cavity can be also engineered into the same cavity, and thus an ultra high-Q mechanical resonator can be confined, which is one of the main focuses of this work.

1.2.1 Photonic Crystal

Periodic potentials in solids give rise to dispersion and propagation of electrons, which create gaps in allowed frequencies for the propagating electronic waves. Similarly, periodic changes of refractive index in a dielectric material will affect the allowed propagating solutions of an electromagnetic wave, and can give rise to electromagnetic bandgaps, in which certain frequencies of the electromagnetic wave cannot propagate [23, 24].

Starting from Maxwell's equation in a structure with periodic relative permittivity,

$$\varepsilon(\mathbf{r}) = \varepsilon(\mathbf{r} + \mathbf{R}), \tag{1.22}$$

the master equation for the magnetic field can be shown as

$$\nabla \times \left[\frac{1}{\varepsilon(\mathbf{r})} \nabla \times \mathbf{H}(\mathbf{r}) \right] = \left(\frac{\omega}{c} \right)^2 \mathbf{H}(\mathbf{r}). \tag{1.23}$$

The solution to Eqn. 1.23 takes this form according to Bloch's Theorem [25]

$$\mathbf{H}(\mathbf{r}, t) = \mathbf{H}_0 e^{i\mathbf{k}\cdot\mathbf{r}} h_{\mathbf{r}}(\mathbf{r}), \tag{1.24}$$

where $\mathbf{k}$ is the wave-vector and $h_{\mathbf{r}}(\mathbf{r})$ is a periodic function on the lattice. The spatial mode profiles for frequencies can be calculated using Equation 1.23, and catalogue the solutions to their spatial wave-vector eigenvalue $\mathbf{k}$, eventually yielding a *band structure* diagram for a periodic structure if all $\mathbf{k}$ are solved, describing the relationship between frequency and wave-vector for each normal mode. Figure 1.2 shows an example of an one-dimensional photonic crystal. For electromagnetic fields of certain frequencies in the bandgap of the structure, field intensity attenuate very fast in the photonic crystal and can be reflected on the boundaries.

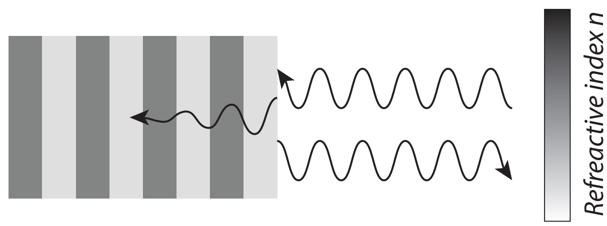

Figure 1.2: **One dimensional photonic crystal.** Periodic regions of high and low refractive indeces with certain lattice constants can lead to constructive or destructive interference of electromagnetic waves.

In this work, both quasi-one-dimensional nanobeam type of photonic crystals and quasi-two-dimensional ‘snowflake‘ type of photonic crystals are used. We etch holes into dielectric (usually silicon) membranes, where holes can be elliptical, ‘snowflake‘ or other optimized shapes. The etched area provides a lower effective refractive index and the unetched area provides a higher effective refractive index.

1.2.2 Phononic Crystal

An engineered periodic structure can also be used in trapping and guiding mechanical waves propagating in solids. Similarly to photons and electrons, on the periodically patterned dielectric, it also produces nontrivial bandgaps which prohibits the propagation of elastic waves. The speed of light and speed of sound in dielectric material are different, such that an optical cavity design for near-IR photons yields bandgaps for phonons on the order of GHz.

In this work, both one-dimensional phononic crystals and two-dimensional phononic crystals are used. The one-dimensional nanobeam type of phononic crystals have mechanical bandgaps only in even-z-symmetry, contrary to the photonic crystal cavity case where the two-dimensional ‘cross‘ and ‘snowflake‘ type of phononic crystals have full mechanical bandgaps in all symmetries. Unlike electromagnetic waves, mechanical waves of any frequency cannot propagate in vacuum around the structure. Based on the property of this full bandgap, a nano-mechanical GHz resonator with an unprecedented quality factor around 50 billion at cryogenic environment was realized, which will be discussed in later chapters.

1.2.3 Optomechanical Crystals Cavity

Similarly to a Fabry-Perot cavity discussed in the previous section, a photonic/phononic cavity can be formed with two mirrors, where photonic crystal and phononic crystal with appropriate photonic and phononic bandgaps are worked as these two mirrors. By creating a defect in the lattice, it perturbs the crystal symmetry and forms a resonant cavity. The defect can be simply removing a hole from an uniform crystal structure or change the dimensions of an one unit cell slightly. The breaking of symmetry by the defect here can host modes at frequencies within the bandgap, which can only be localized in the defect region since mode frequencies are prohibited in surrounding photonic/phononic crystals. Figure 1.3 shows an example of creating a defect cavity in a perfect one-dimensional periodic structure by replacing several higher index periods with lower index periods.

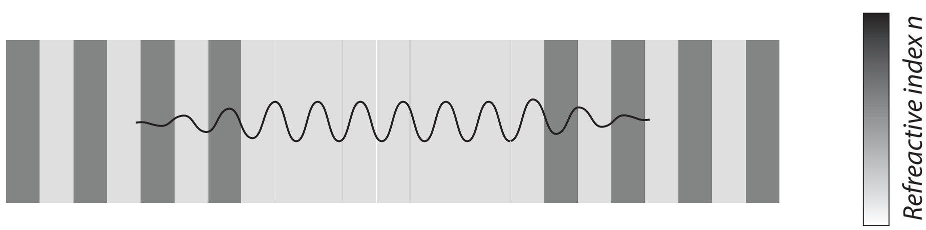

Figure 1.3: **One dimensional photonic crystal cavity.** An optical cavity is constructed by two end-mirror regions, while several higher index periods are replaced by lower index periods in central region. optical field of certain frequencies can be localized in the center defect region.

Care needs to be taken in building the defect. Firstly, electromagnetic waves can be scattered into the surrounding vacuum (if the photonics crystal is not three-dimensional), some of the designs of defect region need to be adiabatic tailored. Secondly, optimization of optomechanical coupling requires better overlap of intensity of optical field and mechanical displacement field, which can also be tuned by defect cavity design. More details of cavity design is discussed in Chapter 2 with a design example of quasi-2D OMC cavity.

1.2.4 Optomechanical Coupling

In a Fabry-Perot cavity model as described in the previous section, distance between the two end-mirrors is modulated by circulating photons reflected on the mirrors. The mechanism is different in OMC cavity. There are two coupling mechanisms. First, a 'moving boundry' where the mechanical motion displaces the boundaries of the dielectric structure, second, a 'photoelastic' effect where the strain field in the dielectric can change the dielectric constant of the material. Both mechanisms can cause the frequency of optical mode to shift.

Optomechanical coupling rate g_{OM} is the rate of change of the optical resonance frequency over mechanical displacement. For a mechanical displacement amplitude, β, $g_{\mathrm{OM}} = \partial\omega_c/\partial\beta$. The optical mode energy density depends on the electric field $\mathbf{E}$ and dielectric constant $\varepsilon(\mathbf{r})$, to first order in perturbation theory, the change in energy can be calculated using the unperturbed eigenvectors [26, 27]

$$g_{\mathrm{OM}} = \frac{\partial\omega_c}{\partial\beta} = -\frac{\omega_c}{2}\frac{\int d^3\mathbf{r}\,\mathbf{E}^*(\mathbf{r})\cdot\frac{\partial\varepsilon(\mathbf{r})}{\partial\beta}\mathbf{E}(\mathbf{r})}{\int d^3\mathbf{r}\,\mathbf{E}^*(\mathbf{r})\cdot\varepsilon(\mathbf{r})\mathbf{E}(\mathbf{r})}. \tag{1.25}$$

For the 'moving boundary' part of g_{OM}, strain-induced components in ε are ignored and calculated as

$$g_{\mathrm{OM,bnd}} = -\frac{\omega_c}{2}\frac{\int dA\,\mathbf{q}(\mathbf{r})\cdot\hat{n}(\mathbf{r})(\Delta\varepsilon\langle\mathbf{E}_{\|}(\mathbf{r})\rangle^2 - \Delta\varepsilon^{-1}\langle\mathbf{D}_{\perp}(\mathbf{r})\rangle^2)}{\int d^3\mathbf{r}\varepsilon(\mathbf{r})\langle\mathbf{E}(\mathbf{r})\rangle^2}, \tag{1.26}$$

where $\mathbf{q}(\mathbf{r})$ is the normalized mechanical displacement field, $\Delta\varepsilon = \varepsilon_{\mathrm{dielectric}} - \varepsilon_{\mathrm{vacuum}}$, $\hat{n}$ is surface normal vector, and $\mathbf{E}_{\|}$ and $\mathbf{E}_{\perp}$ represent the parallel and perpendicular components of the electromagnetic fields. Similarly, for calculation of 'photoelastic' component of g_{OM}, the boundary is assumed to be static and $g_{\mathrm{OM,ph}}$ is calculated according to [28]:

$$g_{\mathrm{OM,ph}} = \frac{\epsilon_0\epsilon_{\mathrm{r}}^2\omega_c}{2}\frac{\int dV E_{\mathrm{i}}^*(\mathbf{r})E_{\mathrm{j}}(\mathbf{r})p_{\mathrm{ijkl}}S_{\mathrm{kl}}(\mathbf{r})}{\int d^3\mathbf{r}\epsilon(\mathbf{r})|\mathbf{E}(\mathbf{r})|^2}, \tag{1.27}$$

where $\mathbf{S}$ is defined as the strain tensor in terms of the displacement field, $S_{\mathrm{ij}} = \left(\frac{\partial q_{\mathrm{i}}}{\partial r_{\mathrm{j}}} + \frac{\partial q_{\mathrm{j}}}{\partial r_{\mathrm{i}}}\right)$, and $\mathbf{p}$ is the rank-four photoelastic tensor of the material. The vacuum optomechanical coupling rate is expressed as

$$g_0 = x_{\text{zpf}} g_{\text{OM}} \tag{1.28}$$

$$= x_{\text{zpf}}(g_{\text{OM,ph}} + g_{\text{OM,bnd}}), \tag{1.29}$$

where x_{zpf} is the zero-point fluctuation of mechanical mode. Therefore g_0 describes the optical cavity frequency shift due to the zero-point mechanical fluctuation, and it can be calculated from unperturbed mechanical and optical eigenmodes if optical and mechanical properties of the material are known.

1.3 1D Nanobeam OMC, Quasi-2D OMC and Cross Phononic Crystal

1.3.1 1D Nanobeam OMC Cavity

In this work, two kinds of OMC cavities are used. One is one-dimensional OMC and the other is quasi-two-dimensional OMC. The 1D nanobeam OMC cavity is used in this work for 'Ultra high-Q mechanical resonator'. In a beam formed by patterning a suspended thin-film (220 nm) Si layer, dielectric material is removed into elliptical holes periodically as shown in Figure 1.4. The 'mirror' unit cell (Figure 1.4a) has a bandstructure as shown in Figure 1.4b, and a *pseudo*-bandgap exists around $\omega_c/2\pi = 194$ THz. In the quasi-2D OMC devices, confinement in the transverse ($\hat{y}$) is achieved by 'snowflake' crystals, but in nanobeam devices, the transverse ($\hat{y}$) and out-of-plane ($\hat{z}$) confinements are achieved by total internal reflection due to index contrast between Si and the surrounding vacuum. However, the bands of other polarization and presence of the light cone [27] can couple strongly to radiation modes, this is why the photonic bandgap of the mirror region is called a *pseudo*-bandgap.

In order to form a cavity from the optomechanical crystals, both the lattice constant and elliptical hole geometry are modulated adiabatically along the length of the beam in the nanobeam OMC. A symmetric optical potential [27] is formed in the cavity central defect region of the nanobeam, in which there exists a confined optical mode. Finite-element method (FEM) simulation of the transverse in-plane electric field magnitude $|E_y|$ for the fundamental optical mode at $\omega_c/2\pi = 194$ THz (free-space wavelength $\lambda_c \approx 1550$ nm) is shown in Figure 1.4c.

A FEM simulation of the displacement field magnitude of the *breathing* acoustic mode at $\omega_m/2\pi = 5.0$ GHz is also shown in Figure 1.4d. Similarly to quasi-2D

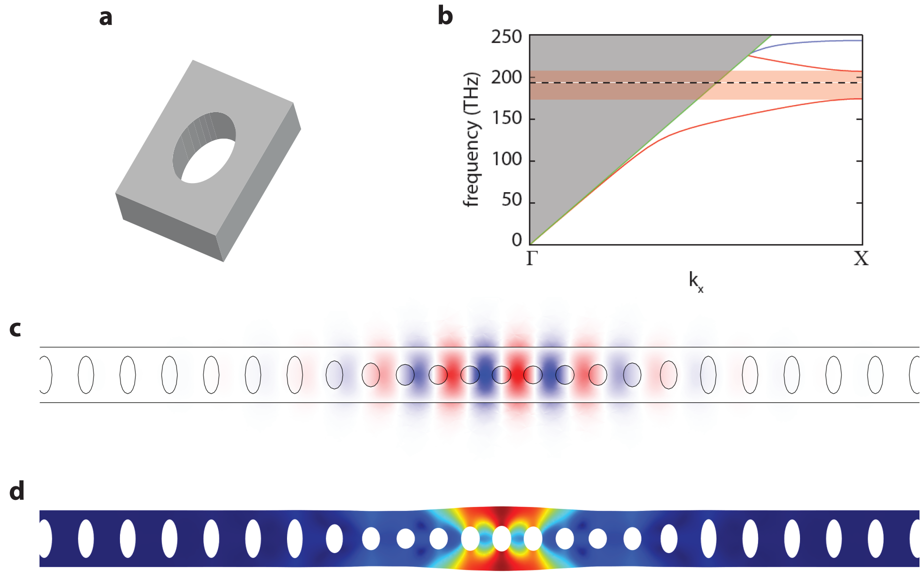

Figure 1.4: **Nanobeam OMC. a**, A unit cell of the end-mirror portion of a nanobeam OMC, and **b**, the photonic band structure of the mirror. A pseudo-bandgap exists near $\omega/2\pi$ = 200 THz, and dashed black line indicates the defect cavity frequency. Bands shown in red (blue) corresponds to odd (even) y-symmetry. **c**, Finite-element method (FEM) simulation of the transverse in-plane electric field magnitude $|E_y|$ for the fundamental optical mode at $\omega_c/2\pi$ = 194 THz (free-space wavelength $\lambda_c \approx$ 1550 nm). **d**, FEM simulation of the displacement field magnitude of the "breathing" acoustic mode at $\omega_m/2\pi$ = 5.0 GHz.

OMC device, the central defect region of the nanobeam is tailored from phononic unit cells, which provide a *pseudo*-bandgap as detailed [27].

1.3.2 Optical Coupling to 1D Nanobeam OMC Cavity with Side-Coupling

In order to route light in and out of nanobeam OMC, we employ a lensed optical fiber in an End-Fire configuration. The lensed-fiber focuses the $\sim$ 8 μm diameter Gaussian mode of a single-mode fiber to a beam waist of 2.5 μm at a working distance of approximately 14 μm from an on-chip waveguide 1D coupling facet. Single-pass coupling efficiencies as high as 72% are realizable [29]. For routing light from the on-chip 1D coupling waveguide to the optical cavity itself, a side-coupling technique is employed.

In the side-coupling method, the waveguide mode is evanescently coupled to a nanobeam optical cavity located adjacent to the waveguide, as shown in a later section (Figure 1.15). The cavity loading efficiency η_κ is tunable through the gap size between the nanobeam and waveguide beam. The extrinsic optical quality factor $Q_e \equiv \omega_c/\kappa_e$ increases exponentially with the gap size. This scheme also allows placement of a nanobeam cavity on both sides of the waveguide, doubling the number of devices which can be measured by a single lensed fiber alignment.

1.3.3 Quasi-2D OMC Cavity

A significant roadblock of 1D nanobeam OMC cavities for quantum applications is the very weak, yet non-negligible parasitic optical absorption in current devices [9, 10, 11, 12, 13]. Optical absorption, thought to occur due to surface defect states [30, 31], together with inefficient thermalization (due to the 1D nature of silicon OMC crystals currently in use) can yield significant heating of the hypersonic (> GHz) mechanical mode of the device. At ultralow temperatures ($\lesssim$ 0.1 K), where microwave systems can be reliably operated as quantum devices, this absorption leads to significant heating of the local phonon bath within a microsecond upon applying an optical pulse with a power large enough to detect single phonons at appreciable rates [9]. Moreover, this hot bath can persist even after the removal of the light field for timescales on order of the achievable decoherence times for superconducting microwave qubits, significantly compromising the utility of OMCs integration with superconducting microwave systems.

A new quasi-2D OMC cavity is designed in this work in order to increase the thermal conductance from the cavity region to bulk substrate, such that the mechanical mode of interest experiences much lower bath occupancy compared to 1D structures with the same number of intracavity photons (n_c). We demonstrate an over 50-fold improvement in back-action per photon over previous reports [32, 33]. The quasi-2D OMC design will be discussed in more detail in Chapter 2 with design process and device fabrication considerations.

1.3.4 Cross Phononic Crystal

Due to the fact that neither the nanobeam cavity nor the quasi-2D cavity does not provide full three-dimensional mechanical bands, the *breathing* mechanical resonance can still couple to leaky mechanical modes in the mirror region and leak to the bulk Si substrate. Also, fabrication imperfections can break the $\hat{z}$-symmetry of the device, which will further cause some overlap with the mode profile of propagating modes in the mirror portion of the nanobeam, and thus increase the intrinsic damping of the *breathing* mode. The impact of fabrication imperfections will be discussed in the following sections. In this work, the mechanical loss rate of the OMC structure needs to be minimized. To minimize mechanical clamping losses, the quasi-2D and nanobeam OMC are surrounded by a periodic mechanical shield structure, designed to have a complete phononic bandgap at the quasi-2D or nanobeam OMC mechanical frequency [34, 35]. As the phonons are also prohibited from radiating into the $\hat{z}$ direction, the bandgap is fully three-dimensional. Geometrically, the structure consists of a square lattice of cross-shaped holes, or equivalently, an array of squares connected to each other via narrow bridges. The phononic bandgap in this mechanical shield structure comes from the frequency separation between the resonances of the individual squares, which is at higher frequencies, and lower frequency bands with frequencies strongly dependent on the width of the connecting narrow bridges, a_c-h_c, where a_c is lattice constant and h_c is the height of cross holes as indicated in Fig. 1.6a and Fig. 1.5b. We analyze SEM images of realized structures to provide parameters for our FEM simulation. We also include filleting of the inner and outer corners (r_1 and r_2 in Fig. 1.5b and Fig. 1.6a) in our simulations, arising from the technical limitations of state-of-the-art nanofabrication techniques. For the ‘cross‘ shield used in quasi-2D OMC, a bandgap > 4 GHz is achieved centered ~ 10 GHz, through tuning of the cross lattice constant a_c, cross height h_c and width w_c (as shown in Fig. 1.6b). For the ‘cross‘ shield used in nanobeam OMC, a bandgap > 3 GHz is achieved centered ~ 5 GHz (as shown in Fig. 1.5a).

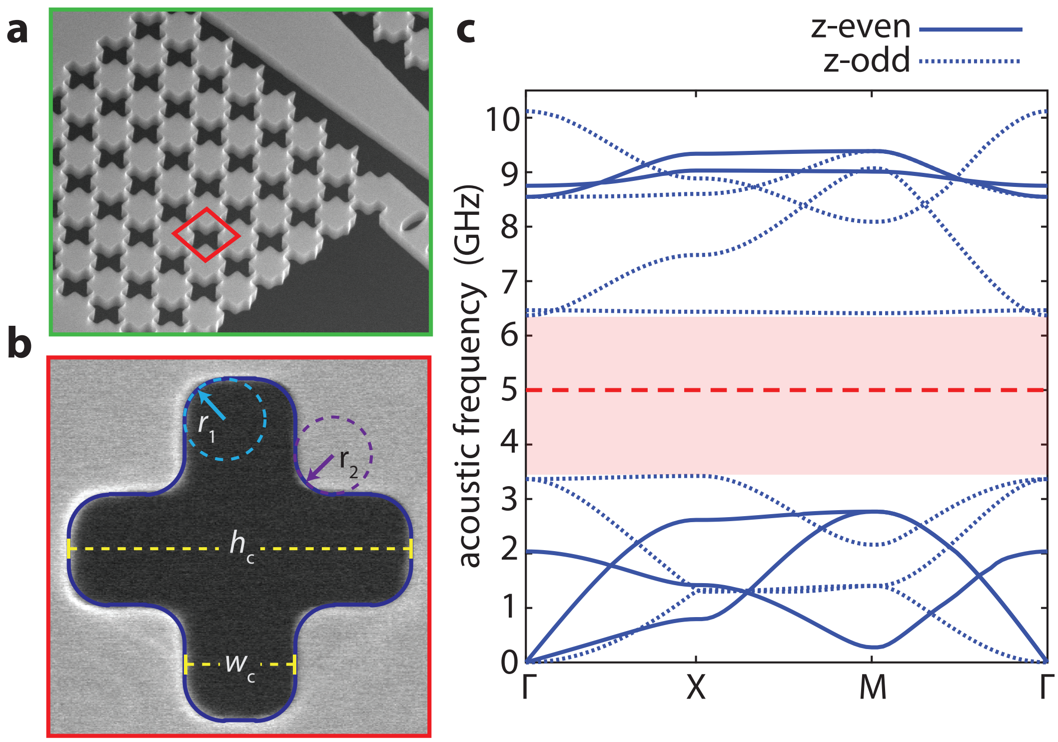

Figure 1.5: **Phononic shield design for 5GHz.** **a**, SEM image showing the nanobeam clamping geometry. **b**, SEM image of an individual unit cell of the cross-crystal acoustic shield. The dashed lines show fitted geometric parameters used in simulation, including cross height (h_c = 474 nm), cross width (w_c = 164 nm), inner fillet radius (r_1), and outer fillet radius (r_2). **c**, Simulated acoustic band structure of the realized cross-crystal shield unit cell, with the full acoustic bandgap highlighted in pink. Solid (dotted) lines correspond to modes of even (odd) symmetry in the direction normal to the plane of the unit cell. The dashed red line indicates the mechanical breathing-mode frequency at $\omega_m/2\pi$ = 5.0 GHz.

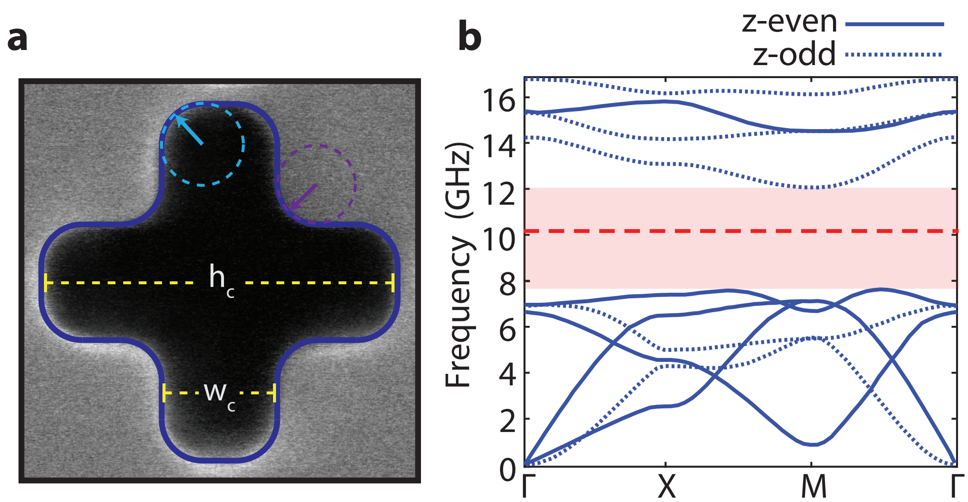

Figure 1.6: **Phononic shield design for 10GHz.** **a** SEM image of an individual unit cell of the cross-crystal acoustic shield. The dashed lines show fitted geometric parameters used in simulation, including cross height (h_c = 223 nm), cross width (w_c = 75 nm), inner fillet radius (r_1), and outer fillet radius (r_2). **b** band structure of the realized cross-crystal shield unit cell, with the full bandgap highlighted in pink. Solid (dotted) lines correspond to modes of even (odd) symmetry in the direction normal to the plane of the unit cell. The dashed red line indicates the mechanical breathing-mode frequency at $\omega_m/2\pi$ = 10.27 GHz.

1.4 Impact of Fabrication Imperfections on Optical Mode

In this work, the nanobeam OMCs usually have a simulated optical quality factor exceeding 1×10^6 and the quasi-2D OMCs have an even higher simulated optical quality factor exceeding 2×10^7 due to the additional confinement from 2D photonic crystals. However, the experimentally measured values are regularly at least one order of magnitude smaller even for well established structures [35, 36]. The reason for this is due to imperfections of the fabricated devices, because of which the mode of interest can couple to the bands of other polarization and the light cone [27]. To increase the yield for fabricating higher quality devices and to develop improved fabrication procedures, it is key to determine the impacts of different fabrication imperfections and figure out the bottlenecks for the current device optical quality factors.

To analyze the impact of occurring fabrication imperfections, here FEM simulations [37] of the optical properties is performed on a ‘flower‘ OMC cavity. The ‘flower‘ OMC is a variation of ‘snowflake‘ OMC developed in collaboration with Hannes Pfeifer [38], and the cavity used in this case is built using the same principle as the quasi-2D OMC cavity. Optical and mechanical mode profiles of ‘flower‘ OMC cavity are shown in Fig. 1.7.

The fabrication imperfections introduced during the fabrication processes have both systematic and random effects onto the resulting device geometry. Systematic deviations can thereby be investigated by single simulations, while quantifying random effects requires the simulation of ensembles of imperfect device geometries. The simulation domain is embedded inside a 4.5 μm air filled margin before scattering boundaries are applied. Within the thin silicon film plane, six and five rows of isolating mirror cells were used towards the 2D crystal and the waveguide, respectively.

Five common imperfections are investigated in this section. Tilted side-walls, boot features at the edge profiles, deviations of the silicon thin film thickness are considered systematic effects due to fabrication condition. Random disorders for both position and shape of fabricated geometry features are introduced due to technical limitations of the overall accuracy of electron beam lithography which are considered random effects.

Their impact on the reachable optical quality factor was simulated for different sizes of the respective effect. Tilted side-walls and boot features both appear due to non-ideal conditions within the reactive ion etching of the silicon layer. Tilts thereby

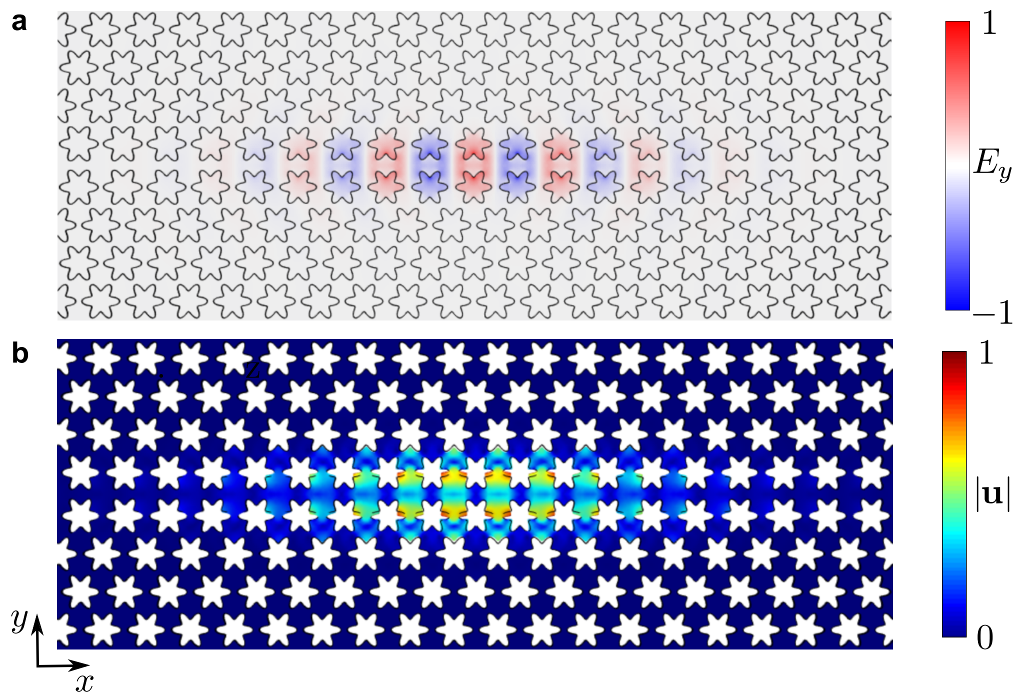

Figure 1.7: **Flower OMC mode profile.** **a** FEM-simulated mode profile (E_y component of the electric field) of the fundamental optical resonance $\omega_o/2\pi$ = 200 THz, with red (blue) corresponding to positive (negative) field amplitude. **b** Simulated displacement profile of fundamental mechanical resonance at $\omega_o/2\pi$ = 11.3 GHz.

manifest themselves by an angle of the etched shape that is approximated here by a scaling of the geometry features between the top and the bottom surface of the device layer. Boots arise from etch rate variations at the end of the etch process, when the buried oxide layer of the silicon on insulator (SOI) wafer is reached. They appear as a small necking at the base of the device layer. Variations of the thickness of the silicon device layer can stem both from variations in the manufacturing of SOI wafers and from silicon surface treatments that are used to clean and smoothen the surface [39]. They usually consist of an oxidization and a subsequent HF etch step that removes the oxidized layer and terminates the surface with hydrogen bonds that lead to reduced absorption from adsorbed water molecules [36, 39, 40, 41]. The results of the simulations are shown in Fig. 1.8. None of the individual imperfections has a large effect on the reachable quality factors for small to moderate sizes of the resulting geometry imperfection. If they are combined, they can however give a considerable contribution to the degradation of the reachable optical quality factor of the fabricated optomechanical crystal cavities.

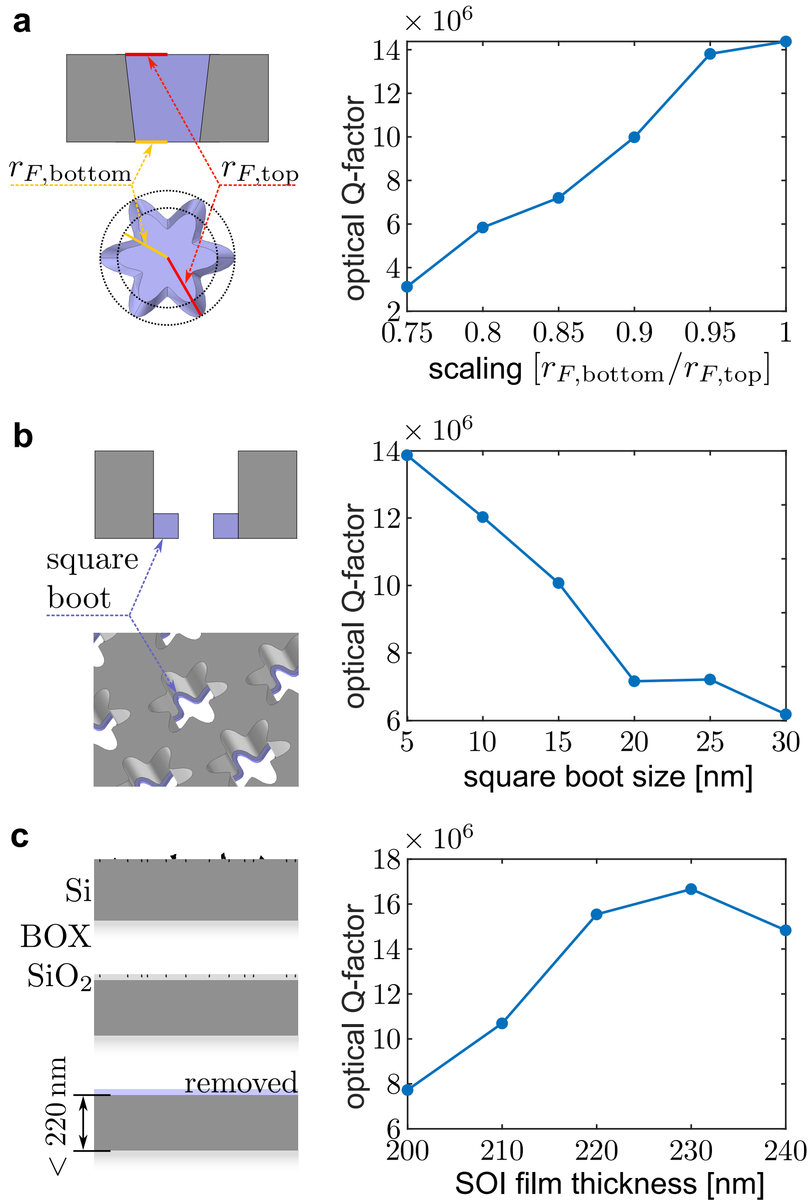

Figure 1.8: **Systematic imperfections of optical mode**. Sketches of simulated geometry imperfections (left) and the corresponding internal quality factor dependence as retrieved from FEM simulations. **a**, The impact of tilted side-walls generated by a scaling of geometry features between the top and bottom face of the silicon device layer. Common tilts correspond to scaling $\gtrsim 0.95$. **b**, The effect of boot features with a square type profile at the base of the device layer. The smallest mesh edge of the simulations was in this case reduced to 5 nm (usual boot sizes around 5 nm). **c**, The effect of the device layer thicknesses on the optical quality factors. On the left is a sketch of a surface treatment used to clean the surface from dirt and cracks by an oxidization and a subsequent HF treatment.

For the random disorder of both position and shape of fabricated geometry features, the investigated geometry imperfections include deviations of the position and the shape of the flower features in the optomechanical crystal cavity design. The deviations from the perfect feature geometry are normally distributed to reflect the random nature of the fabrication imperfections. The probability density P for a certain shift or deformation δ is therefore given by

$$P(\delta) = \frac{1}{\sqrt{2\pi\sigma_P}} \exp\left(-\frac{\delta^2}{2\sigma_P^2}\right). \tag{1.30}$$

The standard deviation σ_P defining the width of the distribution gives a measure of the uncertainty of shape or position. Within a single simulation $P(\delta)$ represents the distribution of all deviations of all features within the simulated geometry. For the case of the position disorder, the uncertainty relates to the full displacement of the flower features from the perfect position meaning that $\sigma_P = \sqrt{\sigma_{P,x}^2 + \sigma_{P,y}^2}$, where $\sigma_{P,x/y}$ specify the standard deviation in the respective in-plane direction. The deviations of the flower shape includes 12 independent shifts δ_i of the flower boundary at each petal or notch of each flower feature in the geometry. Unrealistic sharp steps in the contours are avoided by a smooth build-up and decrease of the deviation within its surrounding 60° angle φ segment of the flower. It follows a displaced cosine, as $\delta_i(\varphi) = \delta_i \cdot \theta(\varphi) \cdot \theta(60° - \varphi) \cdot (1 + \cos(3\pi + 6\varphi))/2$, for the deformation δ_i appearing at $\varphi = 30°$. $\theta(\circ)$ denotes the Heaviside function. Schematics of the different imperfection types are shown on the left of Fig. 1.9.

In order to get statistical data for the impact of the different imperfections, 10 individual structures were simulated per value of σ_P. The average values $\bar{Q}$, standard deviations σ_Q and results of the individual simulations of the internal quality factors are shown on the right of Fig. 1.9. As shown in [42], the effect of the imperfections on the average reached Q-factor can be understood in terms of an additional loss channel scaling with σ_P^2, which can be expressed as

$$\bar{Q}(\sigma_P) = \frac{1}{\frac{1}{Q_{\text{ideal}}} + A_{\text{imp}}\sigma_P^2}. \tag{1.31}$$

A_{imp} is thereby a constant specific to a geometry imperfection and cavity geometry that describes the sensitivity of the structure towards the respective imperfection. It can be retrieved by a fit of data from the simulated ensembles as shown in Fig. 1.9. Here A_{imp} values for position, shape and combined are fitted to be 5.4×10^{-7} 1/nm^2, 7.55×10^{-7} 1/nm^2, 1.35×10^{-6} 1/nm^2 correspondingly.

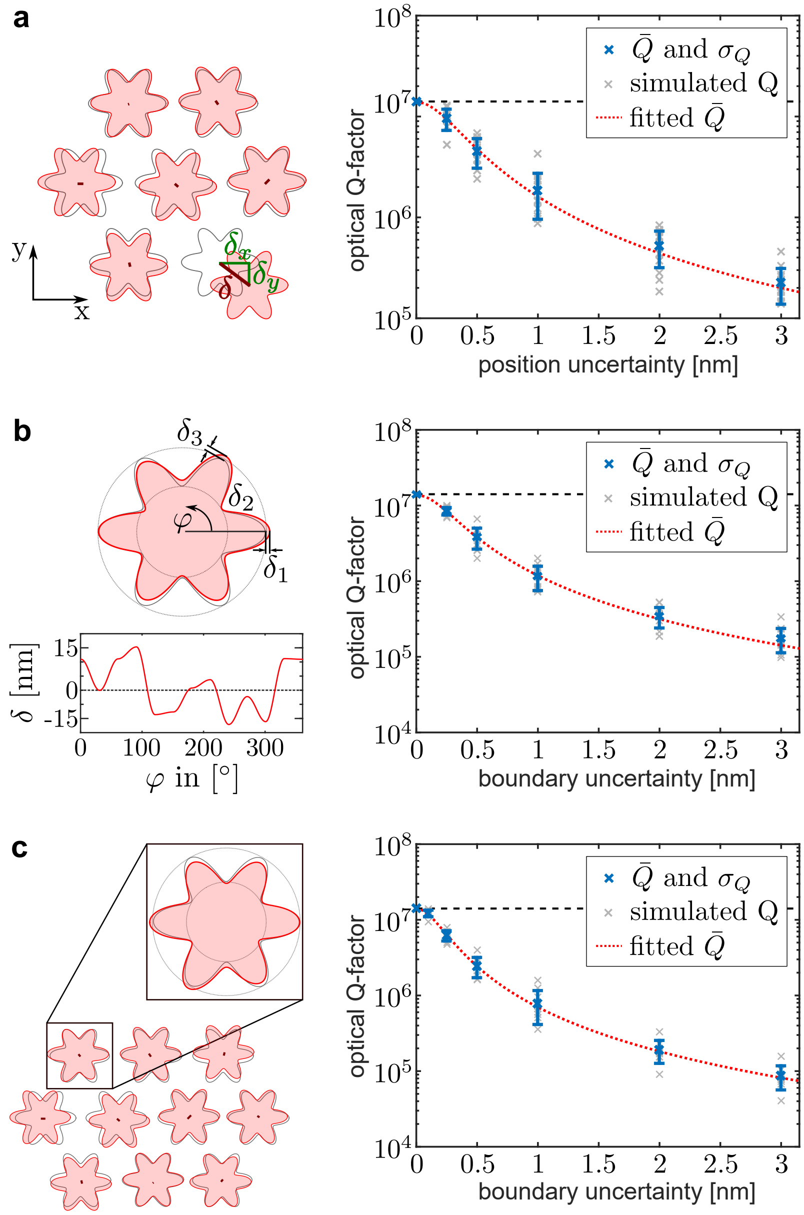

Figure 1.9: **Random imperfections of optical mode**. Sketches of simulated geometry imperfections (left) and the corresponding internal quality factor dependence as retrieved from FEM simulations of ensembles. Red geometries in the sketches represent the disordered geometry, gray geometries indicate the unperturbed structure. The rows correspond to **a**, position, **b**, shape and **c**, combined disorder of the flower features, where the σ_P of both disorder types were set equal in **c**. Within the quality factor dependence graphs the errorbars around the mean quality factors $\bar{Q}$ of the ensembles indicate the standard deviation $\pm\sigma_Q$ at each uncertainty.

1.5 Impact of Fabrication Imperfections on Mechanical Mode

Apart from the effect of fabrication imperfections on the optical modes, they also affect the acoustic properties of optomechanical structures. A degradation of the mechanical quality factor can however be compensated by an increasing number of shielding acoustic mirror cells [43, 44], since no radiation into the free space occurs. In this section, a study on how disorder can weaken acoustic shields is introduced.

Similar to the study in the previous section on impact of fabrication imperfection on optical modes, we consider several systematic and random disorder effects of both position and size of fabricated geometry features, with a nanobeam OMC cavity surrounded by ‘cross‘ acoustic shields. The bandgaps of designed cross acoustic shields used in this work are ~ 3 GHz centered around the mode of interest of nanobeam OMC (~ 5 GHz). The gap of cross shields may decrease if the size of cross holes fabricated are different from design. Thus the effect of acoustic shield gap size and the mismatch between the nanobeam OMC mechanical frequency and center frequency of cross acoustic shields are also studied in this section.

Tilted side-walls and boot features both appear due to non-ideal conditions within the reactive ion etching of the silicon layer. Variations of the thickness of the silicon device layer can stem both from variations in the manufacture of SOI wafers and from silicon surface treatments that are used to clean and smoothen the surface [39]. However, simulations show that all these systematic fabrication imperfections have negligible impact on the mechanical quality factor of nanobeam OMC surrounded by cross acoustic shields.

For the random disorder for both position and size of fabricated geometry features, the investigated geometry imperfections include deviations of the position and the size of nanobeam elliptical holes, acoustic shields cross holes, as well as roughness in the beam. In investigating the roughness in the beam, ~ 40 points are randomly selected on the beam edge along the length of the nanobeam, and position of these points are randomized the same way as position of elliptical and cross holes. The deviations from the perfect feature geometry are normally distributed to reflect the random nature of the fabrication imperfections. The probability density P for a certain shift or deformation δ is the same as in the previous section. Within a single simulation, $P(\delta)$ represents the distribution of all deviations of all features within the simulated geometry. For the case of the position disorder, the uncertainty relates to the full displacement of the elliptical holes, cross holes, or beam edge points from the perfect position meaning that $\sigma_P = \sqrt{\sigma_{P,x}^2 + \sigma_{P,y}^2}$, where $\sigma_{P,x/y}$ specify the standard deviation in the respective in-plane direction. The deviations of the elliptical holes include two independent shifts of the size of elliptical holes which are the two axes of ellipse. The deviations of the size of cross holes include four independent shifts which are the length and width of two rectangles.

In order to get statistical data for the impact of the different imperfections, 10 individual structures were simulated per value of σ_P. The average values $\bar{Q}$, standard deviations σ_Q and results of the individual simulations of the mechanical quality factors are shown in of Fig. 1.10. Results show that positions of nanobeam elliptical holes, acoustic shields cross holes and roughness in the beam are the major reason for mechanical quality factor degradation, while the size of nanobeam holes elliptical and acoustic shields cross holes have negligible impact on mechanical quality factor.

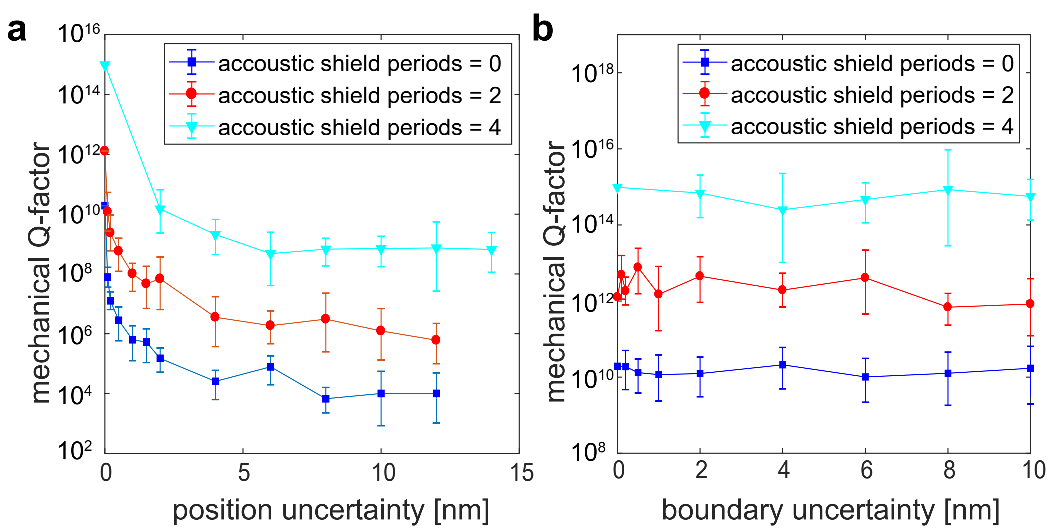

Figure 1.10: **Random imperfections of mechanical mode**. **a**, combined position of elliptical holes, cross holes and beam edge points, as well as **b**, size of elliptical holes and ‘cross‘ holes disorder of the nanobeam surrounded by cross features, where the σ_P of both disorder types were set equal in **a**. Within the quality factor dependence graphs, the errorbars around the mean quality factors $\bar{Q}$ of the ensembles indicate the standard deviation $\pm\sigma_Q$ at each uncertainty.

Although the small randomness in the sizes of acoustic shield cross holes has negligible effects on the mechanical quality factor of OMC cavity, the acoustic bandgap size does change if cross holes systematical deviate the optimized design. Mechanical quality factor of nanobeam *breathing* mode are simulated with different cross geometries and thus different bandgap sizes. The band structures are plotted in Fig. 1.11, with bandgaps of ~ 2GHz, ~ 1GHz, and no bandgap. The corresponding mechanical quality factor versus different number of acoustic shield periods are also plotted on the right side of Fig. 1.11.

Similarly, the center of bandgaps of acoustic shields and the nanobeam *breathing* mode frequency can change if hole sizes have systematical deviations from the optimized design. The impact from mismatch between the center of acoustic bandgap frequency and nanobeam *breathing* mode frequency are also studied and plotted in Fig. 1.12. Band structures and indicators of nanobeam *breathing* mode frequency are plotted on the left and corresponding mechanical quality factor versus different numbers of acoustic shield periods plotted on the right side of Fig. 1.12. Results in Fig. 1.12a show that the mechanical quality factor starts to decrease only if the nanobeam *breathing* mode frequency becomes much higher (~ 1.5 GHz) than the higher edge of bandgap, while results in Fig. 1.12b show that the mechanical quality factor slowly decreases if the nanobeam *breathing* mode frequency approaches the lower edge of bandgap, although it is still in the bandgap. The different behavior of mismatch between bandgap center frequency and nanobeam *breathing* mode frequency may come from the nature of different individual bands in the band structure of the cross. The degradation of the mechanical quality factor due to fabrication imperfections comes from the fact that the fabrication randomness will introduce coupling of modes between different symmetries. The nanobeam *breathing* mode couples to the bulk silicon substrate very weakly due to acoustic bandgap of cross. Different bands in the band structure of the nanobeam and crosses have distinct coupling rate with bulk silicon substrate, the *breathing* mode coupling to other modes thus leads to mechanical damping of the *breathing* mode.

Here in this work, we explore the limits of acoustic damping and coherence of a microwave acoustic nanocavity with the cross phononic crystal shield. The results of acoustic ringdown measurements at millikelvin temperatures show that damping due to radiation is effectively suppressed by the phononic shield, with *breathing* mode quality factors reaching $Q = 4.9 \times 10^{10}$. In order to achieve this, radiation loss of mechanical mode of interest (the *breathing* mode) is effectively suppressed. In Chapter 4, there is a more detailed discussion of impact of fabrication imperfections on the mechanical quality factor of the specific nanobeam OMC devices used in this work.

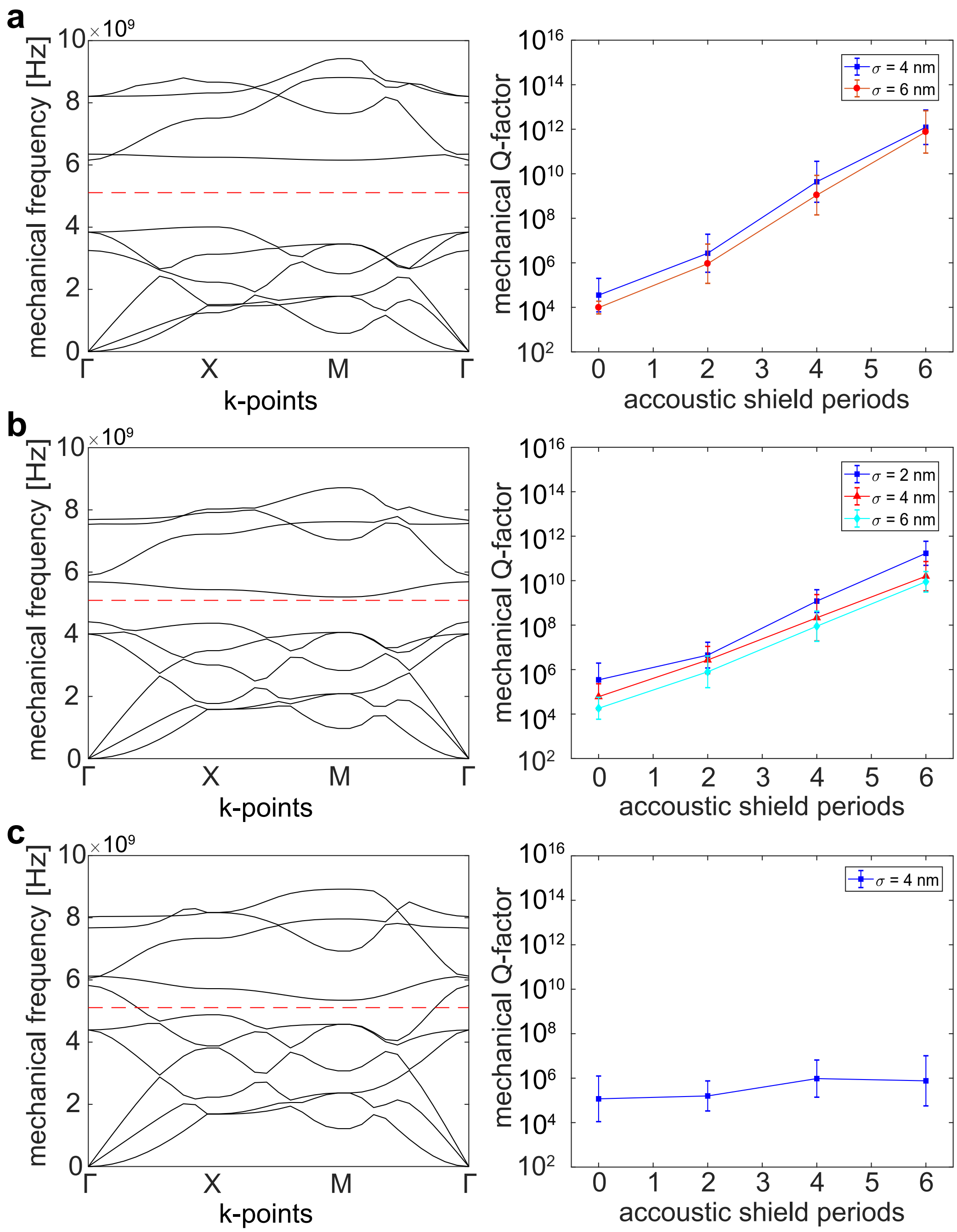

Figure 1.11: **Effects of acoustic bandgap size**. Mechanical quality factor versus different number of acoustic shield periods on the right side, with corresponding band structures on the left side for **a**, large bandgap (∼ 2 GHz), **b**, small bandgap (∼ 1 GHz) and **c**, no bandgap (= 0 GHz). Selected position uncertainty of σ = 2, 4, 6 nm are plotted for different bandgap sizes.

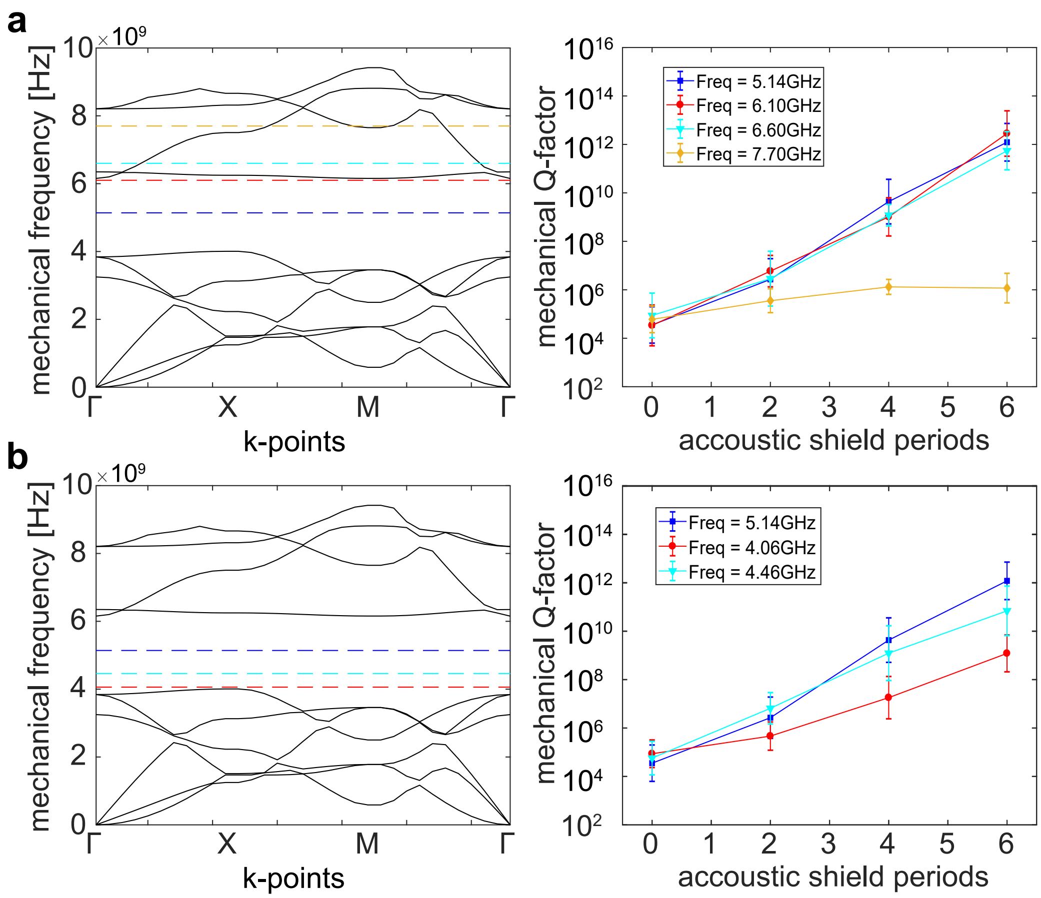

Figure 1.12: **Effects of acoustic bandgap frequency mismatch**. **a**, Effects of center frequency of acoustic bandgap mismatches with nanobeam *breathing* mode frequency for acoustic shields with bandgap ~ 2 GHz. **a**, Mechanical quality factor versus different numbers of acoustic shield periods for nanobeam *breathing* modes higher than the center frequency of acoustic bandgap. Bandgaps and *breathing* mode frequencies are indicated in the left plot. **b**, Mechanical quality factor versus different number of acoustic shield periods for nanobeam *breathing* modes lower than center frequency of acoustic bandgap. Bandgaps and *breathing* mode frequencies are indicated in the left plot.

1.6 Nanofabrication Methods of OMC Devices

In this work, all of the OMC devices and superconducting circuits presented in later chapters were performed in the Painter Group 10,000/1,000 cleanroom and at the shared campus cleanroom Kavli Nanoscience Institute (KNI). In summary, the nanobeam OMC devices and quasi-2D OMC devices were fabricated using a silicon-on-insulator wafer with a silicon (Si) device layer thickness of 220 nm and buried-oxide layer thickness of 3 μm. The device geometry was defined by electron-beam lithography followed by inductively coupled plasma reactive ion etching (ICP-RIE) to transfer the pattern through the 220 nm Si device layer. Photoresist was then used to define a 'trench' region of the chip to be etched and cleared for fiber access to device waveguides. In the unprotected trench region of the chip, the buried-oxide layer is etched using a highly anisotropic plasma etch, and the handle Si layer is cleared to a depth of 100 μm using an isotropic plasma etch. The devices were then undercut using a vapor-HF etch and cleaned in a piranha solution before a final vapor-HF etch to remove the chemically-grown oxide. In fabrication, devices were spatially grouped into arrays in which the number of acoustic radiation shield periods is scaled while all other geometric parameters are held nominally identical.

Two kinds of silicon-on-insulator (SOI) wafers were used in this work. Wafer from Soitec has a Si device layer thickness 220 nm, buried oxide (BOX) layer 3 μm, handle Si thickness 500 μm, crystal orientation $\langle 1,0,0 \rangle$, resistivity $\rho \sim 5-15\,\Omega\cdot$cm, diced into dies of either 5×13 mm or 5×10 mm. Wafer from SEH has a device layer Si thickness 220 nm, buried oxide (BOX) layer 3 μm, handle Si thickness 725 μm, crystal orientation $\langle 1,0,0 \rangle$, resistivity $\rho > 3000\ \Omega\cdot$cm, diced into dies of either 10×10 mm or 5×10 mm.

The fabrication process for end-fire OMCs is a two layer process. However, testing devices, which only need to be suspended and can be optically addressed by a tapered fiber or other out-of-plane mechanism (such as an on-chip grating), do not need the 1D optical coupling waveguide for coupling to lensed fiber. Thus testing devices can be fabricated with a single layer process. An overview of the single layer process is shown in Figure 1.13, and a summary of major steps is listed here for single layer process. More detailed fabrication processes can be found in [45],

1. Pre-cleaning of the substrate chip before application of resist. A solvent rinse in acetone (ACE) followed by isopropanol (IPA) is used to remove protective photoresist coating or an adhesive film added in the wafer dicing process.

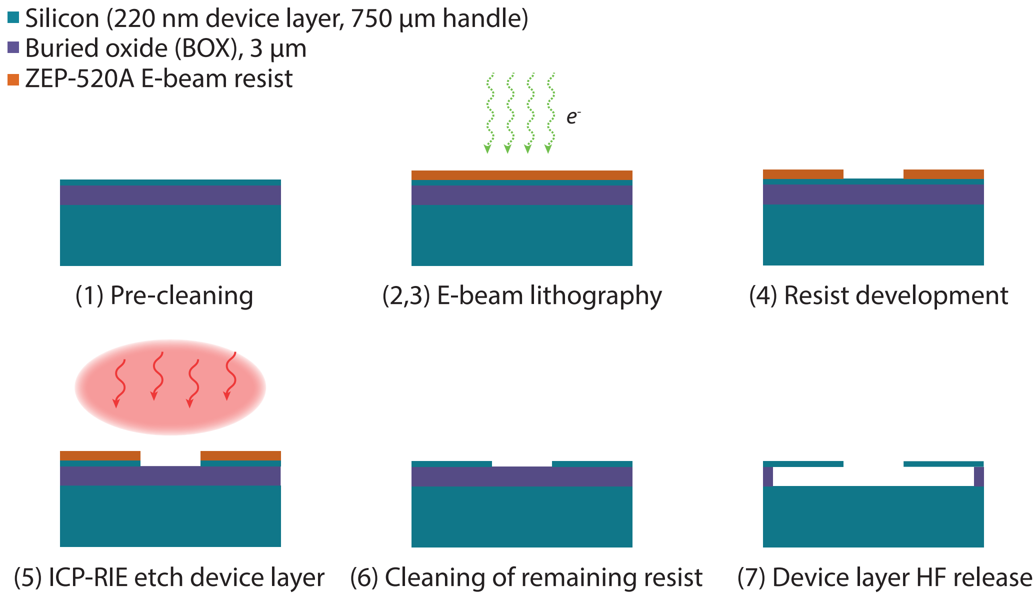

Figure 1.13: **Single-layer process flow of SOI.** Numbering in the single layer process flow is corresponding to steps listed in the text. After spinning and baking of e-beam resist, it is patterned via e-beam lithography to define the OMC. Plasma etching (ICP-RIE) is used to transfer the pattern into the 220 nm silicon device layer. After the resist is cleaned, the buried oxide layer is removed via HF etching to suspend the optical structures.

2. Spinning and baking of electron beam lithography resist. After a pre-baking of the pre-cleaned chip using a hotplate, ZEP-520A e-beam resist is spinning applied to the surface of the chip, it is used in this work for defining OMCs because of its high e-beam resolution. Then, the resist is hardened by post-baking using a hotplate.

3. Electron beam lithography. The OMC devices patterns are defined in the resist using e-beam lithography.

4. Development of e-beam resist. Chips after e-beam lithography are submerged in a ZED-N50 (a development solvent) for development of resist, and then rinsed in Methyl isobutyl ketone (MIBK).

5. Reactive-ion etching. Inductively-coupled plasma reactive-ion etching (ICP-RIE) is used to etch the exposed area by e-beam lithography, thus transfer the OMC device pattern from the e-beam resist to the top 220 nm silicon layer.

Combination of reactive species C_4F_8 and SF_6 are used in this work which is a standard *pseudo-Bosch* etching process [46].

6. Cleaning of remaining resist. Remaining e-beam resist is removed by submerging the chip in a strong solvent, typically Trichloroethylene (TCE) solution.

7. Device layer release. The buried oxide underneath the OMC device needs to be removed in order to *release* the device silion layer. Hydrofluoric acid (HF), either vapor-HF or 40% aqueous solutions is used as etchant for SiO_x.

Additional steps are needed for End-fire optical coupling. In order for a lensed fiber to access the 1D coupling waveguide in End-Fire devices, the center of fiber (with a diameter of $\sim$ 128 μm) needs to be aligned with device layer of chip. After transferring the OMC patterns from e-beam resist to silicon device layer, patterning lithography (photo-lithography is preferred here since a large area needs to be patterned) step followed by a deep etch into the handle silicon wafer in the region abutting the 1D coupling waveguide, forming a *trench* in the silicon.

Photoresist (Megaposit SPR220-7.0) is used to mask the devices during the dry plasma etch into the handle silicon layer. A flow of the two-layer fabrication process is shown in Figure 1.14 and Table 1.1.

In addition to the first 6 steps for Single layer process, before Step 7, the following steps are added as the second layer process:

1. Spinning and baking of photolithography resist. After a pre-baking of the pre-cleaned chip using a hotplate, Megaposit SPR220-7.0 photoresist is spinning applied to the surface of the chip to an average thickness of 7 μm, it is used in this work for defining deep etching region for End-fire process. The resist is hardened by post-baking using a hotplate.

2. Photolithography. The photoresist is exposed using UV light (365 nm *i*-line exposure) using a Karl Suss MA6 Mask Aligner to form a simple rectangular mask pattern which covers all the devices on the chip and leaves the trench region of the substrate unmasked.

3. Development of photoresist.

Table 1.1: End-fire process flow details.

Step	Parameter	Value	Time/Notes
Pre-cleaning	Rinse ACE, IPA	-	N_2 blow-dry
Spin ZEP-520A resist	Pre-bake	180 °C	3 min
	Spin speed	8000 rpm	60 s
	Ramp rate	2500 rpm/s	-
	Bake	180 °C	2 min
Electron-beam lithography	Dose	180 – 210 μC/cm^2	Beam current 140 – 300 pA, resolution 1.5 nm
Development	ZED-N50 developer	-	2 min 30 s
	MIBK rinse	-	30 s
Si etch	-	-	More details in Table 1.3
ZEP Resist cleaning	TCE or ZDMAC	90 °C	5 min
	(Optional) Piranha clean	80 °C	10 min, DI water rinse (x2)
Surface preparation	Buffered-HF (10 : 1)	-	10 s, DI water rinse (x2)
Spin Megaposit SPR 220-7.0	Spin speed	4000 rpm	60 s
	Ramp rate	1500 rpm/s	-
SPR resist Edge-bead removal	-	-	Wet polyester swab with TCE, swipe with hand
SPR resist bake	Pre-bake	90 °C	60 s
	Bake	115 °C	3 min
Photolithography	Source	365 nm (*i*-line)	40 s, 280 W, soft exposure, 30 μm W.E.C.
	Resist settling	-	Let sit for 75 min
Post-bake resist	Ramp temperature	100 – 115 °C	2 min, let cool completely
Development	MF CD-26	-	90 – 150 s, continue in 30 s increments as needed
	DI water rinse	-	5 s
Si etch	-	-	More details in 1.3
Silicon oxide etch	-	-	More details in 1.3
Silicon handle etch	-	-	More details in 1.3
Resist cleaning	NMP	150 °C on hot plate	Pipette after 60 s to remove crust layer, sit 2 hours
	Rinse ACE, IPA	-	N_2 blow dry
Release	Vapor HF	-	4 μm undercut etch
Cleaning	Piranha or O_2 plasma clean	80 °C for Piranha	10 min, DI water rinse (x3) or 20 min
Surface preparation	Vapor HF	-	Flash cycle etch

Table 1.3: ICP-RIE optimized etch recipe parameters.

Parameter	**Substrate SOI layer**		
	Device-layer Si	SiO_2	Handle Si
C_4F_8 flow (sccm)	84	70	0
SF_6 flow (sccm)	30	0	300
O_2 flow (sccm)	0	5	0
RF power (W)	15.5	150	0
ICP power (W)	600	2200	1200
D.C. bias (V)	76	165	0
Chamber pressure (mTorr)	15	10	100
Helium pressure (Torr)	10	5	10
Helium flow (sccm)	5.0-6.0	5.0-6.0	5.0-6.0
Table temperature (°C)	15	15	20
Etch rate (nm/min)	45	220	2500

4. Reactive-ion etching. First, the silicon device layer is etched using a recipe identical to the single layer process. Second, the BOX layer is etched anisotropically using a high-DC-bias ($>$ 150 V) plasma etch using C_4F_8 and O_2. Lastly, the silicon handle is etched with an isotropic plasma etch using pure SF_6 and no DC bias.

5. Cleaning of remaining photoresist. Remaining photoresist is removed by submerging the chip in a strong solvent, typically N-Methyl-2-pyrrolidone (NMP) solution, followed by a piranha (3:1 sulfuric acid to hydrogen peroxide) cleaning step.

6. Device layer release. The buried oxide underneath the OMC device needs to be removed in order to *release* the device silicon layer. Hydrofluoric acid (HF), either vapor-HF or 40% aqueous solution, is used as etchant for SiO_x.

The result of the two-layer process is shown in Figure 1.15. Arrays of OMC devices are fabricated in the silicon device layer, where the deep trench allows an optical fiber to address the arrays of 1D coupling waveguides. A zoom-in of an individual End-fire coupled nanobeam is also plotted in Figure 1.15. More details about the individual End-fire coupled nanobeam will be discussed in Chapter 4.

Among all the steps in both the single layer process and two-layers process, the most critical steps are patterning the OMC patterns into device layers, which includes e-beam lithography and ICP-RIE etching. There are systematic deviations between

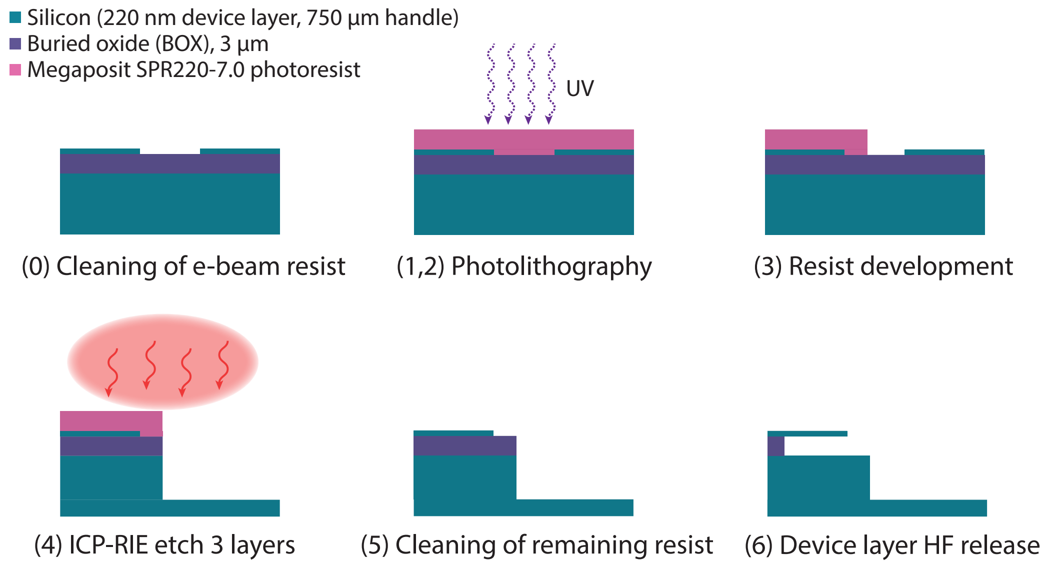

Figure 1.14: **End-fire device two layer process flow.** Numbering in the single layer process flow is corresponding to steps listed in the text. Illustration begins with a patterned silicon device layer of an SOI sample. A 7 μm-thick photoresist (Megaposit SPR220-7.0) is used in a photolithography layer to protect the device region of the chip while exposing a *trench* region to subsequent etches. A highly anisotropic ICP-RIE etch is used to etch the device layer and buried oxide in the trench region, and a further deep etch is performed to clear the handle silicon to a depth of $\sim$ 100 μm in order to allow fiber access to waveguides patterned in the device layer. The deep etch may be either (1) an isotropic SF_6 etch with no DC voltage bias, or (2) a standard Bosch etch using C_4F_8 and SF_6 in alternation. The photoresist is then stripped and the sample is cleaned in piranha solution. Finally, a vapor-HF undercut releases the End-fire devices.

the CAD designs sent to e-beam lithography tool. If all the process steps are kept unchanged, these systematic deviations are also kept constant between fabrication runs. In order to find these systematic deviations, SEM images of previous fabrication run were taken and fitted. Differences between the SEM images and optimized design were extracted from fitting, and then feedback to the next fabrication iteration. More details of the SEM images fitting feedback method will be introduced together with the quasi-2D OMC design in Chapter 2.

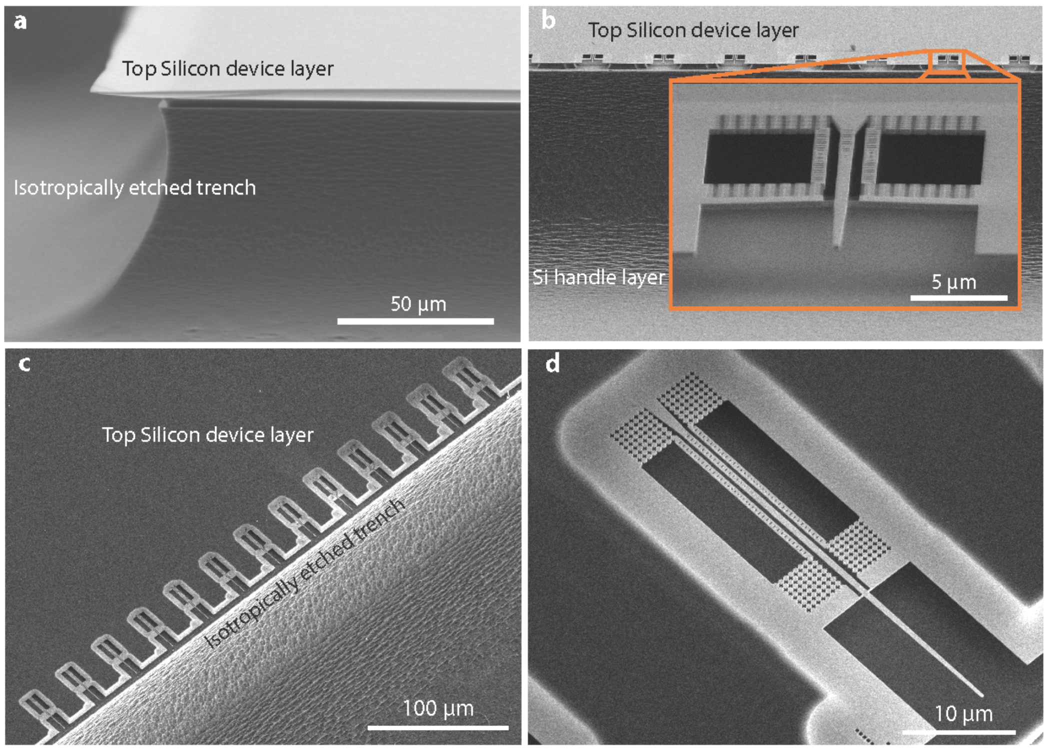

Figure 1.15: **End-fire device illustration.** Scanning electron microscope (SEM) image of nanobeam devices sample fabricated using the End-fire process outlined in Table 1.1. **a**, Side-view of an isotropically etched trench, with curved profile in the handle silicon, BOX layer was removed by HF. **b**, Front-view of part of a devices array patterned in the silicon device layer. The center of optical fiber will be aligned to the same height of the device and swept along the device layer between individual devices during measurements. **c**, Top-view of the device array. **d**, An individual End-fire nanobeam device with a nanobeam OMC on either side of a central coupling waveguide.

Chapter 2

DESIGN AND FABRICATION CONSIDERATIONS OF A QUASI-2D OMC CAVITY

The principle of building a defect cavity in photonic/phononic crystals was briefly introduced in Chapter 1. In this Chapter, design procedures of OMC cavities will be discussed in details with an example of quasi-two-dimensional OMC cavity with simulated optical scattering quality factor $Q_{\text{scat}} > 20 \times 10^6$ and high vacuum optomechanical coupling rate $g_0 \approx 1.4$ MHz. The quasi-2D OMC devices have several key improvements over 1D nanobeam OMC devices, such as a potentially higher loaded optical quality factor Q_{o} in the fabricated devices and higher optomechanical coupling due to better confinement of the optical field by photonic crystals in lateral direction, easier for planar integration of optomechanical circuits, as well as better thermal conductance to the surrounding substrate due to better connectivity. As will be discussed in detail in Chapter 6, optical pump causes parasitic heating in the OMC cavity, which decreases the effective quantum cooperativity C_{eff} of the system. A highly desirable route toward minimizing the effects of optical-absorption heating in thin-film semiconductor OMCs is planar quasi-2D OMCs, as opposed to 1D OMCs such as the nanobeam, in order to increase thermal conductance between the cavity and the surrounding cold fridge-temperature bath. In the quasi-2D device presented in this work, the thermal contact area between the cavity and the surrounding substrate is increased by a factor of ~ 40 relative to the nanobeam, allowing the optically-excited bath of hot phonons to dissipate faster and lower the effective hot phonon bath temperature experienced by the cavity mode. Further more, C_{eff} is directional proportional to g_0^2 and loaded optical quality factor Q_{o}. The increased g_0 and optical quality factor of quasi-2D OMC also benefit C_{eff} of the system.

2.1 Design of a Quasi-Two-Dimensional Optomechanical Crystals Cavity

Our quasi-2D optomechanical crystal defect cavities were designed around the silicon-on-insulator (SOI) materials platform, which naturally provides for a thin Si device layer of a few hundred nanometers in which both microwave-frequency acoustic modes and near-infrared optical modes can be guided in the vertical direction [34]. Here, we focus on the fundamental transverse-electric-like (TE-like) optical modes and the fundamental vertically guided acoustic modes of even parity about the center of the thin Si slab (vector mirror symmetry $\sigma_z = +1$). The cavity design consists of three major steps.

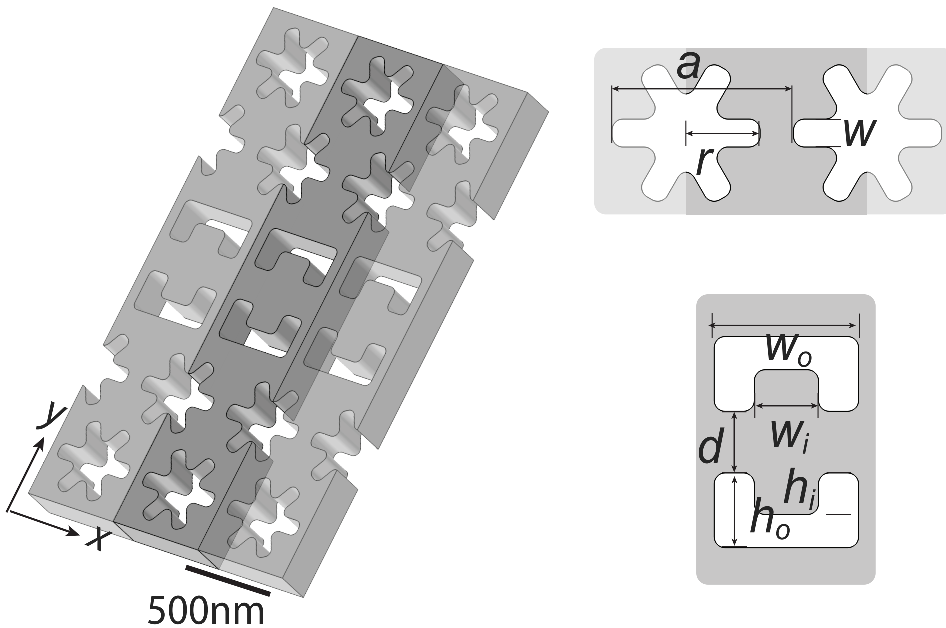

Figure 2.1: **Quasi-2D OMC unit cell.** Unit cell schematic of a linear waveguide formed in the snowflake crystal. Guided modes of the waveguide propagate along the x-axis.

First, we start with a periodically patterned quasi-2D slab structure with both phononic and photonic bandgaps in which to host the optomechanical cavity. Here, we use the 'snowflake' crystal with a hexagonal lattice [34] as shown in Fig. 2.1. The snowflake crystal provides a pseudo-bandgap for TE-like optical guided waves and a full bandgap for all acoustic mode polarizations. Finite-element-method (FEM) simulations of the optical and acoustic modes of the snowflake crystal were performed using the COMSOL software package [37], with nominal snowflake parameters corresponding to a Si slab thickness of $t = 220$ nm and $(a, r, w) = (500, 205, 75)$ nm, resulting in a TE-like guided mode photonic band gap extending over optical frequencies of 180 - 240 THz (vacuum wavelength 1250 - 1667 nm) and an acoustic bandgap covering 8.85 - 11.05 GHz.

Second, we created a line-defect in the snowflake lattice by replacing one row of snowflake unit cells with a customized unit cell that localizes mechanical and optical

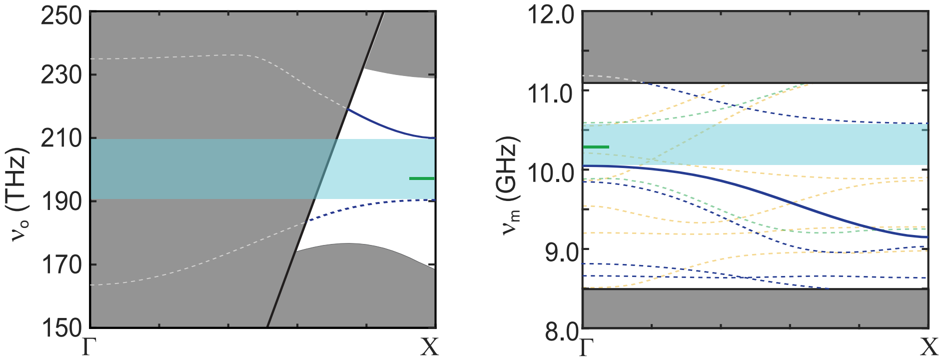

Figure 2.2: **Quasi-2D OMC band structure.** Photonic (left) and phononic (right) band structure of the linear waveguide (only modes of even symmetry about the center of the silicon slab are shown for photonic band structure). The solid blue curves are waveguide bands of interest; dashed lines are the other guided modes; shaded light blue regions are band gaps of interest; green tick mark indicates the cavity mode frequencies; gray regions denote the continua of propagating modes outside of the snowflake crystal band gap. (Green dashed lines indicate even σ_z and odd σ_y modes, yellow dashed lines denote odd σ_z modes.)

modes to the line-defect, and crucially, produces a large optomechanical coupling between the co-localized waves. The line-defect in the snowflake lattice acts as a waveguide for photon and phonon modes that lie within the bandgaps of the surrounding snowflake lattice. For the design studied here, we replaced one row of snowflakes with a set of 'C'-shaped holes. This design took inspiration from the one-dimensional nanobeam OMCs reported in Ref. [35], in which a mechanical breathing mode of the nanobeam is strongly coupled to a co-localized photonic mode. Optomechanical coupling in this sort of design is a result of both bulk (photoelastic) [47] and surface (moving boundary) [48] effects. The 'C' shape allows for large overlap of the stress induced by the acoustic mode with the optical mode intensity in the bulk of the Si device layer, while also focusing the optical mode at the air-Si boundary which greatly increases the moving boundary contribution to the optomechanical coupling. The guided-mode vacuum coupling rate of a unit cell for the line-defect waveguide (g_Δ) was calculated, and iteration in the waveguide unit cell design was performed to optimize g_Δ prior to forming a full cavity structure [34]. Photonic and phononic bandstructure diagrams of the optimized waveguide unit cell are shown in Figs. 2.2a and 2.2b, respectively. From these bandstructures, we see that there is a guided-mode bandgap for the fundamental, $\sigma_z = +1$ optical modes which extends over optical frequencies from 190 THz to 210 THz (vacuum wavelength 1430 to 1580 nm), while simultaneously there exists an acoustic guided-mode bandgap for $\sigma_z = +1$ acoustic modes covering frequencies from 10 GHz to 10.6 GHz. These two guided-mode bandgaps of the line-defect waveguide are used in the next design step to form localized cavity resonances along the length of the line-defect waveguide.

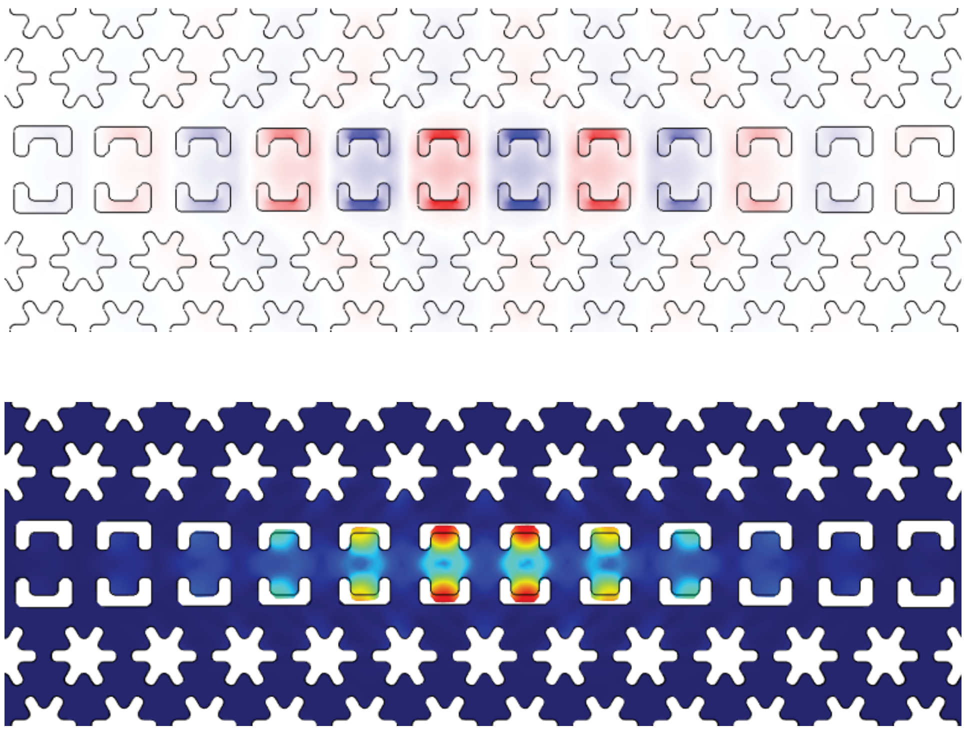

Figure 2.3: **Quasi-2D OMC mode profile.** FEM-simulated mode profile (E_y component of the electric field) of the fundamental optical resonance $\omega_o/2\pi$ = 194 THz, with red (blue) corresponding to positive (negative) field amplitude. Simulated displacement profile of fundamental mechanical resonance at $\omega_o/2\pi$ = 10.27 GHz. Here, the magnitude of the displacement is represented by color (large displacement in red, zero displacement in blue).

The final step in the cavity design involves introducing a tapering of the line-defect waveguide properties along the waveguide propagation direction (x-axis). Here, we utilize a modulation of the 'C'-shape parameters that increase quadratically in amplitude with distance along the x-axis of the line-defect waveguide from a designated center position within the waveguide (the center of the cavity). This introduces an approximate quadratic shift of the frequency of the waveguide modes with distance from the cavity center. For waveguide modes near a band-edge, this can result in the localization of the modes as these modes are pushed into a bandgap away from the cavity center. As detailed in Supplementary Note 2, a Nelder-Mead simplex search algorithm was used to obtain a tapered cavity structure with simultaneously high optical Q-factor and large optomechanical coupling between co-localized optical and acoustic modes. Figures 2.3a and 2.3b display the resulting simulated field profiles of the fundamental optical resonance ($\omega_c/2\pi$ = 194 THz, λ_c = 1550 nm) and coupled acoustic resonance ($\omega_m/2\pi$ = 10.27 GHz) of the optimized 2D OMC cavity, respectively. The co-localized modes have a theoretical vacuum optomechanical coupling rate of $g_0/2\pi$ = 1.4 MHz, and the optical mode has a theoretical scattering-limited quality factor of $Q_{\text{scat}} = 2.1 \times 10^7$ in a cavity structure with seven rows of snowflakes at each side of the line-defect waveguide and seven mirror unit cells of the waveguide at each end of the cavity.

2.2 Design Optmization of Quasi-Two-Dimensional OMC Cavity

Finite element method (FEM) simulations of the OMC cavity geometry are used to determine the optical and mechanical cavity mode frequencies (ω_o and ω_m), vacuum optomechanical coupling rate, g_0, and scattering-limited optical quality factor, Q_s. To maximize $\gamma_{\text{OM}} = 4g_0^2 n_c/\kappa$, we would like to maximize both the g_0 and loaded Q-factor Q_{opt}. Intrinsic quality factors of fabricated devices rarely get higher than $Q_i \sim 10^6$, due to fabrication imperfections and optical absorption. Also, simulated Q_s is generally high ($Q_s > 5 \times 10^6$) for a properly formed optical cavity due to two-dimensional mirrors in quasi-2D OMC cavities. Therefore, we restrict simulated Q_s to be larger than 2×10^6 to prevent radiative scattering from harming the quality factor in the realized device. We assign each design a fitness value simply given by $F \equiv -|g_0|$. We have here a 9 parameter optimization problem, which are d, h_i, w_i, h_o, w_o, $h_{i,c}$, $w_{i,c}$, $h_{o,c}$, $w_{o,c}$, where $h_{i,c}$, $w_{i,c}$, $h_{o,c}$, $w_{o,c}$ are the parameters of the 'C'-shape holes in the center of the cavity. Parameters of the other cavity 'C'-shape holes between the mirror and the center on both sides are quadratically modulated toward the center holes. Note that a, r and w are previously optimized for the large optical and mechanical bandgaps, and the thickness of the device layer, t, is fixed by the choice of substrate.

For a computationally expensive fitness function with a large parameter space, a good choice of optimization algorithm is the Nelder-Mead method [49]. A simplex search algorithm does not have smoothness requirements for the fitness function, such that it is quite resistant to simulation noise. A modern variant of this method

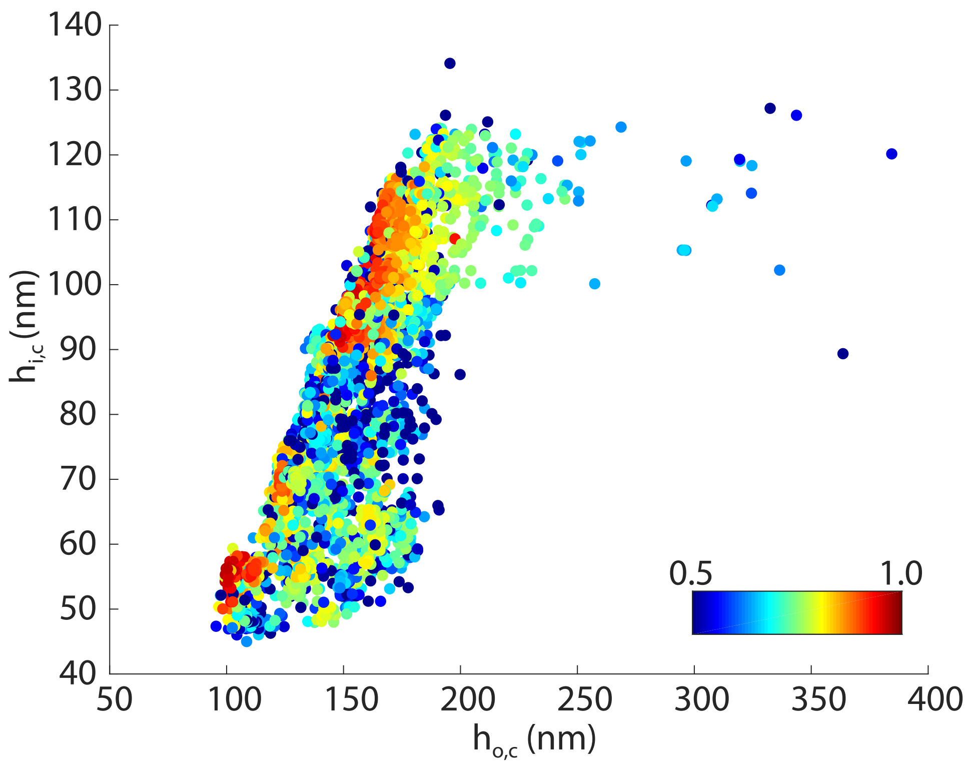

Figure 2.4: **Design Optmization of Quasi-Two-Dimensional OMC Cavity** Nelder-Mead simplex search pattern. A slice of the multidimensional parameter space explored by the Nelder-Mead minimization method. The color of the points indicates the normalized value of the fitness function. This slice includes multiple Nelder-Mead search runs with randomly generated starting points and convergence to multiple hot-spots in the two-dimensional space of $h_{i,c}$ and $h_{o,c}$.

is also implemented in the fminsearch function of MATLAB. An optimization for quasi-2D OMC design is created as follow:

1. To ensure that realizable geometry is generated in a simulation, the parameter sets need to meet certain conditions. For example, $h_\mathrm{o} - h_\mathrm{i} \geq 60$ nm (55 nm for some of the iterations) and $w_\mathrm{o}/2 - w_\mathrm{i}/2 \geq 60$ nm, where 60 nm is a conservative gap size we can realize with the limits of our device fabrication. Therefore, parameter sets are bounded for the generation of initial values and intermediate steps with the Nelder-Mead method.

2. Randomly generate an initial parameter set (d, h_i, w_i, h_o, w_o, $h_\mathrm{i,c}$, $w_\mathrm{i,c}$, $h_\mathrm{o,c}$, $w_\mathrm{o,c}$) within the bounds we set in step 1.

3. Run the optical simulation to determine the optical wavelengths (ω_o) of all the optical modes near 1550 nm with scattering-limited Q-factors larger than a threshold value (in practice only the fundamental mode we are interested in for most cases). If this fails, set $F = 0$ and go to step 6.

4. Scale all parameters except t, including a, r, and w, to move the optical mode with highest Q_scat to approximately 1550 nm.

5. Run the optical simulation again, in addition to the mechanical simulation, with scaled parameters, to determine ω_o, ω_m and g_0, and compute the fitness of the current scaled parameter set. If F did not change appreciably over the last few iterations, we reached a local minimum. Otherwise, we choose a new initial point by going to step 6.

6. Generate a new parameter set via the Nelder-Mead method and go to step 3.

By continually repeating the optimization algorithm, we mitigate the problem of converging on the local minimum. A visual representation of the search pattern is shown in supplementary figure 2.4. We follow these steps until we have a design with a g_0 and Q_s that we are satisfied with. The visual representation of supplementary figure 2.4 is formed by $\sim$ 5000 individual simulations (each individual simulation is defined after step 5 has finished successfully). We slice the multidimensional parameter space with $h_{i,c}$, $h_{o,c}$, since the gap formed by these two parameters is where both mechanical displacement and optical field are most concentrated. Note that mechanical resonance ω_m also highly depends on $h_{i,c}$. Indeed, we notice that most of the local minima lie on the line formed by $h_{o,c} - h_{i,c} = 60$ nm. This is because the intensity of the optical field on the boundaries of the gap becomes stronger as the gap becomes narrower, hence the larger g_0 by moving boundary effects due to higher overlap between optical and mechanical fields. This means, if we can create a narrower gap in the realized devices, we can potentially get an even higher g_0, but for current measurements, we chose a conservative gap value of $h_{o,c} - h_{i,c} \geq 60$ nm.

2.3 Optical Coupling to Quasi-Two-Dimensional Optomechanical Crystals Cavity

The device sample is mounted at the mixing chamber of the dilution refrigerator, with fiber-to-chip coupling achieved by an End-fire coupling scheme with an anti-reflection-coated tapered lensed fiber [29]. The tapered lensed fiber is placed on a

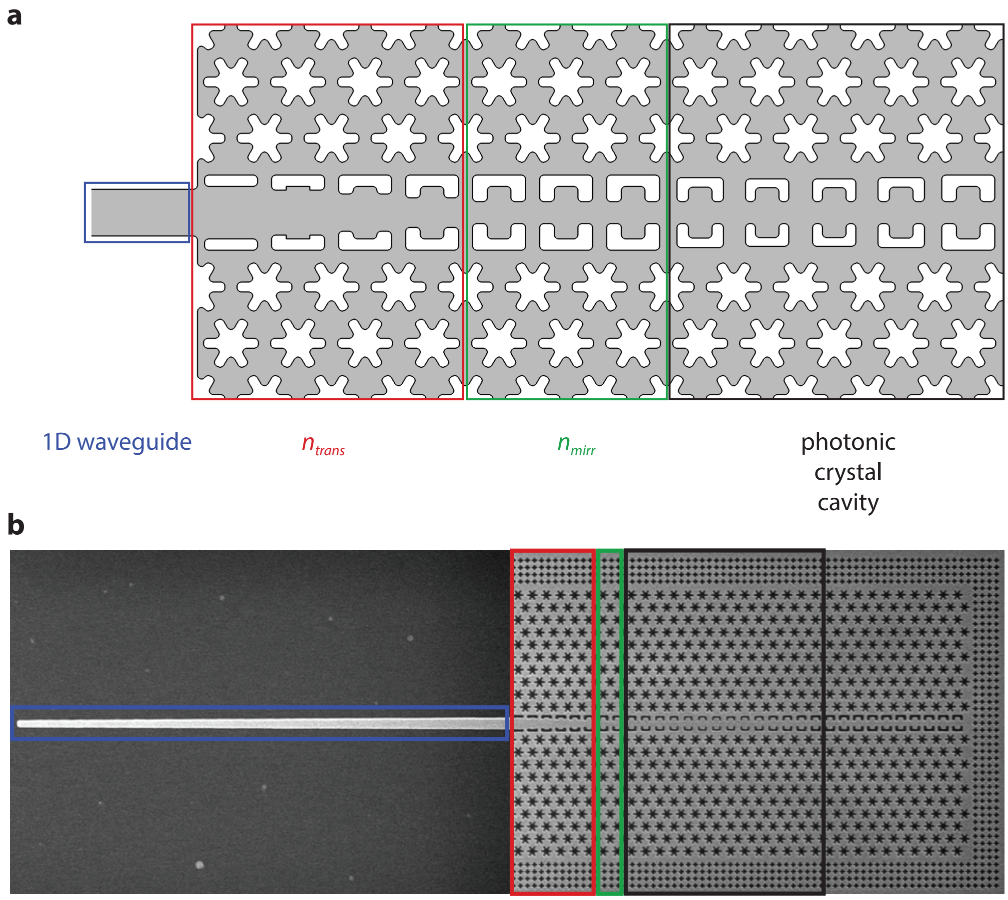

Figure 2.5: **Optical coupler design.** **a** Schematic and **b** SEM image shows design of full device, including OMC cavity (black), 1D coupling waveguide (blue) and 2D coupling waveguide (red).

position encoded piezo xyz-stage in close proximity to the device chip. After cooling the experiment from room temperature to $\approx$ 10mK, we optimize the fiber tip position relative to a 1D tapered waveguide coupler on the device layer by monitoring the reflected optical power on a slow photodetector.

The design of the tapered waveguide coupler is similar to Ref. [50] and [29]. The tip of the waveguide is designed to mode match the field of the waist of lensed fiber. The major distinction for the 2D case from 1D nanobeam design is the other side of the tapered waveguide coupler which is also designed to mode match the line defect waveguide in the 2D region as shown in Fig. 2.5a and b. The mirror in the 2D line defect waveguide region is introduced gradually to avoid excess scattering in

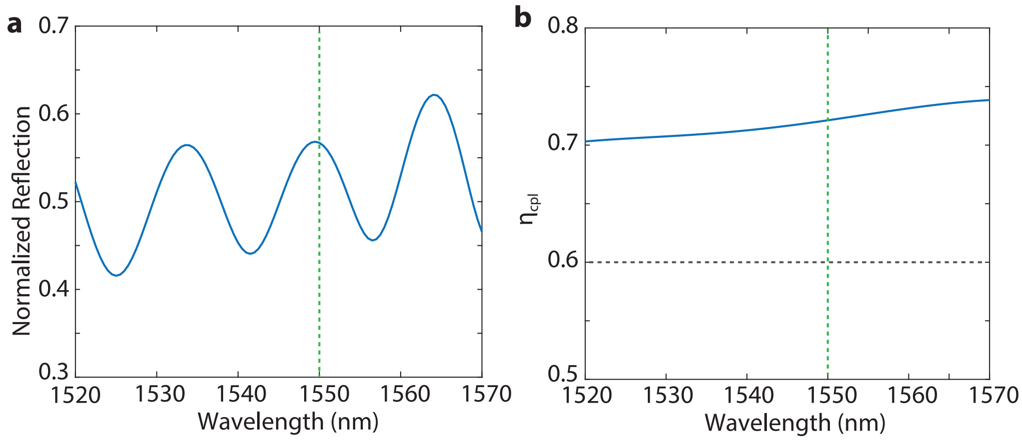

Figure 2.6: **Optical coupler Simulation.** **a** Broadband reflection spectrum of the optimized coupling waveguide design. **b** Estimate (blue solid) and measured (dashed black) single-pass coupling efficiency η_{cpl} .

this region. The shape of the center of the line defect waveguide is slowly changed from a geometry that provides no photonic bandgap, over a number of periods n_{trans}, to the 'C' shape which provides a photonic bandgap. Following n_{trans}, there are a variable number of mirror periods n_{mirr}. Reducing n_{mirr} will make a partially transparent mirror which serves as one side of the cavity's end-mirrors. In this way, a controllable amount of the incident light is permitted to leak through to the cavity region, while both of the mirror and defective region of the cavity are highly reflective for off-resonant frequencies. The coupling rate between the waveguide and cavity is exponentially dependent on n_{mirr} since light attenuates exponentially in the photonic crystal bandgap.

Figure 2.6a shows the broadband reflection spectrum of the optimized coupler, calculated by a finite-difference-time-domain simulation [51]. The amplitude and free spectral range of fringes in the spectrum are consistent with a low finesse Fabry-Pérot cavity formed by weak waveguide air interface reflection $R \approx 0.6\%$, and the near unity reflectivity photonic crystal mirror at the 2D line defect waveguide. Single-pass coupling efficiency η_{cpl} can be estimated from fringe visibility of broadband reflection spectrum, as shown in Fig.2.6b. The actual measured single-pass efficiencies are $\eta_{cpl} \approx 60.7\%$ for a 0-shield device and $\eta_{cpl} \approx 59.7\%$ for an 8-shield device. The difference between simulations and measurements is attributed to slight fabrication offsets—a small difference on the scale of several nanometers for the two sides of 1D tapered waveguide coupler may cause significant mode mismatch on both sides.

2.3.1 1D Waveguide to 2D Waveguide Coupling

The fiber to 1D waveguide coupling as well as the adiabatic tapering of the 1D waveguide in this quasi-2D OMC cavity device is very similar as in [6]. In this subsection, details about the 1D waveguide to 2D line-defect waveguide coupling will be discussed. Once the light has been coupled into the 1D waveguide, the optical mode needs to be subsequently coupled to 2D line-defect waveguide in order for 'end coupling' into the quasi-2D cavity. The design of 'end coupling' method will be introduced in the next subsection.

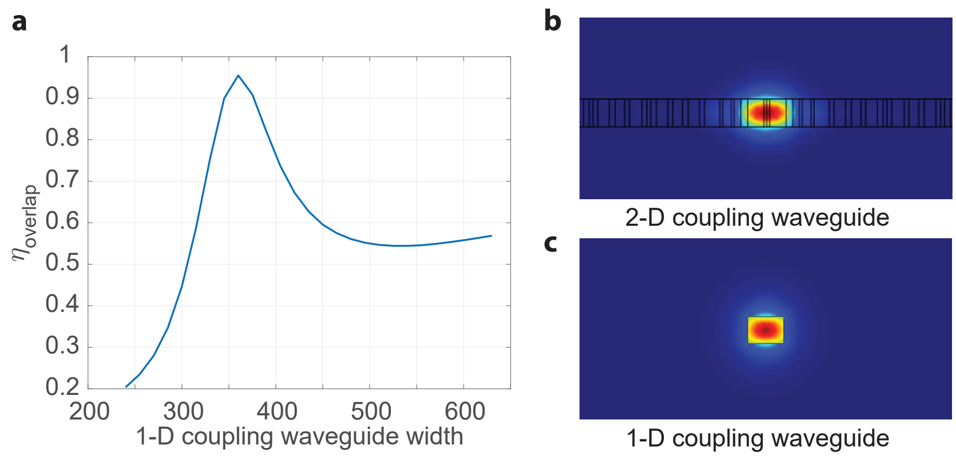

Figure 2.7: **End coupling overlap.** **a**, 1D Waveguide to 2D waveguide coupling efficiency η_{overlap} as a function of the 1D waveguide width (width of the side connecting 2D waveguide). **b**, FEM-simulated mode profiles of optical power in 1D waveguide and 2D waveguide.

For the quasi-2D photonic crystal structures used in this work, to which we wish to couple, only possess bandgaps for the TE-like polarizations where the electric field lies predominantly in the plane of the device layer (the $z = 0$ plane). Thus, we need only consider a single bound mode of each waveguide, with transverse field vectors $\mathbf{E}_{1\mathrm{D}}$ and $\mathbf{E}_{2\mathrm{D}}$ for the input 1D waveguide and output 2D waveguide, respectively. The 1D waveguide to 2D waveguide coupling efficiency η_{overlap} can be derived to be

$$\eta_{\mathrm{overlap}} = \mathrm{Re}\left[\frac{|\int dA(\mathbf{E}_{1\mathrm{D}} \times \mathbf{H}_{2\mathrm{D}}{}^{*}) \cdot \hat{x}|^2}{\int dA(\mathbf{E}_{2\mathrm{D}} \times \mathbf{H}_{2\mathrm{D}}{}^{*}) \cdot \hat{x}}\right] \frac{1}{\mathrm{Re}[\int dA(\mathbf{E}_{1\mathrm{D}} \times \mathbf{H}_{1\mathrm{D}}{}^{*}) \cdot \hat{x}]} \tag{2.1}$$

where $\hat{x}$ is the direction of propagation. The guided modes were calculated with FEM methods [37].In this work, the device layer has a fixed thickness (220nm Silicon), and the design of 2D waveguide is mostly decided by optomechanical crystal unit cell design. Thus optimization of the coupling efficiency only involves computed η_{overlap} as a function of width of 1D waveguide.

In Fig. 2.7a, η_{overlap} versus width of 1D waveguide is plotted, and we extract the maximum overlap integral efficiency of this 1D to 2D junction is 94%. Note that a small amount of reflection is neglected in this efficiency estimation, however, this small reflection together with the small reflection from fiber to 1D waveguide junction and reflection of mirrors in 2D line-defect waveguide create a weak resonant cavity, which will contribute to extra parasitic optical heating at milliKelvin temperature for quasi-2D devices in this work. This small reflection will be addressed in detail in Chapter 6. FEM-simulated mode profiles of optical power in 1D waveguide and 2D waveguide are also plotted in Fig. 2.7b and c.

2.3.2 Butt-Coupling from 2D Waveguide to Cavity

In this subsection, coupling from 2D waveguide to quasi-2D OMC cavity will be briefly introduced. Once the light has been coupled into the 2D waveguide, two approaches exist in order to further couple light into OMC cavity, either 'side-coupling' as designed in 1D nanobeam devices, or 'butt-coupling' used in quasi-2D devices. In this subsection, only the 'butt-coupling' approach will be discussed. As shown in Fig. 2.5 and already briefly discussed in the previous subsection, the mirror in the 2D line defect waveguide region is introduced gradually to avoid excess scattering in this region. The shape of the center of the line defect waveguide is slowly changed from a geometry that provides no photonic bandgap, over a number of periods n_{trans}, to the 'C' shape which provides a photonic bandgap. A controllable amount of the incident light is permitted to leak through to the cavity region. Since the cavity region is still highly reflective for non-resonant light, cavity region works as perfect mirror for light detuned from cavity resonance. Coupling rate between the waveguide and cavity (κ_{e}) is exponentially dependent on n_{mirr} and n_{trans} since light is attenuated exponentially in the mirror region.

FEM simulation of total load optical Q-factor (Q_{t}) and extrinsic Q-factor (Q_{e}) versus n_{trans} and for different n_{mirr} are plotted in Fig. 2.8a. FEM-simulated mode profiles of optical power for selected n_{trans} are also plotted in Fig. 2.8b. Note that the intrinsic Q-factor (Q_{i}) is not observed to be affected over a wide range of n_{trans} and n_{mirr}. The

Q_i of fabricated devices in this work is mainly limited by fabrication imperfections and was discussed in Chapter 1. FEM simulations show that, with modest Q_e values from 5×10^5 to 2×10^6, Q_i is limited to $\approx 5 \times 10^6$, where fabrication imperfection usually limit realized Q_i to below 1×10^6 in this work.

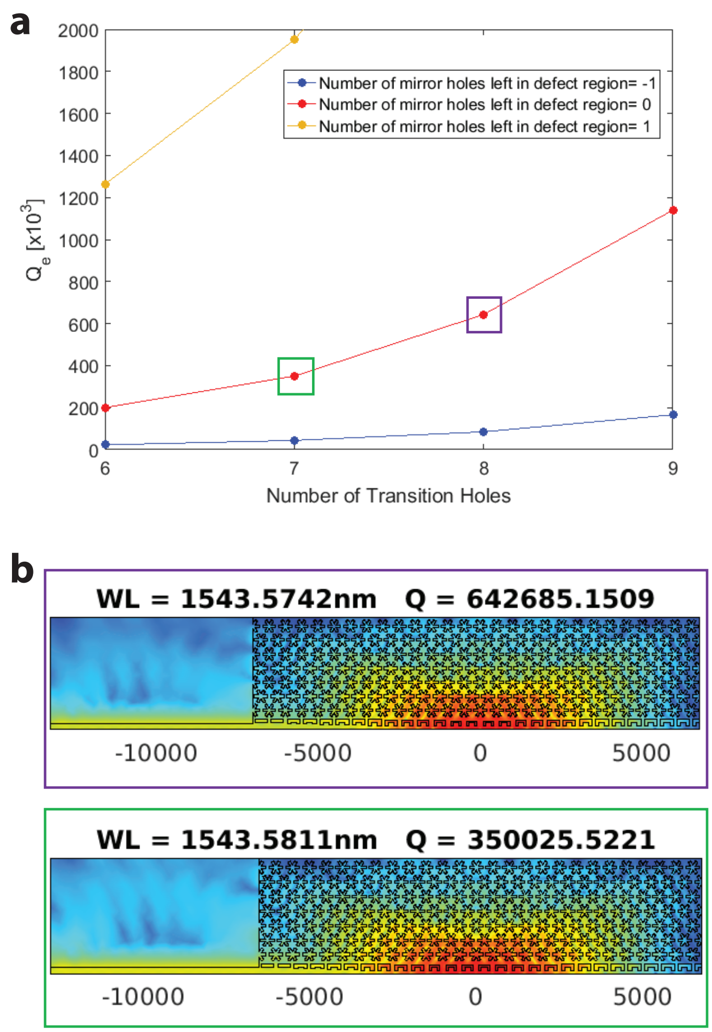

Figure 2.8: **2D waveguide to cavity extrinsic coupling.** **a**, 2D waveguide to cavity extrinsic coupling quality factor (Q_E) as a function of n_{trans} for different number n_{mirr}. **b**, FEM simulation of the optical field intensity for a butt-coupled quasi-2D cavity, normalized to its maximum and displayed on a logarithmic scale.

2.4 Imaging Feedback in Fabrication for Quasi-2D OMC Devices

The minimum critical features sizes in the quasi-2D devices are kept as 60 nm, for example, $h_o - h_i \geq 60$ nm, where 60 nm is a conservative gap size we can realize with the limits of our device fabrication. This minimum size is limited by the size requested using the e-beam pattern generator (EBPG) [52] plus a *blow-out* due to enlargement of features sizes comes from back-scattering of electrons during e-bean lithography and anisotropicity in the plasma etching. This *blow-out* value varies on different edges of the structure, therefore, it is necessary to figure out corresponding blow-out values in order to make sure the fabricated devices match the optimized design parameters.

Between fabrication iterations, SEM images of multiple realized devices are analyzed and the geometrical parameters are fitted and fed back into the next fabrication iteration in order to make the fabricated devices as close as possible to the simulation-optimized design parameters. Some examples of fitted 'C'-shape and snowflake holes are shown (red solid lines) in Fig. 2.9b, and corresponding fitted parameters are also plotted in Fig. 2.9b.

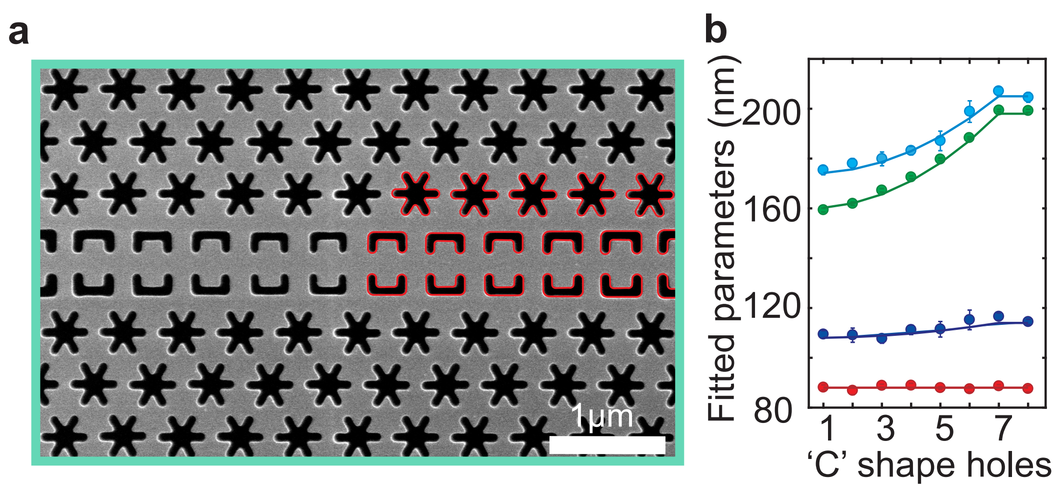

Figure 2.9: **Device fabrication feedback for quasi-2D devices.** **a** SEM image of the center of a OMC cavity with examples of fitting geometries (red solid lines) for 'C' shape holes and snowflake holes. **b** Examples of designed (solid lines) and fitted (dots) geometry parameters in the SEM-fitting feedback method, for h_i (blue), h_o (cyan), $w_i/2$ (red), and $w_o/2$ (green).

2.5 Device Characterization

Fabricated devices are characterized at room temperature (300 K). A dimpled optical fiber was used to evanescently couple light into and out of a 1D tapered coupling waveguide for each device tested. From the normalized optical spectrum (see Fig. 2.10a), we determine the wavelength of the fundamental optical resonance of the quasi-2D OMC to be $\lambda_o = 1558.8$ nm, with a loaded (intrinsic) optical Q-factor of $Q_t = 3.90 \times 10^5$ ($Q_i = 5.30 \times 10^5$). We measured the optomechanically coupled mechanical resonance using a pump-probe scheme with an optical pump frequency at the red motional sideband of the optical cavity [53], from which we find a mechanical frequency of $\omega_\mathrm{m}/2\pi = 10.21$ GHz (see Fig. 2.10b). From fitting the mechanical damping rate, γ, versus applied intra-cavity photon n_c (see Fig. 2.10b inset), we extract a vacuum coupling rate of $g_0/2\pi = 1.09$ MHz.

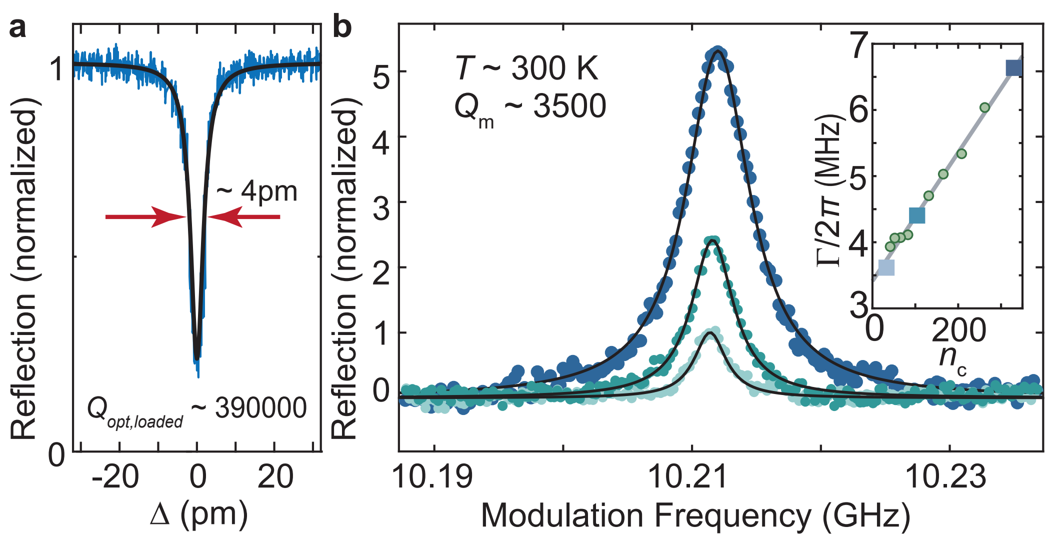

Figure 2.10: **Device characterization of Quasi-2D OMC device.** **a** Normalized wavelength scan of the optical mode of a quasi-2D OMC device with no phononic shielding ('zero-shield'). The wavelength of the fundamental optical resonance of the 2D OMC is determined to be $\lambda_\mathrm{o} = 1558.8$ nm, with a loaded (intrinsic) optical Q-factor of $Q_{opt,loaded} = 3.90 \times 10^5$ ($Q_\mathrm{i} = 5.30 \times 10^5$). **b** Normalized EIT scan of the mechanical mode of interest centered around $\omega_\mathrm{m}/2\pi = 10.21$ GHz at intracavity photons $n_\mathrm{c} = 33$ (light blue), $n_\mathrm{c} = 104$, and $n_\mathrm{c} = 330$ (dark blue). Inset shows mechanical mode linewidth versus n_c. Vacuum coupling rate $g_0/2\pi$ is extracted to be 1.09 MHz.

Chapter 3

OPTICAL MEASUREMENTS TECHNIQUES AT LOW-TEMPERATURE

In this chapter, multiple techniques and experimental methods used in the OMC device characterization at low temperature are presented.

3.1 Measurement Setup At Low-Temperature

3.1.1 Measurement Setup For 1D Nanobeam OMC

The full measurement setup used for 1D nanobeam OMC device characterization is shown in Fig. 3.1. The light source is a fiber-coupled tunable external-cavity diode laser, of which a small portion is sent to a wavemeter (λ-meter) for frequency stabilization. The light is then sent to high-finesse tunable fiber Fabry-Perot filter (Micron Optics FFP-TF2, bandwidth 50 MHz, FSR 20 GHz) to reject laser phase noise at the mechanical frequency, which can contribute to noise-photon counts on the SPDs. After this prefiltering, the light is routed to an electro-optic phase modulator (ϕ-mod) which is driven by an RF signal generator at the mechanical frequency to generate optical sidebands used for locking the detection-path filters. The light is then directed via 2×2 mechanical optical switches into a "high-extinction" path consisting of a series of modulator components which are driven by a digital pulse generator to generate high-extinction-ratio optical pulses. The digital pulse generator is used to synchronize the switching of the modulation components as well as to trigger the time-correlated single-photon-counting (TCSPC) module. Of these modulation components, two are electro-optic intensity modulators which together provide ~60 dB of fast extinction (~20 ns rise and fall times), and two are Agiltron NS 1×1 switches (rise time 100 ns, fall time ~30 μs) which provide a total of 36 dB of additional extinction. The total optical extinction used to generate our optical pulses is approximately 96 dB, which is greater than the cross-talk specification of our mechanical optical switches. For this reason we use two 2×2 switches in parallel to isolate the high-extinction path to ensure that our off-state optical power is limited by our high-extinction modulation components rather than by cross-talk through the mechanical switches. The light is then passed through a variable optical attenuator (VOA) to control the input pulse on-state power level to the cavity, and sent to a circulator which directs the light to a lensed-fiber tip for end-fire coupling to devices inside a dilution refrigerator. The reflected signal is then routed back to either one of two detection setups. The first includes an erbium-doped fiber amplifier (EDFA) and a high-speed photodetector (PD) connected to a spectrum analyzer (SA) and a vector network analyzer (VNA). The second detection path is used for the phonon counting measurements. Here, the light passes through three cascaded high-finesse tunable fiber Fabry-Perot filters (Micron Optics FFP-TF2) inside an insulating housing and then to the SPD inside the dilution refrigerator.

The cascaded fiber Fabry-Perot (FP) filters are aligned to the optical cavity resonance frequency ω_c during measurement such that the signal reaching the SPDs consists of sideband-scattered photons and a small contribution of laser-frequency pump-bleed-through. In total the filters suppress the pump by >100 dB. This bleed-through is calibrated by positioning the laser far off-resonance of the optical cavity, such that the device acts simply as a mirror, while fixing the relative detuning of the filters and the pump laser at the mechanical frequency $\omega_\mathrm{m}/2\pi$ and measuring the photon count rate on the SPDs as a function of laser power.

Additionally, both the FP-filters and the EOMs will drift during measurement and must be periodically re-locked. We therefore regularly stop the measurement and perform a re-locking routine. First, we re-lock the EOMs by applying a sinusoidal dithering signal of ~ 1 V to them while monitoring the optical transmission, then decrease the dithering amplitude gradually to lock to the minimum of transmission. Next we switch out of the high-extinction pulse path (SW-2A,2B) and out of the SPD path (SW-5), drive the phase modulator with a large RF power at $\omega_\mathrm{m}/2\pi$ to generate large optical sidebands at the cavity resonance frequency, and send this light into the FP-filter stack. The transmission through each filter is monitored while a dithering sinusoidal voltage is applied to each filter successively, and the amplitude and DC offset of the dithering signal are adjusted until the optical transmission signal at the desired sideband is maximized. The offset voltage is then held fixed during the subsequent measurement run. The filters will drift due to both thermal fluctuations and acoustic disturbances in their environment, so in order to further improve the filters' stability we have placed them inside a custom-built insulated housing.

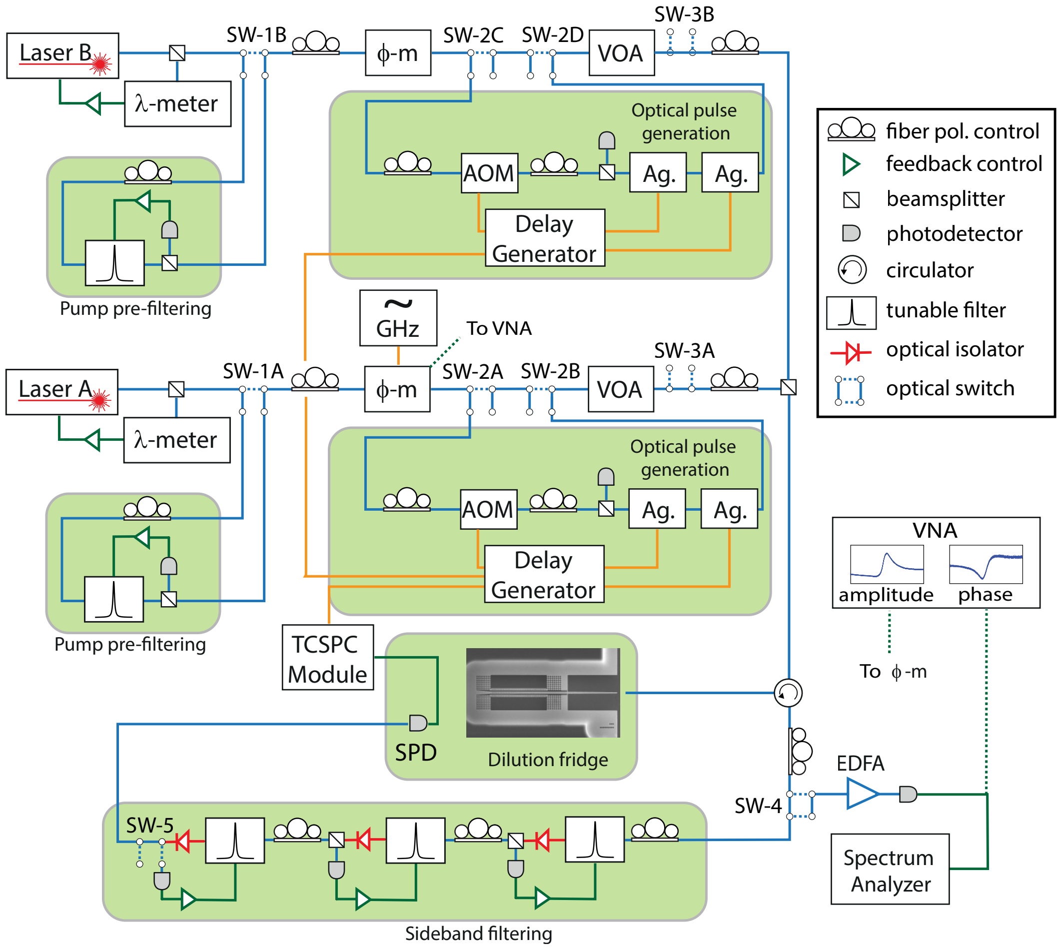

Figure 3.1: **Pulsed-excitation phonon counting measurement setup.** Simplified diagram of the experimental setup used for low-temperature optomechanical device characterization and phonon-counting measurements. Lasers A and B are passed through 50 MHz-bandwidth filters to suppress broadband spontaneous emission noise. Both lasers are equipped with modulation components (AOM, Ag.) for generating high-extinction optical pulses. The modulation components are triggered by a digital delay generator (Laser B components are triggered by the 'master' Laser A generator). Upon reflection from the device under test, a circulator routes the outgoing light to either (1) an EDFA and spectrum analyzer, or (2) a sideband-filtering bank consisting of three cascaded fiber Fabry-Perot filters (Micron Optics FFP-TF2) and the SPD operated at ~ 760 mK. λ-meter: wavemeter, ϕ-m: electro-optic phase modulator, EOM: electro-optic intensity modulator, AOM: acousto-optic modulator, Ag.: Agiltron 1x1 MEMS switch, SW: optical 2×2 switch, VOA: variable optical attenuator, EDFA: erbium-doped fiber amplifier, VNA: vector network analyzer, SPD: single photon detector, TCSPC: time-correlated single photon counting module (PicoQuant PicoHarp 300).

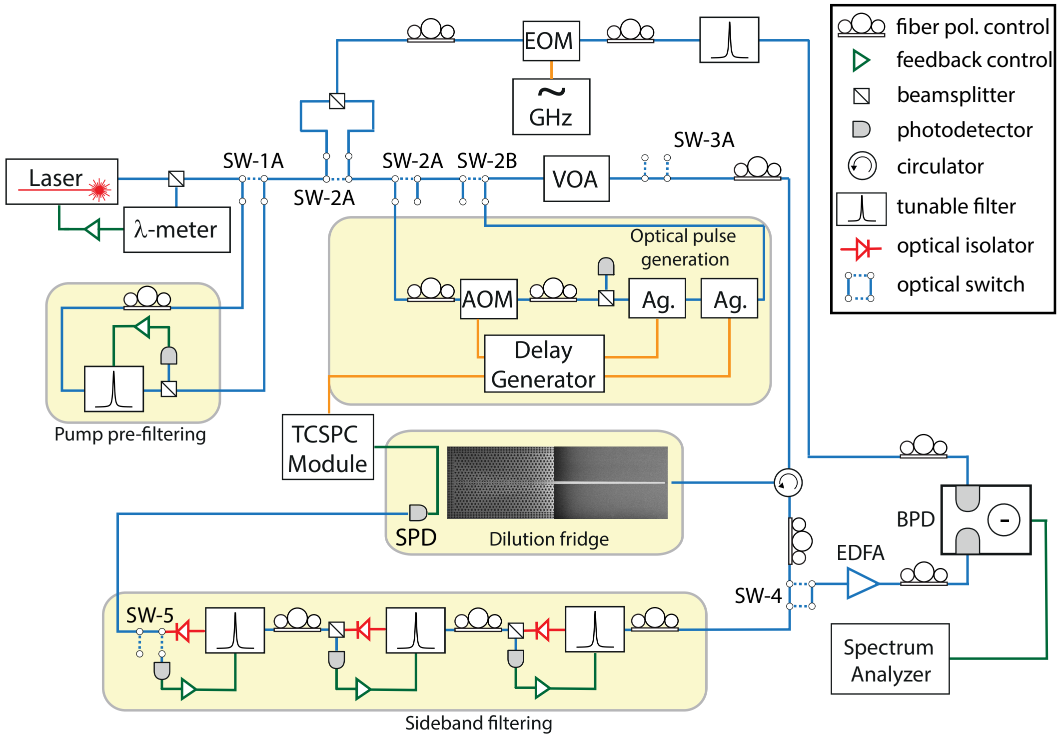

Figure 3.2: **Simplified diagram of the experimental setup used for 2D OMC.** Setup used for low-temperature optomechanical device characterization, heterodyne spectroscopy and phonon-counting measurements. A 1550nm optical signal is passed through 50 MHz-bandwidth filters to suppress broadband spontaneous emission noise, after which it can be switched between heterodyne spectroscopy or phonon-counting path. In the phonon-counting path, a modulation component (AOM, Ag.) is used for generating high-extinction optical pulses. The modulation components are triggered by a digital delay generator. In the heterodyne spectroscopy path, the light is divided into two paths, one path is passed through an electro-optic intensity modulator (EOM) and a filter to generate the local oscillator (LO) signal, the other path is sent to the optomechanical device. Upon reflection from the device under test, a circulator routes the outgoing light to either (1) an EDFA, tunable variable optical coupler, balanced photodiodes (BPD) and spectrum analyzer, or (2) a sideband-filtering bank consisting of three cascaded fiber Fabry-Perot filters (Micron Optics FFP-TF2) and the SPD operated at $\sim$ 760 mK. λ-meter: wavemeter, EOM: electro-optic intensity modulator, AOM: acousto-optic modulator, Ag.: Agiltron 1x1 MEMS switch, SW: optical 2×2 switch, VOA: variable optical attenuator, EDFA: erbium-doped fiber amplifier, BPD: balanced photodiodes, SPD: single photon detector, TCSPC: time-correlated single photon counting module (PicoQuant PicoHarp 300).

3.1.2 Measurement Setup for 2D OMC

The measurement setup used for 2D OMC device characterization is very similar to 1D nanobeam OMC device as shown in Fig. 3.2.

After prefiltering, the light can be switched by 2×2 mechanical optical switches between two paths, a "CW" path which detects the mechanical motion via balanced heterodyne detection of the scattered light, or a "pulsed" path using single-photon detectors. For the CW path, a 90/10 beam-splitter divides the laser source into local oscillator (LO, 90%, 0.5 - 1 mW) and signal (10%) beams. The LO is modulated by an electro-optic modulator (EOM) to generate a sideband at $\delta/2\pi = 50$ MHz from the mechanical frequency and is selected by high-finesse tunable Fabry-Perot filter before recombining it with the signal. The signal path is then sent to a variable optical attenuator and optical circulator which directs the laser to devices under test in the dilution refrigerator. The reflected signal beam carrying mechanical noise sidebands at $\omega_{\mathrm{L}} \pm \omega_{\mathrm{m}}$ is recombined with the LO on a tunable variable optical coupler (VC, not shown), the outputs of which are sent to a balanced photodetector (BPD). The detected difference photocurrent will contain a beat note with an approximate bandwidth γ near the LO detuning δ, chosen to lie within the detection bandwidth of the BPD. The pulsed path is the same as the setup used for 1D nanobeam OMC characterization as discussed in the previous section.

3.2 Calibration of Optomechanical Coupling Rate at Low Temperature

In this section, the method used for the calibration of optomechanical coupling rate at milikelvin remperature is introduced, and quasi-2D OMC measurement data is used as an example.

The measurements presented in this work rely on an accurate calibration of the parametric optomechanical coupling rate $\gamma_{\mathrm{OM}} = 4g_0^2 n_{\mathrm{c}}/\kappa$, where g_0 is vacuum optomechanical coupling rate, κ is the total optical decay rate and n_{c} is the intracavity photon number. The photon number n_{c} at a given power and detuning depends on the single pass fiber-to-waveguide coupling efficiency η_{cpl} and waveguide-to-cavity coupling efficiency $\eta_\kappa = \kappa_{\mathrm{e}}/\kappa$. The fiber-to-waveguide coupling efficiency η_{cpl} is determined by measuring the calibrated reflection level far off-resonance with the optical cavity on the optical power meter, and is found to be $\eta_{\mathrm{cpl}} = 0.59$ for a zero-shield device and $\eta_{\mathrm{cpl}} = 0.6$ for an eight-shield device. The waveguide-to-cavity coupling efficiency η_κ is measured by placing the frequency of the laser far off-resonance, using the VNA to drive an EOM and sweeping an optical sideband through the cavity frequency. Optical response is measured on a high-speed photodiode connected to the VNA signal port. The amplitude and phase response of the cavity is obtained, which are fitted to determine η_κ and κ. We measured $\kappa/2\pi$ = 1.11 GHz and $\eta_\kappa = 0.41$ for a zero-shield device, and $\kappa/2\pi$ = 1.19 GHz $\eta_\kappa = 0.19$ for an eight-shield device. With these three parameters measured, it is possible to determine n_c for an arbitrary input power to the cavities.

$$n_\mathrm{c} = \frac{P_\mathrm{in}}{\hbar\omega_\mathrm{L}} \frac{\kappa_\mathrm{e}}{\Delta^2 + (\kappa/2)^2}. \tag{3.1}$$

To extract the vacuum optomechanical coupling rate g_0, we measure the photon scattering rate per phonon in the mechanical mode. The photon count rate at the SPD for a red- or blue-detuned pump is C.9.

Here, $\Gamma_\mathrm{SB,0} = \eta_\mathrm{det}\eta_\mathrm{cpl}\eta_\kappa\gamma_\mathrm{OM}$ is the detected photon scattering rate per phonon on the SPD with experimental set-up efficiencies included. Here, η_det is the measured overall detection efficiency of the set-up, including losses in the fibers inside and outside of the dilution refrigerator, fiber unions and circulator, insertion losses in the filters and the detection efficiency of the SPD (η_SPD). We can then calibrate $\Gamma_\mathrm{SB,0}$ using a pulsed blue-detuned laser pump ($\Delta = -\omega_\mathrm{m}$). Repetition time ($\tau_\mathrm{per}$) of the blue-detuned pulses is selected to be much longer than $1/\gamma_0$, such that in the beginning of the pulse, the sideband photon count rate is estimated to be $\Gamma \approx \Gamma_\mathrm{SB,0}$ (provided $\Gamma_\mathrm{DCR} + \Gamma_\mathrm{pump}$ is much smaller than $\Gamma_\mathrm{SB,0}$ for relatively large n_c). Figure 3.3 shows an example measurement of calibrating $\Gamma_\mathrm{SB,0}$ and g_0. Using a measurement photon number of $n_\mathrm{c} = 57$, a $\Gamma_\mathrm{SB,0}$ of 2.887×10^3 is measured and $g_0/2\pi = 1.18$ MHz is extracted. Data is taken from a quasi-2D zero shield device.

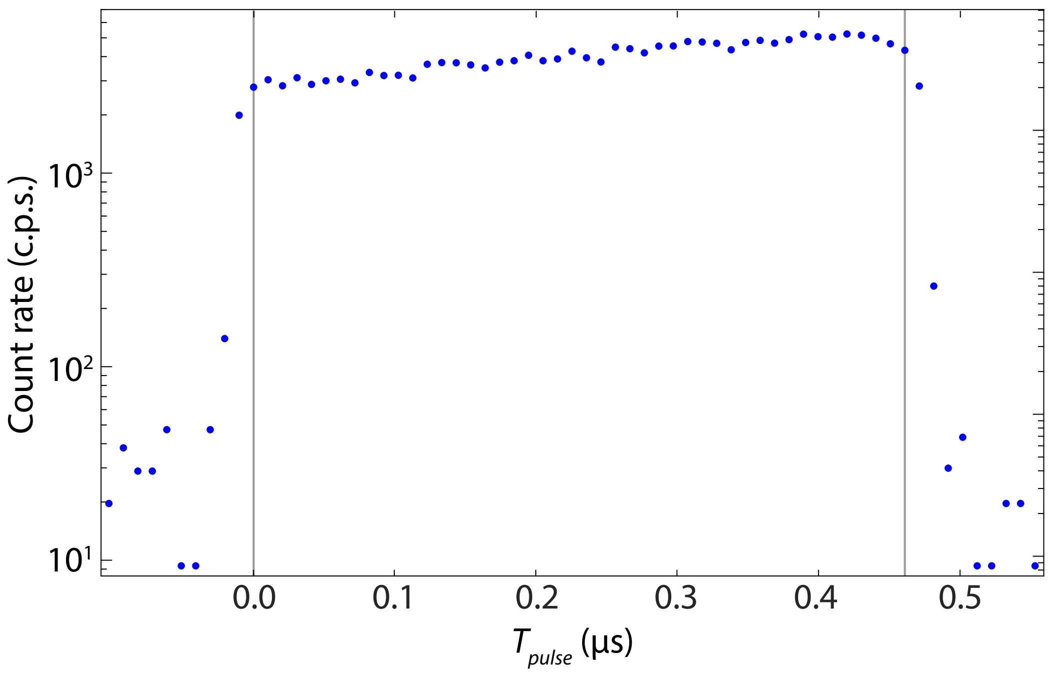

Figure 3.3: **Blue-detuned calibration of sideband photon scattering rate. a**, Plot of photon count rate during optical pulse for $\Delta = -\omega_{\mathrm{m}}$, $n_{\mathrm{c}} = 57$ and $T_{\mathrm{per}} = 0.2$ ms. The count rate of the initial measurement bin during the optical pulse, marked by the let gray vertical line, corresponds to scattered photon count rate of $\Gamma_{\mathrm{SB},0} = 2.887\times10^3$ c.p.s per phonon. During the pulse, optomechanical back-action amplifies the mechanical occupancy at a rate $\gamma_{\mathrm{OM}} - \gamma_{\mathrm{i}}$, while in the pulse-off state the mechanics undergoes free decay to a local fridge bath temperature with effective bath occupancy $n_0 \sim 10^{-3}$. Measurements performed on a zero-shield quasi-2D device with parameters $(\kappa, \kappa_{\mathrm{e}}, g_0, \omega_{\mathrm{m}}, \gamma_0) = 2\pi(1.11$ GHz, 455 MHz, 1.18 MHz, 10.238 GHz, 21.8 kHz).

3.3 Mode Thermalization Measurements

The mode of interest in 1D nanobeam OMC and quasi-2D OMC thermalizes to a base bath temperature T_b which is related to the applied DR temperature T_f through the thermal conductance C_thm of the structure as described in chapter 6. This yields an effective temperature offset between the DR temperature and the bath temperature.

The base bath temperatures of 1D nanobeam OMC devices and quasi-2D OMC devices are both measured and shown in this section. For the quasi-2D OMC, measurement of this base bath temperature uses a low-power ($n_\mathrm{c} = 9.9$) red-detuned pulsed probe and a device with relatively high mechanical damping $\gamma_0 = 21.8$ kHz ($Q_m = 4.69 \times 10^5$) to reduce data integration time. With relatively high mechanical damping, the mechanical mode can quickly be thermalized to its base temperature between subsequent incident optical pulses, such that a rapid measurement repetition rate $1/\tau_\mathrm{per}$ ($\tau_\mathrm{per} \gg \gamma_0^{-1}$) can be chosen. The initial mode occupancy during the pulse then approximately corresponds to bath occupancy n_0. However, as the optical probe turns on during the first several time bins of the pulse, the mode is heated such that the initial observed occupancy exceeds n_0. We therefore extract n_0 by fitting the pulse on-state occupancy data to the full dynamical heating and damping model, and extrapolate the fit back to $T_\mathrm{pulse} = 0$ to estimate the true bath occupancy n_0.

Fig.3.4 shows a fit of bath temperature of quasi-2D OMC, which yields $T_\mathrm{b} = 63$ mK, corresponding to a base mode occupation of $n_0 = 4 \times 10^{-4}$. Calculated curves for $T_\mathrm{b} = 11$ mK (red), 31 mK (yellow), 95 mK (green), 129 mK (cyan) are also plotted for reference.

For the 1D nanobeam OMC, measurement of this base bath temperature is very similar to the quasi-2D case, where fitting data is shown in Fig.3.5, which yields a best fit value $T_\mathrm{b} = 35.6$ mK, corresponding to an initial fridge bath occupancy of $n_0 = 1.1 \times 10^{-3}$. Bounds on the bath temperature are also shown in the figure, where the lower bound of 10 mK is set by the minimum applied fridge temperature, and the upper bound 60 mK corresponds to the directly observed occupancy value in the initial measurement bin.

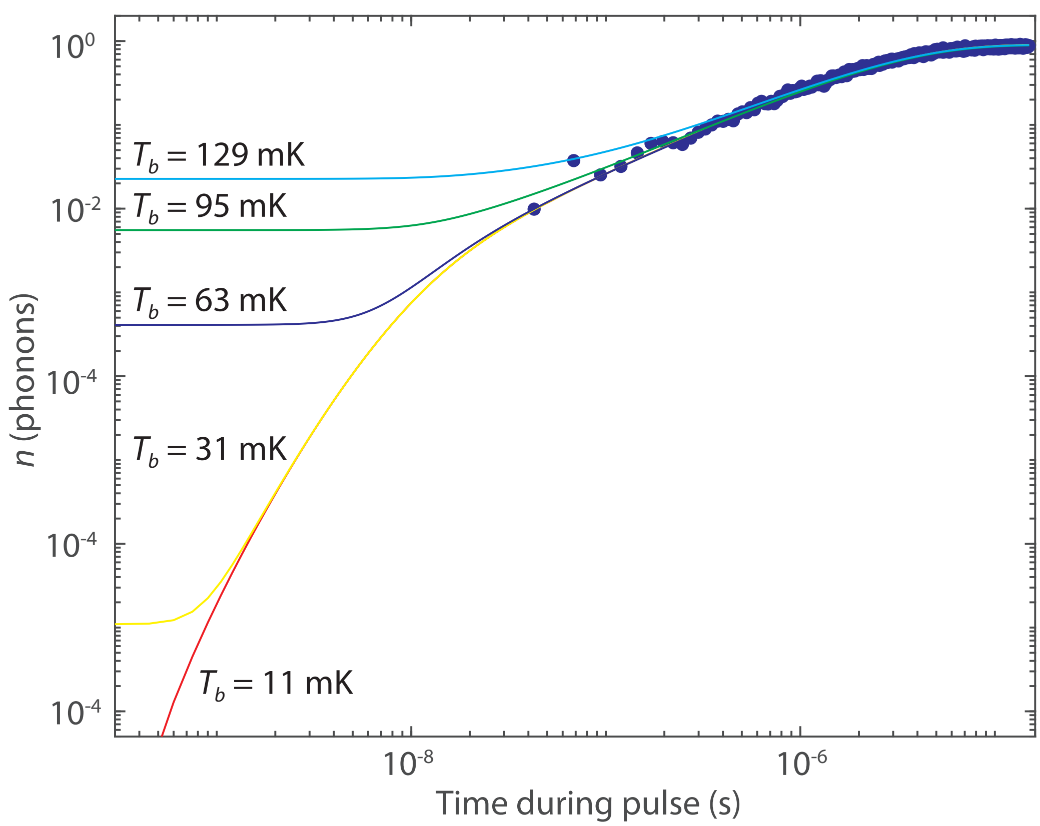

Figure 3.4: **Measurement of the base occupancy of the quasi-2D OMC phonon mode at an applied DR temperature of $T_\mathrm{f} \sim 10$ mK**. Readout photon number is chosen to be small ($n_\mathrm{c} = 9.9$) to minimize parasitic heating during the initial time bins of the pulse. Other measurement parameters are $\tau_\mathrm{pulse} = 10$ μs, $\tau_\mathrm{per} = 250$ μs, bin size 25.6 ns. Measurement is performed on the zero-shield device with parameters (κ, κ_e, g_0, ω_m, γ_0) = 2π(1.11 GHz, 455 MHz, 1.18 MHz, 10.238 GHz, 21.8 kHz). The heating model best-fit corresponds to a base mode temperature of $T_\mathrm{b} = 63$ mK ($n_0 = 4 \times 10^{-4}$, blue solid line). Calculated curves for $T_\mathrm{b} = 11$ mK (red), 31 mK (yellow), 95 mK (green), 129 mK (cyan) are also plotted for reference.

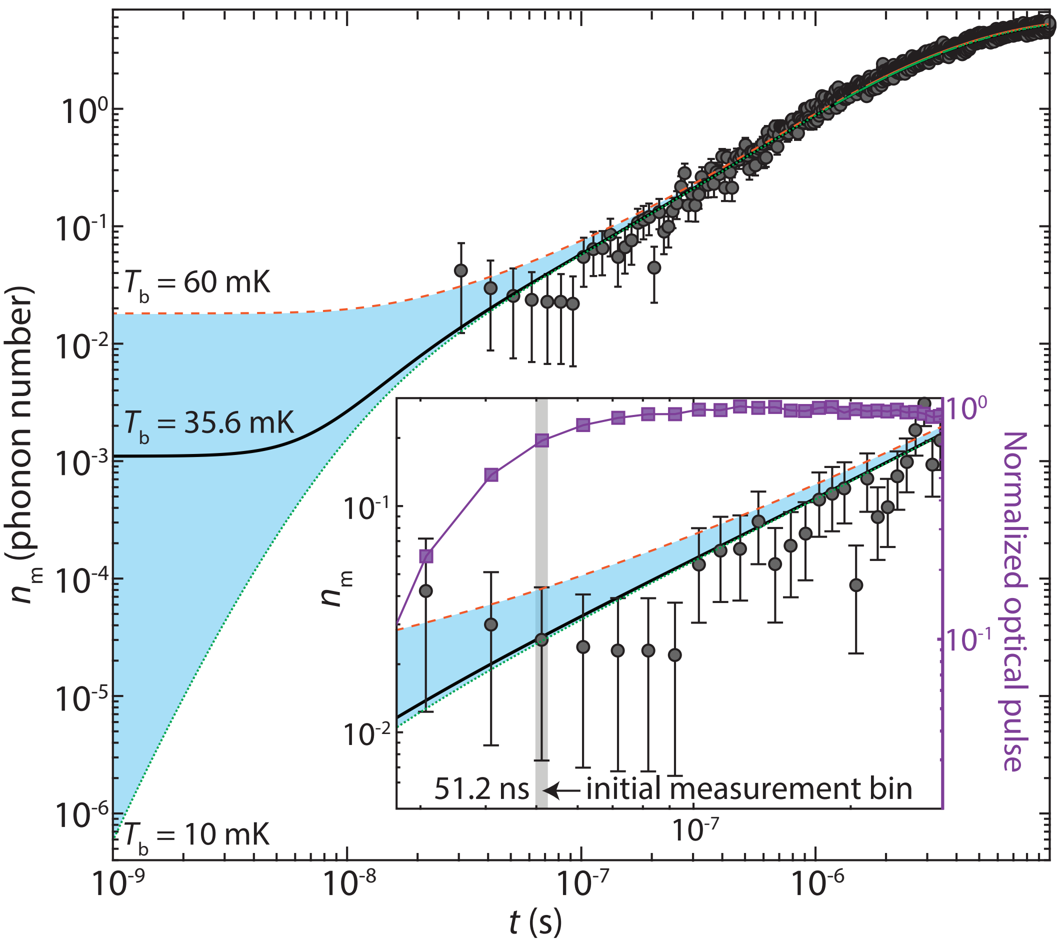

Figure 3.5: **Base occupancy measurement and pulse turn-on dynamics.** Mode occupancy during the pulse on-state of the zero-shield device (device A). The photon number $n_c = 10$ is chosen to be small to minimize parasitic heating during the initial time bins of the pulse (bin size is 10.24 ns.). The model best-fit corresponds to $T_b = 35.6$ mK. Bounding curves to the fit are shown for $T_b = 60$ mK (orange dashed line) and $T_b = 10$ mK (green dotted line). Inset: Overlay plot of the initial time bins of the mode occupancy curve and the input optical pulse (purple squares). Time bins earlier than 51.2 ns occur during the fast rise of the pulse, which occurs at a timescale set by the rise of the EOMs and optical switches. The first measurement bin is chosen at $t = 51.2$ ns, where the input optical pulse has reached > 70% of its nominal on-state value (here $n_c = 10$). For 10.24 ns binning as shown here, the initial measurement bin is bin #5. For 25.6 ns binning as shown in the Main Text figures, the initial bin is bin #2.

3.4 Thermal Ringdown Measurement of Mechanical Resonator

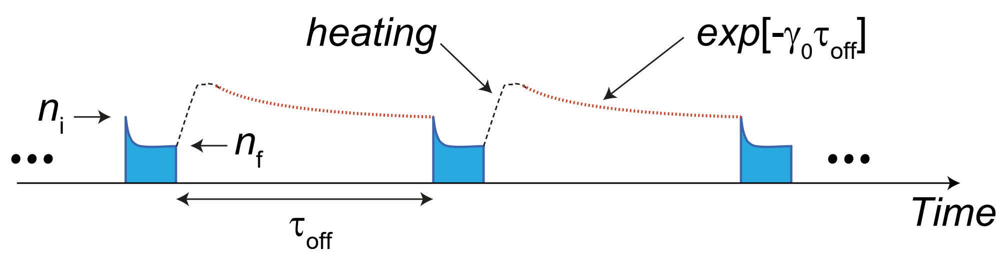

Figure 3.6: **Diagram of a thermal ringdown measurement performed using red-detuned ($\Delta = +\omega_\mathbf{m}$) excitation and readout.** The delay τ_off between subsequent pulses is varied. In the pulse-on state (blue), back-action cools the mode in the beginning of pulse from an initial mode occupancy. The optical-absorption-induced bath simultaneously heats the mode at a rate $\gamma_\text{p} n_\text{p}$, such that at later of the pulse a steady-state mode occupancy is reached. In the pulse-off state (τ_off), the residual phonon bath continues to heat the mode (dotted black line). $\gamma_\text{p}(t)$ is explicitly time dependent and will decay away on the time scales of 10 ms, then, mode occupancy further decays at a rate of γ_0 (dotted red line).

In order to measure the intrinsic mechanical Q-factor of a 1D nanobeam or quasi-2D OMC device by ringdown of the mechanical mode, we use a pulsed optical excitation and photon counting technique as presented in [54, 55]. A laser probe is red- or blue-detuned from the optical cavity by $\Delta = \omega_\text{c} - \omega_\text{l} = \pm\omega_\text{m}$ produces scattering sidebands at ω_c and $\omega_\text{c} \mp 2\omega_\text{m}$ due to emission or absorption of phonons. In a sideband resolved system such as ours ($\omega_\text{m} > \kappa$, where κ is the optical cavity linewidth), an intracavity photon number n_c at the laser frequency produces an effective optomechanical damping rate $\gamma_\text{OM} = \pm 4 g_0^2 n_\text{c}/\kappa$ in the case of red- or blue-detuning, respectively. After filtering the cavity reflection to suppress the pump, we perform photon counting of the Stokes or anti-Stokes sidebands. Because phonon emission and absorption events are correlated with the generation of a scattered photon, photon counting of the cavity frequency sideband is equivalent to phonon counting of the mechanical mode. For a red (blue) detuned pump, the anti-Stokes (Stokes) photon count rate is given by $\eta\gamma_\text{OM}\langle n\rangle$ ($\eta\gamma_\text{OM}(\langle n\rangle + 1)$), where η is the total detection efficiency of sideband-scattered photons and $\langle n\rangle$ is the mechanical mode occupancy. This phonon-counting technique then allows for vacuum-noise calibrated thermometry of the mechanical mode as a function of time during an optical excitation pulse by measuring photon count rates.

We perform ringdown measurements on an eight-shield device by impinging a series of red-detuned ($\Delta = \omega_{\mathrm{m}}$) optical excitation pulses on the device. Light is pulsed on for a duration $\tau_{\mathrm{pulse}} = 10\ \mu$s and then off for a variable time τ_{off}. The reflected photons due to anti-Stokes scattering of the probe laser, which are on-resonance with the optical cavity, are then filtered from the probe laser and sent to a single photon detector producing a photon count rate to be used for phonon counting.

At milliKelvin temperatures, the dynamics of $\langle n \rangle$ during the pulse is dominated by two processes: back-action cooling via the red-detuned pump, and parasitic optical-absorption heating which has previously been characterized in similar devices at milliKelvin temperatures [29, 56]. The optical absorption can be modeled phenomenologically as introducing an effective hot phonon bath of occupancy n_{p} which couples to the mode of interest at a rate γ_{p}. Thus, during the pulse-on state, the total mechanical damping rate is $\gamma = \gamma_0 + \gamma_{\mathrm{p}} + \gamma_{\mathrm{OM}}$, where γ_0 is the intrinsic damping rate to the local milliKelvin DR bath of occupancy n_0. Thus, the steady-state occupancy can be expressed as $n_{\mathrm{f}} = (\gamma_{\mathrm{p}} n_{\mathrm{p}} + \gamma_0 n_0)/\gamma$. The hot phonon bath does not leave the cavity instantaneously after the pulse is turned off, but rather introduces a transient heating lasting several microseconds, resulting in heating to a peak occupancy n_{peak}. At longer times τ_{off} in the pulse-off state, the mechanics undergoes free exponential decay such that

$$n_{\mathrm{i},k+1} = n_{\mathrm{peak},k} e^{-\gamma_0 \tau_{\mathrm{off}}}, \tag{3.2}$$

where the subscript k labels the k^{th} pulse. For each pulse off period τ_{off}, the photon count rate during the pulse is averaged over many cycles to generate a histogram of $\langle n \rangle$ as a function of time τ_{pulse} in the pulse-on state. The initial mode occupancy during the pulse (n_{i}) for different τ_{off} are fitted to obtain an intrinsic decay rate γ_0 as shown in a later chapter, from which we extract an intrinsic decay rate $\gamma_0/2\pi = 8.28$ Hz, corresponding to a mechanical Q-factor of 1.2×10^9 for quasi-2D OMC device, and mechanical Q-factors as high as 5×10^{10} for 1D nanobeam OMC devices.

3.5 Coherent Excitation Methods

3.5.1 Low-Threshold Acoustic Self-Oscillation

Owing to the extremely slow intrinsic damping rate γ_0 observed in the ultra-high-Q nanobeam devices at low temperatures, it is possible to drive the mechanics into the regime of self-sustained oscillations with a blue-detuned pumping laser at very low input optical powers, or equivalently, a very low rate of measurement back-action. The total effective damping rate experienced by the mechanics in the presence of a blue-detuned drive laser is $\gamma = \gamma_\mathrm{i} - \gamma_\mathrm{OM}$, where the intrinsic damping rate $\gamma_\mathrm{i} = \gamma_0 + \gamma_\mathrm{p}$ includes damping γ_0 from both the cold fridge bath (with occupancy $n_0 \approx 10^{-3}$) and from the optical absorption-induced phonon bath at rate γ_p. The usual condition for self-oscillation is that the damping rate is matched by the back-action amplification rate γ_OM:

$$\gamma_\mathrm{OM} = \gamma_0 + \gamma_\mathrm{p}. \tag{3.3}$$

We observe the onset of mechanical self-oscillation at $T_\mathrm{f} = 10$ mK, in which a CW blue-detuned pump laser drives the cavity and the sideband filters are aligned to the cavity resonance ($\Delta = 0$). The scattered photon count rate $\Gamma_\mathrm{SB,0}$ is measured in steady-state. In the setup configuration used for these measurements, an additional VOA is placed in the optical path, elevating the measured SPD dark count rate to 10.8 c.p.s. Sweeping the input power (photon number) n_c results in a sharp increase in detected count rate at the self-oscillation threshold $n_\mathrm{c,thresh} = 2 \times 10^{-3}$ as shown in Figure 3.7, where we estimate the resulting steady-state phonon occupancy to be of order $\langle n \rangle \sim 5 \times 10^4$. At the threshold $n_\mathrm{c,thresh}$, we can estimate the back-action amplification rate $\gamma_\mathrm{OM}/2\pi = 4g_0^2 n_\mathrm{c,thresh}/\kappa \approx 8$ Hz from the known optical device parameters, indicating that the intrinsic damping γ_i is dominated by the bath damping rate: $\gamma_\mathrm{p}(n_\mathrm{c,thresh}) = \gamma_\mathrm{OM}(n_\mathrm{c,thresh}) - \gamma_0 \approx 2\pi(7.9\text{ Hz})$, in good quantitative agreement with the trend measured on a similar device discussed in later chapters.

Upon decreasing the driving power (green data in Figure 3.7), self-oscillation appears to relax at a decreased threshold of $n_\mathrm{c} = 1.4 \times 10^{-3}$, indicating a hysteresis in the measured count rates as a function of input power. This apparent hysteresis likely arises from a change in the *true* intracavity photon number as a function of driving power P_in. We have so far adhered to Equation 3.1 in determining the n_c as a function of P_in; this expression is used to generate the horizontal axis of Figure 3.7,

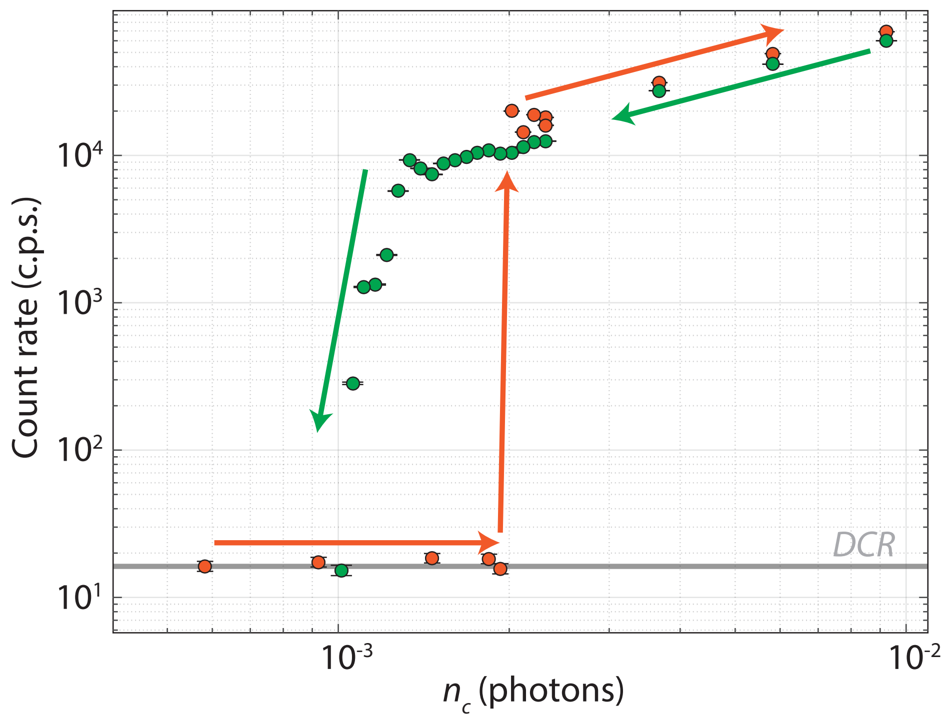

Figure 3.7: **Low-temperature measurement of the self-oscillation threshold in a high-Q nanobeam at T_f = 10 mK.** Under blue-detuned ($\Delta = -\omega_m$) driving the self-oscillation threshold is reached when $\gamma_\mathrm{OM} = \gamma_\mathrm{i}$, here for $n_\mathrm{c,thresh} = 2 \times 10^{-3}$, or $\gamma_\mathrm{OM}/2\pi$ = 8 Hz, for increasing optical power (orange points). Measurements were performed on 1D nanobeam OMC device D.

and so does not represent the true intracavity photon number. However, in order to unambiguously calculate n_c in the presence of large phonon amplitude $\langle n \rangle$, a more thorough calculation is needed which accounts for the effective optical reflection profile in the presence of strong modulation by the mechanical motion.

3.5.2 Electromagnetically Induced Transparency Mechanical Spectroscopy

Electromagnetically induced transparency (EIT) in optomechanical systems allows for a spectral measurement of the mechanical response via observation of a transparency window in the optical reflection spectrum. A pump laser tone at ω_L is amplitude modulated to generate a weak probe tone at $\omega_{\mathrm{s},\pm} = \omega_\mathrm{L} \pm \Delta_\mathrm{p}$. If the pump-cavity detuning is fixed on either the red- or blue-side of the optical cavity ($\Delta = \pm\omega_\mathrm{m}$), the optical susceptibility of the cavity strongly suppresses one of the probe sidebands (at $\omega_{\mathrm{s},\mp}$) and only the other probe sideband will have an appreciable intracavity population. For a red-detuned pump, starting from Heisenberg-Langevin

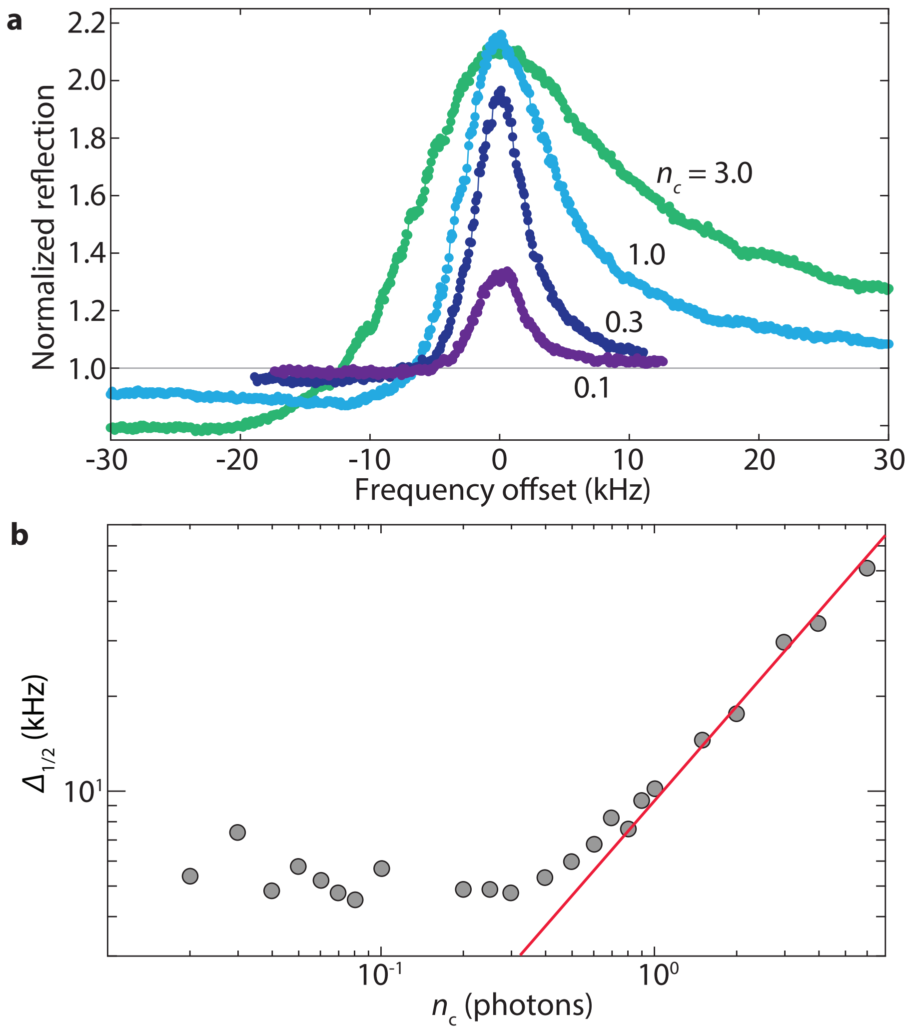

Figure 3.8: **Mechanical mode time-averaged linewidth versus probe power. a,** Time-averaged mechanical mode linewidth as a function of optical pump power. Broadening of the linewidth is due to optical back-action. Solid line is a fit to the back-action damping rate $\gamma_{\mathrm{OM}} = 4g_0^2 n_{\mathrm{c}}/\kappa$, from which we extract an estimated $g_0/2\pi = 1.15$ MHz. Measurements are performed on Device D.

equations of motion for the optical and mechanical fields (Replacing $(\hat{a}, \hat{b}) \longrightarrow (\alpha, \beta)$ and $(\hat{a}_{\text{in}}, \hat{b}_{\text{in}}) \longrightarrow (\alpha_{\text{in}}, \beta_{\text{in}})$ since we only focus on coherent fields here.):

$$\dot{\alpha} = -\left(i\Delta + \frac{\kappa}{2}\right)\alpha - ig_0\alpha(\beta^* + \beta) + \sqrt{\kappa_{\text{e}}}\alpha_{\text{in}}, \tag{3.4}$$

$$\dot{\beta} = -\left(i\omega_m + \frac{\gamma_i}{2}\right)\beta - ig_0|\alpha|^2 + \sqrt{\gamma_i}\beta_{in}, \tag{3.5}$$

take into account:

$$\alpha \approx \alpha_0 + \alpha_- e^{-i\Delta_{\text{p}}t} + \alpha_+ e^{i\Delta_{\text{p}}t}, \tag{3.6}$$

$$\beta \approx \beta_0 + \beta_- e^{-i\Delta_{\text{p}}t} + \beta_+ e^{i\Delta_{\text{p}}t}. \tag{3.7}$$

$$|\alpha_\pm| \ll |\alpha_0| \tag{3.8}$$

$$r(\Delta, \delta) = 1 - \frac{\kappa_{\text{e}}}{\kappa/2 + i(\Delta - (\delta + \omega_{\text{m}})) + \frac{|G|^2}{-i\delta + \gamma_{\text{i}}/2}}, \tag{3.9}$$

for optical sideband generated in the optical path, we arrive at:

$$-i\Delta_{\text{p}}\alpha_\pm = -\left(i\Delta + \frac{\kappa}{2}\right)\alpha_\pm - ig_0\alpha_0\beta_\pm + \sqrt{\kappa_{\text{e}}}\alpha_{\text{in},\pm}, \tag{3.10}$$

$$-i\Delta_{\text{p}}\beta_- = -\left(i\omega_m + \frac{\gamma_i}{2}\right)\beta_- - ig_0(\alpha_0^*\alpha_- + \alpha_0\alpha_+^*) + \sqrt{\gamma_i}\beta_{\text{in,-}}. \tag{3.11}$$

For the red-detuned case where $\Delta = +\omega_m > 0$, in the rotating wave approximation we arrive at

$$\beta_- = \frac{-ig_0(\alpha_0^*\alpha_-) + \sqrt{\gamma_i}\beta_{\text{in,-}}}{-i(\Delta_{\text{p}} - \omega_m) + \frac{\gamma_i}{2}}, \tag{3.12}$$

$$\alpha_- = \left(i(\Delta - \Delta_{\text{p}}) + \frac{\kappa}{2} + \frac{|G|^2}{-i(\Delta_{\text{p}} - \omega_m) + \gamma_i/2}\right)^{-1}\left(\frac{iG\sqrt{\gamma_i}\beta_{\text{in,-}}}{-i(\Delta_{\text{p}} - \omega_m) + \gamma_i/2} - \sqrt{\kappa_{\text{e}}}\alpha_{\text{in,-}}\right), \tag{3.13}$$

with input-output formalism boundary condition

$$\alpha_{\text{out,-}} = \alpha_{\text{in, -}} - \sqrt{\kappa_e}\alpha_-, \tag{3.14}$$

and we derive the interaction of the pump tone and mechanics with the probe sideband yielded reflection coefficienct $r(\Delta, \delta)$ for the probe which contains a transparency window having a width on the scale of the mechanical mode linewidth:

$$r(\delta) = \frac{\alpha_{\text{out,-}}}{\alpha_{\text{in,-}}} = 1 - \frac{\kappa_e}{i(\Delta - (\delta + \omega_m)) + \frac{\kappa}{2} + \frac{|G|^2}{-i\delta + \gamma_i/2}}, \tag{3.15}$$

where we have defined $\delta \equiv \Delta_p - \omega_m$ and $G \equiv g_0\sqrt{n_c}$.

We measure the reflection amplitude $R = |r|^2$ by driving an EOM weakly to generate a probe tone and observing the count rates of sideband-scattered probe photons. The pump is locked at $\Delta = +\omega_m$ and the cascaded filter stack is locked to the cavity frequency. The RF modulation power is chosen to generate a sideband intracavity photon number much smaller than the carrier photon number ($n_{c,+} \ll n_c$) while maintaining a large count rate $\sim 10^5$ c.p.s. at the SPDs to minimize data integration times. This corresponds to modulation indices in the range of $\beta \sim 10^{-3}$ for our system parameters (measurements were performed on 1D nanobeam OMC device D). The modulation frequency Δ_p is swept over a range of about 1 MHz to map out the transparency window. This range is large enough to include the optomechanically-broadened mechanical linewidth which sets the width of the transparency window, but much narrower than the bandwidth of the FFP filters ($\approx$ 50 MHz), allowing for the filters to be stably locked at a single position in the center of the optical cavity line. Figure 3.8 shows the normalized reflection level for various optical probe power levels n_c, as well as fits to the data. The extracted total mechanical linewidth $\gamma = \gamma_i + \gamma_p + \gamma_{OM}$ is plotted in Fig. 3.8. At low probe-power, $\gamma/2\pi$ saturates to a value $\approx$ 4 kHz, which represents time-averaged broadening of the intrinsic mechanical linewidth due to mechanical frequency jitter. With κ and n_c calibrated, the linear portion of the curve which is dominated by back-action damping is fitted to extract the optomechanical coupling rate $g_0/2\pi = 1.15$ MHz.

Same method can also be used for individual fast frequency sweep measurements. Figure. 3.9 shows 4 normalized individual spectrum of rapid frequency sweeps, and each sweep take about 8 seconds in these plots. Jitter of the fast mechanical frequency during this measurement time for each plot appears as one or many individual narrow mechanical response peaks, with each peak bandwidth $\lesssim$ 500 Hz. Even faster sweeps and more detailed analysis of EIT sweeps will be discussed in later chapters.

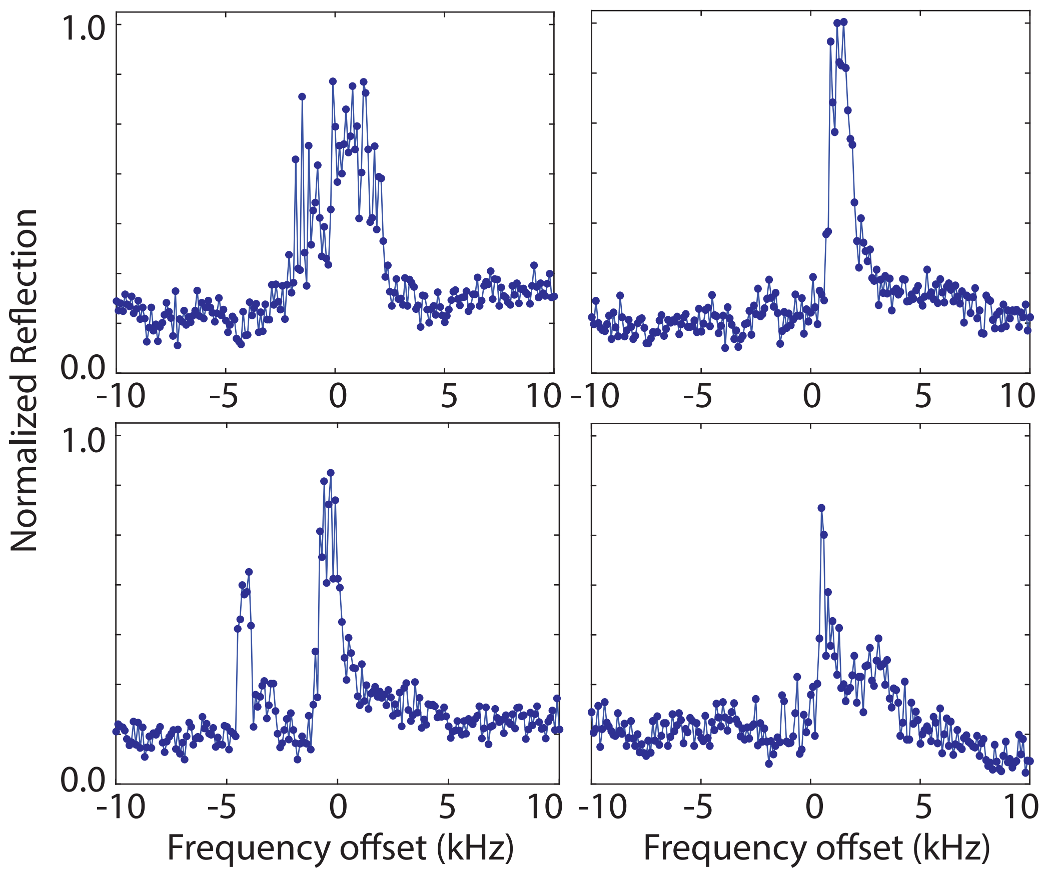

Figure 3.9: **Individual spectrum of rapid frequency sweeps.** Four normalized individual spectrum of rapid frequency sweeps. Data were taken with pump power $n_{\mathrm{c,pump}} = 0.1$, probe power $n_{\mathrm{c,probe}} = 10^{-2}$, frequency resolution 100 Hz, and frequency step dwell time 10 ms.

3.6 Blue-Detuned Pumping and Ringdown

In the limit of high phonon amplitude, we perform ringdown using a pulse sequence consisting of a blue-detuned excitation pulse followed by a red-detuned readout (or *probe*) pulse. Two separate laser sources are usedfor generating the excitation and readout pulses in order to allow a fixed detuning of each laser to avoid instabilities associated with rapid stabilization of the laser frequency on the timescale of the pulse sequencing (tens of μs). Owing to the extremely narrow instantaneous mechani-

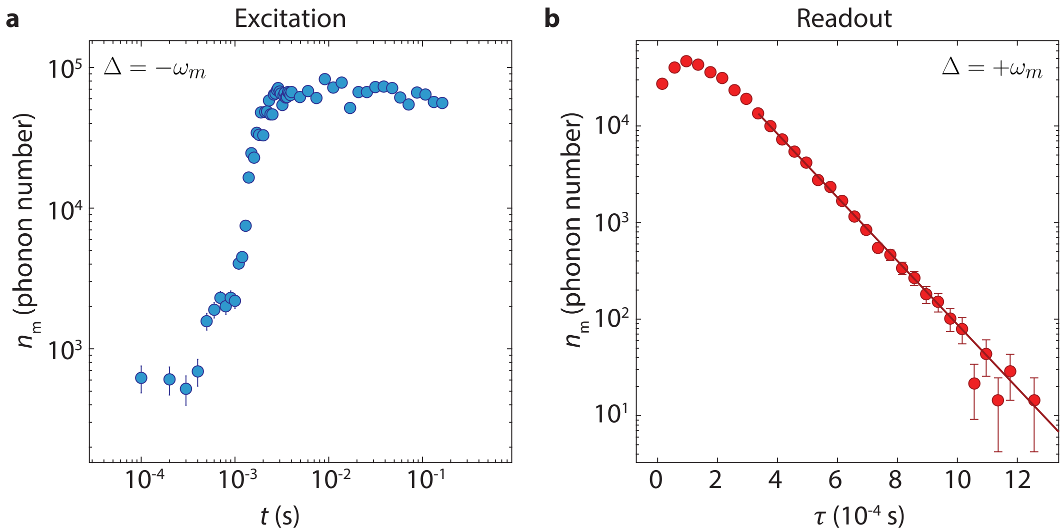

Figure 3.10: **Measurement of the mode occupancy during excitation and readout pulses for high-amplitude ringdown.** **a**, A blue-detuned ($\Delta = -\omega_m$) laser with pulse-on photon number $n_{\text{c,blue}} = 0.15$ drives the mechanics into self-oscillation in a timescale of 2 ms, with a saturated phonon occupancy $\langle n \rangle \approx 5 \times 10^4$. **b**, A red-detuned ($\Delta = +\omega_m$) probe laser with pulse-on photon number $n_{\text{c,red}} = 0.30$ serves to read out the mode occupancy after a variable delay time τ_{off}. Measurements are performed on the 1D nanobeam OMC Device D.

cal mode linewidth, a very small back-action amplification rate $\gamma_{\text{OM}}/2\pi \lesssim 8$ Hz is required to drive the mechanics into the self-oscillation regime. This enables operation at low driving pulse photon number $n_{\text{c,blue}} = 0.15 \gg n_{\text{c,thresh}} = 2 \times 10^{-3}$, in order to minimize the effective temperature and coupling rate of the absorption-induced phonon bath. The steady-state phonon amplitude in the presence of the driving pulse is saturated to $\langle n \rangle \approx 5 \times 10^4$. The driving pulse is turned off, and after a variable delay time τ_{off}, a red-detuned pulse from the readout laser is used to probe the mode occupancy.

The readout photon number $n_{\text{c,red}} = 0.30$ is again chosen small to minimize absorption bath effects, as well as to give a total count rate $\Gamma \propto \Gamma_{\text{SB},0}\langle n \rangle \propto n_{\text{c}}\langle n \rangle$ within the dynamic range of the single-photon detector, which in our amplifier setup has a sensitivity to a maximum count rate of $\sim 2 \times 10^6$ c.p.s. With the present setup efficiencies and device parameters (see caption of Figure 3.10), the detected count rate is approximately $\Gamma = 31$ c.p.s. per phonon per photon at $\Delta = \pm\omega_m$, and the resulting effective upper bound on $n_{\text{c,red}}$ at which the SPD can efficiently detect is 2.2 photons. Now, after the readout pulse is used to probe the mode occupancy, the mode

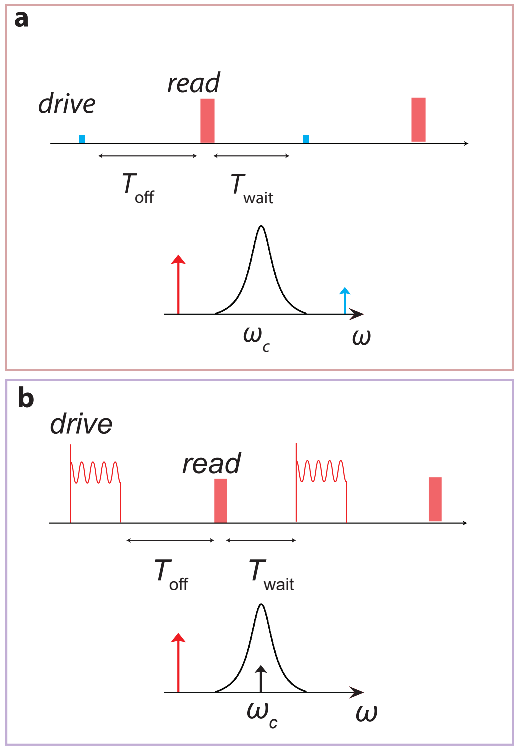

Figure 3.11: **Diagram of coherent excitation and readout pulses for high-amplitude ringdown.** Acoustic excitation is performed coherently by using either **a**, a blue-detuned pump to drive the breathing mode into self-oscillation, or using **b**, an RF-modulated red-detuned pump [53] (lower diagram).

occupancy is cooled via dynamical back-action to near its local bath temperature in preparation for the subsequent series of driving and readout pulses (effectively 're-setting' the measurement). In practice, a single red-detuned pulse is used for both readout and cooling (re-setting). In Figure **??** we show the phonon occupancy during both the driving pulse and the readout pulse. Note that the excited occupancy saturates to $\langle n \rangle \approx 5 \times 10^4$ from an initial occupancy $\langle n \rangle \lesssim 1 \times 10^3$, corresponding to our estimated decay ratio of 50 from one pulse period to the next. A diagram of blue pump excitation and readout pulses for high-amplitude ringdown is shown in Figure 3.11 a.

3.7 Modulated Pump-Probe Excitation and Ringdown

For a finer control of the mechanical mode amplitude during excitation, microwave-frequency modulation of the excitation pulse was used to amplify the mechanics to a fixed phonon amplitude which is tunable by the depth of optical modulation placed on the pump laser tone. This technique allows us to probe the intrinsic energy decay constant γ_0 in the regime lying intermediate between the level of single-phonons and the saturated high-phonon-amplitude limit of self-oscillation.

As shown in Figure 3.11b, in this measurement scheme, a radio-frequency (RF) signal generator is used to drive an electro-optic intensity modulator (EOM) at the mechanical resonance frequency $\omega_m/2\pi$ to generate the probe sideband. The excitation pulse consists of a red-detuned pump carrier tone which is weakly modulated (RF driving power -4 dBm applied to an EOM with $V_\pi = 4.1$ V, giving a modulation index $\beta = 0.11$) to generate a probe sideband at the cavity resonance frequency. Interference between the pump carrier and probe sideband generates a time-dependent radiation pressure force at the difference frequency $\omega_m/2\pi$, which resonantly excites the acoustic mode. A second pulsed laser source is then used to generate the readout optical pulse, which is a red-detuned pulse of fixed frequency and power.

In both the cases of blue-detuned driving and RF-modulated driving ring-up techniques, the total repetition rate of the pulse sequence $1/\tau_{\text{per}}$ is fixed while only the variable delay τ_{off} between the driving pulse and readout pulse is varied. This fixing of the overall duty-cycle of the pulse sequence is performed to eliminate systematic variations in the local absorption-induced bath temperature T_b which, in steady-state, is expected to depend on the average power circulating in the cavity (see Fig. 6.4). We find that the measured ringdown time constant is approximately consistent over more than three orders of magnitude in starting phonon population, from $\langle n \rangle \lesssim 10$ in the case of thermally-excited ringdown measurements to $\langle n \rangle > 2 \times 10^4$ in the case of coherently-excited phonon populations.

Chapter 4

PHONONIC BANDGAP NANO-ACOUSTIC CAVITY WITH ULTRALONG PHONON LIFETIME

Critical to applications such as time keeping and sensing, is the ability of a mechanical resonator to store vibrational energy at a well defined frequency of oscillation with minimal damping. Here, we present measurements at millikelvin temperatures of the microwave-frequency acoustic properties of a crystalline silicon nanobeam cavity incorporating a phononic bandgap clamping structure. Utilizing pulsed laser light to excite a co-localized optical mode of the cavity, we measure the internal acoustic modes with single-phonon sensitivity, yielding a phonon lifetime of up to $\tau_{\mathrm{ph},0} \approx 1.5$ seconds ($Q = 5 \times 10^{10}$) and a coherence time of $\tau_{\mathrm{coh},0} \approx 130$ μs for bandgap-shielded cavities. Potential applications of these ultra-coherent nanoscale resonators range from tests of various collapse models of quantum mechanics to miniature quantum memory elements in hybrid superconducting quantum circuits.

In optics, geometric structuring at the nanoscale has become a powerful method for modifying the electromagnetic properties of a bulk material, leading to metamaterials capable of manipulating light in unprecedented ways [57]. In the most extreme case, photonic bandgaps can emerge in which light is forbidden from propagating, dramatically altering the emission of light from within such materials [58]. More recently, a similar phononics revolution [59] in the engineering of acoustic waves has led to a variety of new devices, from thermal crystals for controlling the flow of heat [59] to phononic topological insulators for scattering-free transport of acoustic waves [60].

Phononic bandgap structures, similar to their electromagnetic counterparts, can be used to modify the emission or scattering of phonons. These ideas have recently been explored in quantum optomechanics [35, 61, 62, 63] and electromechanics [64] experiments to greatly reduce the mechanical coupling to the thermal environment through acoustic radiation. At ultrasonic frequencies and below, one can combine phononic bandgap clamping with a form of ‘dissipation dilution’ in high stress films to realize quality (Q) factors in excess of 10^8 in two-dimensional nanomembranes [62] and approaching 10^9 in one-dimensional strain-engineered nanobeams [63]. At higher, microwave frequencies, the benefit of stress-loading of the film fades as local strain energy dominates [63]. and one is left once again to deal with intrinsic material absorption.

To date, far less attention has been paid to the impact of geometry and phononic bandgaps on acoustic material absorption [65, 66]. Fundamental limits to sound absorption in solids are known to result from the anharmonicity of the host crystal lattice [67, 68]. At low temperatures T, in the Landau-Rumer regime ($\omega\tau_{\text{th}} \gg 1$) where the thermal phonon relaxation rate (τ_{th}^{-1}) is much smaller than the acoustic frequency (ω), a quantum model of 3-phonon scattering can be used to describe phonon-phonon mixing that results in damping and thermalization of acoustic modes [67, 68]. Landau-Rumer damping scales approximately as T^{α}, where $\alpha \approx 4$ depends upon the phonon dispersion and density of states (DOS) [68]. At the very lowest lattice temperatures ($\lesssim$ 10 K), where Landau-Rumer damping has dropped off, a residual damping emerges due to material defects. These two-level system (TLS) defects [69], typically found in amorphous materials, correspond to a pair of nearly degenerate local arrangements of atoms in the solid which can have both an electric and an acoustic transition dipole, and couple to both electric and strain fields. Recent theoretical analysis shows that TLS interactions with acoustic waves can be dramatically altered in a structured material [65].

Here, we explore the limits of acoustic damping and coherence of a microwave acoustic nanocavity with a phononic crystal shield that possesses a wide bandgap for all polarizations of acoustic waves. Our nanocavity, formed from an optomechanical crystal (OMC) nanobeam resonator [35], supports an acoustic breathing mode at $\omega_{\text{m}}/2\pi \approx 5$ GHz and a co-localized optical resonant mode at $\omega_{\text{c}}/2\pi \approx 195$ THz ($\lambda_{\text{c}} \approx 1550$ nm) which allows us to excite and readout mechanical motion using radiation pressure from a pulsed laser source. This minimally invasive pulsed measurement technique avoids a slew of parasitic damping effects – typically associated with electrode materials and mechanical contact [70], or probe fields for continuous readout – and allows for the sensitive measurement of motion at the single phonon level [54]. The results of acoustic ringdown measurements at millikelvin temperatures show that damping due to radiation is effectively suppressed by the phononic shield, with breathing mode quality factors reaching $Q = 4.9 \times 10^{10}$, corresponding to an unprecedented frequency-Q product of f-$Q = 2.6 \times 10^{20}$. Measurement of the frequency jitter of the acoustic resonance is also performed, indicating telegraph-like noise corresponding to a coherence time of $\tau_{\text{coh},0} \approx 130$ μs.

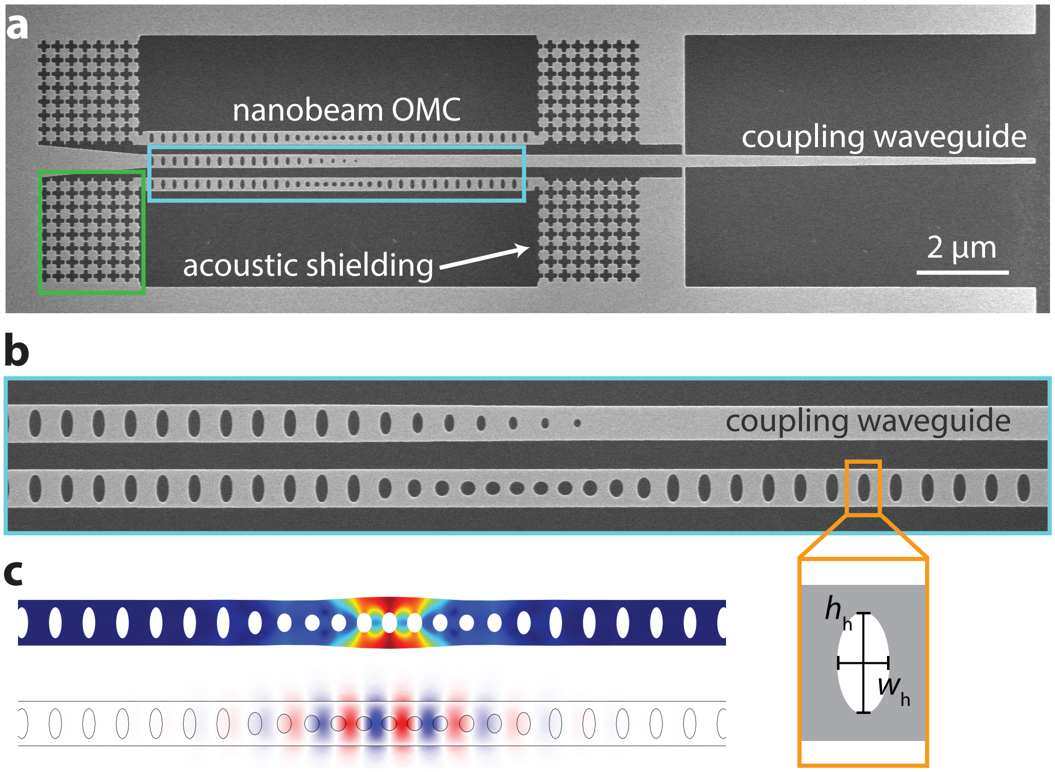

Figure 4.1: **Nanobeam optomechanical crystal design.** **a**, Scanning electron microscope (SEM) image of a full nanobeam optomechanical crystal (OMC) device fabricated on SOI with $N = 7$ periods of acoustic shielding. A central coupling waveguide allows for fibre-to-chip optical coupling as well as side-coupling to individual nanobeam OMC cavities. **b**, SEM image of an individual nanobeam OMC and the coupling waveguide, with enlarged illustration of an individual unit cell in the end-mirror portion of the nanobeam. **c**, FEM simulations of the mechanical (top; total displacement) and optical (bottom; transverse electric field) modes of interest in the nanobeam. Distortion of the mechanical displacement profile is exaggerated for clarity.

The temperature and amplitude dependence of the residual acoustic damping is consistent with relaxation damping of non-resonant TLS, modeling of which indicates that not only does the phononic bandgap directly eliminate the acoustic radiation of the breathing mode but it also reduces the phonon damping of TLS in the host material. The anomalously high measured acoustic Q-factors are thus likely a result of the suppression of phonon emission by TLS, in analogy to the quantum electrodynamics of an atom in a photonic bandgap [58].

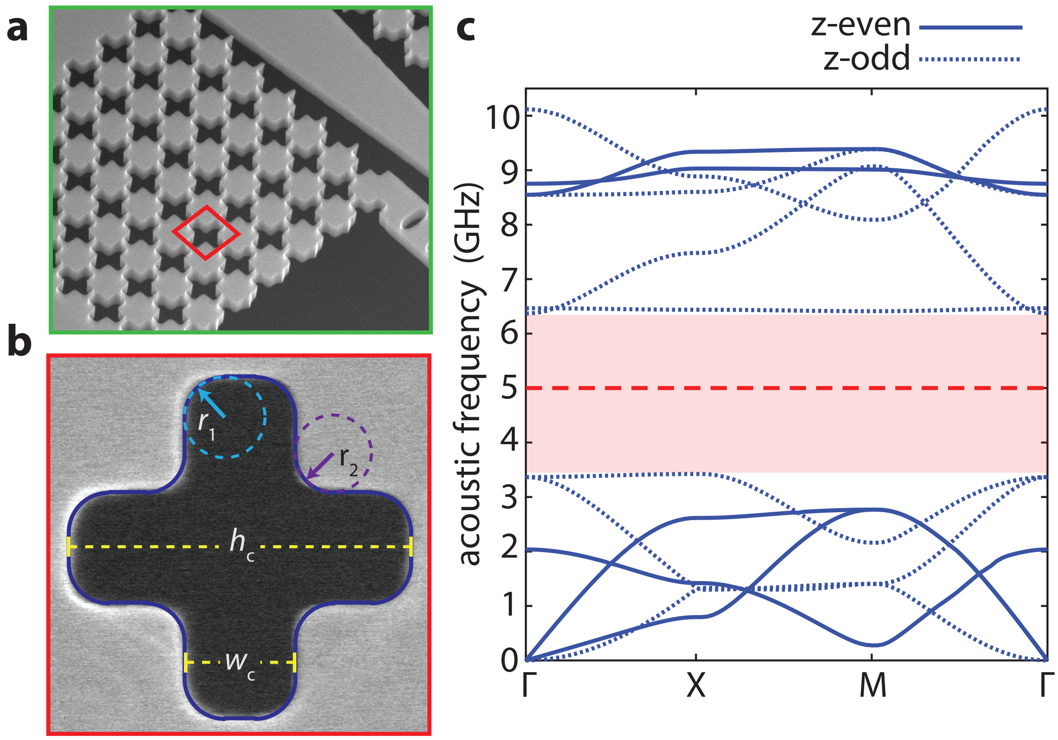

Figure 4.2: **Phononic shield design.** **a**, SEM image showing the nanobeam clamping geometry. **b**, SEM image of an individual unit cell of the cross-crystal acoustic shield. The dashed lines show fitted geometric parameters used in simulation, including cross height (h_c = 474 nm), cross width (w_c = 164 nm), inner fillet radius (r_1), and outer fillet radius (r_2). **c**, Simulated acoustic band structure of the realized cross-crystal shield unit cell, with the full acoustic bandgap highlighted in pink. Solid (dotted) lines correspond to modes of even (odd) symmetry in the direction normal to the plane of the unit cell. The dashed red line indicates the mechanical breathing-mode frequency at $\omega_m/2\pi = 5.0$ GHz.

4.1 Device Design

The devices studied in this work are designed from the 220 nm device layer of a silicon-on-insulator (SOI) microchip. In Figs. 4.1(a-b) we show scanning electron microscope images of a single fabricated device, which consists of a coupling optical waveguide, the nanobeam OMC cavities that support both the microwave acoustic and optical resonant modes, and the acoustic shield that connects the cavity to the surrounding chip substrate. Fig. 4.1(c) shows finite-element method (FEM) simulations of the microwave acoustic breathing mode and fundamental optical mode of the nanobeam cavity. We use the on-chip coupling waveguide to direct laser light to the nanobeam OMC cavities. A pair of cavities with slightly different optical mode frequencies are evanescently coupled to each waveguide. An integrated photonic crystal back mirror in the waveguide allows for optical measurement in a reflection geometry. The design of the OMC cavities, detailed in Ref. [35], uses a tapering of the etched hole size and shape in the nanobeam to provide strong localization and overlap of the breathing mode and the fundamental optical mode, resulting in a vacuum optomechanical coupling rate [35] between photons and phonons of $g_0/2\pi \approx 1$ MHz.

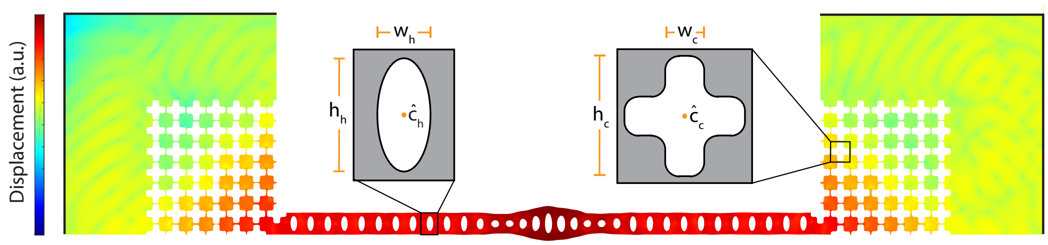

Figure 4.3: **Mode profile of fabrication imperfections.** FEM simulation of the breathing-mode mechanical displacement field for a nanobeam OMC with $N = 6$ periods of acoustic shielding, illustrating localization of the vibrational energy. The geometry in the simulation consists of the nanobeam OMC, acoustic shielding, and the surrounding Si substrate. The borders of the simulation geometry are modeled as an absorbing perfectly-matched layer. The insets show critical parameters of the device geometry. To introduce disorder into the simulations, each of these geometric parameters is drawn from independent Gaussian distributions centered on the nominal design parameter value with standard deviation $\sigma_{\text{pos.}}$ for the center positions and σ_{size} for the diameter or length of holes.

In order to minimize mechanical clamping losses, the nanobeam is anchored to the Si bulk with a periodic cross structure which is designed to have a complete phonic bandgap at the breathing mode frequency [35]. Through tuning of the cross height h_c and width w_c (c.f., Figs. 4.2(a-b)), bandgaps as wide as $\sim$ 3 GHz can be achieved as shown in Fig. 4.2. We analyze SEM images of realized structures to provide accurate structure dimensions for our FEM models, and in particular, we include in our modeling a filleting of the inner and outer corners (r_1 and r_2 in Fig. 4.2c) of the crosses arising from technical limitations of the patterning of the structure.

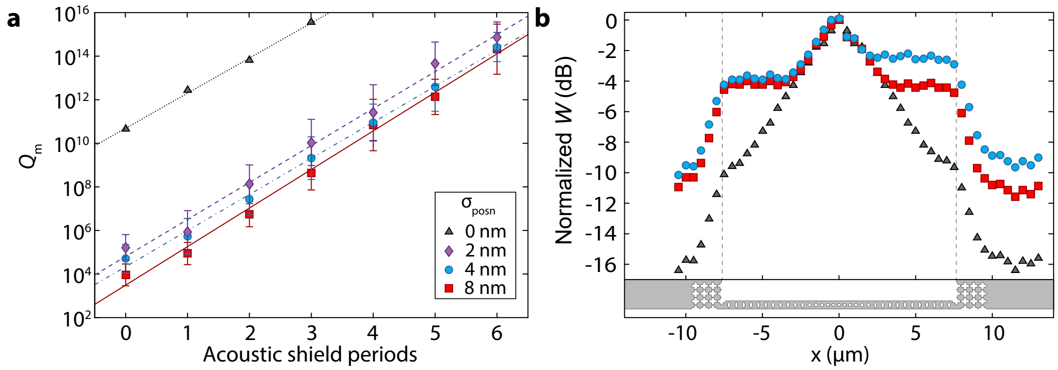

Figure 4.4: **Impact of fabrication imperfections.** **a**, Plot of the simulated mechanical Q-factor due to acoustic radiation from the cavity through the acoustic shielding. The straight lines are exponential fits to the mean data points of the simulation (the error bars indicate the standard deviation of an ensemble of simulations for each shield number and disorder level). **b**, Plots of the normalized acoustic energy density $\mathcal{W}$ along a line cut through the center of the beam for $\sigma_{\text{pos.}}$ = 0 nm (black triangles), 4 nm (blue circles), and 8 nm (red squares).

The use of a phononic bandgap shield is necessitated by the lack of a full gap for the nanobeam cavity. Finite-element method (FEM) numerical modeling indicates that the addition of the cross shield provides significant protection against nanometer-scale disorder which is inherently introduced during device fabrication. In Fig. 4.3 and Fig. 4.4, we present a numerical study of the effects of random fabrication imperfections on the radiative damping of the shielded OMC cavity mode. In this analysis, the center and size of each feature in the etched holes in the cross shield and the nanobeam cavity are drawn from independent random distributions around the mean design values as indicated in the figure caption. We compare in Fig. 4.4(a) the simulated acoustic Q-factor of the ideal, unperturbed cavity structure to that of cavity structures with a fixed level of disorder in the hole sizes (standard deviation, σ_{size} = 4 nm) and varying levels of disorder in the hole centers ($\sigma_{\text{pos.}}$ = 2, 4, 8 nm).

Note that the same level of disorder is applied to both the nanobeam and acoustic shield. An absence of perturbations to the nanobeam cavity, even without any shielding, yields large radiation-limited Q-factors in excess of 10^{10}. This is a result of the quasi-bandgap that exists in the nanobeam mirror section for modes of a specific symmetry about the center-line of the beam; however, any perturbation that breaks this symmetry results in a compromised quasi-bandgap in the nanobeam (Q drops from $\gtrsim 10^{10}$ to $\lesssim 10^5$ for nanometer-scale perturbations). Conversely, the exponential trend of the radiation-limited Q-factor with the number of shield periods is consistently a factor of $\times 5.5$ per additional period, independent of the disorder level. Plots in Fig. 4.4(b) compare the linear acoustic energy density along the axis of the nanobeam, $\mathcal{W}$, for the mode of the unperturbed cavity and the modes of two different realizations of disordered cavities (and shield), highlighting the effectiveness of the acoustic bandgap shield even in the presence of disorder. We plot a line cut of the integrated acoustic energy density $\mathcal{W}$ along the longitudinal ($\hat{x}$) direction of the nanobeam. The partial bandgap of the mirror unit cells of the nanobeam provides some localization of the acoustic energy density, with a simulated cavity-mode mechanical Q-factor on the order of 10^5 for $\sigma_{\text{posn}} = 2$ nm, in reasonable agreement with measured values of $Q \approx 4 \times 10^5$. The acoustic energy density decays rapidly in the full-bandgap shield region. Here the modeling results yield a scaling $Q \propto e^{1.7 \times N_{\text{shield}}}$, where N_{shield} is the discrete number of cross shield periods. Numerically this trend of exponential increase of Q with shield period number continues to larger N_{shield}, though, as we will detail below, material limits to the mechanical losses become relevant for $N_{\text{shield}} > 4$.

In this analysis, the unit cells of the acoustic radiation shield are parameterized by nominal parameters h_{c} and w_{c} as introduced above, as well as a nominal center coordinate c_{c}. Similarly, the unit cells of the nanobeam OMC are parameterized by the elliptical hole height h_{h}, width w_{h}, and center coordinate c_{h}. A given instance of the cavity structure is then generated by each of these geometric parameters for every unit cell from an independent Gaussian distribution centered on the nominal design value and having standard deviation σ in units of nm (the center coordinates with standard deviation $\sigma_{\text{pos.}}$ and the hole-size with σ_{size}).

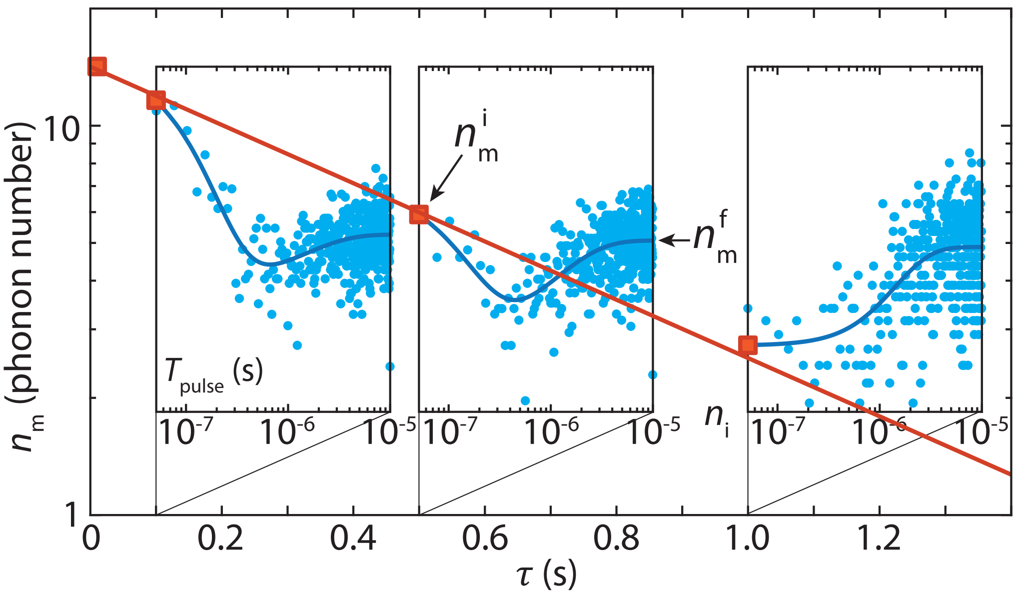

Figure 4.5: **Thermal ringdown measurements of the acoustic breathing mode.** Ringdown measurements of a 7-shield device (1D nanobeam OMC device C) for readout pulse amplitude of $n_c = 320$. The series of inset panels show the measured (and fit; solid blue curve) anti-Stokes signal during the optical pulse at a series of pulse delays.

4.2 Ringdown measurements of ultra high-Q acoustic modes

To investigate the efficacy of the acoustic shielding in practice, we have fabricated and characterized arrays of devices with a scaling of the cross period number from $N_{\text{shield}} = 0$ to 10, with all other design parameters held constant. Optical measurements of the acoustic properties of the OMC cavity were performed at millikelvin temperatures in a dilution refrigerator. The sample containing an array of different OMC devices was mounted directly on a copper mount attached to the mixing chamber stage of the fridge, and a single lensed optical-fiber was used positioned using a 3-axis stage to couple light into and out of each device [54]. In a first set of measurements of acoustic energy damping, we employ a single pulsed laser scheme to perform both excitation and readout of the breathing mode (as described in Chapter 3).

Plotting the initial mode occupancy at the beginning of the fit readout pulse (n_{m}^{i}) versus delay time τ_{off} between pulses, we plot the ringdown of the stored phonon number in the the breathing mode as displayed in Fig. 4.5 for a device with $N_{\text{shield}} = 7$.

Performing a series of ringdown measurements over a range of devices with varying N_{shield}, and fitting an exponential decay curve to each ringdown we produce the Q-factor plot in Fig. 4.6. We observe an initial trend in Q-factor versus shield number which rises on average exponentially with each additional shield period, and then saturates for $N_{\text{shield}} \geq 5$ to $Q_{\text{m}} \gtrsim 10^{10}$. As indicated in Fig. 4.5 these Q values correspond to ringdown of small, near-single-phonon level amplitudes. We also perform ringdown measurements at high phonon amplitude using two additional methods as discussed in the previous chapter. These methods use two laser tones to selectively excite the acoustic breathing mode using a $\times 1000$ weaker excitation and readout optical pulse amplitude ($n_{\text{c}} \lesssim 0.3$). The measured ringdown curves, displayed in Fig. 4.5, show the decay from initial phonon occupancies of 10^3-10^4 of an 8-shield device (1D nanobeam OMC device D; square purple data point in Fig. 4.6). The two methods yield similar breathing mode energy decay rates of $\gamma_0/2\pi = 0.108$ Hz and 0.122 Hz, the smaller of which corresponds to a Q-value of $Q_{\text{m}} = 4.92^{+0.39}_{-0.26} \times 10^{10}$ and a phonon lifetime of $\tau_{\text{ph,0}} = 1.47^{+0.09}_{-0.08}$ s. Comparing all three excitation methods with widely varying optical-absorption-heating and phonon amplitude, we consistently measure $Q_{\text{m}} \gtrsim 10^{10}$ for devices with $N_{\text{shield}} \geq 5$.

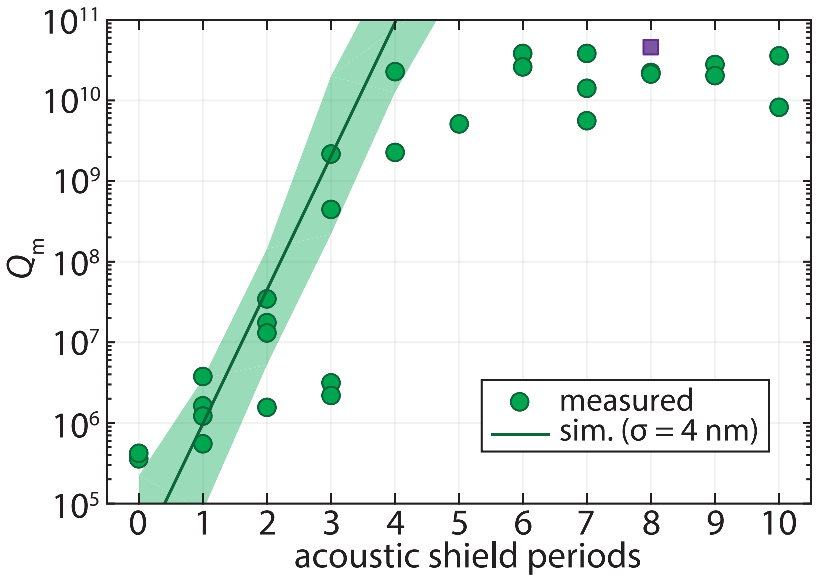

Figure 4.6: ***Q*-factor versus number of acoustic shield periods.** Plot of the measured breathing mode Q-factor versus number of acoustic shield periods N_{shield}. The solid green line is a fit to the corresponding simulated radiation-limited Q-factor for devices with standard deviation (SD) $\sigma = 4$ nm disorder in hole position and size, similar to the value measured from device SEM image analysis. The shaded green region is corresponding to the range of simulated Q values (ensemble size 10) within one SD of the mean.

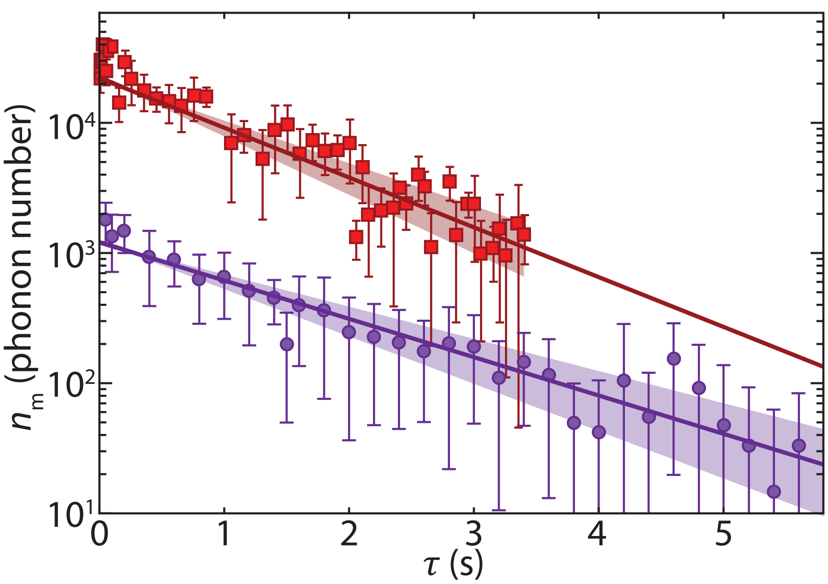

Figure 4.7: **Coherent ringdown measurements of the acoustic breathing mode.** Ringdown measurements performed on an eight-shield device (device D) at large phonon amplitude. For blue-detuned driving (red squares) the fit decay rate is $\gamma_0/2\pi = (0.122 \pm 0.020)$ Hz. For modulated-pump driving (purple circles) the fit decay rate is $\gamma_0/2\pi = (0.108 \pm 0.006)$ Hz. The error bars are the 90% confidence intervals of the measured values of n_m^i. The shaded regions are the 90% confidence intervals for the exponential fit curves.

4.3 Origin of the Residual Damping

In order to understand the origin of the residual damping for large N_{shield} we also measured the temperature dependence of the energy damping rate, breathing mode frequency, and full width at half maximum (FWHM) linewidth of the breathing mode for the highest Q 8-shield device (1D nanobeam OMC device D). In Fig. 4.8(a) we plot the energy damping rate which shows an approximately linear rise in temperature up to $T_{\text{f}} \approx 100$ mK, and then a much faster $\sim (T_{\text{f}})^{2.4}$ rise in the damping. Using the two-tone coherent excitation method [53], we plot in Fig. 4.8(b) the measured breathing mode acoustic spectrum at $T_{\text{f}} = 7$ mK and pump power $n_{\text{c}} = 0.1$. The top plot shows rapid spectral scans (40 ms per scan) in which the probe frequency is swept across the acoustic resonance. These rapid scans show a jittering acoustic line with a roughly $\Delta\omega_{\text{m}}/2\pi \approx 1$ kHz linewidth, consistent with the predicted magnitude of optical back-action ($\gamma_{\text{OM}}/2\pi \approx 820$ Hz) and hot bath damping ($\gamma_{\text{p}}/2\pi \approx 120$ Hz) at the $n_{\text{c}} = 0.1$ measurement power. An ensemble average of these scans, taken over several minutes, yields a broadened and reduced contrast acoustic line of FWHM $\Delta_{1/2}/2\pi = 4.05$ kHz.

Note that in Fig. 4.8(b) we are measuring the acoustic line with the laser light on, as opposed to the ringdown measurements of Fig. 4.6, Fig. 4.5 and Fig. 4.7, in which the laser light is off. Lowering the optical pump power to reduce back-action and absorption-induced damping limits further the already low signal-to-noise ratio, and scanning more slowly begins to introduce frequency jitter into the measured line. As such, we can only bound the intrinsic low temperature coherence time of the breathing mode to $\tau_{\text{coh},0} \gtrsim 2/\Delta\omega_{\text{m}} \approx 0.3$ ms.

As will be detailed in the next chapter, estimates of the magnitude of Landau-Rumer damping of the breathing mode indicate that 3-phonon scattering in Si is far too weak at $T_{\text{f}} \lesssim 1$ K to explain the measured damping. Analysis of the interactions of TLS with the localized acoustic modes of the confined geometry of the OMC cavity structure, however, show that TLS interactions can explain all of the observed breathing mode behavior.

Utilizing the advanced methods of nanofabrication and cavity optomechanics has provided a new toolkit to explore quantum acoustodynamics in solid-state materials. Continued studies of the behavior of TLS in similar engineered nanostructures to the OMC cavity of this work may lead to, among other things, new approaches to modifying the behavior of quasi-particles in superconductors [71], mitigating decoherence in superconducting [72] and color center [73] qubits, and even new coherent TLS-based qubit states in strong coupling with an acoustic cavity [74]. The extremely small motional mass (m_{eff} = 136 fg [35]) and narrow linewidth of the OMC cavity also make it ideal for precision mass sensing [75] and in exploring limits to alternative quantum collapse models [76]. Perhaps most intriguing is the possibility of creating a hybrid quantum architecture consisting of acoustic and superconducting quantum circuits [77, 78], where the small scale, reduced cross-talk, and ultralong coherence time of quantum acoustic devices may provide significant improvements in connectivity and performance of current quantum hardware.

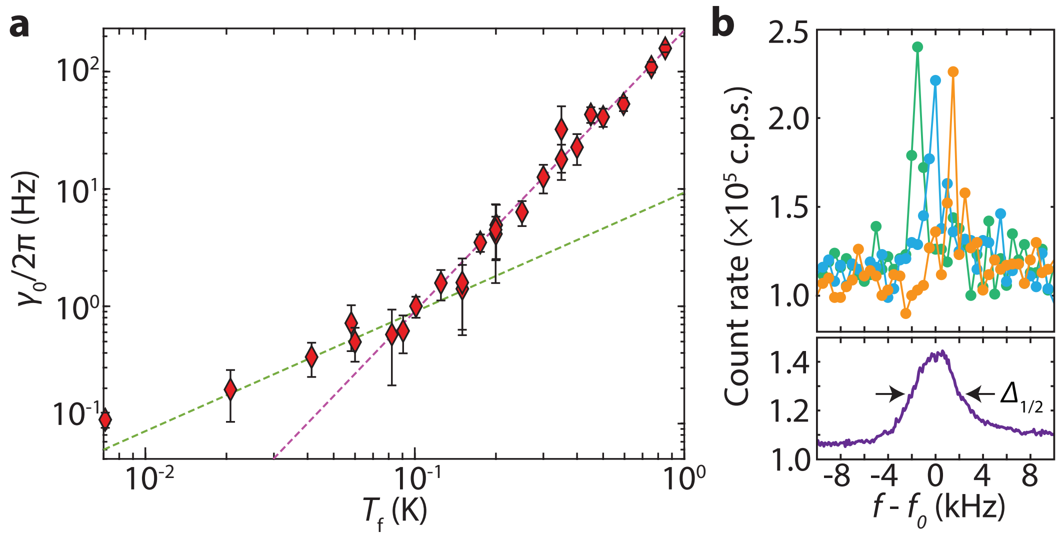

Figure 4.8: **Temperature dependence of acoustic damping and frequency jitter.** a, Plot of the measured breathing mode energy damping rate, $\gamma_0/2\pi$, as a function of fridge temperature (T_f). Dashed green (magenta) curve is a fit with temperature dependence $\gamma_0 \sim T_\mathrm{f}^{1.01}$ ($\gamma_0 \sim T_\mathrm{f}^{2.39}$). Error bars are 90% confidence intervals of the exponential fit to measured ring down curves. **b**, Two-tone coherent spectroscopy signal. Upper plot: three individual spectrum of rapid frequency sweeps with a frequency step size of 500 Hz and dwell time of 1 ms (RBW $\approx$ 0.5 kHz). Lower plot: average spectrum of rapid scan spectra taken over minutes, showing broadened acoustic response with FWHM linewidth of $\Delta_{1/2}/2\pi$ = 4.05 kHz. The large on-resonance response corresponds to an estimated optomechanical cooperativity of $C \equiv \gamma_\mathrm{OM}/(\gamma_0 + \gamma_\mathrm{p}) \gtrsim 1.1$, consistent with the predicted magnitude of back-action damping $\gamma_\mathrm{OM}/2\pi \approx 817$ Hz and bath-induced damping $\gamma_\mathrm{p}/2\pi \approx 120$ Hz at the measurement pump power level $n_\mathrm{c} = 0.1$. Data presented in (**a**-**b**) are for device D.

4.4 Summary of Device Parameters

For reference, here we provide a look-up table for each of these devices and their measured optical and mechanical properties.

Table 4.1: **Measured optical and acoustic device parameters.** ρ_r is the Si device layer resistivity of the SOI wafer from which the device was fabricated (as provided by the manufacturer), λ_c is the optical mode wavelength, κ is the measured total optical linewidth, κ_e is the measured coupling rate between the OMC cavity mode and the on-chip waveguide, g_0 is the measured vacuum optomechanical rate, ω_m is the measured breathing mode frequency, and $\gamma_0/2\pi$ is the measured breathing mode damping from ringdown measurements at $T_f = 7$ mK.

Device	shield #	ρ_r [Ω-cm]	λ_c [nm]	$\kappa/2\pi$ [GHz]	$\kappa_e/2\pi$ [MHz]	$g_0/2\pi$ [MHz]	$\omega_m/2\pi$ [GHz]	$\gamma_0/2\pi$ (Hz)
A	0	5-20	1541.850	1.507	778	0.713	5.053	14.1×10^3
B	6	5-20	1539.285	1.13	605	~ 0.713	5.013	0.21
C	7	5-20	1538.716	1.21	362	~ 0.713	5.014	0.27
D	8	$> 5 \times 10^3$	1538.971	0.575	131	1.15	5.31	0.108
E	7	5-20	~ 1540	1.244	261	0.833	4.98	0.33

4.5 Ringdown Measurements of Ultra High-Q Acoustic Modes in Quasi-2D Devices

Ultra-high mechanical quality factors are also observed in the quasi-2D OMC devices. In order to measure the intrinsic mechanical Q-factor of a quasi-2D OMC device, the same thermal ringdown method was used as the 1D nanobeam OMC devices. We used the pulsed optical excitation and photon counting techniques as presented in Chapter 3. We performed ringdown measurements on a device which had a phononic shield composed of eight cross unit cells (see Section 1.3.4), by impinging a series of red-detuned ($\Delta = \omega_{\mathrm{m}}$) optical excitation pulses on the device. The laser was pulsed on for a duration $\tau_{\mathrm{pulse}} = 10\ \mu$s and then off for a variable time τ_{off}. The initial mode occupancy during the pulse (n_{i}) for different τ_{off} is fitted to obtain an intrinsic decay rate γ_0 as shown in Fig. 4.9c, from which we can extract an intrinsic decay rate $\gamma_0/2\pi = 8.28$ Hz, corresponding to a mechanical Q-factor of 1.2×10^9 and f-Q product of 1.2×10^{19}.

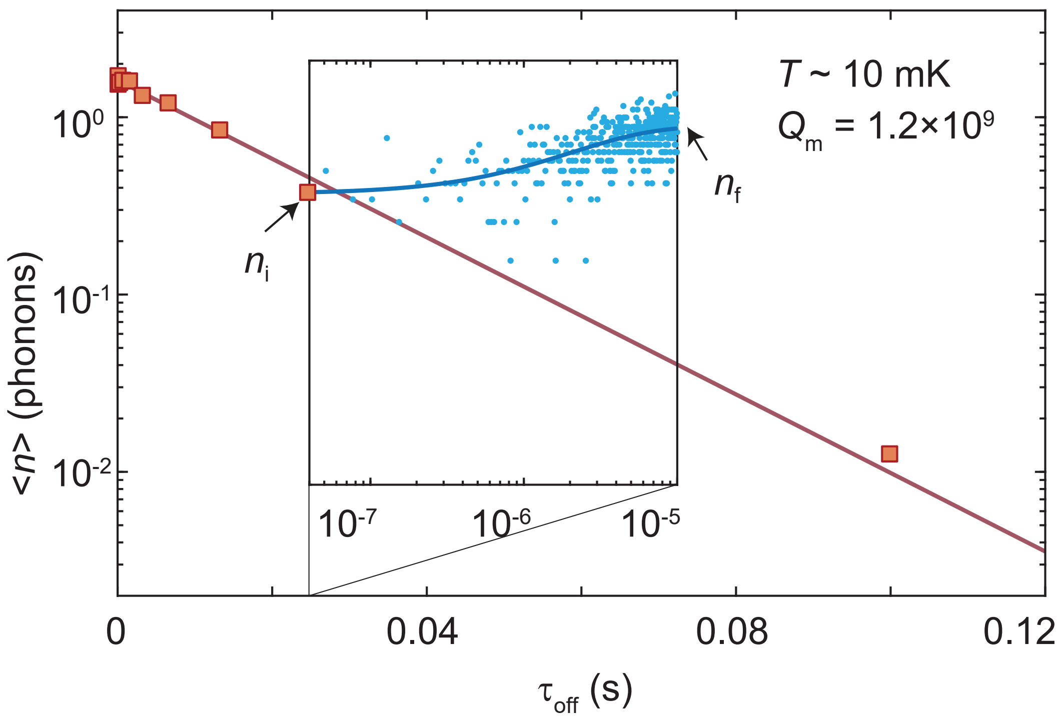

Figure 4.9: **Ringdown measurement of quasi-2D OMC device**. Thermal ringdown measurement performed on an eight-shields device. The initial phonon occupancy n_i (orange squares) is measured for τ_off = (0.4, 0.8, 1.67, 3.33, 6.66, 13.33, 25, 100) ms using a readout photon number n_c = 60. The phonon amplitude decay is fitted to extract an intrinsic mechanical damping rate γ_0 = 8.28 Hz, corresponding to a mechanical Q-factor of 1.217×10^9. Inset shows the measured occupancy during the pulse-on at each τ_off value; blue circles are data and solid lines are fits. The eight-shield device has parameters (κ, κ_e, g_0, ω_m, γ_0) = 2π(1.187 GHz, 181 MHz, 1.182 MHz, 10.02 GHz, 8.28 Hz).

Chapter 5

PHONON DAMPING AND DECOHERENCE AT SUB-KELVIN TEMPERATURE

The origin of the residual damping for large N_{shield} was briefly discussed in the previous chapter. In this chapter, we will explore the origins of acoustic energy damping and phonon decoherence in general and in OMC devices at low temperature. We will mostly ignore the phonon energy damping by radiation of ballistic phonons into the bulk material through the acoustic bandgap shield in this chapter, but mainly focus on Landau-Rumer damping of the breathing mode and the interactions of TLS with the localized acoustic modes of the confined geometry of the OMC cavity structure in different temperature regimes.

In the previous chapter, we discussed that the intrinsic low temperature coherence time of the breathing mode can only be bounded to $\tau_{\text{coh},0} \gtrsim 130$ μs. Further information can, however, be gleaned by measuring the linewidth and center frequency of the ensemble averaged spectrum as a function of n_{c} (Fig. 5.1(a)) and T_{f} (Fig. 5.1(b)). The width of the frequency jitter spectrum, averaged over minutes, is roughly independent of optical pump power and temperature down to the lowest measurable pump powers ($n_{\text{c}} = 0.02$) and up to $T_{\text{f}} = 800$ mK. The center frequency, on the other hand, shifts up in frequency with both temperature and optical power. The frequency shift versus T_{f} is consistent with the frequency shift versus n_{c} if the hot bath temperature is used as a proxy for the fridge temperature.

Estimates of the magnitude of Landau-Rumer damping of the breathing mode indicate that 3-phonon scattering in Si is far too weak at $T_{\text{f}} \lesssim 1$ K to explain the measured damping. Analysis of the interactions of TLS with the localized acoustic modes of the confined geometry of the OMC cavity structure, however, show that TLS interactions can explain all of the observed breathing mode behavior. In this analysis, detailed in the following sections, FEM simulation is used to find the frequencies and radiation-limited damping rates of the acoustic quasi-normal modes of the OMC cavity structure. An estimate of the spectral density of TLS within the breathing mode volume ($V_m \approx 0.11$ $(\mu\text{m})^3$) is ascertained from estimated surface oxide (~ 0.25 nm [79]) and etch-damage (~ 15 nm [80]) layer thicknesses in the Si device, and bulk TLS density found in amorphous materials [69]. Using the resulting effective spectral density of interacting TLS, $n_{0,m} \approx 20$ GHz^{-1}, and average TLS transverse and longitudinal deformation potentials of $\bar{M} \approx 0.04$ eV and $\bar{D} \approx 3.2$ eV, respectively, yields breathing mode damping and frequency shifts which are in excellent agreement with the measured data. The estimated level of frequency jitter is also found in agreement with the measured value, assuming all TLS are being pumped via the same optical absorption that drives the hot bath.

Several key observations can be drawn from the TLS damping modeling. The first is that the typical T^3 dependence of TLS relaxation damping of acoustic waves is dependent on the phonon bath DOS into which the TLS decay [65, 66]. In the OMC cavity the phonon DOS is strongly modified from a three-dimensional bulk material. This directly results in the observed weak temperature dependence of the acoustic damping for $T_\mathrm{f} \lesssim 100$ mK, where the thermally activated TLS interact resonantly with an approximately one-dimensional phonon DOS. A second point to note is that the TLS resonant damping is strongly suppressed due to the phononic bandgap surrounding the OMC cavity. Estimates of the phonon-induced spontaneous decay rate of TLS in the bandgap is on the order of Hz; combined with the discrete number of TLS in the small mode volume of the breathing mode, acoustic energy from the breathing mode cannot escape via resonant coupling to TLS. The observed lack of saturation of the breathing mode energy damping with either temperature or phonon amplitude is further evidence that non-resonant relaxation damping – due to dispersive coupling to TLS – is dominant [69]. Finally, the small average number of estimated TLS in V_m which are thermally activated at the lowest temperatures (~ 2), leads to significant variation in the simulated TLS relaxation damping at $T_\mathrm{f} \sim 10$ mK. This is consistent with the observed fluctuations from device-to-device in the low-temperature Q_m for devices with $N_\mathrm{shield} > 5$ (see Fig. 4.6).

Several subtle points regarding the energy decay and coherence measurements should be noted. First, the breathing mode spectral linewidth, and thus the coherence time, is measured in the presence of a (albeit weak) laser pump field. This is in contrast to the energy decay measurements which are performed with the laser pulsed off. Although we did not observe a power dependence at low optical power to the measured long-time FWHM of the acoustic linewidth, the influence of the laser field on the acoustic mode coherence time (through inadvertent pumping of TLS for instance) cannot be ruled out. Second, the pump-probe technique used to measure the acoustic spectrum excites the breathing mode to an estimate mode occupancy of order 1000; the single-phonon coherence time of relevance to many quantum applications may be reduced from the measured high-phonon number. With the recent demonstration of strong dispersive coupling of a superconducting qubit to similar nanomechanical acoustic cavities [78], measurement of single-phonon coherence time in the absence of light fields should be possible. Additionally, the low-frequency character of the breathing mode frequency noise measured in this work indicates that the effective acoustic coherence time may be substantially increased towards the energy decay time through techniques such as dynamic decoupling. Finally, the attribution of the residual damping and the frequency jitter noise to TLS, and in particular TLS at the Si surface of the etched nanoscale devices, indicates that further study of the dependence of the acoustic damping and coherence on surface preparation and surface damage removal may prove particularly fruitful.

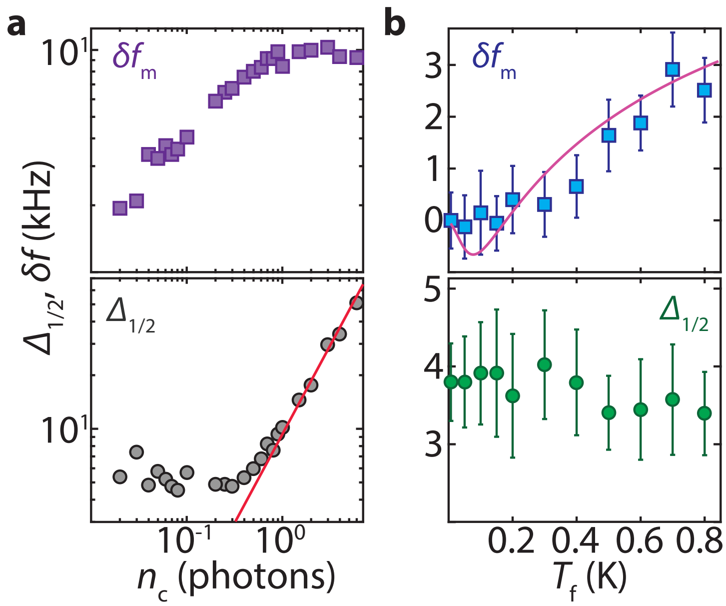

Figure 5.1: **Temperature dependence of acoustic frequency jitter.** **a**, Plot of the measured breathing mode energy damping rate, $\gamma_0/2\pi$, as a function of fridge temperature (T_f). Dashed green (magenta) curve is a fit with temperature dependence $\gamma_0 \sim T_\mathrm{f}^{1.01}$ ($\gamma_0 \sim T_\mathrm{f}^{2.39}$). Error bars are 90% confidence intervals of the exponential fit to measured ringdown curves. **b**, Two-tone coherent spectroscopy signal. Upper plot: three individual spectrum of rapid frequency sweeps with a frequency step size of 500 Hz and dwell time of 1 ms (RBW $\approx$ 0.5 kHz). Lower plot: average spectrum of rapid scan spectra taken over minutes, showing broadened acoustic response with FWHM linewidth of $\Delta_{1/2}/2\pi$ = 4.05 kHz. The large on-resonance response corresponds to an estimated optomechanical cooperativity of $C \equiv \gamma_{\mathrm{OM}}/(\gamma_0 + \gamma_\mathrm{p}) \gtrsim 1.1$, consistent with the predicted magnitude of back-action damping $\gamma_{\mathrm{OM}}/2\pi \approx$ 817 Hz and bath-induced damping $\gamma_\mathrm{p}/2\pi \approx$ 120 Hz at the measurement pump power level $n_\mathrm{c} = 0.1$. Data presented in (**a**-**b**) are for device D.

5.1 3-Phonon-Scattering Damping Model

The anharmonicity of the atomic lattice in solid-state materials leads to frequency mixing of the approximate harmonic modes (the phonons) of the lattice. This frequency mixing - of all different orders - within a continuum of modes leads to different forms of phonon damping depending on the damped phonon frequency (ω_s), wavelength (λ_{q_s}), and the lattice temperature [68, 81]. At low temperatures where phonon relaxation times (τ) are long, and at relatively high phonon frequencies, the dominant source of phonon damping due to the anharmonic lattice potential results from 3-phonon scattering processes in the so-called Landau-Rumer limit ($\omega_s\tau \gg 1$) [67, 82]. In this limit a single-mode relaxation time (SMRT) approximation [68] can be made in which only the damped phonon mode under consideration is disturbed from equilibrium and the other two phonon modes involved in the scattering are assumed to be frozen at their equilibrium occupancies. Using the SMRT approximation one can calculate the 3-phonon-scattering damping rate from second-order perturbation theory of the quantum mechanical model of the anharmonic lattice. At higher temperatures where the thermal phonon relaxation rate ($1/\tau$) is very fast, or for very low frequency phonons, this approximation breaks down and one enters the Akhiezer limit of phonon damping where $\omega_s\tau \ll 1$ [83]. In this limit a phenomenological model is employed in which the strain wave of a phonon mode induces a redistribution of thermal phonons via the lattice anharmonicity, and damping occurs due to relaxation of the thermal phonons back towards thermal equilibrium. If in addition the phonon wavelength is long relative to the mean free path of thermal phonons (l_{th}), then a local temperature can be defined and damping can also occur via diffusion of thermal phonons. In this limit, $\omega_s\tau \ll 1$ and $l_{th}/\lambda_{q_s} \ll 1$, energy in the acoustic wave is carried away in heat flow due to temperature gradients on the scale of λ_{q_s}, and the resulting relaxation process is called thermoelastic damping [84].

As we are concerned with microwave frequency acoustic waves and sub-Kelvin temperatures, the dominant phonon-phonon scattering damping is expected to arise from 3-phonon scattering under the SMRT approximation. In what follows we present a model of such Landau-Rumer damping utilizing leaky quasi-modes [85]. This quasi-mode picture arises naturally in the context of the OMC cavity structure, in which localized acoustic modes are weakly coupled to the continuum of phonon modes in the surrounding substrate via the peripheral clamping of the Si device layer to the underlying Si dioxide BOX layer (c.f., Fig. 5.4). We follow closely the derivation of 3-phonon scattering in Ref. [68], although with slight adjustments to the notation to accommodate the use of quasi-normal modes. The notation developed here will also be used in the analysis of two-level system damping described in the next section.

For a displacement vector field $u_\alpha(\mathbf{r})$, with u the local amplitude of atomic displacement in direction α from equilibrium, the stored potential energy to second and third order in the displacement field can be written as,

$$\mathcal{V}_2 \equiv \text{2nd-order elastic (potential) energy} \tag{5.1}$$
$$= \frac{1}{2}\int \mathrm{d}^3 r \, J^{\alpha\gamma}{}_{\beta\delta} \frac{\partial u_\alpha}{\partial r_\beta}\frac{\partial u_\gamma}{\partial r_\delta}, \tag{5.2}$$

and

$$\mathcal{V}_3 \equiv \text{third-order elastic (potential) energy} \tag{5.3}$$
$$= \frac{1}{3!}\int \mathrm{d}^3 r \, A^{lmn}{}_{ijk} \frac{\partial u_l}{\partial r_i}\frac{\partial u_m}{\partial r_j}\frac{\partial u_n}{\partial r_k}. \tag{5.4}$$

Here, $J^{\alpha\gamma}{}_{\beta\delta}$ is in general a rank 4 tensor whose coefficients are the 2nd-order elastic coefficients of the material which relate strain to stress and have units of energy density. $A^{lmn}{}_{ijk}$ is a rank 6 tensor with coefficients arising from the lowest order anharmonicity of the lattice. $\partial u_{\alpha/\partial r_\beta}$ is a rank 2 tensor representing the local strain created by the displacement vector field $u_\alpha(\mathbf{r})$.

From these expressions we can define the total elastic energy density for a classical acoustic wave oscillating harmonically in mode s as,

$$h(\bar{\bar{e}}_s(\mathbf{r})) \equiv \text{(classical) strain field elastic energy density} \tag{5.5}$$
$$= \frac{1}{2} J^{\alpha\gamma}{}_{\beta\delta} \left(e_s(\mathbf{r})\right)_\alpha{}^\beta \left(\left(e_s(\mathbf{r})\right)_\gamma{}^\delta\right)^*, \tag{5.6}$$

where $\bar{\bar{e}}_s(\mathbf{r})$ is a complex strain tensor field related to the real (physical) strain tensor field by,

$$\frac{\partial\left(u_s(\mathbf{r})\right)_i}{\partial r_j} \equiv \text{(classical) strain tensor field of mode } s \tag{5.7}$$

$$\equiv \mathrm{Re}\left(\left(e_s(\mathbf{r})\right)_i^{\ j}\right) \tag{5.8}$$

$$= \mathrm{Re}\left(\bar{\bar{e}}_s(\mathbf{r})\right). \tag{5.9}$$

Note that we have used the fact that for a harmonic wave the cycle averaged potential and kinetic energies are equal (and thus the total wave energy is twice the potential energy), and $h(\bar{\bar{e}}_s(\mathbf{r}))$ should therefore be strictly considered as the energy density averaged over a single cycle in time and a single wavelength in space. We also define a normalized complex strain field for mode s having a peak strain value of approximately unity (exactly unit for tensor-averaged fields) and a peak energy density of $\bar{J}$,

$$\overline{\bar{\bar{e}}_s(\mathbf{r})} \equiv \text{normalized classical strain field for mode } s \tag{5.10}$$

$$= \frac{(\bar{J})^{1/2}\bar{\bar{e}}_s(\mathbf{r})}{\left(\max[h(\bar{\bar{e}}_s(\mathbf{r}))]\right)^{1/2}}, \tag{5.11}$$

where $\bar{J}$ is the tensor-average of the harmonic elastic coefficients,

$$\bar{J} \equiv \text{tensor-averaged 4th-order elastic tensor} \tag{5.12}$$

$$= \left\langle \frac{1}{2}\bar{\bar{J}} \right\rangle_{\mathrm{t}} = \frac{1}{2\cdot 3^4}\left(\sum_{\alpha,\gamma,\beta,\delta}\left(J^{\alpha\gamma}{}_{\beta\delta}\right)^2\right)^{1/2}. \tag{5.13}$$

The effective mode volume over which the strain energy of mode s is localized can also be defined as,

$$V_s \equiv \text{effective mode volume of mode } s = \frac{\int h(\bar{\bar{e}}_s(\mathbf{r}))\mathrm{d}^3r}{\max[h(\bar{\bar{e}}_s(\mathbf{r}))]}. \tag{5.14}$$

The peak strain amplitude of mode s containing half a quanta of energy, i.e., the ‘vacuum’ strain level, is given by,

$$e_{\mathrm{vac},s} \equiv \text{vacuum strain field amplitude for mode } s \tag{5.15}$$

$$= \sqrt{\frac{\hbar\omega_s}{2\bar{J}V_s}}, \tag{5.16}$$

where $\hbar\omega_s$ is the mode s energy quantum. From the peak strain amplitude of vacuum and the normalized strain field we can define a quantum strain field operator,

$$\hat{\bar{\bar{e}}}_s(\mathbf{r}) \equiv \text{quantum strain tensor field operator for mode } s \tag{5.17}$$

$$= (e_{\mathrm{vac},s})\left[\hat{b}_s\overline{\bar{\bar{e}}_s(\mathbf{r})} + \hat{b}_s^{\dagger}\left(\overline{\bar{\bar{e}}_s(\mathbf{r})}\right)^*\right] \tag{5.18}$$

where $\hat{b}_s$ and $\hat{b}_s^{\dagger}$ annihilate and create individual phonon quanta in mode s. The corresponding quantum interaction Hamiltonian for 3-phonon scattering can then be written in terms of triplets of quantum strain field operators directly from the third-order elastic potential energy relation in Eq. (5.4),

$$\hat{\mathcal{H}}_{\text{3-ph}} \equiv \text{3-phonon interaction Hamiltonian} \tag{5.19}$$

$$= \frac{1}{3!}\sum_{s\,s'\,s''}\int \mathrm{d}^3r \left(A^{lmn}{}_{ijk}\right)\left(\hat{\bar{\bar{e}}}_s(\mathbf{r})\right)_l^{\;i}\left(\hat{\bar{\bar{e}}}_{s'}(\mathbf{r})\right)_m^{\;j}\left(\hat{\bar{\bar{e}}}_{s''}(\mathbf{r})\right)_n^{\;k}. \tag{5.20}$$

5.1.1 Type-I Scattering Processes

3-phonon scattering, as it pertains to damping of a particular mode s, can be categorized into two classes of processes [68]. Type-I scattering involves the mode of interest, mode s, as a ‘daughter’ phonon which combines with another ‘sibling’ phonon (mode s') to create a higher frequency ‘parent’ phonon (mode s''). The reverse process is also of type-I. Type-II scattering has the mode s of interest as the high frequency parent phonon.

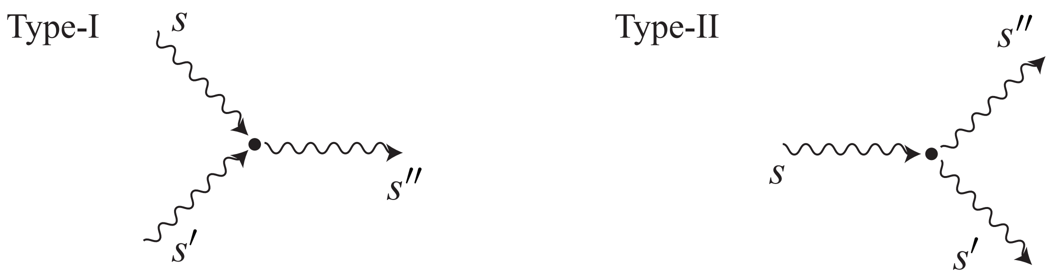

Figure 5.2: **3-phonon-scattering damping processes.** 3-phonon-mixing decay processes may be either Type I or Type II. Due to the reduced density of states at low frequency in the quasi-1D nanobeam structure, Type I processes are expected to dominate over Type II.

The 3-phonon interaction Hamiltonian for type-I scattering is given in terms of phonon creation and annihilation operators as,

$$\hat{\mathcal{H}}^{\text{3-ph}}_{s+s'\rightleftharpoons s''} \equiv A^{s''}_{ss'}\hat{b}_s\hat{b}_{s'}\hat{b}^{\dagger}_{s''} + A^{ss'}_{s''}\hat{b}^{\dagger}_s\hat{b}^{\dagger}_{s'}\hat{b}_{s''}, \tag{5.21}$$

where

$$\begin{aligned} A^{s''}_{ss'} &= \left(A^{ss'}_{s''}\right)^* && (5.22)\\ &\equiv \left[(e_{\text{vac},s})(e_{\text{vac},s'})(e_{\text{vac},s''})\right]\int \left(A^{lmn}{}_{ijk}\right)\left(\bar{\bar{e}}_s(\mathbf{r})\right)^i_l\left(\bar{\bar{e}}_{s'}(\mathbf{r})\right)^j_m\left(\left(\bar{\bar{e}}_{s''}(\mathbf{r})\right)^*\right)^k_n \mathrm{d}^3r. && (5.23)\end{aligned}$$

Calculating to 2nd-order in perturbation theory, the energy shift in the phonon Fock state $|n_s, n_{s'}, n_{s''}\rangle$ is given by,

$$\begin{aligned}\left\langle(\delta E_{n_s,n_{s'},n_{s''}})^{\text{I}}_{\text{3-ph}}\right\rangle = \sum_{s's''}\Bigg[&\frac{\left|\left\langle n_s-1, n_{s'}-1, n_{s''}+1|A^{s''}_{ss'}\hat{b}_s\hat{b}_{s'}\hat{b}^{\dagger}_{s''}|n_s, n_{s'}, n_{s''}\right\rangle\right|^2}{\hbar\left((\omega_s+\omega_{s'}-\omega_{s''})-i(\Gamma_s+\Gamma_{s'}-\Gamma_{s''})\right)}\\ &+\frac{\left|\left\langle n_s+1, n_{s'}+1, n_{s''}-1|A^{ss'}_{s''}\hat{b}^{\dagger}_s\hat{b}^{\dagger}_{s'}\hat{b}_{s''}|n_s, n_{s'}, n_{s''}\right\rangle\right|^2}{\hbar\left((\omega_{s''}-\omega_s-\omega_{s'})-i(\Gamma_{s''}-\Gamma_s-\Gamma_{s'})\right)}\Bigg]. \end{aligned} \tag{5.24}$$

Note that we have used a modified form of non-Hermitian perturbation theory [85, 86], suitable for leaky quasi-normal modes, in which the finite linewidth of the phonon quasi-modes are included in the denominator of Eq. (5.24). Also implicit in our use of 2nd-order perturbation theory is that the phonon-phonon coupling is weak. Collecting terms and specifically identifying mode s as the breathing acoustic mode of the OMC cavity (labeled by m), we have for the complex level shift,

$$\left\langle \left(\delta E_{n_m, n_{s'}, n_{s''}}\right)^{\mathrm{I}}_{\text{3-ph}} \right\rangle = \sum_{s's''} \left(\frac{\left|A^{s''}_{m\,s'}\right|^2 \left[n_m n_{s'}(n_{s''}+1) - (n_m+1)(n_{s'}+1)n_{s''}\right]}{\hbar\left((\omega_\mathrm{m} + \omega_{s'} - \omega_{s''}) - i(\Gamma_m + \Gamma_{s'} - \Gamma_{s''})\right)} \right). \tag{5.25}$$

We now invoke the single mode relaxation time approximation, and assume that only mode m is perturbed from equilibrium,

$$\left\langle \left(\delta E_{m,s',s''}\right)^{\mathrm{I}}_{\text{3-ph}} \right\rangle_{\text{smrt}} = \sum_{s's''} \left(\frac{\left|A^{s''}_{m\,s'}\right|^2 \left[(\bar{n}_m + \delta n_m)\bar{n}_{s'}(\bar{n}_{s''}+1) - (\bar{n}_m + \delta n_m + 1)(\bar{n}_{s'}+1)\bar{n}_{s''}\right]}{\hbar\left((\omega_\mathrm{m} + \omega_{s'} - \omega_{s''}) - i(\Gamma_m + \Gamma_{s'} - \Gamma_{s''})\right)} \right), \tag{5.26}$$

where $\bar{n}$ are the thermal equilibrium mode occupancies and δn_m is the perturbation in phonon number of the breathing mode from equilibrium. Taking the difference between the complex level shift for $\delta n_m + 1$ and δn_m, we find for the single photon energy shift in mode m,

$$\left\langle \hbar\left(\delta\tilde{\omega}_m\right)^{\mathrm{I}}_{\text{3-ph}} \right\rangle_{\text{smrt}} = \sum_{s's''} \left(\frac{\left|A^{s''}_{m\,s'}\right|^2 \left[\bar{n}_{s'} - \bar{n}_{s''}\right]}{\hbar\left((\omega_\mathrm{m} + \omega_{s'} - \omega_{s''}) - i(\Gamma_m + \Gamma_{s'} - \Gamma_{s''})\right)} \right). \tag{5.27}$$

Assuming the phonon mode linewidths are energy-damping limited ($\Gamma_s = \gamma_s/2$), we find for the change in the energy damping rate of mode m due to type-I 3-phonon scattering,

$$\left\langle \left(\delta\gamma_m\right)^{\mathrm{I}}_{\text{3-ph}} \right\rangle_{\text{smrt}} \equiv \frac{-2\mathrm{Im}\left\langle \hbar\left(\delta\tilde{\omega}_m\right)^{\mathrm{I}}_{\text{3-ph}} \right\rangle_{\text{smrt}}}{\hbar\delta n_m} \tag{5.28}$$

$$= \frac{1}{\hbar^2}\sum_{s's''} \left(\frac{\left|A^{s''}_{m\,s'}\right|^2 (\gamma_{s''} - \gamma_{s'} - \gamma_m)\left[\bar{n}_{s'} - \bar{n}_{s''}\right]}{(\omega_\mathrm{m} + \omega_{s'} - \omega_{s''})^2 + (\frac{\gamma_m + \gamma_{s'} - \gamma_{s''}}{2})^2} \right)$$

$$\approx \frac{1}{\hbar^2}\sum_{s's''} \left(\frac{\left|A^{s''}_{m\,s'}\right|^2 (\gamma_{s''})\left[\bar{n}_{s'} - \bar{n}_{s''}\right]}{(\omega_\mathrm{m} + \omega_{s'} - \omega_{s''})^2 + (\frac{\gamma_m + \gamma_{s'} - \gamma_{s''}}{2})^2} \right), \tag{5.29}$$

where in the last approximate equality we have neglected the unperturbed damping of the two ‘child’ phonons (m and s') and only included the quasi-mode damping of the ‘parent’ phonon (s'') into which the mode m decays in the type-I process.

Equation (5.29) can be approximately evaluated using the relation between the 'mode-averaged' ($\langle\cdot\rangle_{\mathrm{m}}$) third-order elastic constants and the Grüneisen parameter [68],

$$\left\langle\left|A^{lmn}{}_{ijk}\right|^2\right\rangle_{\mathrm{m}} \equiv \text{mode-averaged 3-phonon scattering strength} \approx 4\rho_{\mathrm{Si}}^2 v_{\mathrm{Si}}^4 \gamma_{\mathrm{G}}^2 \quad (5.30)$$

where mode averaging is taken over different bulk phonon mode directions and polarizations. This allows us to write for the 3-phonon scattering amplitude,

$$A_{ms'}^{s''} \approx \left(2\rho_{\mathrm{Si}} v_{\mathrm{Si}}^2 \gamma_{\mathrm{G}}\right) \left[(e_{\mathrm{vac},m})(e_{\mathrm{vac},s'})(e_{\mathrm{vac},s''})\right] \left(\mathcal{F}_{m\,s'}^{s''} V_m\right), \quad (5.31)$$

in which $\mathcal{F}_{m\,s'}^{s''}$ is a mode overlap factor, or equivalently, for plane wave modes, a phase-matching term. The mode overlap factor is less than or equal to unity and depends approximately upon the tensor-averaged normalized strain fields of each of the three modes participating in the scattering process,

$$\mathcal{F}_{m\,s'}^{s''} = \frac{1}{V_m} \int \left(\left\langle\overline{\bar{\bar{e}}_m(\mathbf{r})}\right\rangle_{\mathrm{t}}\right) \left(\left\langle\overline{\bar{\bar{e}}_{s'}(\mathbf{r})}\right\rangle_{\mathrm{t}}\right) \left(\left\langle\overline{\bar{\bar{e}}_{s''}(\mathbf{r})}\right\rangle_{\mathrm{t}}\right)^* \mathrm{d}^3 r \lesssim 1. \quad (5.32)$$

As with the elastic constants, we define a tensor-averaged strain field as,

$$\langle\bar{\bar{e}}_s(\mathbf{r})\rangle_{\mathrm{t}} \equiv \text{tensor-averaged local strain field amplitude of mode } s \quad (5.33)$$

$$= \frac{1}{3^2}\left(\sum_{i,j}\left(e_s(\mathbf{r})_i^j\right)^2\right)^{1/2}. \quad (5.34)$$

5.1.2 Type-II Scattering Processes

Following a similar procedure for type-II scattering ($m \rightleftharpoons s' + s''$) yields a complex energy level shift in Fock state $|n_m, n_{s'}, n_{s''}\rangle$,

$$\left\langle\left(\delta E_{m,s',s''}\right)_{\text{3-ph}}^{\mathrm{II}}\right\rangle = \frac{1}{2}\sum_{s's''}\left(\frac{\left|A_{s's''}^{m}\right|^2\left[n_{s'}n_{s''}(n_m+1)-(n_{s'}+1)(n_{s''}+1)n_m\right]}{\hbar\left((\omega_{s'}+\omega_{s''}-\omega_{\mathrm{m}})-i(\Gamma_{s'}+\Gamma_{s''}-\Gamma_m)\right)}\right). \quad (5.35)$$

Assuming the SMRT approximation and taking the difference between the energy level shifts for displaced phonon numbers of $\delta n_m + 1$ and δn_m yields the single photon complex energy level shift,

$$\left\langle \hbar \left(\delta \tilde{\omega}_m\right)^{\mathrm{II}}_{\text{3-ph}} \right\rangle_{\mathrm{smrt}} = \frac{1}{2} \sum_{s's''} \left(\frac{\left|A^m_{s's''}\right|^2 \left[-(1 + \bar{n}_{s'} + \bar{n}_{s''})\right]}{\hbar \left((\omega_{s'} + \omega_{s''} - \omega_{\mathrm{m}}) - i(\Gamma_{s'} + \Gamma_{s''} - \Gamma_m)\right)} \right), \quad (5.36)$$

and the perturbation in the energy damping rate of mode m due to type-II 3-phonon scattering,

$$\left\langle (\delta \gamma_m)^{\mathrm{II}}_{\text{3-ph}} \right\rangle_{\mathrm{smrt}} = \frac{1}{2\hbar^2} \sum_{s's''} \left(\frac{\left|A^m_{s's''}\right|^2 (\gamma_{s'} + \gamma_{s''} - \gamma_m) \left[1 + \bar{n}_{s'} + \bar{n}_{s''}\right]}{(\omega_{s'} + \omega_{s''} - \omega_{\mathrm{m}})^2 + (\frac{\gamma_{s'}+\gamma_{s''}-\gamma_m}{2})^2} \right). \quad (5.37)$$

In Section 5.3 we use Eqs. (5.29) and (5.37) to numerically evaluate the expected damping of the breathing mode due to 3-phonon scattering with numerically simulated quasi-normal modes of the OMC cavity.

5.1.3 3-phonon Scattering in Bulk Si

In order to compare the estimated 3-phonon scattering in the restricted geometry of the OMC cavity to that of a bulk material, here we consider a simplified model of 3-phonon scattering in bulk Si in which we treat Si as an isotropic acoustic material. We are primarily interested in Normal ($\mathcal{N}$), type-I scattering processes. $\mathcal{N}$ processes due to the low temperature, and thus low frequency of the acoustic phonons involved in the scattering, and type-I scattering due to the suppression of type-II scattering processes in the effectively one-dimensional OMC cavity for phonon frequencies below that of the breathing mode. As derived in Ref. [68], for such a bulk material system the acoustic damping of mode s under the single mode relaxation time approximation can be written as,

$$(\gamma_s)^{\mathcal{N}-\mathrm{I}}_{\text{3-ph,bulk}} = \frac{\hbar v_p \left\langle \gamma_{\mathrm{G}} \right\rangle^2}{4\pi \rho_{\mathrm{Si}} \left\langle v^2_{\mathrm{Si}} \right\rangle} \sum_{p'p''} \left(v^2_{p'} v^2_{p''} \right)^{-1}$$
$$\int_{\mathcal{R}[p',p'']} \mathrm{d}\omega_{s'} \left(\omega_{s'}\right)^2 \left(\omega_{s'} + \omega_s\right)^2 \left(\bar{n}[\hbar\omega_{s'}/k_B T] - \bar{n}[\hbar(\omega_{s'} + \omega_s)/k_B T]\right), \quad (5.38)$$

where p, p', and p'' label the acoustic polarization of the modes s, s', and s'', respectively. The region of integration, $\mathcal{R}[p, p']$, depends upon the acoustic velocity dispersion versus frequency and polarization (having assumed an isotropic bulk model with no directional dispersion). Rewriting in terms of normalized frequencies ($y = \omega(\hbar/k_B T)$), yields the following simplified form of the phonon damping,

$$(\gamma_s)^{\mathcal{N}-\mathrm{I}}_{\text{3-ph,bulk}} = \frac{\hbar v_p \left\langle \gamma_{\mathrm{G}} \right\rangle^2 (k_B T/\hbar)^5}{4\pi \rho_{\mathrm{Si}} \left\langle v_{\mathrm{Si}}^2 \right\rangle} \sum_{p' p''} \left(v_{p'}^2 v_{p''}^2 \right)^{-1} \left\{ \int_{\mathcal{R}[p',p'',T]} \mathrm{d}y_{s'} \, (y_{s'})^2 \, (y_{s'} + y_s)^2 \, (\bar{n}[y_{s'}] - \bar{n}[y_{s'} + y_s]) \right\}. \tag{5.39}$$

The integral in curly brackets is unitless and depends on temperature through both the integration range and the constant $y_s = \hbar\omega_s/k_B T$.

Neglecting frequency dispersion, $\mathcal{R}[p', p'']$ takes on a relatively simple form for the various acoustic polarization scenarios. Due to polarization dispersion, the only allowed Normal, type-I scattering processes are: $L_s + L_{s'} \rightleftharpoons L_{s''}$, $L_s + T_{s'} \rightleftharpoons L_{s''}$, $T_s + L_{s'} \rightleftharpoons L_{s''}$, and $T_s + T_{s'} \rightleftharpoons L_{s''}$, where L (T) corresponds to longitudinal (transverse/shear) polarization acoustic waves. The breathing mode is of mixed polarization character, so all four combinations are potentially relevant for comparison to the numerical calculations performed using the quasi-modes of the OMC structure. Defining normalized wavevector magnitudes for the three acoustic waves ($x = |\mathbf{q}_s|/q_D$, $x' = |\mathbf{q}_{s'}|/q_D$, $x'' = |\mathbf{q}_{s''}|/q_D$), the integration range $\mathcal{R}[p, p']$ for x' is given by:

$$L_s + L_{s'} \rightleftharpoons L_{s''}\colon\ x' = \{0, 1 - x\} \rightarrow \omega_{s'} \simeq \{0, \omega_D\}, \tag{5.40}$$

$$T_s + L_{s'} \rightleftharpoons L_{s''}\colon\ x' = \{x_1 x, 1 - r x\} \rightarrow \omega_{s'} \simeq \{(x_1/r)\omega_s, \omega_D\}, \tag{5.41}$$

$$T_s + T_{s'} \rightleftharpoons L_{s''}\colon\ x' = \{x_1 x, x/x_1\} \rightarrow \omega_{s'} \simeq \{(x_1/r)\omega_s, (1/x_1 r)\omega_s\}, \tag{5.42}$$

$$L_s + T_{s'} \rightleftharpoons L_{s''}\colon\ x' = \{0, x/x_3\} \rightarrow \omega_{s'} \simeq \{0, (1/x_3 r)\omega_s\}, \tag{5.43}$$

where $q_D = \pi/a$ is the Debye wavevector for an atomic lattice constant a, $\omega_D = q_D \left\langle v_{\mathrm{Si}} \right\rangle$, $r = v_{\mathrm{t}}/v_{\mathrm{l}}$ (≈ 0.69 in the [100] direction), $x_1 = (1 - r)/(1 + r) \approx 0.18$, and $x_3 = (1 - r)/2 \approx 0.15$. For a breathing mode at 5 GHz, the corresponding lower frequency cut-off for the integration range of both TLL and TTL scattering would approximately be 1.3 GHz. The upper frequency cut-off of TTL and LTL scattering would be 40 GHz and 47 GHz, respectively. At temperatures below approximately 50 mK these processes would turn off, and they would saturate for temperatures above approximately 2 K. In what follows we consider the LLL scattering combination for comparison as it has effectively unlimited integration range and thus will contribute at both low and high temperatures relative to $T = \hbar\omega_s/k_B$ ($\approx$ 200 mK for the breathing mode).

5.2 TLS Damping Model

In addition to phonon-phonon scattering, another possible form of damping for the acoustic breathing mode is due to coupling to tunneling states (TS) or two-level systems (TLS). TS (or similar TLS) states correspond to a generic defect state in a solid-state material, typically an amorphous material, in which two local arrangements of atoms are nearly degenerate in energy. The two different atomic arrangements can have both a permanent electric and acoustic dipole associated with them, and atoms can tunnel between the two different arrangements. The TS and TLS models are two different phenomelogical models that are used to describe a wide variety of microscopic situations. Generically, in the TS model one has an asymmetry energy Δ which corresponds to the energy difference between the lowest energy level in each of the local potential energy profiles defining the two independent atomic arrangements, and a tunneling energy Δ_0 related to the energy barrier between the two local atomic arrangements (see Fig. 5.3(a)). One diagonalizes the two lowest energy states of the two atomic arrangements into hybridized modes $|\psi_1\rangle$ and $|\psi_2\rangle$, whose energy difference is dependent upon a longitudinal dipole matrix element and which can be coupled via a transition dipole matrix element. In the TS model the ratio of the longitudinal dipole coupling to transition dipole coupling strength depends on the ratio of asymmetry energy to tunneling energy. The TLS model treats the longitudinal and transition dipole couplings as independent.

In the diagonal basis of the TS with asymmetry energy Δ and tunneling energy Δ_0, the interaction between the TS and a stress wave of phonon mode s is,

$$\hat{\mathcal{H}}_{\text{int, TS}-s} \approx \left(\frac{\Delta_0}{E}\hat{\sigma}_x + \frac{\Delta}{E}\hat{\sigma}_z\right)\bar{\gamma}_{\text{TS}}\hat{\bar{e}}_s(\mathbf{r}_0), \tag{5.44}$$

where $\mathbf{r}_0$ is the point-like location of the TS and $E = (\Delta^2 + \Delta_0^2)^{1/2}$ is the TS transition energy. Here we treat the stress interaction as approximately scalar, hence, $\bar{\gamma}_{\text{TS}}$ and $\hat{\bar{e}}_s$ are the tensor-averaged deformation potential and stress operator, respectively. The corresponding TLS interaction Hamiltonian is given by,

$$\hat{\mathcal{H}}_{\text{int, TLS}-s} \approx (M\hat{\sigma}_x + D\hat{\sigma}_z)\,\hat{\bar{e}}_s(\mathbf{r}_0), \tag{5.45}$$

where M is a transverse coupling potential and D is a longitudinal coupling potential. We will follow a TLS model in what follows as it simplifies some of the analysis;

however, it is important to note that the TLS model is more constrained than the TS model in that the ratio of transverse and longitudinal coupling is fixed for a given TLS energy. This has the effect of eliminating the wide range of possible excited state decay rates for TS of a fixed energy. In fitting our data with a TS model we found that a model with rather narrow Δ_0 distribution whose mean scales approximately with E fit best, which is effectively a TLS model.

We define corresponding (tensor-averaged) transverse and longitudinal vacuum coupling rates as,

$$\bar{g}_{\mathrm{t},s}(\mathbf{r}_0) = \frac{M}{\hbar}(e_{\mathrm{vac},s}) \left\langle \overline{\bar{\bar{e}}_s(\mathbf{r}_0)} \right\rangle_{\mathrm{t}} \tag{5.46}$$

and

$$\bar{g}_{\mathrm{l},s}(\mathbf{r}_0) = \frac{D}{\hbar}(e_{\mathrm{vac},s}) \left\langle \overline{\bar{\bar{e}}_s(\mathbf{r}_0)} \right\rangle_{\mathrm{t}} \tag{5.47}$$

respectively, allowing us to write for the interaction Hamiltonian,

$$\hat{\mathcal{H}}_{\mathrm{int,\,TLS}-s} \approx \hbar \left[\bar{g}_{\mathrm{t},s}(\mathbf{r}_0)\hat{\sigma}_x + \bar{g}_{\mathrm{l},s}(\mathbf{r}_0)\hat{\sigma}_z \right] \left(\hat{b}_s + \hat{b}_s^\dagger \right). \tag{5.48}$$

Including the bare TLS and phonon energy terms, we have for the total Hamiltonian,

$$\hat{\mathcal{H}}_{\mathrm{TLS}-s} \approx \frac{\hbar\omega_{\mathrm{TLS}}}{2}\hat{\sigma}_z + \hbar\omega_s \left(\hat{b}_s^\dagger \hat{b}_s + 1/2 \right) + \hbar \left[\bar{g}_{\mathrm{t},s}(\mathbf{r}_0)\hat{\sigma}_x + \bar{g}_{\mathrm{l},s}(\mathbf{r}_0)\hat{\sigma}_z \right] \left(\hat{b}_s + \hat{b}_s^\dagger \right), \tag{5.49}$$

where ω_{TLS} is the bare transition frequency of the TLS ($E = \hbar\omega_{\mathrm{TLS}}$). The $\hat{\sigma}_x$ interaction term leads to 'resonant' decay into the phonon bath and a bath-dependent level shift of the TLS which can be treated using 2nd-order perturbation theory. The $\hat{\sigma}_z$ interaction term gives rise to 'relaxation'-type processes of higher-order in perturbation theory.

5.2.1 TLS Decay into the Phonon Bath

We first consider a single TLS interacting with the phonons as a dissipative bath (the roles will be reversed when we consider the damping of a given phonon mode). We assume that the TLS decay primarily through resonant $\hat{\sigma}_x$ interactions with the phonon bath, neglecting the $\hat{\sigma}_z$ interaction term. Also, owing to the finite-size of the acoustic cavity structure studied here, we work in a discrete basis of phonon quasi-normal modes. The bare phonon modes of the acoustic cavity have a complex frequency due to coupling to the phonons of the substrate, $\tilde{\omega}_s = \omega_s - i\Gamma_s$, where ω_s is the real angular frequency and $\Gamma_s = \gamma_s/2 + \Gamma_{s,\phi}$ is the phonon *amplitude* decoherence rate given by the sum of half the energy decay rate (γ_s) and the pure dephasing rate ($\Gamma_{s,\phi}$) of the phonon mode. From 2nd-order perturbation theory [85, 87] we find a complex frequency shift of the TLS transition given by,

$$(\delta\tilde{\omega}_{\mathrm{TLS}})_s \approx \left(2\bar{g}_{\mathrm{t},s}^2(n_s + 1/2)\right)\left[\frac{1}{\tilde{\Delta}_{\mathrm{TLS},s}} + \frac{1}{\tilde{\Delta}_{\mathrm{TLS},s} + 2\tilde{\omega}_s}\right], \tag{5.50}$$

where n_s is the phonon occupancy of mode s and $\tilde{\Delta}_{\mathrm{TLS},s} \equiv \tilde{\omega}_{\mathrm{TLS}} - \tilde{\omega}_s$ is the near-resonant complex detuning. Here we have included the non-resonant term as it contributes non-negligibly to the TLS frequency shift (the real part of Eq. (5.50)) when summing over contributions from phonon modes of large detuning. Implicit in our use of 2nd-order perturbation theory is that the TLS-s coupling remains in a small coupling limit ($|\bar{g}_{\mathrm{t},s}|/|\tilde{\Delta}_{\mathrm{TLS},s}| \ll 1$) where non-degenerate perturbation theory is accurate. One can also utilize quasi-degenerate perturbation theory [87] to determine the complex frequency shift without restriction on the strength of the coupling; however, the formulae are more complex and require careful elimination of non-physical solutions. For simplicity of presentation, here we limit ourselves to the small coupling limit. Below, in performing numerical calculations with specific TLS ensembles we found that the small coupling limit is adequate due to the low spectral density of phonon quasi-modes and TLS, and consequently the very unlikely situation where $|\bar{g}_{\mathrm{t},s}|/|\tilde{\Delta}_{\mathrm{TLS},s}| \gtrsim 1$.

One can arrive at a similar result in Hamiltonian form by rotating to a dressed TLS basis that diagonalizes Eq. (5.49) in the N-excitation manifold to 2nd-order in the small parameter $\bar{g}_{\mathrm{t},s}/|\tilde{\omega}_{\mathrm{TLS}} - \tilde{\omega}_s|$,

$$\hat{\mathcal{H}}^{\mathrm{eff,res.}}_{\mathrm{TLS}-s} \approx \hbar\left(\tilde{\omega}_{\mathrm{TLS}}\right)\frac{\hat{\sigma}_z}{2} + \hbar\left(\tilde{\omega}_s + \frac{\bar{g}_{\mathrm{t},s}^2}{\tilde{\Delta}_{\mathrm{TLS},s}}\hat{\sigma}_z\right)\left(\hat{b}_s^\dagger\hat{b}_s + 1/2\right), \tag{5.51}$$

where we have included only the 'resonant' σ_x interaction for now. Due to our use of quasi-normal modes for both TLS and mode s, $\hat{\mathcal{H}}^{\mathrm{eff,res.}}_{\mathrm{TLS}-s}$ is an effective Hamiltonian with complex energy eigenvalues. We see from this effective Hamiltonian that the resonant σ_x interaction leads both to a dressing of the TLS and the phonon mode: (i) viewed as a Stark-like shift of the TLS, the dressed complex frequency of the TLS is $\tilde{\omega}'_{\text{TLS}} = \tilde{\omega}_{\text{TLS}} + (2\bar{g}_{\text{t},s}^2/\tilde{\Delta}_{\text{TLS},s})\langle\hat{b}_s^\dagger\hat{b}_s + 1/2\rangle$, (ii) viewed as a TLS state-dependent shift of the phonon frequency, the dressed complex frequency of the mode s is $\tilde{\omega}'_s = \tilde{\omega}_s + (\bar{g}_{\text{t},s}^2/\tilde{\Delta}_{\text{TLS},s})\langle\hat{\sigma}_z\rangle$. The absence of the non-resonant term $[(\tilde{\Delta}_{\text{TLS},s} + 2\tilde{\omega}_s)^{-1}]$ in Eq. (5.51) is due to our restriction to the N-excitation manifold.

Returning to Eq. 5.50 and focusing on the damping effect of the phonon mode s on the TLS, we extract the imaginary component of $\delta\tilde{\omega}_{\text{TLS}}$ corresponding to the phonon-induced decoherence rate of the TLS,

$$\left(\delta\Gamma_{2,\text{TLS}}\right)_s = -\text{Im}\left[(\delta\tilde{\omega}_{\text{TLS}})_s\right] \approx \frac{2\bar{g}_{\text{t},s}^2\left(\Gamma_s - \Gamma_{2,\text{TLS}}\right)(n_s + 1/2)}{(\omega_{\text{TLS}} - \omega_{\text{s}})^2 + (\Gamma_{2,\text{TLS}} - \Gamma_s)^2}. \tag{5.52}$$

Assuming the TLS primarily decohere through the phonon bath such that the bare $\Gamma_{2,\text{TLS}} \approx 0$ (neglecting other bath contributions and TLS-TLS dephasing, for instance), and neglecting pure dephasing of the phonon mode ($\Gamma_{s,\phi} = 0$), we can write for the phonon-induced energy decay rate of the TLS due to mode s,

$$\left(\delta\Gamma_{1,\text{TLS}}\right)_s \approx 2\left(\delta\Gamma_{2,\text{TLS}}\right)_s \approx \left[\frac{\bar{g}_{\text{t},s}^2}{(\omega_{\text{TLS}} - \omega_{\text{s}})^2 + (\gamma_s/2)^2}\right](\gamma_s(2n_s + 1)). \tag{5.53}$$

For a phonon bath in thermal equilibrium at temperature T we have that $2n_s + 1 = \coth(\hbar\omega_{\text{s}}/2k_B T)$. Summing over the discrete set of quasi-normal phonon modes allows us to write for the total phonon-induced $\Gamma_{1,\text{TLS}}$ as a function of phonon bath temperature,

$$\left(\delta\Gamma_{1,\text{TLS}}\right)_{\text{ph}} \approx \sum_s \left[\frac{\bar{g}_{\text{t},s}^2\gamma_s}{(\omega_{\text{TLS}} - \omega_{\text{s}})^2 + (\gamma_s/2)^2}\right](\coth(\hbar\omega_{\text{s}}/2k_B T)). \tag{5.54}$$

One recovers the standard result for a TLS interacting with a continuum phonon bath [69] by integrating Eq. (5.54) weighted by the appropriate phonon density of states per unit frequency, $\rho_{\text{ph}}[\omega_{\text{s}}]$,

$$\left(\delta\Gamma_{1,\text{TLS}}\right)_{\text{ph,cont.}} \approx 2\pi\rho_{\text{ph}}[\omega_{\text{TLS}}](\bar{g}_{\text{t},s}[\omega_{\text{TLS}}])^2(\coth[\hbar\omega_{\text{TLS}}/2k_B T]). \tag{5.55}$$

For a three-dimensional (3D) bulk material the (polarization-averaged) phonon bath density of states is $\rho_{\text{ph}} = (V/(2\pi^2\bar{v}^3))\omega_{\text{s}}^2$, where $\bar{v}$ is an average acoustic velocity in the material. The phonon modes of a homogeneous bulk are plane waves with vacuum strain amplitude $e_{\text{vac},s} = (\hbar\omega_s/2\bar{J}V)^{1/2}$, where $\bar{J}$ is a (2nd-order in strain) elastic energy density coefficient or bulk modulus of the material. The acoustic velocity and bulk modulus can be related to the bulk material mass density, $\bar{\rho}_{\text{m}} = \bar{J}/\bar{v}^2$. Substituting these values into Eq. (5.55) yields for an average TLS coupled to a phonon bath in a 3D bulk,

$$\left(\delta\Gamma_{1,\text{TLS}}\right)_{\text{ph,3D}} \approx \left(\frac{\bar{M}^2\omega_{\text{TLS}}^3}{2\pi\hbar\bar{J}\bar{v}^3}\right)\left(\coth[\hbar\omega_{\text{TLS}}/2k_BT]\right) \tag{5.56}$$

$$= \left(\frac{\bar{M}^2\omega_{\text{TLS}}^3}{2\pi\hbar\bar{\rho}_{\text{m}}\bar{v}^5}\right)\left(\coth[\hbar\omega_{\text{TLS}}/2k_BT]\right), \tag{5.57}$$

where $\bar{M}$ is an averaged (over TLS orientation and acoustic polarization) transverse coupling potential. For future reference we also quote here the corresponding result for a quasi two-dimensional (2D) material, corresponding to a plate of large area and thickness t smaller than the acoustic wavelength,

$$\left(\delta\Gamma_{1,\text{TLS}}\right)_{\text{ph,2D}} \approx \left(\frac{\bar{M}^2\omega_{\text{TLS}}^2}{2\hbar\bar{\rho}_{\text{m}}\bar{v}^4 t}\right)\left(\coth[\hbar\omega_{\text{TLS}}/2k_BT]\right), \tag{5.58}$$

and a quasi one-dimensional (1D) material, corresponding to a beam of long length and small cross-sectional dimension $\bar{w}$ relative to the acoustic wavelength,

$$\left(\delta\Gamma_{1,\text{TLS}}\right)_{\text{ph,1D}} \approx \left(\frac{\bar{M}^2\omega_{\text{TLS}}}{2\hbar\bar{\rho}_{\text{m}}\bar{v}^3\bar{w}^2}\right)\left(\coth[\hbar\omega_{\text{TLS}}/2k_BT]\right). \tag{5.59}$$

In a prelude to what follows, we note that the frequency scaling with bath dimension will set the temperature scaling of the non-resonant TLS 'relaxation' damping of acoustical modes; hence, a 3D phonon bath will yield a T^3 dependence, a 2D bath a quadratic T^2 dependence, and a 1D bath will result in a linear T dependence.

5.2.2 'Resonant' TLS Damping and Frequency Shift of Acoustic Cavity Quasi-modes

In contrast to the analysis of the prior sub-section, we now reverse roles and consider the TLS to be a bath for the acoustic phonon modes of the structure. In particular, we are interested in the localized high-Q phonon mode which lies within the phononic bandgap of the acoustic radiation shield. As such, this phonon mode should have much smaller intrinsic (radiation) damping to the substrate than the average phonon bath mode considered in the previous sub-section. We first consider the effects of the $\hat{\sigma}_x$ TLS-phonon interaction. Referring to Eq. (5.51), the 'resonant' ($\hat{\sigma}_x$) contribution to the TLS state-dependent shift in the complex phonon frequency is given by,

$$(\delta\tilde{\omega}_s)_{\mathrm{TLS,res}} \approx \left(\bar{g}_{\mathrm{t},s}^2[\mathbf{r}_{\mathrm{TLS}}]\langle\hat{\sigma}_z\rangle\right)\left[\frac{1}{\tilde{\Delta}_{\mathrm{TLS},s}} + \frac{1}{\tilde{\Delta}_{\mathrm{TLS},s} + 2\tilde{\omega}_s}\right], \tag{5.60}$$

where $\mathbf{r}_{\mathrm{TLS}}$ is the spatial location of the TLS in the acoustic cavity and we have added in by hand the non-resonant $[(\tilde{\Delta}_{\mathrm{TLS},s} + 2\tilde{\omega}_s)^{-1}]$ term as found in the perturbation analysis of Eq. (5.50). For a TLS in thermal equilibrium at temperature T one has $\langle\hat{\sigma}_z\rangle = -\tanh[\hbar\omega_{\mathrm{TLS}}/2k_B T]$. Considering interaction with an ensemble of TLS and summing over this ensemble yields for the TLS state-dependent shift in the real part of the frequency of the phonon mode s,

$$\begin{aligned}(\delta\omega_{\mathrm{s}})_{\mathrm{res}} \approx \sum_{\mathrm{TLS}} \mathrm{Re}\,[(\delta\tilde{\omega}_s)_{\mathrm{TLS}}] = -\sum_{\mathrm{TLS}} \left(\bar{g}_{\mathrm{t},s}^2[\mathbf{r}_{\mathrm{TLS}}]\tanh[\hbar\omega_{\mathrm{TLS}}/2k_B T]\right) \\ \times\left[\frac{\omega_{\mathrm{TLS}} - \omega_{\mathrm{s}}}{(\omega_{\mathrm{TLS}} - \omega_{\mathrm{s}})^2 + (\Gamma_{2,\mathrm{TLS}} - \Gamma_s)^2} + \frac{\omega_{\mathrm{TLS}} + \omega_{\mathrm{s}}}{(\omega_{\mathrm{TLS}} + \omega_{\mathrm{s}})^2 + (\Gamma_{2,\mathrm{TLS}} + \Gamma_s)^2}\right].\end{aligned} \tag{5.61}$$

Substituting for $\Gamma_{2,\mathrm{TLS}}$ the estimated energy decay rate due to coupling to the rest of the phonon bath found in Eq. (5.53) and a pure dephasing rate ($\Gamma_{\phi,\mathrm{TLS}}$), and assuming the phonon mode m of interest has a much smaller decoherence rate than the *dressed* TLS, we have that,

$$\begin{aligned}(\delta\omega_{\mathrm{m}})_{\mathrm{res}} \approx -\sum_{\mathrm{TLS}} \left(\bar{g}_{\mathrm{t},m}^2[\mathbf{r}_{\mathrm{TLS}}]\tanh[\hbar\omega_{\mathrm{TLS}}/2k_B T]\right) \\ \times\left[\frac{\omega_{\mathrm{TLS}} - \omega_{\mathrm{m}}}{(\omega_{\mathrm{TLS}} - \omega_{\mathrm{m}})^2 + ((\delta\Gamma_{1,\mathrm{TLS}})_{\mathrm{ph}}/2 + \Gamma_{\phi,\mathrm{TLS}})^2} + \frac{\omega_{\mathrm{TLS}} + \omega_{\mathrm{m}}}{(\omega_{\mathrm{TLS}} + \omega_{\mathrm{m}})^2 + ((\delta\Gamma_{1,\mathrm{TLS}})_{\mathrm{ph}}/2 + \Gamma_{\phi,\mathrm{TLS}})^2}\right].\end{aligned} \tag{5.62}$$

Similarly, the energy damping rate of mode m due to resonant interaction processes with the TLS bath is given by,

$$(\delta\gamma_{\mathrm{m}})_{\mathrm{res}} \approx \sum_{\mathrm{TLS}} -2\mathrm{Im}\left[(\delta\tilde{\omega}_m)_{\mathrm{TLS}}\right] \approx \sum_{\mathrm{TLS}} \left[\frac{\left(\bar{g}^2_{\mathrm{t},m}[\mathbf{r}_{\mathrm{TLS}}]\tanh[\hbar\omega_{\mathrm{TLS}}/2k_BT]\right)(\delta\Gamma_{1,\mathrm{TLS}})_{\mathrm{ph}}}{(\omega_{\mathrm{TLS}}-\omega_{\mathrm{m}})^2+((\delta\Gamma_{1,\mathrm{TLS}})_{\mathrm{ph}}/2+\Gamma_{\phi,\mathrm{TLS}})^2}\right], \tag{5.63}$$

where we have neglected the non-resonant term $[(\tilde{\Delta}_{\mathrm{TLS},s}+2\tilde{\omega}_s)^{-1}]$ due to its much weaker contribution to the Lorentzian damping function. Note that we have not included the $\Gamma_{\phi,\mathrm{TLS}}$ contribution in the numerator of Eq. (5.63) as it adds pure dephasing to the phonon mode m.

One recovers the standard result for damping of a phonon interacting with a continuum TLS bath [69] by integrating Eq. (5.63) weighted by the TLS density of states per unit *angular* frequency in the acoustic mode volume, $n_{0,m}/2\pi \equiv \hbar n_0\eta_{\mathrm{surf}}V_m$,

$$(\delta\gamma_{\mathrm{m}})_{\text{res, cont.}} \approx (2\pi)(\hbar\eta_{\mathrm{surf}}n_0V_m)\overline{\bar{g}^2_{\mathrm{t},m}[\mathbf{r}_m]}\tanh[\hbar\omega_{\mathrm{m}}/2k_BT] \tag{5.64}$$

$$\approx \left(\frac{\pi\bar{M}^2\omega_{\mathrm{m}}}{\bar{\rho}_{\mathrm{m}}\bar{v}^2}\right)(\eta_{\mathrm{surf}}n_0)\tanh[\hbar\omega_{\mathrm{m}}/2k_BT], \tag{5.65}$$

where $\eta_{\mathrm{surf}}n_0$ is the effective bulk TLS density per unit volume per unit energy, and the average transverse coupling rate for TLS in the acoustic mode volume is approximately, $\overline{\bar{g}^2_{\mathrm{t},m}[\mathbf{r}_m]} \approx (\bar{M}/\hbar)^2(\hbar\omega_{\mathrm{m}}/2\bar{\rho}_{\mathrm{m}}\bar{v}^2V_m)$. Following a similar averaging over the cavity mode volume and integration over a TLS density in Eq. (5.62), one obtains the corresponding frequency shift of the breathing mode due to resonant interaction with a continuum of TLS,

$$\begin{aligned}(\delta\omega_{\mathrm{m}})_{\text{res, cont.}} &\approx -(\hbar\eta_{\mathrm{surf}}n_0V_m)\overline{\bar{g}^2_{\mathrm{t},m}[\mathbf{r}_m]}\\ &\times \mathrm{Re}\left\{\int_0^{\omega_{\max}} \mathrm{d}\omega_{\mathrm{TLS}}\tanh[\hbar\omega_{\mathrm{TLS}}/2k_BT]\left(\frac{1}{(\omega_{\mathrm{TLS}}-\omega_{\mathrm{m}})+i\Gamma_{2,\mathrm{TLS}}}+\frac{1}{(\omega_{\mathrm{TLS}}+\omega_{\mathrm{m}})-i\Gamma_{2,\mathrm{TLS}}}\right)\right\},\end{aligned} \tag{5.66}$$

where $\omega_{\max}$ is the maximum transition frequency of the TLS ensemble. The integral can be evaluated using the digamma function [88], yielding the following simplified result,

$$(\delta\omega_{\mathrm{m}})_{\text{res, cont.}} \approx \left(\frac{\bar{M}^2\omega_{\mathrm{m}}}{\bar{\rho}_{\mathrm{m}}\bar{v}^2}\right)(\eta_{\mathrm{surf}}n_0)\left(\mathrm{Re}\left\{\Psi\left[\frac{1}{2}+i\frac{\hbar\omega_{\mathrm{m}}}{2\pi k_BT}\right]\right\}-\ln\left[\frac{\hbar\omega_{\max}}{2\pi k_BT}\right]\right). \tag{5.67}$$

5.2.3 'Relaxation' TLS Damping and Frequency Shift of Acoustic Cavity Quasi-modes

Relaxation damping of acoustic cavity modes results not from direct energy exchange with nearly-resonant TLS, but rather from the shift in the TLS transition frequencies due to the σ_z interaction of Eq. (5.45). This shift, which is linear in the stress amplitude of the acoustic modes and oscillates in time with the frequency of the acoustic mode, displaces the TLS from equilibrium. During this oscillatory displacement out of equilibrium the TLS will relax back towards equilibrium at a rate given by the TLS energy decay rate, stealing away energy from the acoustic mode in the process. Microscopically this is a process involving higher-order perturbation interactions between the TLS and the phonon bath. As such, here we follow the standard semi-classical analysis of relaxation damping by considering the acoustic dipole response of the TLS to a (classical) strain field [69, 88].

The magnitude of the longitudinal acoustic dipole of a TLS is given by $\langle\bar{\bar{p}}_a\rangle_\text{t} \equiv D\langle\hat{\sigma}_z\rangle$. For a small amplitude, harmonic strain field oscillating in mode s, $\langle\bar{\bar{e}}_s[\mathbf{r};\omega_s]\rangle_\text{t}$, the harmonically oscillating component of the longitudinal acoustic dipole is linearly related to the applied strain at the site of TLS through a (tensor-averaged) susceptibility, $\langle\bar{\bar{\chi}}_\text{rel}[\omega_s]\rangle_\text{t} \equiv \langle\delta\bar{\bar{p}}_a[\omega_s]\rangle_\text{t}/\langle\bar{\bar{e}}_s[\mathbf{r}_\text{TLS};\omega_s]\rangle_\text{t}$, where $\langle\delta\bar{\bar{p}}_a[\omega_s]\rangle_\text{t} = D(\delta\langle\hat{\sigma}_z[\omega_s]\rangle)$, $\delta\langle\hat{\sigma}_z\rangle = (\langle\hat{\sigma}_z\rangle - \langle\hat{\sigma}_z\rangle_\text{eq.})$, and $\langle\hat{\sigma}_z\rangle_\text{eq.} = -\tanh[\hbar\omega_\text{TLS}/2k_BT]$ is the TLS inversion in thermal equilibrium. Solving the Bloch equations assuming a finite relaxation rate to equilibrium of $\Gamma_{1,\text{TLS}}$, the displacement of the inversion from equilibrium follows the applied harmonic strain with a phase lag,

$$\delta\langle\hat{\sigma}_z\rangle \approx \frac{\partial\langle\hat{\sigma}_z\rangle_\text{eq.}}{\partial\omega_\text{TLS}}\frac{\partial\omega_\text{TLS}}{\partial\langle\bar{\bar{e}}_s\rangle_\text{t}}\left(\frac{1-i\omega_s(\Gamma_{1,\text{TLS}})^{-1}}{1+(\omega_s(\Gamma_{1,\text{TLS}})^{-1})^2}\right)\langle\bar{\bar{e}}_s\rangle_\text{t}. \tag{5.68}$$

From Eq. (5.49) one can show that $\partial\omega_\text{TLS}/\partial\langle\bar{\bar{e}}_s\rangle_\text{t} = (2D/\hbar)$, and $\partial\langle\hat{\sigma}_z\rangle_\text{eq.}/\partial\omega_\text{TLS} = (\hbar/2k_BT)\,\text{sech}^2[\hbar\omega_\text{TLS}/2k_BT]$. This yields for the relaxation susceptibility,

$$\langle\bar{\bar{\chi}}_\text{rel}[\omega_s;\omega_\text{TLS}]\rangle_\text{t} = \left(\frac{D^2}{k_BT}\right)\left(\frac{1-i\omega_s(\Gamma_{1,\text{TLS}})^{-1}}{1+(\omega_s(\Gamma_{1,\text{TLS}})^{-1})^2}\right)\text{sech}^2[\hbar\omega_\text{TLS}/2k_BT]. \tag{5.69}$$

The complex energy shift of the acoustic mode due to its interaction with the TLS is given by $(\delta\tilde{E}_s)_\text{TLS} \approx \langle\bar{\bar{p}}_a\rangle_\text{t}(\langle\bar{\bar{e}}_s[\mathbf{r}_\text{TLS}]\rangle_\text{t})^*$. Noting the complex energy shift can be related to a complex frequency shift in the acoustic resonance through the stored phonon number (n_s), $(\delta\tilde{E}_s)_\text{TLS} = \hbar(\delta\tilde{\omega}_s n_s)$, and writing the local applied strain amplitude in terms of phonon number, $\langle \bar{\bar{e}}_s[\mathbf{r}_{\mathrm{TLS}}]\rangle_{\mathrm{t}} = (e_{\mathrm{vac},s})(\overline{\langle \bar{\bar{e}}_s[\mathbf{r}_{\mathrm{TLS}}]\rangle_{\mathrm{t}}})\sqrt{n_s}$, yields for the complex frequency shift in quasi-mode s due to relaxation interactions with a single TLS,

$$(\delta\tilde{\omega}_s)_{\mathrm{TLS,rel}} \approx \frac{(\overline{\langle \bar{\bar{e}}_s[\mathbf{r}_{\mathrm{TLS}}]\rangle_{\mathrm{t}}})^2 (e_{\mathrm{vac},s})^2}{\hbar} \langle \bar{\bar{\chi}}_{\mathrm{rel}}[\omega_s;\omega_{\mathrm{TLS}}]\rangle_{\mathrm{t}}. \tag{5.70}$$

For a given quasi-mode m of interest, interacting with an ensemble of TLS, the corresponding frequency shift due to relaxation processes is given by,

$$\begin{aligned}
(\delta\omega_{\mathrm{m}})_{\mathrm{rel}} = \sum_{\mathrm{TLS}} \mathrm{Re}\left[(\delta\tilde{\omega}_m)_{\mathrm{TLS,rel}}\right] &\approx \sum_{\mathrm{TLS}} \frac{\omega_{\mathrm{m}}(\overline{\langle \bar{\bar{e}}_m[\mathbf{r}_{\mathrm{TLS}}]\rangle_{\mathrm{t}}})^2 \mathrm{Re}\left[\langle \bar{\bar{\chi}}_{\mathrm{rel}}[\omega_{\mathrm{m}};\omega_{\mathrm{TLS}}]\rangle_{\mathrm{t}}\right]}{2\bar{\rho}_{\mathrm{m}}\bar{v}^2 V_m} \\
&\approx \sum_{\mathrm{TLS}} \frac{(\overline{\langle \bar{\bar{e}}_m[\mathbf{r}_{\mathrm{TLS}}]\rangle_{\mathrm{t}}})^2 D^2 (\Gamma_{1,\mathrm{TLS}})^2}{2\omega_{\mathrm{m}}\bar{\rho}_{\mathrm{m}}\bar{v}^2 V_m k_B T} \mathrm{sech}^2[\hbar\omega_{\mathrm{TLS}}/2k_B T] \\
&= \sum_{\mathrm{TLS}} \left(\frac{\bar{g}_{1,m}[\mathbf{r}_{\mathrm{TLS}}]}{\omega_{\mathrm{m}}}\right)^2 \left(\frac{\hbar(\Gamma_{1,\mathrm{TLS}})^2}{k_B T}\right) \mathrm{sech}^2[\hbar\omega_{\mathrm{TLS}}/2k_B T].
\end{aligned} \tag{5.71}$$

Similarly, the relaxation energy damping rate of mode m is given by,

$$\begin{aligned}
(\delta\gamma_{\mathrm{m}})_{\mathrm{rel}} = -2\sum_{\mathrm{TLS}} \mathrm{Im}\left[(\delta\tilde{\omega}_m)_{\mathrm{TLS,rel}}\right] &\approx -\sum_{\mathrm{TLS}} \frac{\omega_{\mathrm{m}}(\overline{\langle \bar{\bar{e}}_m[\mathbf{r}_{\mathrm{TLS}}]\rangle_{\mathrm{t}}})^2 \mathrm{Im}\left[\langle \bar{\bar{\chi}}_{\mathrm{rel}}[\omega_{\mathrm{m}};\omega_{\mathrm{TLS}}]\rangle_{\mathrm{t}}\right]}{\bar{\rho}_{\mathrm{m}}\bar{v}^2 V_m} \\
&\approx \sum_{\mathrm{TLS}} \frac{(\overline{\langle \bar{\bar{e}}_m[\mathbf{r}_{\mathrm{TLS}}]\rangle_{\mathrm{t}}})^2 D^2 \Gamma_{1,\mathrm{TLS}}}{\bar{\rho}_{\mathrm{m}}\bar{v}^2 V_m k_B T} \mathrm{sech}^2[\hbar\omega_{\mathrm{TLS}}/2k_B T] \\
&= \sum_{\mathrm{TLS}} \left(\frac{2\bar{g}_{1,m}^2[\mathbf{r}_{\mathrm{TLS}}]}{\omega_{\mathrm{m}}}\right) \left(\frac{\hbar\Gamma_{1,\mathrm{TLS}}}{k_B T}\right) \mathrm{sech}^2[\hbar\omega_{\mathrm{TLS}}/2k_B T].
\end{aligned} \tag{5.72}$$

Since we are concerned with high frequency, microwave phonon modes and TLS at cryogenic temperatures, we have safely assumed that we are in the non-adiabatic limit, $\omega_{\mathrm{m}}\Gamma_{1,\mathrm{TLS}}^{-1} \gg 1$.

Assuming resonant phonon damping is the dominant decay mechanism for TLS, and substituting $(\delta\Gamma_{1,\mathrm{TLS}})_{\mathrm{ph,cont.}}$ for $\Gamma_{1,\mathrm{TLS}}$ in Eqs. (5.71-5.72), yields the standard relations for the frequency shift and energy damping for an acoustic mode interacting with a TLS bath in a bulk material which supports a phonon continuum.

For a uniform spectral density of states for the TLS, as assumed here, integrating over ω_{TLS} yields a phonon relaxation damping of $(\delta\gamma_{\text{m}})_{\text{rel}} \sim T^d$, where d is the dimension of the phonon bath. This is a result of the fact that $\text{sech}^2[\hbar\omega_{\text{TLS}}/2k_B T]$ effectively limits the TLS frequency integral to frequencies below $\approx k_B T$ (i.e., relaxation damping is limited to thermally occupied TLS), and within this range of frequencies $\coth[\hbar\omega_{\text{TLS}}/2k_B T] \approx 2k_B T/\hbar\omega_{\text{TLS}}$. This observation is especially important for the nanoscale optomechanical structures under study, where at the temperatures and corresponding frequencies considered, the relevant phonon bath density of states varies between something approximating a 1D bath at temperatures below 100 mK to something approximating a 2.5D bath at temperatures between 100 mK and 1 K. The influence of the geometric patterning of the optomechanical structure also plays a role, modifying the phonon density of states in extreme ways by introducing phononic bandgaps and flat band regions. As we will show below using numerical methods to calculate the full spectrum of quasi-acoustic-modes of the optomechanical structure, the temperature dependence of the relaxation damping rate due to TLS can indeed be significantly modified from that in bulk.

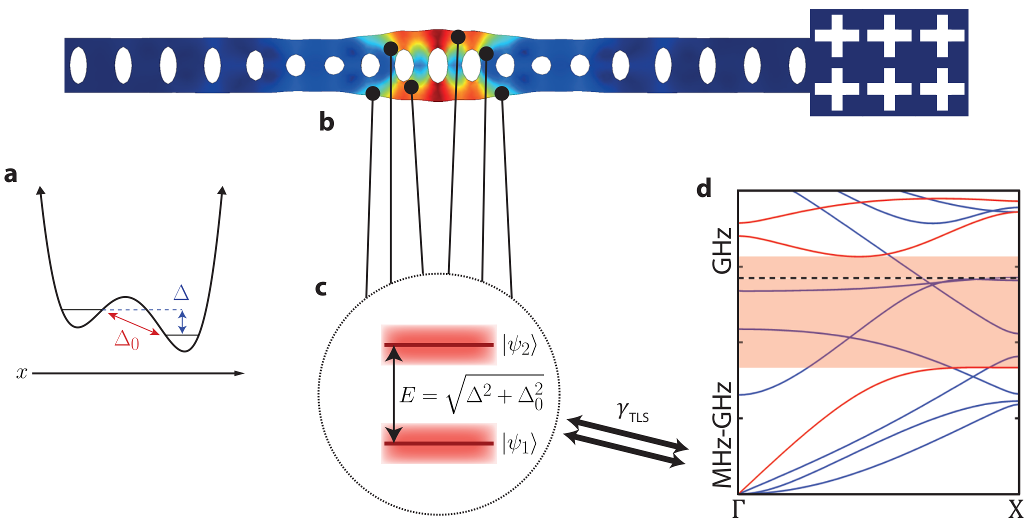

Figure 5.3: **Simulation of TLS strain coupling to OMC cavity.** **a**, Double potential well energy profile of a tunneling-state (TS), showing the asymmetry energy Δ and the tunneling energy Δ_0 between left and right localized potentials. **b** FEM-simulated mode profile of the breathing mode of the OMC cavity, indicating surface-localized TS states which are strain coupled through deformation potential $\bar{\gamma}_{\mathrm{TLS}}$. **c**, TS energy diagram, showing the transition energy, $E = (\Delta^2 + \Delta_0^2)^{1/2}$, between hybridized modes $|\psi_1\rangle$ and $|\psi_2\rangle$ which are mixtures of left and right localized states of the TS double potential well. **d**, Acoustic bandstructure of the OMC nanobeam, with blue (red) bands correspond to even (odd) vector parity acoustic modes with respect to in-plane mirror symmetry. The dashed black curve corresponds to the localized breathing mode frequency. The shaded orange region corresponds to the bandgap of the surrounding acoustic shield.

5.3 Numerical Modeling of TLS Interactions and Acoustic Damping in the OMC Cavity

In order to more accurately account for the complex geometry of the optomechanical crystal structure studied and its impact on the phonon mode spectrum and TLS dynamics, we have performed numerical simulations of the acoustic resonances (quasi-modes) of the structure for frequencies below 100 GHz. One half of the simulated structure is shown schematically in Fig. 5.3, and includes one of the pair of OMC cavities, the optical coupling waveguide, and the phononic shield which make up a single 'device'. In practice, such a device is clamped from below at its periphery through the connection of the top Si device layer to the underlying 3 μm thick SiO_x buried oxide (BOX) layer, which itself is grown on top of a thick (500 μm) Si handle layer. Simulations are performed using the COMSOL finite-element-method solver, using the Amazon AWS cloud computing resources to simulate various parts of the phonon spectrum in parallel. Acoustic perfectly matched layers (PML) at the periphery of the structure are used as a radiation boundary condition.

A series of different meshing schemes are used to cover the acoustic frequency spectrum up to 100 GHz. For all frequencies we utilize a fine mesh with maximum element size of 20 nm in the OMC cavity and phononic shield regions. This yields a meshing resolution of roughly 3-4 points per wavelength even at the highest (100 GHz) frequencies considered. As a result of memory and computing time limitations, we adjust the meshing and structure layout as a function of frequency in the rest of the structure outside of the OMC cavity and shield. For acoustic frequencies below 10 GHz the full structure shown in Fig. 5.5(b) is simulated, which includes at its periphery a micron thick (in depth and height) BOX layer followed by the PML radiation boundary. For these frequencies a lower mesh density (maximum mesh size of 250 nm) is utilized in the BOX and PML regions, providing a minimum of roughly 4 points per wavelength resolution for modes up to 10 GHz. The simulated quasi-modes of the structure are therefore damped through their acoustic radiation into the BOX layer, with no further acoustic reflections considered (such as at the Si handle layer). For frequencies above 10 GHz we remove the BOX clamping region and apply the PML layers right at the boundary of the phononic shield, as shown in Fig. 5.5(c). At these higher frequencies we utilize the same fine mesh in the PML as in the OMC cavity region (maximum mesh size of 20 nm). The thought in doing this is that the BOX clamping region plays less of a role for these short wavelength phonons that can effectively propagate within the thin Si device layer without major reflection at this boundary, hence the removal of the BOX layer and application of the PML region in the Si device layer right at the exit of the acoustic shield. More important is that we provide a fine mesh in the PML to avoid unintended reflections. Beyond 100 GHz the resulting memory requirements and computation time are prohibitive, and given the temperature range of interest ($\lesssim$ 1 K), 100 GHz frequency is a natural cut-off point. In addition to the above meshing strategy, in order to reduce the memory and computation time we apply a mirror boundary condition along the center of the structure, running down the middle of the coupling waveguide, and double the number of modes recorded in simulation.

For each acoustic resonance found in the simulation we not only record the frequency (ω) and energy damping rate (γ), but also calculate the per phonon strain tensor at 101 locations in the acoustic mode volume V_m of the high-Q breathing mode. These locations were chosen to be in random locations in the Si device layer, but within δw = 15 nm of the Si-air interface, as this is where we expect TLS to be located due to etch damage. A fixed set of 101 positions are evaluated for all acoustic modes. Plots showing the resulting energy damping rate, effective phonon mode density, and average squared strain in the mode volume V_m as a function of phonon frequency are shown in Figs. 5.5(a-c). Noteworthy in these plots is the position of the fundamental phononic bandgap of the acoustic shield, which is shown as a semi-transparent blue band from approximately 3.5 to 6.5 GHz. As can be seen, a significant change in the local strain amplitude and mode density occurs around this phononic bandgap. Below the bandgap, the mode density is roughly constant at 1 mode every 5 MHz (a bin size of 50 MHz was used when estimating this spectral quasi-mode density), consistent with that of an effectively 1D system. Within the bandgap of the acoustic shield, the mode density drops, and then above the bandgap the mode density rises a little faster than linearly with frequency, corresponding to that of a 2.4-D system. Below the bandgap the per-phonon strain in mode volume V_m is quite small, and then rises within and above the phononic bandgap frequency due to the localization of modes within the shield. The energy damping rate plot shows that a portion of the modes become substantially less damped in and around the bandgap as expected.

5.3.1 Numerical Simulation of 3-phonon Scattering

Table 5.1: **3-phonon scattering model parameters.**

Parameter	Description	Value	Refs./Notes
$\left\langle \mathcal{F}_{m\,s'}^{s''} \right\rangle_{\mathrm{m}}$	average 3-phonon mode overlap factor	0.01	≅ phase matching term
$\langle \gamma_{\mathrm{G}} \rangle_{\mathrm{m}}$	mode averaged Grüneisen parameter at cryogenic temperature ($T < 4K$)	0.24	[89]
v_{t}	transverse acoustic phonon velocity in bulk Si ([100] dir., [011] pol.)	8.4×10^3 m/s	[90, 91]
v_{l}	longitudinal acoustic phonon velocity in bulk Si ([100] dir. and pol.)	5.8×10^3 m/s	[90, 91]
$\left\langle v_{\mathrm{Si}}^2 \right\rangle$	average square of acoustic phonon velocity in bulk Si ([100] dir.)	$(7.6 \times 10^3\ \mathrm{m/s})^2$	
ρ_{Si}	Si mass density	2.33×10^3 kg/m^3	[90]
$\left\langle e_{\mathrm{vac},m}^2 \right\rangle$	average strain squared of vacuum for mode m within V_m	2.25×10^{-8}	COMSOL sim.

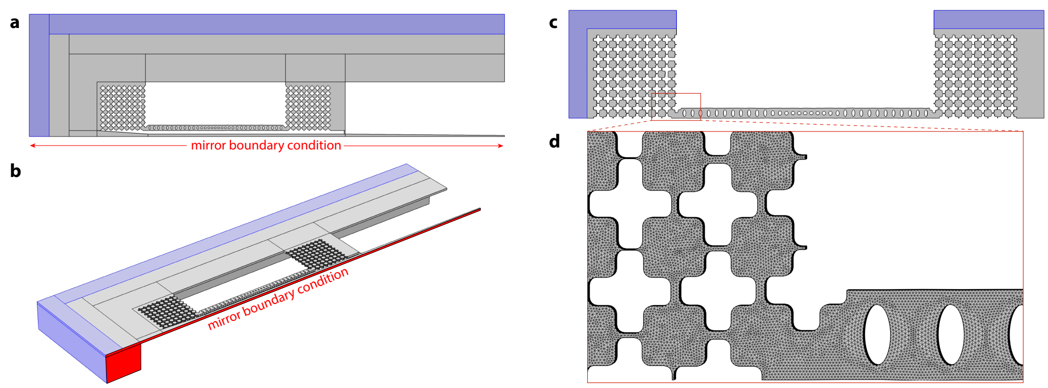

Figure 5.4: **FEM simulation of 3-phonon scattering layout and mesh.** **a**, Top view of the FEM-simulated structure for phonon frequencies below 10 GHz. Blue regions correspond to PML radiation boundaries. The structure is mirrored about the center axis of the coupling waveguide (red arrows and label). A maximum mesh size of 20 nm is utilized in the OMC cavity and phononic shield regions. A maximum mesh size of 250 nm is set in the surrounding periphery and PML regions. The mesh resolution is smoothly varied between the two regions. **b**, Isometric view of the same structure in (**a**), showing the underlying BOX clamping layer and the corresponding PML layers. The bottom of the BOX layer has a fixed boundary condition applied to it. **c** Top view of the reduced FEM-simulation volume for phonon frequencies between 10-100 GHz. Again, the blue region is an acoustic PML. All other boundaries other than PML are set to free boundaries. The maximum mesh size is now 20 nm throughout the entire structure, including the PML. **d**, Zoom-in of the red box region in (**c**), showing the dense meshing of the nanobeam and shield.

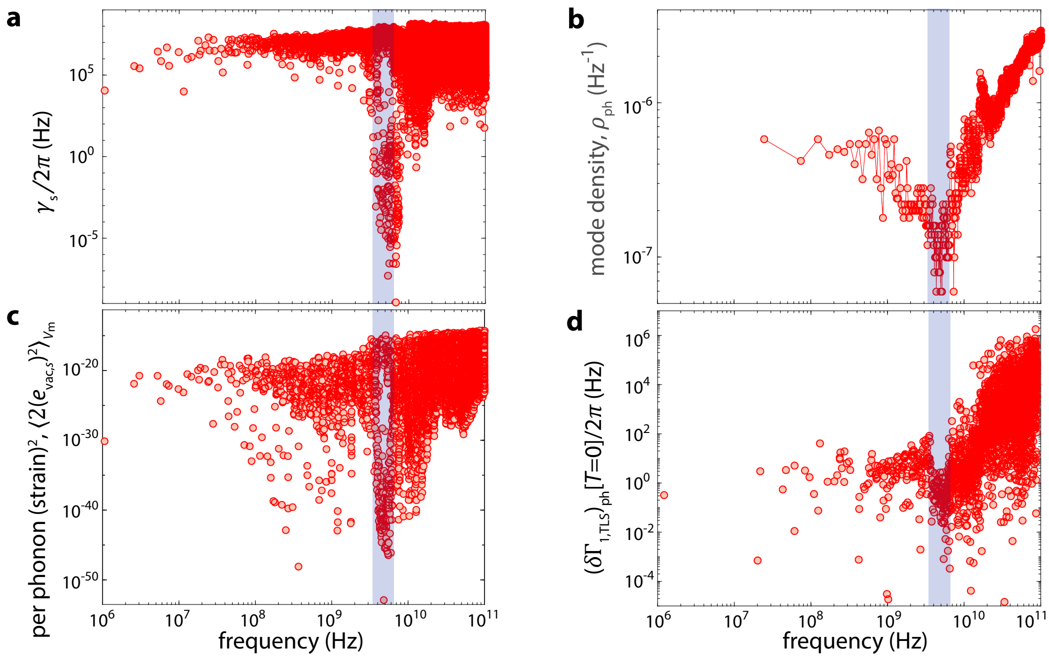

Figure 5.5: **Model phonon and TLS properties.** In this model, phonons of the Si optomechanical slab structure are simulated using a FEM numerical solver. The simulation volume consists of the two optomechanical cavities, fiber coupling waveguide, and 10 period phononic shield. As in the fabricated devices, the Si slab is clamped at the periphery of the optomechanical structure to the underlying SiO_x BOX layer of the SOI. An acoustic radiation boundary condition consisting of a perfectly-matched layer allows for radiation to escape into the external Si slab and underlying substrate. All phonon resonances up to 100 GHz frequency are calculated. The lowest phononic bandgap of the shield is shown as a transparent blue band. **a**, Acoustic radiation damping rate for phonon quasi-modes of the optomechanical structure. **b**, Spectral phonon mode density, spectrally averaged over 20 MHz bin size. **c**, Per-phonon squared strain value within mode volume V_m for each of the phonon-quasi modes. Here, the sum of the square of the strain components are averaged over 201 positions within the acoustic mode volume of the breathing mechanical mode. **d**, For an exemplary ensemble instance, zero temperature TLS decay rate of each of the $N_{\text{TLS},m} = 3920$ randomly oriented and distributed within V_m due to resonant ($\hat{\sigma}_x$) coupling to phonon quasi-modes of the optomechanical structure.

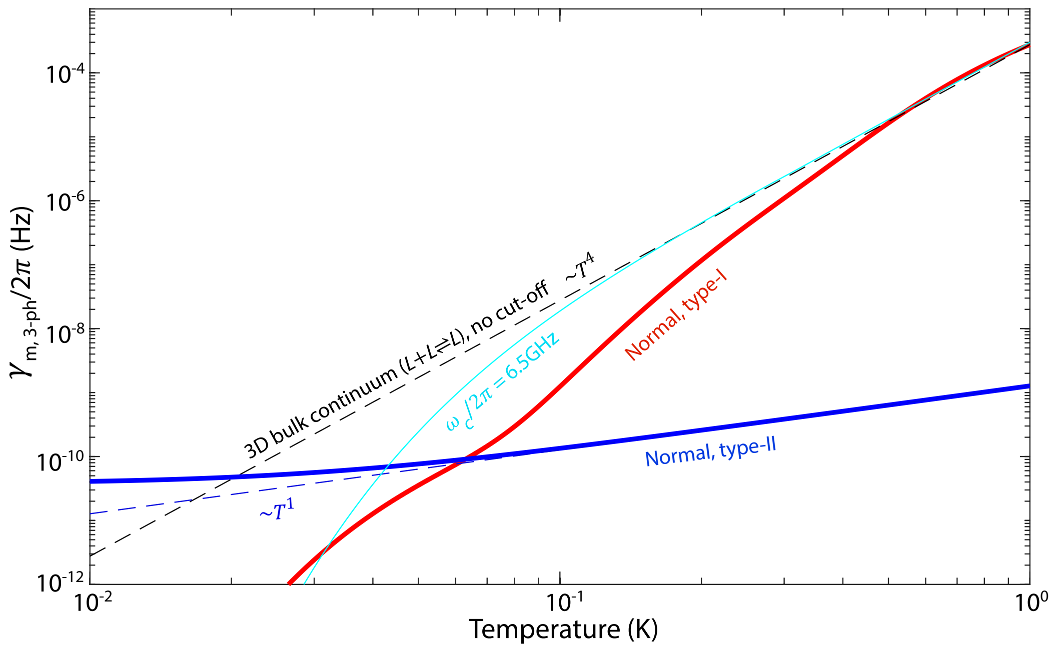

Figure 5.6: **3-phonon scattering model.** Simulation of the acoustic damping due to 3-phonon scattering of the localized breathing mechanical mode with other quasi-modes of the OMC cavity structure of Fig. 5.5. Parameters used in the modeling are listed in Tab. 5.1. Both type I (solid red curve) and type II (solid blue curve) scattering processes involving the breathing mode are modeled. For comparison, we also plot the estimated 3-phonon-scattering damping rate due to type-I processes for longitudinally polarized phonons ($L + L \rightleftharpoons L$) in bulk Si. For the bulk simulation we plot the estimated damping rate without a low-frequency cut-off (dashed black curve), and with a low-frequency cut-off (solid cyan curve) corresponding to the top of the first phononic bandgap ($\omega_c/2\pi = 6.5$ GHz). In all cases we only include Normal scattering processes, and neglect Umklapp scattering, due to the low temperature range considered ($T \lesssim 1$ K).

Utilizing Eqs. (5.29), (5.37), and (5.39), along with the parameters listed in Tab. 5.1 and the COMSOL-simulated acoustic modes of the OMC cavity structure (c.f., Fig. 5.4), in Fig. 5.6 we plot the calculated acoustic damping of the localized 5 GHz breathing mode due to 3-phonon scattering at temperatures below 1 K. The resulting temperature-dependent damping rate using the numerically computed acoustic quasi-modes of the OMC cavity are shown as a solid red curve for $\mathcal{N}$-I processes and a solid blue curve for $\mathcal{N}$-II processes. Damping arising from $\mathcal{N}$-II scattering processes is largely suppressed in the OMC cavity structure due to the reduced density of phonon states lying below the breathing mode frequency, a consequence of the effectively reduced dimensionality of the OMC nanobeam at these acoustic wavelengths. At temperatures below $T = \hbar\omega_{\mathrm{m}}/k_B \approx 200$ mK the $\mathcal{N}$-II damping rate approaches the spontaneous decay rate of the breathing mode, whereas at higher temperatures the damping rate increases linearly with temperature. The $\mathcal{N}$-I damping rate, on the other hand, increases rapidly towards a high temperature scaling of $\sim T^4$. Again, at temperatures below $T = \hbar\omega_{\mathrm{m}}/k_B \approx 200$ mK the $\mathcal{N}$-I damping rate drops rapidly due to the reduced density of available phonon states in the OMC structure. This is another manifestation of the 'phonon bottleneck' effect discussed above in regards to the optically-induced hot phonon bath. Energy deposited into high frequency phonons decays to lower frequency phonons through processes like the 3-phonon mixing studied here, however, when the phonon wavelengths approach the dimension of the structure the reduced density of phonon states results in a precipitous drop in the nonlinear phonon scattering, effectively trapping the energy in phonons above a certain cut-off frequency.

For comparison purposes we have plotted the estimated damping for an isotropic Si bulk material involving $L + L \rightleftharpoons L$ acoustic scattering. The black dashed curve (solid cyan curve) is the bulk damping rate without (with) a low-frequency cut-off for the range of integration in the $\mathcal{N}$-I process. The cut-off frequency for the solid cyan curve is $\omega_c/2\pi = 6.5$ GHz, chosen to match the top of the first phononic bandgap of the acoustic shield in the OMC cavity structure (c.f., Fig. 5.5). The temperature scaling for the bulk scattering (above cut-off) is approximately T^4. An average overlap factor $\left\langle \mathcal{F}_{m\,s'}^{s''} \right\rangle = 0.01$ was assumed in the quasi-mode modeling, resulting in a reasonable correspondence with the $\mathcal{N}$-I bulk damping at temperatures above 400 mK.

Although the 3-phonon scattering rapidly rises with temperature ($\sim T^4$), for temperatures below 1 K where the size-scale of the OMC cavity structure comes into play, the magnitude of 3-phonon scattering is estimated to be substantially smaller than that measured in our experiment. In the following subsection we consider a more likely source of the observed damping, two-level systems, which act as an intermediate bath between phonons, greatly increasing the predicted damping rate.

5.3.2 Numerical Modeling of TLS-phonon Interactions in the OMC Cavity

The coupling of the high-Q acoustic breathing mode of the OMC cavity to TLS defect states depends on a number factors. First and foremost there is the spatial and spectral density of the TLS, which determine the number of interacting defect states with the breathing mode. In order to constrain the TLS density to a realistic value we consider here that the majority of the TLS are associated with defects in a near-surface layer of the etched Si structure making up the OMC cavity. We assume no TLS defects in the bulk of the crystalline Si layer. The thickness of the defective surface layer of Si depends greatly on its preparation.

In our case, we have used an inductively-coupled reactive ion etch (ICP-RIE) to pattern the 220 nm thick Si device layer. The ICP-RIE etch utilizes an SF_6:C_4F_8 gas chemistry, with low RF power ($\approx$ 30 W) and low DC-bias voltage ($\approx$ 70 V), to reduce optimize the shape of the etched sidewall and to attempt to reduce etch-induced damage on the sidewalls of the etched Si. Nonetheless, it is well known that these etch processes still produce a variety of damages to the exposed near-surface layers of Si in the process. Typically in RIE etching [80, 92, 93, 94], a surface consisting of a super-surface top layer of fluoro-carbons ($\sim$ 5 nm) and Si-oxygen ($\sim$ 1.5 nm) is followed by a sub-surface heavily damaged layer containing Si-carbon (among other impurities) that can penetrate into the bulk to depths of tens of nanometers. Here we assume an etched sidewall damage layer thickness of δw = 15 nm. In order to reduce Si oxide growth on the top and bottom surface layers of the released Si device (i.e., those layers that do not see the ICP-RIE etch) we ‘flash’ the sample with an anhydrous vapor HF etch prior to inserting it into the vacuum of the dilution refrigerator (time between flash and vacuum pump down in the cryostat is $\lesssim$ 45 minutes). Ideally, this removes surface oxide layers and leaves a hydrogen-terminated Si surface nominally free of oxides. To be conservative, however, we also assume a δt = 0.25 nm surface oxide layer [79, 95] on the top and bottom surfaces of the released Si device layer. This yields a volume fraction of damaged Si in our devices which is η_{surf} = 0.29.

Assuming a bulk TLS density commensurate with that in vitreous Si dioxide, n_0 =

1.04 states/J/m^3 [69], this yields a spectral density of TLS that lies within the acoustic cavity volume of the breathing mode of only $n_{0,m} \sim 20$ states/GHz. For a TLS population that is uniformly distributed spectrally [96], this yields only ~ 2000 TLS with transition frequencies lying below 100 GHz that are in the cavity mode volume. Note that we simulate an ensemble TLS size of $N_{\text{TLS},m} = 3920$, taking into account TLS that are within a spatial region of twice that of the cavity mode volume.

The resonant interaction of those TLS that lie spatially in the breathing mode cavity volume V_m and have their transition frequency spectrally nearby the $\omega_{\text{m}}/2\pi \approx 5$ GHz acoustic resonance frequency is determined by the magnitude of the transverse coupling deformation potential, M. These TLS not only act as a bath to damp the breathing mode, but their temporal fluctuations from ground to excited state and back, lead to fluctuations in the acoustic environment of the breathing mode, producing both a frequency jitter of the mechanical mode and an overall shift in the resonance frequency that depends on the TLS temperature through its average excited state population [69, 88]. The acoustic frequency shift due to non-resonant TLS interacting through longitudinal $\hat{\sigma}_z$-coupling is negligible compared to the resonant $\hat{\sigma}_x$-coupling term. As such, the magnitude of the transverse coupling parameter is chosen in our model to be $M = 0.07$ eV, yielding an average transverse vacuum coupling rate to the breathing mode for TLS in V_m of $\langle \bar{g}_{\text{t},m}/2\pi \rangle \sim 100$ kHz. The corresponding dispersive shift due to the nearest resonant TLS (on average) is then approximately $\langle \delta f_{m,\text{max}} \rangle \cong n_{0,m} (\bar{g}_{\text{t},m}/2\pi)^2 \sim 1.5$ kHz. This level of dispersive shift is in line with both the measured frequency jitter ($\Delta_{1/2} \approx 3.5$ kHz) and the frequency shift around $T \approx \hbar\omega_{\text{m}}/k_{\text{B}}$ for device D.

The non-resonant relaxation interactions of TLS with the breathing mode is via a longitudinal coupling deformation potential, D. With the transverse coupling rate set nominally by the measured frequency jitter and temperature-dependent frequency shift of the breathing mode, the longitudinal deformation potential is adjusted to approximately match the measured acoustic damping rate of the breathing mode at the lowest fridge measurement temperatures ($T_{\text{f}} \approx 7$ mK). A value of $D = 5.6$ eV (angle-averaged $\bar{D} = 3.23$ eV) gives a reasonable fit to the measured data. Typical values in the literature for averaged D and M parameters are on the order of 1 eV [69, 96], although these values are hard to distinguish separately from the TLS density [97]. The large value of D and small value of M indicate a set of TLS (or TS) states which have a large asymmetry energy and small tunneling energy. Other parameters and their assumed values in our model are listed, along with references and comments, in Table 5.2.

The calculated zero-temperature energy decay rate of an ensemble of 3920 TLS, randomly chosen from 101 fixed positions within the breathing mode cavity mode volume, with randomly oriented acoustic dipoles, and with randomly chosen frequency below 100 GHz is displayed in Fig. 5.5(d). This calculation, following Eq. (5.54), uses the simulated acoustic strain and radiative decay rate of the localized quasi-mode phonons of the suspended and peripherally-clamped OMC structure whose properties are also displayed in Fig. 5.5. Several points are worth noting here. The first is that the small number of TLS in the small acoustic mode volume V_m and the small number of localized quasi-normal phonon modes at low frequency means a significant spectral fluctuation in the decay rate of TLS with transition frequency below $\sim$ 1 GHz. Within the phononic bandgap of the OMC cavity (3.5 – 6.5 GHz), there is a dramatic reduction in the decay rate of TLS, down to levels on the order of 1 Hz. Above the phononic bandgap, the TLS zero-temperature decay rate rises rapidly, roughly as the cube of the TLS transition frequency, consistent with the approximate 2D phonon quasi-mode density to which the TLS are coupled (c.f., Fig. 5.5(c).

Figure 5.7 displays the resulting damping (c.f., Eqs.(5.63,5.72)) and frequency shift (c.f., Eqs.(5.62,5.71)) of the high-Q breathing mode versus temperature due to coupling with the TLS bath in the acoustic mode volume V_m. In these simulations we performed 500 trial runs of random TLS ensembles. Both the average and standard deviation of the damping and frequency shift are shown. Also shown are the effects of both 'resonant' $\hat{\sigma}_x$-interactions and 'relaxation' $\hat{\sigma}_z$-interactions with the TLS. As can be clearly seen, the resonant TLS damping of the breathing mode at the lowest temperatures $T_\mathrm{f} \lesssim 100$ mK is predicted to be roughly an order of magnitude smaller than the relaxation damping. In addition, as the temperature is increased above that of $\hbar\omega_\mathrm{m}/k_\mathrm{B} \approx 200$ mK, the resonant damping term begins to saturate due to the thermal excitation of TLS. The overall suppression of the resonant TLS damping is due to the presence of the acoustic bandgap, which dramatically reduces the decay rate of TLS nearly-resonant with the breathing mode due to a lack of localized quasi-normal phonon modes in the gap. Instead, the typically weaker relaxation damping from non-resonant TLS outside the acoustic bandgap dominates the simulated breathing mode damping.

The correspondence of the simulated TLS relaxation damping of the breathing

Table 5.2: **TLS damping model parameters.**

Parameter	Description	Value	Refs./Notes
D	longitudinal coupling deformation potential	5.6 eV	fit value (see also [69, 96, 97])
$\bar{D}$	angle-averaged longitudinal coupling	3.23 eV	$\equiv D/\sqrt{3}$
M	transverse coupling deformation potential	0.07 eV	fit value (see also [69, 96, 97])
$\bar{M}$	angle-averaged transverse coupling	0.04 eV	$\equiv M/\sqrt{3}$
δw	Si device layer etched sidewall damage layer thickness	15 nm	[80, 92, 93, 94]
δt	Si device layer top and bottom oxide thickness	0.25 nm	[79, 95]
η_{surf}	damaged material/surface oxide volume fraction	0.29	estimated from δt, δw
m	high-Q breathing mode label	N/A	
ω_{m}	mode m frequency	5.3 GHz	COMSOL sim.
V_m	mode m acoustic mode volume	0.11 $(\mu\mathrm{m})^3$	COMSOL sim.
$\langle e^2_{\mathrm{vac},m}\rangle$	average strain squared of vacuum for mode m within V_m	2.25×10^{-8}	COMSOL sim.
n_0	TLS density per unit volume per unit energy	1.04 states/J/m^3	[69]
$n_{0,m}$	TLS density per unit frequency in V_m ($\equiv (\hbar 2\pi) n_0 \eta_{\mathrm{surf}} V_m$)	22.1 states/GHz	calculated
$N_{\mathrm{TLS},m}$	estimated number of TLS in $2 \times V_m$ with $f \leq 100$ GHz	3920	calculated
$\Gamma_{\phi,\mathrm{TLS}}/2\pi$	TLS pure dephasing rate	10 kHz	[69, 98]
Λ_{TLS}	TLS excitation rate (due to optical pumping)	2 Hz	$\sim (2 \times 10^{-3})(\gamma_{\mathrm{p}} n_{\mathrm{p}})$ at $n_{\mathrm{c}} = 0.1$
$\langle \bar{g}_{\mathrm{t},m}/2\pi\rangle$	average transverse vacuum coupling rate to mode m for TLS in V_m	$\sim$ 100 kHz	calculated
$\langle \bar{g}_{\mathrm{l},m}/2\pi\rangle$	average longitudinal vacuum coupling rate to mode m for TLS in V_m	$\sim$ 8.6 MHz	calculated
$\langle \delta f_{m,\max}\rangle$	average dispersive shift of mode m for nearest resonant TLS	$\sim$ 1.5 kHz	calculated ($\cong n_{0,m}(\bar{g}_{\mathrm{t},m}/2\pi)^2$)

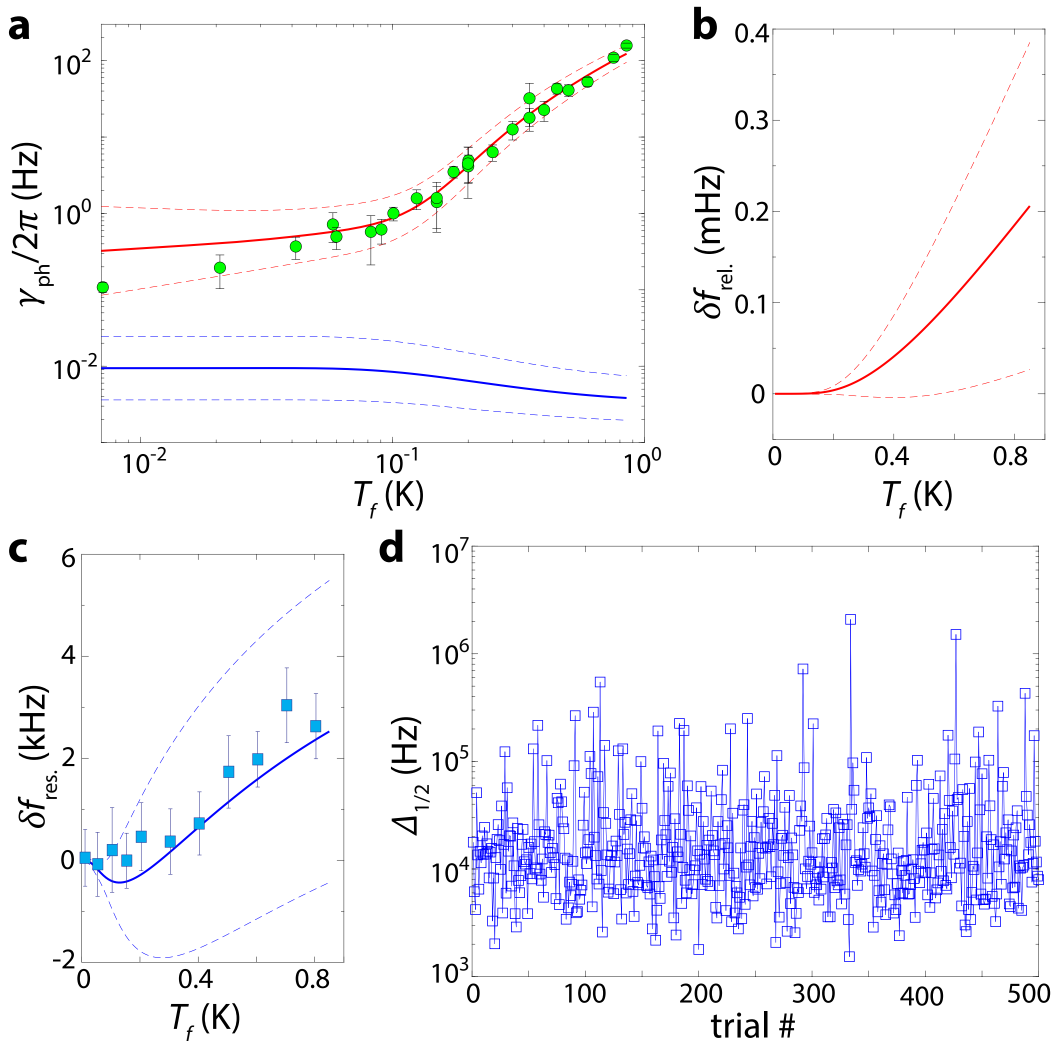

Figure 5.7: **Modeled breathing mode interactions with a TLS bath.** Modeling was performed using the acoustic mode and TLS properties found in Tab. 5.2. Simulations were performed using 100 ensemble instances of $N_{\mathrm{TLS},m} = 3920$ randomly positioned (sampled from a set of 101 fixed positions) and oriented TLS within the breathing mode acoustic volume, V_m. The transition energy of each TLS are also sampled from a random distribution. **a**, Relaxation (red curves) and resonant (blue curves) damping of the acoustic breathing mode versus TLS bath temperature. Solid (dashed) curves represent the average (1-σ standard deviation in log-space) of the 500 simulation trials run. Measured damping of device D is shown as filled green circles. **b**, Breathing mode frequency shift versus temperature due to relaxation and **c** resonant TLS interactions. The solid cyan curve is a curve resulting from single TLS ensemble trial. Measured frequency shift of mode of device D is shown as filled blue squares. **d**, Full-width half-maximum of the time-averaged frequency jitter of the breathing acoustic mode resulting from resonant interactions with all of the TLS for each of the 500 trial ensembles. Here we assume a $\Lambda_{\mathrm{TLS}} = 2$ Hz excitation rate of each TLS due to weak optical absorption.

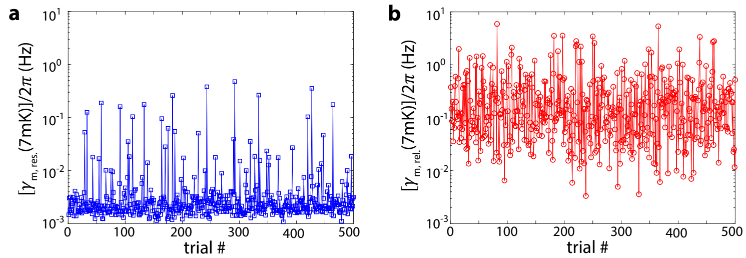

Figure 5.8: **Fluctuation from trial-to-trial in the simulated low temperature damping at 7mK. a**, Simulated TLS-resonant-interaction damping at temperature $T = 7$ mK of breathing mode as a function of different TLS ensemble trials. **b**, Simulated TLS-relaxation damping at temperature $T = 7$ mK of breathing mode as a function of different TLS ensemble trials.

mode with the measured breathing mode damping is striking not only in the overall magnitude of the predicted damping but also in its temperature dependence. At temperatures below $T_\mathrm{f} \approx 100$ mK, where the thermally excited TLS that contribute to relaxation damping have transition frequencies below the acoustic bandgap and interact with a quasi-1D phonon bath, the damping is seen to have a reduced, linear to sub-linear dependence with temperature. Above $T_\mathrm{f} \approx 100$ mK, thermal excitation of TLS with transition frequencies above that of the acoustic bandgap begin to contribute to the damping. In this spectral range the phonon density of states in the OMC cavity structure is approximately linear with frequency, resulting in TLS decay times which scale quadratically with transition frequency. This sets the temperature scaling of the breathing mode relaxation damping, which is also seen to scale approximately quadratically with temperature above $T_\mathrm{f} \approx 100$ mK.

Another feature of the simulated TLS damping of the breathing mode is the large fluctuation from trial-to-trial in the low temperature ($T_\mathrm{f} \lesssim 100$ mK) portion of the damping versus temperature curve. This shows up as a large variance in magnitude and temperature trend of the relaxation damping at these low temperatures in simulation. The dashed curves in Fig.5.7(a) represent the range of temperature curves within one standard deviation of the mean curve *on a log scale*. In order to better appreciate what the level of fluctuations in the predicted low temperature damping are for both resonant and relaxation TLS damping of the breathing mode, we plot in Fig. 5.8 the trial-to-trial variations of the simulated damping factors at $T_\mathrm{f} = 7$ mK. The variations are substantial, with a standard deviation in log-space of a little over an order of magnitude. This is consistent with our measured observations, as can be gleaned from the plot of measured breathing mode energy damping rates versus phononic bandgap shield number. For acoustic shield periods greater than about 6, where radiation damping is estimated to be minimal, the measured damping rates also range over a little over an order of magnitude. This variance is explained in the TLS model by the very small number (handful) of TLS with transition frequency below 100 MHz within the breathing mode volume, which owing to their random positioning and orientation, results in a large variation in breathing mode damping.

The simulated frequency shift versus temperature, for both resonant and relaxation interactions with the TLS ensemble, is shown in Fig. 5.7(b) and (c). In these plots we have referenced the frequency shift to that at the lowest measured temperature ($T_\mathrm{f} \approx 7$ mK). The relaxation component of the frequency shift is estimated to be in the milli-Hz range, far below the kHz-scale frequency shift due to resonant interactions with the TLS. The resonant TLS frequency shift of the breathing mode versus temperature has a simulated mean curve averaged over the 500 ensemble trials that roughly follows the digamma function response of Eq. (5.62), with the breathing mode frequency initially shifting lower and then beginning to increase around $\hbar\omega_\mathrm{m}/k_\mathrm{B} \approx 200$ mK, followed by a monotonic (logarithmic) increase in frequency for higher temperatures. The simulated frequency shift versus temperature curve has a large variance however (range of curves within standard deviation of mean curve are bounded by dashed curves), depending sensitively on the magnitude and sign of the detuning of the TLS closest to resonance with the breathing mode. The measured frequency shift with temperature of device D is plotted alongside the simulated resonant component of the TLS-induced frequency shift in Fig. 5.7(b), showing good correspondence with the mean curve.

The measured frequency jitter when averaged over minutes has a spectral full-width at half-maximum (FWHM) of $\Delta_{1/2} \approx 3.5$ kHz, approximately independent of temperature ($T_\mathrm{f} = 7 - 850$ mK) and optical probing power ($n_\mathrm{c} = 0.3 - 0.02$). Over $\lesssim 0.1$ s timescales one can resolve this frequency jitter in the time domain. In order to estimate the amount of frequency jitter that the acoustic breathing mode might incur due to interactions with TLS we have assumed in our simulations that all TLS are being excited at a rate faster than the measurement averaging time of a few minutes. Assuming all TLS are fluctuating independently, we can then write using Eq. (5.62) without the temperature dependence and assuming that $(\Delta\sigma_z)^2 \equiv \langle\hat{\sigma}_z^2\rangle - \langle\hat{\sigma}_z\rangle^2 = 1$,

$$\Delta_{1/2} = 2(2\log[2])\Bigg(\sum_{\mathrm{TLS}}\left(\bar{g}_{\mathrm{t},m}^{2}[\mathbf{r}_{\mathrm{TLS}}]\right)^{2} \times\left\{\frac{\omega_{\mathrm{TLS}}-\omega_{\mathrm{m}}}{(\omega_{\mathrm{TLS}}-\omega_{\mathrm{m}})^{2}+((\delta\Gamma_{1,\mathrm{TLS}})_{\mathrm{ph}}/2+\Gamma_{\phi,\mathrm{TLS}})^{2}}+\frac{\omega_{\mathrm{TLS}}+\omega_{\mathrm{m}}}{(\omega_{\mathrm{TLS}}+\omega_{\mathrm{m}})^{2}+((\delta\Gamma_{1,\mathrm{TLS}})_{\mathrm{ph}}/2+\Gamma_{\phi,\mathrm{TLS}})^{2}}\right\}^{2}\Bigg)^{1/2}, \tag{5.73}$$

where the prefactor $2(2\log[2])$ accounts for the conversion between the standard deviation and the FWHM of a normal distribution.

TLS excitation occurs naturally through thermal excitation, although the rate of excitation in that case depends strongly on temperature, which we do not observe in our measurements. However, we also know that the optical probing of the mechanics can lead to optical-absorption-induced excitation of a hot bath that damps the mechanics. It seems reasonable then to assume that the same optical absorption would also excite a broad spectrum of TLS, thus leading to their contribution to the breathing mode frequency jitter. In the model we have taken the optical-absorption-induced pumping rate of the TLS to be $\Lambda_{\mathrm{TLS}} = 2$ Hz, which for context represents 0.2% of the hot bath heating rate $\gamma_{\mathrm{p}}n_{\mathrm{p}}$ of the breathing mode at $n_{\mathrm{c}} = 0.1$. So even if the TLS are driven much more weakly than the breathing mode due to optical absorption effects, one would need to probe at lower optical probe powers than currently accessible in our experiments ($n_{\mathrm{c}} = 0.02$) to see a reduction in the time-averaged frequency jitter of the mechanics, where time averaging is performed over a second or longer. Note that pumping-induced saturation effects of the TLS have also been included in the simulation although their effects on both the damping and the overall frequency shift is minor.

The resulting simulated frequency jitter FWHM of the breathing mode, $\Delta_{1/2}$, is plotted in Fig. 5.7(d) for each of the 500 trial TLS ensembles. The variation from trial-to-trial of the frequency jitter is substantial, with the jitter ranging from kHz to (in rare cases) MHz. Although the measured frequency jitter of device D lies on the low end of this spectrum at $\Delta_{1/2} \approx 3.5$ kHz, this device is also on the low end of the range of measured values in our experience. As an example, the measured linewidth of another high-Q device (device E) is shown in Fig. 5.9. In this case, the linewidth at low optical probe power is found to saturate to a FWHM of ~ 40 kHz, closer to the mean simulated value. The large fluctuation in the measured frequency jitter from device-to-device, consistent with the model, is again an indication of the sensitivity of the breathing mode to a select few TLS in the near-resonant regime.

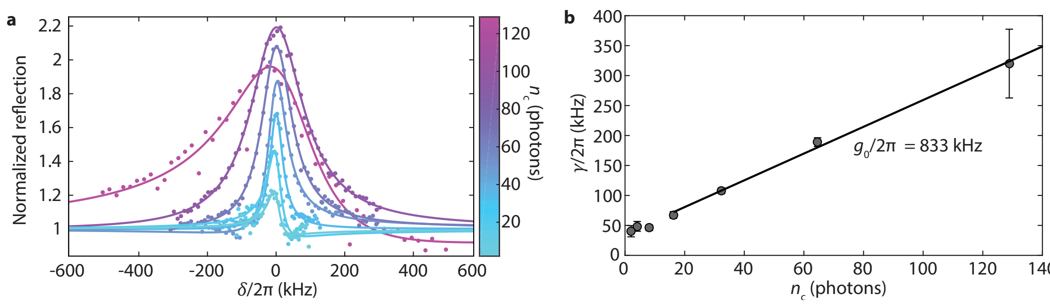

Figure 5.9: **EIT linewidth measurements of Device E at $T_\mathbf{f}$ = 10 mK. a**, Normalized reflection amplitude for probe photons as a function of pump photon number. The reflection peak represents an EIT-like transparency window approximately centered within the bare optical cavity line ($\sim$ 1 GHz wide). Asymmetry in the trace at $n_\mathrm{c} = 129$ can be attributed to an effective detuning shift, likely caused by thermal shifting of the cavity at high input power. These EIT measurements were performed on a device E having seven acoustic shield periods and mechanical $Q = 1.5 \times 10^{10}$ measured via ringdown. **b**, Plot of the fit mechanical linewidth versus pump photon number from the EIT curves of (**a**). At $n_\mathrm{c} \lesssim 10$, the time-averaged mechanical linewidth saturates to 40 kHz due to mechanical frequency jitter. At higher n_c, the mechanical mode is broadened by optomechanical back-action, the slope of which yields $g_0/2\pi = 833$ kHz.

Chapter 6

OPTICAL ABSORPTION INDUCED PHONON BATH AND QUANTUM COOPERATIVITY

Recent advances in optomechanical systems, in which mechanical resonators are coupled to electromagnetic waveguides and cavities [7, 99], have led to a series of scientific and technical advances in precision sensing [100, 101], nonlinear optics [102, 103], nonreciprocal devices [16, 104], and topological phenomena [105, 106]. In addition, such systems have demonstrated macroscopic quantum phenomena, including laser cooling of mechanical resonators into their quantum ground state [20, 21, 22], probabilistic preparation of quantum states [10, 11, 12, 13], squeezed light [103, 107], and coherent transduction between photons with different energies [108, 109, 110, 111, 112].

Optomechanical crystals (OMCs), where electromagnetic [23, 24] and elastic [113, 114] modes overlap within a lattice, can be fabricated in thin-film dielectrics and engineered to yield strong coupling between cavity photons and phonons [7]. Previous work has realized one-dimensional silicon OMC cavities with a vacuum optomechanical coupling rate greater than 1 MHz [27, 115]. There are advantages in using phonons within a quantum information network. For example, within the solid state, all optical and electronic phenomena strongly depend on the crystal lattice—local distortions of the lattice, i.e. mechanical phonons, could connect dissimilar degrees of freedom such as superconducting qubits operating at gigahertz frequencies [116, 117] with atomic/optical states. Also, unlike photons, phonons do not radiate into free space; therefore, due to their reduced crosstalk, long lifetimes [56] and small device footprint, it is natural to envision mechanical modes carrying and storing quantum information [118, 119].

A significant roadblock to further application of one-dimensional (1D) OMC cavities for quantum applications is the very weak, yet non-negligible parasitic optical absorption in current devices [9, 10, 11, 12, 13]. Optical absorption, thought to occur due to surface defect states [30, 31], together with inefficient thermalization (due to the 1D nature of silicon OMC crystals currently in use) can yield significant heating of the hypersonic (> GHz) mechanical mode of the device. At ultralow temperatures ($\lesssim 0.1$ K), where microwave systems can be reliably operated as quantum devices, this absorption leads to significant heating of the local phonon bath within a microsecond upon applying an optical pulse with a power large enough to detect single phonons at appreciable rates [9]. Moreover, this hot bath can persist even after the removal of the light field for timescales on order of the achievable decoherence times for superconducting microwave qubits, significantly compromising the utility of OMCs as transducers between superconducting qubits and optical photons.

The most relevant figure-of-merit for quantum optomechanical applications is the effective quantum cooperativity ($C_{\text{eff}} \equiv C/n_{\text{b}}$), corresponding to the standard photon-phonon cooperativity (C) divided by the Bose factor of the effective thermal bath (n_{b}) coupled to the acoustic mode of the cavity [9, 102, 110]. In previous experiments with nanobeam OMC cavities at millikelvin temperatures, the quantum cooperativity was substantially degraded due to the heating and damping caused by the optical-absorption-induced hot bath. The heating of the acoustic cavity mode by the optically-generated hot bath can be mitigated through several different methods. The simplest approach in a low temperature environment is to couple the cavity more strongly to the surrounding cold bath of the chip, or through addition of another cold bath as in experiments in a ^{3}He buffer gas environment [18, 120]. This method can be quite effective in decreasing the acoustic mode thermal occupancy in the presence of optical absorption; however, the effectiveness of the method relies on increasing the coupling to baths other than the optical channel, which necessarily decreases the overall photon-phonon quantum cooperativity.

Here we employ a strategy that makes use of the frequency-dependent density of phonon states within a phononic bandgap structure to overcome this limitation. Using a two-dimensional (2D) OMC cavity [32, 33, 121] the thermal conductance between the hot bath and the cold environment is greatly increased due to the larger contact area of the 2D structure with the bath, while the acoustic mode of interest is kept isolated from the environment through the phononic bandgap of the structure. By keeping the intrinsic damping of acoustic mode low, this method is a promising route to realizing $C_{\text{eff}} > 1$. Initial work in this direction, performed at room temperature, utilized snowflake-shaped holes in a Si membrane to create a quasi-2D OMC with substantially higher optical power handling capability, although with a relatively low optomechanical coupling of $g_0/2\pi = 220$ kHz [33].

In this Chapter, a microscopic model and corresponding theory of this optical heating bath is firstly introduced. Several measurement techniques of relative heating bath parameters, together with measurment data for 1D nanobeam and quasi-2D OMCs are also discussed. This chapter demonstrates that the improved quasi-2D OMC device has an over 50-fold improvement in back-action per photon over previous reports [32, 33], and a much higher thermal conductance (×42) compared to 1D structures at millikelvin temperatures. Most importantly, we demonstrate a Q-factor of 1.2×10^9 for the 10 GHz optomechanically-coupled acoustic mode of the cavity and a C_{eff} greater than unity under continuous-wave optical pumping. $C_{\mathrm{eff}} > 1$ is a crucial threshold for realizing a variety of optomechanical applications in silicon optomechanical crystals. For example, to efficiently gather statistics in order to calculate quantum correlations, a continuous scheme with a large intra-cavity photon number is critical [14, 15, 16, 17, 18, 19]. Also, it is suitable for realizing applications such as signal transduction of itinerant quantum signals [109, 110, 111, 112].

6.1 Microscopic Model of Optical Absorption Induced Bath

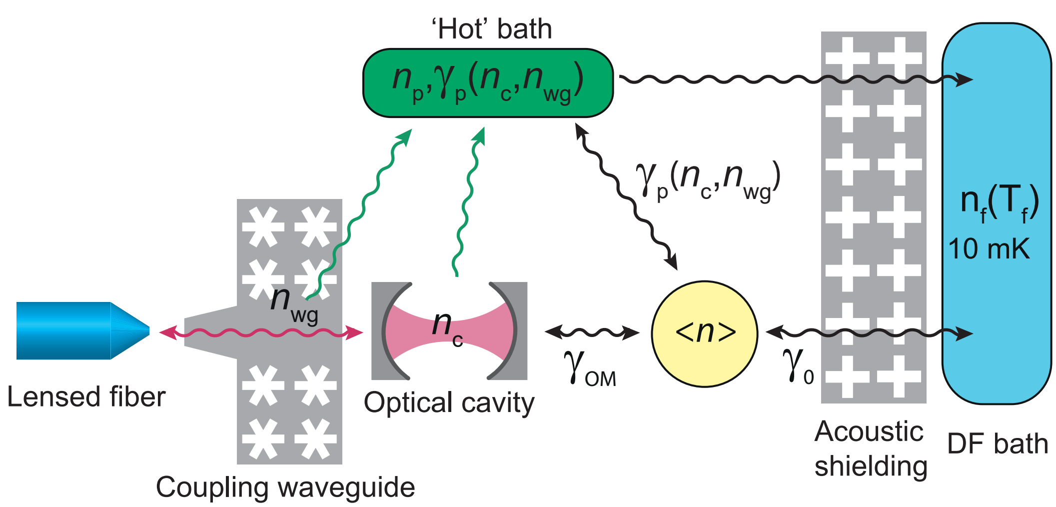

Figure 6.1: **Optical absorption heating bath.** Diagram illustrating the proposed model of heating of the mechanics due to optical absorption and the various baths coupled to the localized mechanical mode (see text for details).

To understand the heating properties of OMC devices due to optical absorption, a proposed microscopic model for this heating and damping [29] is illustrated in Fig 6.1. This model represents both 1D nanobeam and quasi-2D OMCs. The source of optical absorption in our silicon OMC device is most likely due to electronic defect states at the surface of material [30, 31]. The mechanical mode of interest is weakly coupled through the acoustic shielding to the surrounding DR environment with a rate γ_0, and is coupled via phonon-phonon scattering to the optically-generated high frequency phonons (temperature T_p, occupancy n_p at ω_m) near the OMC cavity with a rate γ_p.

6.2 Theoretical Model of Optical Absorption Induced Bath

Optical absorption is found to induce additional parasitic heating and damping of the high-Q acoustic breathing mode of the Si OMC devices at millikelvin temperatures. This absorption heating is thought to proceed through excitation of sub-bandgap electronic defect states at the Si surfaces which undergo phonon-assisted decay, generating a local bath of thermal phonons coupled to the high-Q breathing mode [29]. We may gain some understanding of the optically-induced bath by considering a simple model of phonon-phonon interactions which can couple the optically-induced hot phonon bath to the breathing mode. As we are concerned in this work with the phonon dynamics at low bath temperature ($T_\mathrm{b} \lesssim 10$ K), and the acoustic mode of interest is at microwave frequencies, the phonon-phonon interactions leading to heating and damping of the breathing mode can be understood in terms of a Landau-Rumer scattering process [68, 122]. In this context, we may consider a simple model in which our mode of interest at frequency ω_m is coupled to higher-frequency bath phonon modes at frequencies ω_1 and ω_2, with $\omega_2 - \omega_1 = \omega_m$. Then we may write the scattering rates into and out of the mode of interest to first order in perturbation theory [29, 68] as $\Gamma_+ = A(n_m + 1)(n_2 + 1)n_1$ and $\Gamma_- = An_m n_2(n_1 + 1)$, respectively, where n_1, n_2, and n_m are the number of phonons in each mode involved in the scattering and A is a constant describing the Si lattice anharmonicity. Then the overall rate of change in the occupancy of the mode of interest is

$$\dot{n}_m = \Gamma_+ - \Gamma_- = -A(n_1 - n_2)n_m + An_2(n_1 + 1). \tag{6.1}$$

This expression has exactly the form of a harmonic oscillator coupled to a thermal bath with rate $\gamma_\mathrm{p} = A(n_1 - n_2)$ and effective occupancy $n_\mathrm{p} = An_2(n_1 + 1)/\gamma_\mathrm{p}$. Assuming thermal occupancies for each of the higher frequency phonon modes of the hot bath, $n_{1,2} = n_\mathrm{B}[\hbar\omega_{1,2}/k_\mathrm{B}T_\mathrm{p}] \equiv 1/(\exp\{[\hbar\omega_{1,2}/k_\mathrm{B}T]\} - 1)$, and using the identity $n_\mathrm{B}[x + x'](n_\mathrm{B}[x] + 1) = (n_\mathrm{B}[x] - n_\mathrm{B}[x + x'])n_\mathrm{B}[x']$ [68], one finds that the mode m thermalizes with the hot bath via 3-phonon scattering to an effective occupancy which is $n_\mathrm{p} = n_\mathrm{B}[\hbar\omega_\mathrm{m}/k_\mathrm{B}T_\mathrm{p}]$. This result holds when the hot bath thermalizes to some temperature independent of the interactions with mode m.

In the real material system of the nanobeam, the local hot phonon bath at elevated temperature T_b is expected to be generated as electronic states at $\sim$ eV energy undergo phonon-assisted relaxation processes, emitting a shower of high-frequency phonons which subsequently decay by a cascade of nonlinear multi-phonon interactions into a bath of GHz phonons. Due to the geometric aspect ratio of the thin-film nanobeam, the local density of phonon states becomes restricted at lower frequency, decreasing the rates of phonon-phonon scattering at low frequency relative to those of a bulk crystal with a 3D Debye density of states. The beam thickness (t = 220 nm, width $w \approx 560$ nm, length $l \approx 15$ μm) corresponds to a relatively high cutoff frequency in the vicinity of $\omega_{\mathrm{co}}/2\pi \approx v_l/(2t) \approx 20$ GHz, where $v_l = 8.433$ km/s is the longitudinal-phonon velocity in Si. This cutoff frequency imposes an effective phonon *bottleneck* preventing further rapid thermalization to lower-lying modes and a resulting buildup in the bath phonon population above the bottleneck. For phonon frequencies below the cutoff, where the wavelength is large enough to approach the lattice constant of the acoustic bandgap clamping region, the reflectivity of the clamping region increases as ballistic radiation out of the nanobeam is suppressed. The result is a reduced density of phonon states near and below the cutoff, where the nanobeam supports quasi-discrete (and long-lived, especially in the vicinity of the mirror bandgap and acoustic shield bandgap) phonon modes at lower frequency as outlined in Fig. 6.2. The phenomenological coupling rate γ_{p} describes the rate at which the lower-lying modes—in particular the breathing mode at 5 GHz—are coupled to the elevated-temperature bath of higher-frequency phonons above the bottleneck.

In the context of this proposed phonon-bottleneck model, we now consider instead of a discrete pair of modes n_1 and n_2 a quasi-continuum of high-frequency bath modes coupled to the mode of interest via some anharmonicity matrix element $A(\omega; \omega_m)$. We will assume that the thermal phonons populating the bath have sufficient time to thermalize amongst each other before decaying, or in other words, that they couple to each other at a mixing rate γ_{mix} much greater than their coupling rates to the external environment or to the lower-lying phonon modes. Under this assumption, we may define an effective local temperature T_{p} such that the occupancy of a bath phonon at frequency ω is given by the Bose-Einstein occupation factor

$$n_{\mathrm{bath}}[\omega; T_{\mathrm{p}}] \equiv n_{\mathrm{B}}[\hbar(\omega - \omega_{\mathrm{co}})/k_{\mathrm{B}}T_{\mathrm{p}}] = \frac{1}{e^{\hbar(\omega-\omega_{\mathrm{co}})/k_{\mathrm{B}}T_{\mathrm{p}}} - 1}, \tag{6.2}$$

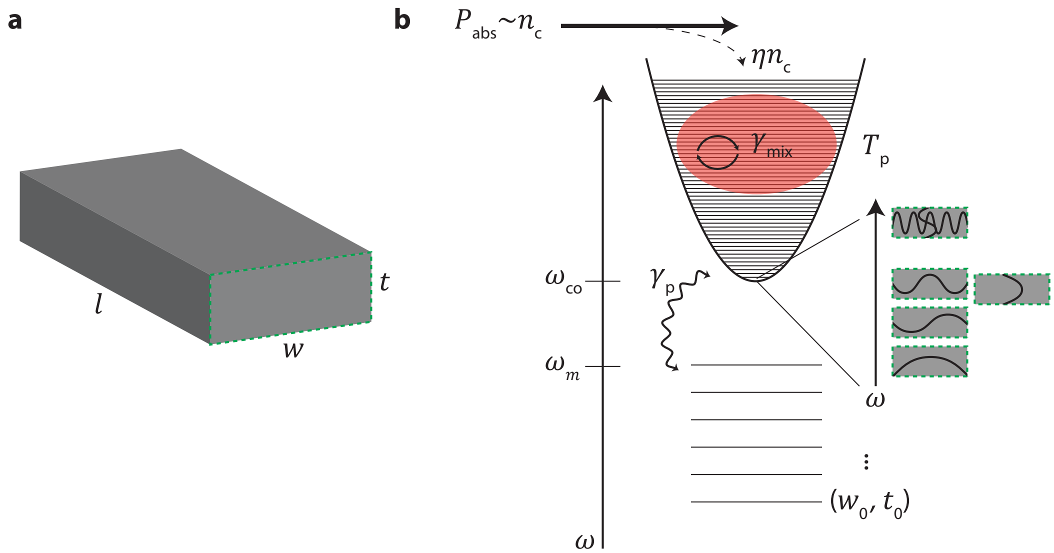

Figure 6.2: **Impact of the phonon-bottleneck on the optical-absorption bath.** **a**, Cross-sectional dimensions of the thin-film nanobeam. **b**, Absorption of sub-Si-bandgap photons gives rise to phonon-assisted decay of THz phonons into a local bath of GHz phonons in the nanobeam. This bath is expected to experience a bottleneck at a cutoff frequency corresponding to the cross-sectional dimensions of the nanobeam, such that a high-frequency phonon bath accumulates and thermalizes among itself to a local temperature T_b at rate γ_{mix}. In the vicinity of the bottleneck frequency the relevant normal modes of the beam are those shown in the inset (black lines are schematics of the local strain in the beam). The lowest-lying discrete mode (w_0, t_0) is a fundamental bowstring mode of the nanobeam at $\sim$ 20 MHz.

where ω_{co} represents the new effective ground-state frequency due to the phonon bottleneck effect, and $n_B[x] = 1/(\exp[x] - 1)$ is the Bose distribution.

The temperature of the optically-induced hot phonon bath, T_p, can then be related to the absorbed optical power P_{abs} using a model of the lattice thermal conductivity in the low temperature limit. Assuming the optical absorption process is linear, we can write the absorbed optical power as a fraction η of the optical pump power: $P_{abs} = \eta P_{in} = \eta' n_c$. In steady state, the power output into the phonon bath is equal to its input, $P_{out} = P_{abs} \sim n_c$. The lattice thermal conductivity at low temperatures, where phonon transport is ballistic, scales as a power law of the phonon bath temperature [123, 124], $G_{th} \sim (T_p)^{\alpha}$. The power law exponent α is equal to the effective number of spatial dimensions d of the material/structure under consideration. Effectively, the hot phonon bath radiates energy as a black body, with radiated power scaling as $(T_p)^{\alpha+1}$ via Planck's law. In the case of a structure with 2D phonon density of states, such as the OMC cavity in the frequency range from

10-100 GHz (c.f., Fig. 5.5), $\alpha = d = 2$ and the hot phonon bath temperature scales as $T_\mathrm{p} \sim P_\mathrm{out}^{1/3} \sim n_\mathrm{c}^{1/3}$. This approximate scaling is expected to be valid so long as phonons in the hot phonon bath approximately thermalize each other upon creation from optical absorption events, and then radiate freely (balistically) into the effective zero temperature substrate. The picture one has then is that the hot bath phonons make multiple passes within the OMC cavity region, scattering with other phonons leading to thermalization, and then eventually radiating into the substrate, i.e., the OMC cavity is still a good cavity for many phonons in the acoustic frequency region above the phononic bandgap.

In analogy with Equation 6.1, for a phonon bath density of states $\rho(\omega)$ we can calculate the effective coupling rate γ_p between the hot phonon bath and the mode of interest due to 3-phonon scattering:

$$\gamma_\mathrm{p} = \int_{\omega_\mathrm{co}}^{\infty} \mathrm{d}\omega \; A[\omega;\omega_\mathrm{m}]\rho[\omega]\rho[\omega+\omega_\mathrm{m}] \left(n_\mathrm{bath}[\omega] - n_\mathrm{bath}[\omega+\omega_\mathrm{m}]\right). \tag{6.3}$$

In a simple continuum elastic model [29, 68], the product of the anharmonicity matrix element $A[\omega;\omega_m]$ and the density of states is taken to obey a polynomial scaling $A[\omega;\omega_m]\rho[\omega]\rho[\omega+\omega_\mathrm{m}] = A'(\omega-\omega_\mathrm{co})^a$ for some constants A' and a, where we have introduced the cut-off frequency below which we assume the density of states is zero. With this assumption,

$$\begin{aligned}
\gamma_\mathrm{p} &\cong A' \int_{\omega_\mathrm{co}}^{\infty} \mathrm{d}\omega \; (\omega-\omega_\mathrm{co})^a \left(n_\mathrm{bath}[\omega] - n_\mathrm{bath}[\omega+\omega_\mathrm{m}]\right) && (6.4)\\
&= A' \int_{\omega_\mathrm{co}}^{\infty} \mathrm{d}\omega \; (\omega-\omega_\mathrm{co})^a \left(\frac{n_\mathrm{bath}[\omega+\omega_\mathrm{m}](n_\mathrm{bath}[\omega]+1)}{n_\mathrm{B}[\hbar\omega_\mathrm{m}/k_\mathrm{B}T_\mathrm{p}]}\right) && (6.5)\\
&= \frac{A'}{n_\mathrm{B}[\hbar\omega_\mathrm{m}/k_\mathrm{B}T_\mathrm{p}]+1} \int_{\omega_\mathrm{co}}^{\infty} \mathrm{d}\omega \; (\omega-\omega_\mathrm{co})^a \left(n_\mathrm{bath}[\omega](n_\mathrm{bath}[\omega+\omega_\mathrm{m}]+1)\right), && (6.6)
\end{aligned}$$

where in the last line we used the identity $n_\mathrm{B}[x+x'](n_\mathrm{B}[x]+1)/n_\mathrm{B}[x'] = (n_\mathrm{B}[x+x']+1)n_\mathrm{B}[x]/(n_\mathrm{B}[x']+1)$. Making a change of variables to $x \equiv \hbar(\omega-\omega_\mathrm{co})/k_\mathrm{B}T_\mathrm{p}$ in the integral in Eq. (6.6), we have

$$\gamma_\mathrm{p} \cong \left(\frac{A'}{n_\mathrm{B}[x_\mathrm{m}]+1}\right)\left(\frac{k_\mathrm{B}T_\mathrm{p}}{\hbar}\right)^{a+1} \int_0^{\infty} \mathrm{d}x \; x^a \left(n_\mathrm{B}[x](n_\mathrm{B}[x+x_\mathrm{m}]+1)\right) \tag{6.7}$$

where $x_\mathrm{m} = \hbar\omega_\mathrm{m}/k_\mathrm{B}T_\mathrm{p}$. The integral in Equation 6.7 depends on temperature only through x_m, and in the small and large x_m limit (corresponding to low and high temperature), is relatively independent of x_{m}. If we assume that the anharmonicity element $A[\omega;\omega_m]$ is approximately frequency independent, and the only frequency dependence in $A'(\omega-\omega_{\mathrm{co}})^a$ comes from the phonon density of states, then $a \approx 2(d-1)$ for a phonon bath of dimension d. We can thus make a general observation about the scaling of the bath-induced damping rate γ_{p} in the low ($x_{\mathrm{m}} \gg 1$) and high ($x_{\mathrm{m}} \ll 1$) temperature regimes:

$$\gamma_{\mathrm{p}} \propto \begin{cases} \left(\frac{k_{\mathrm{B}}T_{\mathrm{p}}}{\hbar}\right)^a \sim n_{\mathrm{c}}^{2(d-1)/(d+1)} & \text{for } T_{\mathrm{p}} \gg \frac{\hbar\omega_m}{k_{\mathrm{B}}}, \\ \left(\frac{k_{\mathrm{B}}T_{\mathrm{p}}}{\hbar}\right)^{a+1} \sim n_{\mathrm{c}}^{(2d-1)/(d+1)} & \text{for } T_{\mathrm{p}} \ll \frac{\hbar\omega_{\mathrm{m}}}{k_{\mathrm{B}}}, \end{cases} \tag{6.8}$$

for a generic hot phonon bath of dimension d. In a structure such as the OMC nanobeam cavity we expect the dimensionality of the effective bath density of states to be reduced relative to the Debye 3D density of states for a bulk crystal. Here we will assume - consistent with numerical simulations of the OMC structure - that the phonon bath has a two-dimensional density of states corresponding to $a = 2$. In this case, we have the following scaling of the damping factor with intra-cavity photon number,

$$\gamma_{\mathrm{p}} \propto \begin{cases} \left(\frac{k_{\mathrm{B}}T_{\mathrm{p}}}{\hbar}\right)^2 \sim n_{\mathrm{c}}^{2/3} & \text{for } T_{\mathrm{p}} \gg \frac{\hbar\omega_{\mathrm{m}}}{k_{\mathrm{B}}}, \\ \left(\frac{k_{\mathrm{B}}T_{\mathrm{p}}}{\hbar}\right)^3 \sim n_{\mathrm{c}} & \text{for } T_{\mathrm{p}} \ll \frac{\hbar\omega_{\mathrm{m}}}{k_{\mathrm{B}}}. \end{cases} \tag{6.9}$$

Upon thermalizing with the hot phonon bath, the effective thermal occupancy n_{p} of the high-Q breathing mode of the acoustic cavity can be found from a similar rate equation analysis as considered for the 3-mode scattering in Eq. (6.1). Integrating over all the possible 3-phonon scattering events involving the mode of interest at frequency ω_{m} yields,

$$\begin{aligned} n_{\mathrm{p}} &= \frac{1}{\gamma_{\mathrm{p}}}\int_{\omega_{\mathrm{co}}}^{\infty} \mathrm{d}\omega\; A[\omega;\omega_{\mathrm{m}}]\rho[\omega]\rho[\omega+\omega_{\mathrm{m}}]n_{\mathrm{bath}}[\omega+\omega_{\mathrm{m}}]\left(n_{\mathrm{bath}}[\omega]+1\right]) && (6.10) \\ &\cong \frac{n_{\mathrm{b}}[\omega_{\mathrm{co}}+\omega_{\mathrm{m}}]A'}{\gamma_{\mathrm{p}}}\int_{\omega_{\mathrm{co}}}^{\infty} \mathrm{d}\omega\; \omega^a\left(n_{\mathrm{bath}}[\omega]-n_{\mathrm{bath}}[\omega+\omega_{\mathrm{m}}]\right) && (6.11) \\ &= n_{\mathrm{B}}[\hbar\omega_{\mathrm{m}}/k_{\mathrm{B}}T_{\mathrm{p}}]. && (6.12) \end{aligned}$$

We therefore have a characteristic scaling behavior for the effective phonon occupancy n_{p} coupled to the cavity mode of interest that is,

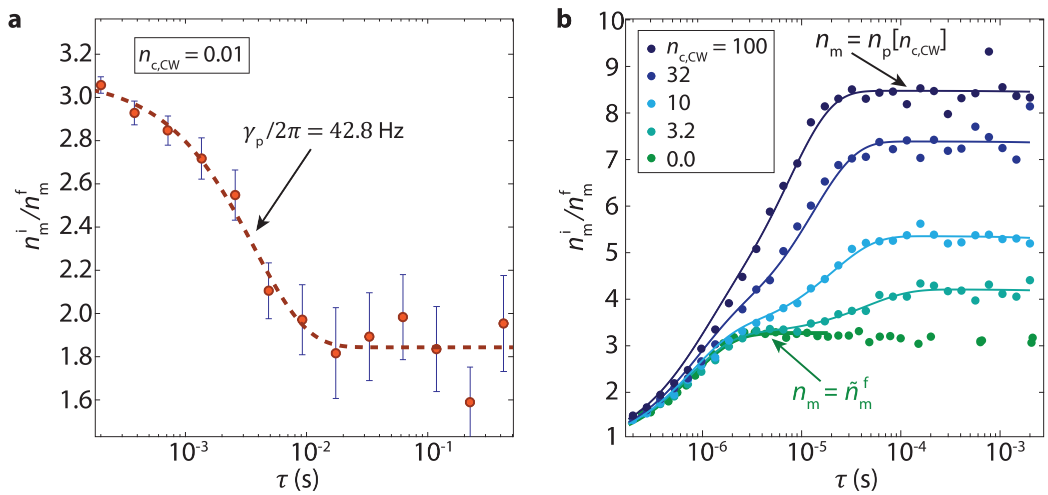

Figure 6.3: **Measurement techniques for extracting the optical-bath-induced damping rate γ_p.** **a**, Ringdown measurement in the presence of a continuous-wave pump laser with an average intracavity photon number of $n_{c,CW} = 10^{-2}$. The total decay rate is $\gamma = \gamma_p + \gamma_0$, and with $\gamma_0/2\pi = 0.21$ Hz known from separate measurements, $\gamma_p/2\pi = 42.8$ Hz is extracted directly from the fitted decay rate. **b**, At larger n_c, the bath-heating induced by the pump laser causes net heating in the pulse-off state. Here, the heating is fitted to the phenomenological model of Eq. (6.14) to extract γ_p due to the CW laser pump. Measurements were performed on a six-acoustic-shield device (device B) with parameters (κ, κ_e, g_0, ω_m, γ_0) = 2π(1.13 GHz, 605 MHz, 713 kHz, 5.013 GHz, 0.21 Hz) and with a readout photon number $n_{c,RO} = 569$.

$$n_p \propto \begin{cases} \left(\frac{k_B T_p}{\hbar\omega_m}\right) \sim n_c^{1/(d+1)} \overset{d=2}{=} n_c^{1/3} & \text{for } T_p \gg \frac{\hbar\omega_m}{k_B}, \\ \exp\{[-\hbar\omega_m/k_B T_p]\} & \text{for } T_p \ll \frac{\hbar\omega_m}{k_B}. \end{cases} \tag{6.13}$$

6.3 Measurement of Optical-Absorption-Induced Damping in 1D Nanobeam OMC

In order to measure the additional bath-induced damping rate γ_p, we use a pump-probe technique employing two laser sources. The pump laser is tuned to optical resonance ($\Delta = 0$) to eliminate dynamical back-action effects ($\gamma_{OM} = 0$), and impinges on the cavity in continuous-wave (CW) operation. The pump laser generates a steady-state intracavity photon population $n_{c,CW}$ and an absorption-induced bath at elevated temperature in the steady state. A second pulsed laser, the probe laser, is tuned to the red motional sideband of the cavity ($\Delta = +\omega_m$) and is used to periodically read out the phonon occupancy, where the scattering rate of the probe laser at the beginning of the probe pulse provides an estimate of n_{p} due to the CW laser alone. Application of the probe laser not only allows readout of the breathing mode occupancy, but also produces an excess absorption-induced bath above and beyond that of the background CW laser alone. When the readout probe pulse is turned off, the breathing mode initially heats due to the excess hot bath created by the probe pulse (over several microseconds; see Fig. 6.4(c)), and then after this excess hot bath evaporates away leaving a breathing mode occupancy of n_{f}', it relaxes back to its steady-state occupancy set by the CW laser, $\langle n\rangle[n_{\mathrm{c,CW}}] = (\gamma_{\mathrm{p}}[n_{\mathrm{c,CW}}]n_{\mathrm{p}}[n_{\mathrm{c,CW}}] + \gamma_0 n_0)/(\gamma_{\mathrm{p}}[n_{\mathrm{c,CW}}] + \gamma_0)$. The rate of relaxation is set by the modified total damping rate of $\gamma_0 + \gamma_{\mathrm{p}}[n_{\mathrm{c,CW}}]$. By observing this modified exponential decay rate we directly extract $\gamma_{\mathrm{p}}[n_{\mathrm{c,CW}}]$, with γ_0 known from independent ringdown measurements in the absence of the CW background laser. For example, in Fig. 6.3(a) we show the measured ringdown of a high-Q six-shield device (device B; $\gamma_0/2\pi = 0.21$ Hz) for a CW pump laser photon number of $n_{\mathrm{c,CW}} = 10^{-2}$, from which we extract $\gamma_{\mathrm{p}}/2\pi = 42.8$ Hz.

For large $n_{\mathrm{c,CW}}$ ($\gtrsim 1$) the steady-state occupancy of $\langle n\rangle[n_{\mathrm{c,CW}}]$ becomes larger than the occupancy $\tilde{n}_{\mathrm{m}}^{\mathrm{f}}$ at the end of the readout pulse. The readout pulse *should* cool the breathing mode, after all, and it is only the absorption-induced heating caused by the readout pulse itself that manifests as a ring down in absence of heating from the CW laser. For large $n_{\mathrm{c,CW}}$ then, γ_{p} is estimated by observing a ring-*up* in the pulse-off state from the final pulse occupancy $\tilde{n}_{\mathrm{m}}^{\mathrm{f}}$ to the elevated $\langle n\rangle[n_{\mathrm{c,CW}}]$. Figure 6.3(b) shows a representative data set for extracting γ_{p} at $n_{\mathrm{c,CW}} > 1$, where an initial fast rise is observed in the mode occupancy in the pulse-off state from $n_{\mathrm{m}}^{\mathrm{f}}$ to $\tilde{n}_{\mathrm{m}}^{\mathrm{f}}$ due to the aforementioned excess bath created by the readout pulse, followed by a slower second heating stage from $\tilde{n}_{\mathrm{m}}^{\mathrm{f}}$ to $n_{\mathrm{c,CW}}$. As discussed in more detail in Section 6.5, we can fit the ring-up curve after the readout pulse is turned off by considering a phenomenological model including decay of the readout-induced hot bath,

$$\begin{aligned}\dot{\langle n\rangle} = &-\left\{\gamma_0 + \gamma_{\mathrm{p}}[n_{\mathrm{c,RO}}]e^{-\zeta_{\gamma_{\mathrm{p}}}\tau_{\mathrm{off}}} + \gamma_{\mathrm{p}}[n_{\mathrm{c,CW}}]\right\}\langle n\rangle \\ &+ \left\{\gamma_{\mathrm{p}}[n_{\mathrm{c,RO}}]e^{-\zeta_{\gamma_{\mathrm{p}}}\tau_{\mathrm{off}}} + \gamma_{\mathrm{p}}[n_{\mathrm{c,CW}}]\right\}(n_{\mathrm{p}}[n_{\mathrm{c,RO}}]e^{-\zeta_{n_{\mathrm{p}}}\tau_{\mathrm{off}}} + n_{\mathrm{p}}[n_{\mathrm{c,CW}}]). \quad (6.14)\end{aligned}$$

We first measure the transient readout-induced bath in the absence of the CW laser (dark green curve in Fig. 6.3b), from which a fit to Eq. (6.14) yields $n_{\mathrm{p}}[n_{\mathrm{c,RO}}] = 40$ phonons, $\gamma_{\mathrm{p}}[n_{\mathrm{c,RO}}]/2\pi = 9.55$ kHz, $\zeta_{\gamma_{\mathrm{p}}}/2\pi = 143$ kHz, and $\zeta_{n_{\mathrm{p}}}/2\pi = 15.9$ kHz.

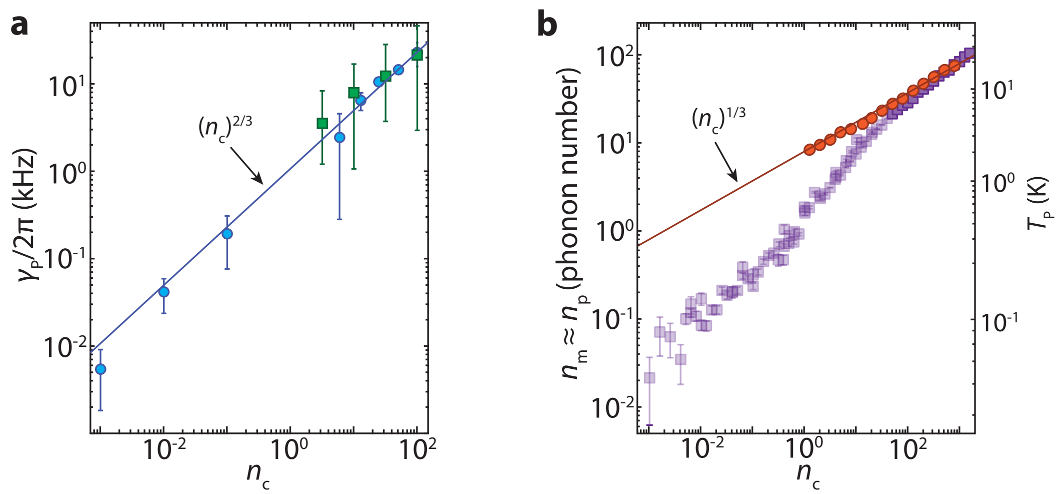

Figure 6.4: **Measured steady-state properties of the optical-absorption-induced bath.** **a**, Plot of γ_p versus n_c for six-shield (blue circles) and zero-shield (green squares) devices. The solid line is a power-law fit to the six-shield device data: $\gamma_p/2\pi = (1.07\text{ kHz}) \times n_c^{2/3}$. The zero-shield device (device A) has parameters (κ, κ_e, g_0, ω_m, γ_0) = 2π(1.507 GHz, 778 MHz, 713 kHz, 5.053 GHz, 14.1 kHz). The six shield device (device B) has parameters (κ, κ_e, g_0, ω_m, γ_0) = 2π(1.13 GHz, 605 MHz, 713 kHz, 5.013 GHz, 0.21 Hz). **b**, Plot of n_p versus n_c for zero-shield (purple symbols) and six-shield (orange circles) devices. Purple squares represent the measured mode occupancy corrected for heating induced by the readout laser tone. The right-hand axis gives the effective bath temperature T_p which corresponds to the measured bath occupancy. Translucent squares show data taken in the regime where the intrinsic decay rate γ_0 is comparable to the bath-induced damping γ_p, indicating that the raw measured occupancy begins to deviate substantially from the inferred occupancy given in the plot. The solid line is a fit to the six-shield data giving $n_p = (7.94) \times n_c^{1/3}$. **c**, Normalized phonon occupancy during and after the optical pulse. Squares are data points and the solid line is a best fit to the dynamical model. During the pulse, back-action cooling occurs at a timescale $\gamma_{OM}^{-1} \approx 100$ ns. The optical-absorption-induced bath simultaneously heats the mode at a rate $\gamma_p n_p$, such that at long T_{pulse} a steady-state mode occupancy n_f is reached. In the pulse-off state (gray squares), the residual phonon bath heats the mode at a rate $\gamma_p(t)n_p(t)$, where the bath damping and effective occupancy are explicitly time-dependent. A full dynamical model of the bath heating is used to generate the fit (dotted line). The purple data point in the off-state plot ($\tau_{off} = 200\ \mu$s) corresponds to off-state delay for the measured intra-pulse data shown in the on-state plot.

With these readout-induced bath values known, Eq. (6.14) is numerically integrated to fit the entire heating curve in the pulse-off state to extract the additional CW-pump-induced damping $\gamma_p[n_{c,CW}]$.

The results of the measured optical-absorption-induced damping γ_p versus n_c are summarized in Fig. 6.4(a) for measurements on both a six-shield (device B) and a zero-shield (device A) nanobeam device. The observed power law scaling fits well to $\gamma_\mathrm{p}/2\pi = (1.07\text{ kHz}) \times n_\mathrm{c}^{2/3}$, in agreement with the scaling predicted in Eq. (6.9) for a 2D density of states for the bath phonon population. Note that the much lower γ_0 of the six-shield device allows a much wider range of γ_p (and thus n_c) to be explored.

6.4 Measurement of Optical-Absorption-Induced Bath Occupancy in 1D Nanobeam OMC

In order to measure the bath occupancy n_p, again two different methods are used to probe the high- and low-photon-number dependencies of the bath. To measure the bath occupancy at photon numbers $n_\mathrm{c} \gtrsim 1$, a simple readout technique may be used in which a single readout laser is sent to the cavity in continuous-wave operation. The laser is tuned to cavity resonance ($\Delta = 0$) and the resulting sideband scattered photon count rate appearing at either the lower or upper frequency mechanical sideband ($\Delta = \pm\omega_m$) will be

$$\Gamma = \Gamma_\mathrm{noise} + \left(\frac{\kappa}{2\omega_m}\right)^2 \Gamma_{\mathrm{SB},0}\langle n\rangle. \tag{6.15}$$

With the sideband filters aligned to either of the mechanical sidebands of the cavity, the observed count rate is used to extract an equivalent occupancy $\langle n\rangle = n_\mathrm{p}$ at various pump powers n_c. The results are shown in Fig. 6.4b (orange circles) for a six-shield device (device B), exhibiting a power-law scaling of $n_\mathrm{p} = (7.94) \times n_\mathrm{c}^{1/3}$ in agreement with the model in the limit of high bath temperature $T_\mathrm{p} \gg \hbar\omega_m/k_\mathrm{B} \approx 200$ mK. The right-hand axis of Fig. 6.4 gives the effective bath temperature T_p corresponding to the measured occupancy, indicating that the measurement regime is indeed well in the high temperature limit.

At lower photon numbers $n_\mathrm{c} \lesssim 1$, and corresponding lower $n_\mathrm{p} \approx \langle n\rangle$, the SNR of the counting of photons scattered from cavity resonance into either mechanical sideband begins to drop below 1 due to the large sideband resolution factor $(2\omega_\mathrm{m}/\kappa)^2$ of the OMC cavity (c.f., Eq. (6.15)). In this regime, an alternative measurement method is employed in which a CW pump laser generates a steady-state optical-absorption bath while a second pulsed readout laser is used to probe the breathing mode occupancy (see Fig. 6.5). The background pump laser is detuned to $\Delta/2\pi = 1$ GHz from the

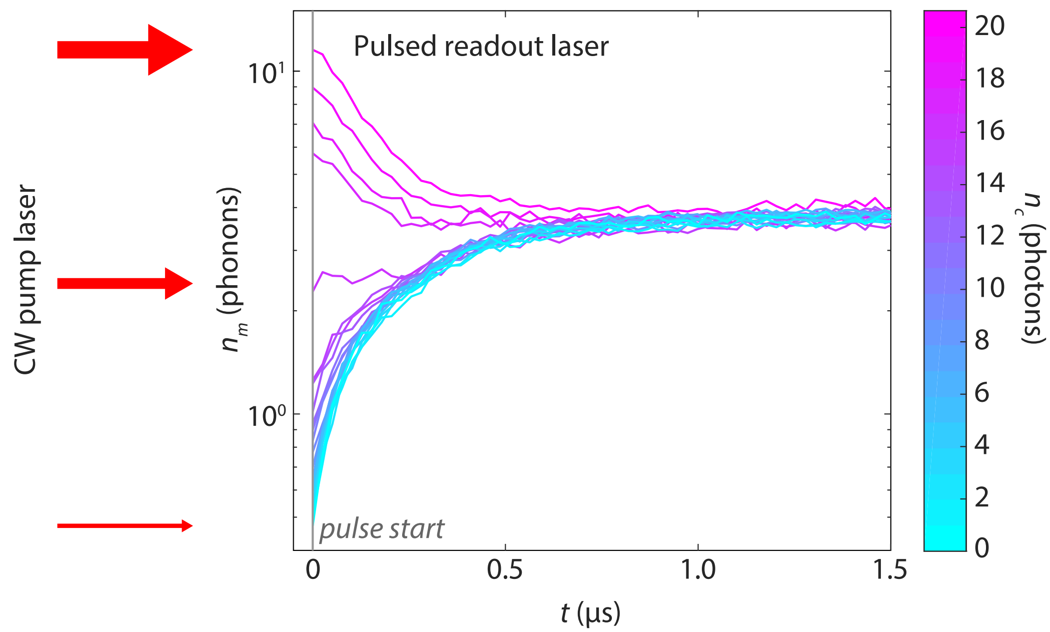

Figure 6.5: **Pulsed measurements of the bath occupancy in a low-Q nanobeam cavity.** A continuous-wave background laser (red arrows, detuning $\Delta/2\pi \approx 1$ GHz) is used to generate a constant stead-state absorption bath, while a pulsed readout laser (readout $n_{\mathrm{c,RO}} = 50.6$) is used to probe the resulting bath occupancy for various background laser powers $n_{\mathrm{c,CW}}$. The initial measured occupancy during the pulse is given by $n_{\mathrm{m}}^0 \approx (n_{\mathrm{p}}\gamma_{\mathrm{p}} + n_0\gamma_0)/(\gamma_{\mathrm{p}} + \gamma_0) + \tilde{n}_0$, where $\tilde{n}_0$ is residual occupancy due to the finite heating occurring before the first readout time bin. Measurements were performed on the zero-shield device (device A) with parameters (κ, κ_{e}, g_0, ω_{m}, γ_0) = 2π(1.507 GHz, 778 MHz, 713 kHz, 5.053 GHz, 14.1 kHz).

cavity resonance to minimize back-action as well as bleed-through counts through the sideband filters aligned at $\Delta = 0$. The initial measured occupancy n_{m}^0 during the pulse is a measure of the pump-induced bath occupancy; however, it includes a small residual occupancy $\tilde{n}_0 \approx 0.04$ due to heating caused by the readout laser prior to the first measurement time bin of the pulse-on state. We define a corrected occupancy $n_{\mathrm{m}}^* \equiv n_{\mathrm{m}}^0 - \tilde{n}_0$ which denotes the measured mode occupancy which is coupled to the fridge bath as well as the absorption-bath induced by the pump laser:

$$n_{\mathrm{m}}^* = \frac{n_{\mathrm{p}}\gamma_{\mathrm{p}} + n_0\gamma_0}{\gamma_{\mathrm{p}} + \gamma_0}. \tag{6.16}$$

With n_0, γ_0, and the power-dependence of γ_{p} known from independent measurements, we can estimate the equivalent bath occupancy

$$n_{\mathrm{p}}[n_{\mathrm{c}}] = \frac{n_{\mathrm{m}}^{*}\gamma_{\mathrm{p}}[n_{\mathrm{c}}] + (n_{\mathrm{m}}^{*} - n_0)\gamma_0}{\gamma_{\mathrm{p}}[n_{\mathrm{c}}]}. \tag{6.17}$$

Using this second method, over a much larger span of n_{c}, the behavior of the effective bath occupancy n_{p} for a zero-shield device with intrinsic damping rate $\gamma_0/2\pi = 14.1$ kHz is shown in Fig. 6.4b as purple squares. Note that measurement of the very high-Q six-shield device (device B) using the pulsed readout scheme is not practical due to the extremely long relaxation times required between readout pulses (we did, however, verify for a few values of n_{c} that the two schemes give consistent results). For $n_{\mathrm{c}} \gtrsim 1$, again we find good agreement for the zero-shield device with a power-law scaling $n_{\mathrm{p}} \propto n_{\mathrm{c}}^{1/3}$ for $T_{\mathrm{b}} \gg \hbar\omega_m/k_{\mathrm{B}}$. Not only is the scaling of n_{p} versus n_{c} the same for both zero-shield and six-shield devices, but so is the absolute value of n_{p}. For $n_{\mathrm{c}} \lesssim 1$, $\gamma_{\mathrm{p}}(n_{\mathrm{c}}) \approx \gamma_0$ for the zero-shield device and the measured occupancy n_{m}^{*} deviates substantially from n_{p} as the breathing mode thermalizes more strongly with the external substrate temperature set by the fridge ($T_{\mathrm{f}} \approx 10$ mK). In this range we have plotted n_{m}^{*} in translucent purple squares to distinguish it from the region of parameter space where n_{m}^{*} is expected to faithfully represent n_{p}.

6.5 Measurement of Optical-Absorption-Induced Bath Dynamics in 1D Nanobeam OMC

The hot bath created by the application of laser light resonant with the optical mode of the OMC cavity does not instantaneously appear when the laser light is turned on, nor does it instantaneously vanish once the laser is turned off. Rather, there is a somewhat complicated bath dynamics that can be inferred from careful study of the temporal variation of the scattered photon signal from the readout pulse due to excitation of the mechanical breathing mode by the hot phonon bath. Using the measured breathing mode occupancy as a proxy one can infer many subtle features of the bath dynamics.

Figure 6.6(a) shows the measured scattered photon signal due to a pulsed readout tone applied on the lower motional sideband of the optical cavity ($\Delta = +\omega_{\mathrm{m}}$) of a high mechanical Q-factor six-shield OMC device (device B). Here the readout pulses are $\tau_{\mathrm{pulse}} = 4$ μs long and a variable delay τ_{off} is applied between each successive optical readout pulse. The scattered photons from the readout pulse are filtered by the filter bank resonantly aligned with the optical cavity resonance ($\Delta = 0$), thus yielding a photon count rate throughout the readout pulse which is proportional to the average occupancy of the mechanical breathing mode $\langle n \rangle$. This is shown in Fig. 6.6(a) for a time bin resolution of 10.24 ns, with the first measurement bin occurring at $t = 100$ ns after the pulse-on signal is applied in order to ensure that the optical pulse amplitude has settled and reached its maximum value. In the left panel of Fig. 6.6(b) we plot time-varying normalized breathing mode occupancy, corresponding to the ratio of the measured signal during the pulse to that at the very end of the pulse. This curve is not a single-shot measurement, but rather averaged over thousands of pulses, for which the normalized signal avoids small, slow drifts in the efficiency of the measurement apparatus. In the right panel we plot the normalized initial measurement bin occupancy (still taken to be at 100 ns after the readout pulse is turned on) as a function of the off-state delay time τ_{off} between successive pulses.

Several things are quickly evident from these plots of the measured breathing mode occupancy during and after the applied optical pulse. During the pulse we expect the optomechanical back-action to induce damping and cooling of the breathing mode at a rate $\gamma_{\mathrm{OM}}[n_{\mathrm{c}}]$. Without any parasitic heating effects from the applied optical pulse, the breathing mode should cool down to its equilibrium occupancy, ideally very close to zero at the fridge temperature ($T_{\mathrm{f}} = 10$ mK). This does not occur, but rather the breathing mode occupancy is seen to initially cool to a few phonons over ~ 300 ns, and then slowly heat to a steady-state phonon occupancy at the end of the pulse of $n_{\mathrm{m}}^{\mathrm{f}} = 4.2$ phonons (c.f., Fig. 6.6(a)). Similarly, once the optical pulse is turned off and light has left the optical cavity, the breathing mode occupancy starts to heat again, levelling off after a few microseconds following a slight overshoot to a modified post-pulse value of $\langle n \rangle[0] = 27$ phonons ($\rightarrow n_{\mathrm{m}}^{\mathrm{i}} = 13.6$ phonons in the first masurement bin; c.f., Fig. 6.4(b)). This strange dynamics is a result of the coupling of the breathing mode to the optical-absorption-induced hot bath. The slight undershoot of the cooling and slow heating in the pulse-on state is a result of a slow turn on of the hot bath. Similarly, the transient post-optical-pulse heating results from the slow decay of the hot bath, now without the cooling from optomechanical back-action.

Noticeably, the timescales for the turn on (~ 400 ns) of the bath and the turn off (~ 3 μs) of the bath are different. Less evident from these plots, but nonetheless very clear when attempting to model the hot bath dynamics, is that there seems to be two components to the bath, one whose turn on and turn off transients are

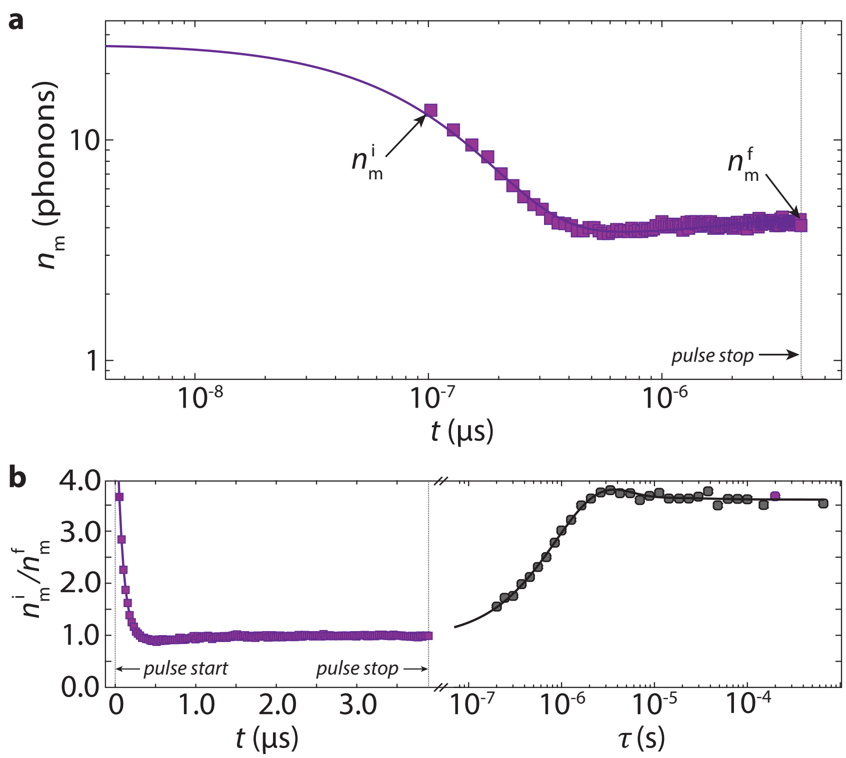

Figure 6.6: **Measured pulse dynamics of the breathing mode occupancy and the optical-absorption-induced bath. a**, Phonon occupancy of the breathing mode as a function of time t during the red-detuned ($\Delta = +\omega_m$) optical excitation pulse. Here, the time delay between successive pulses is $\tau_{\mathrm{off}} = 654\mu$s. Squares are data points and the solid line is a best fit to the dynamical model. The nanobeam device is device B with six periods of acoustic shielding, and device parameters (κ, κ_e, g_0, ω_m, γ_0) = 2π (1.13 GHz, 605 MHz, 713 kHz, 5.013 GHz, 0.21 Hz). During the pulse, back-action cooling occurs at a timescale $\gamma_{\mathrm{OM}}^{-1} \approx 100$ ns. Note that the initial mode occupancy $\langle n \rangle[0] = 27$ phonons is determined by extrapolating the model fit back to $t = 0$, while the earliest measurement bin has an occupancy of $n_{\mathrm{m}}^{\mathrm{i}} = 13.6$ phonons. The optical-absorption-induced bath heats the mode at a rate $\gamma_{\mathrm{p}}(t)n_{\mathrm{p}}(t)$, such that for long enough τ_{pulse} a steady-state mode occupancy $n_{\mathrm{m}}^{\mathrm{f}}$ is reached. Here $n_{\mathrm{m}}^{\mathrm{f}} = 4.2$ phonons. The measurement time resolution bin size is 10.24 ns. **b**, Normalized breathing mode phonon occupancy during (left) and after (right) the optical pulse. In the pulse-off state (gray squares), the residual phonon bath heats the mode at a rate $\gamma_{\mathrm{p}}(\tau_{\mathrm{off}})n_{\mathrm{p}}(\tau_{\mathrm{off}})$, where the bath damping and effective occupancy are explicitly time-dependent. The purple data point in the off-state plot at $\tau_{\mathrm{off}} = 200$ μs indicates the pulse shown in the on-state plot. For all panels, the measurements were performed using an on-state readout intra-cavity photon number of $n_{\mathrm{c}} = 569$, and the solid curves correspond to the phenomenological model including the dynamics of the optical-absorption-induced bath, fit to the data using the parameters shown in Table 6.1.

very rapid (effectively instantaneous with the optical field), and one with much slower relaxation times. Even more subtle is that to get very good agreement with the measured initial transient in the breathing mode occupancy in the immediate aftermath of turning off the optical pulse, it seems that the hot-bath damping factor, γ_p, should be modeled with a more rapid relaxation rate than that of the hot bath occupancy, n_p. It may be that this is also the case in the transient dynamics during the pulse-on state, however, in the pulse-off state the relaxation rate of the measured breathing mode occupancy is far more sensitive to the value of γ_p as it dominates the total relaxation rate of the breathing mode in the absence of appreciable γ_OM.

The model used to fit the data in Fig. 6.6 consists of a set of coupled differential equations involving the breathing mode occupancy, the hot bath damping factor, and the effective hot bath occupancy. The rate equation for the breathing mode occupancy is given by,

$$\dot{n}_\mathrm{m} = -(\gamma_\mathrm{p} + \gamma_\mathrm{OM} + \gamma_0)\langle n \rangle + \gamma_\mathrm{p} n_\mathrm{p} + \gamma_0 n_0 \tag{6.18}$$

where in the pulse-on state $\gamma_\mathrm{OM} = \gamma_\mathrm{OM}[n_\mathrm{c}]$ will take on a large value on the order of 1 MHz for a readout pulse amplitude of a few hundred intra-cavity photons, and in the pulse-off state $\gamma_\mathrm{OM} \approx 0$ due to the large extinction ($\gtrsim$ 80 dB) and rapid timescale of the turn-off the optical pulse (20 ns). During the pulse-on state the rate equations for the fast (F) and slow (S) components of the hot bath damping factor and effective occupancy are,

$$\dot{(\gamma_\mathrm{p})}_{\mathrm{F(S)}}(t) = -(\theta_{\gamma_\mathrm{p}})_{\mathrm{F(S)}} \left\{ (\gamma_\mathrm{p})_{\mathrm{F(S)}}(t) - (\delta_\mathrm{b})_{\mathrm{F(S)}} \gamma_\mathrm{p}[n_{\mathrm{c,RO}}] \right\}, \tag{6.19}$$

and

$$\dot{(n_\mathrm{p})}_{\mathrm{F(S)}}(t) = -(\theta_{n_\mathrm{p}})_{\mathrm{F(S)}} \left\{ (n_\mathrm{p})_{\mathrm{F(S)}}(t) - (\delta_\mathrm{b})_{\mathrm{F(S)}} n_\mathrm{p}[n_{\mathrm{c,RO}}] \right\}, \tag{6.20}$$

where $t = \{0, \tau_\mathrm{pulse}\}$ is the time from the start of the pulse to the end of the pulse, $(\theta_{\gamma_\mathrm{p}})_{\mathrm{F(S)}}$ and $(\theta_{\gamma_\mathrm{p}})_{\mathrm{F(S)}}$ are the pulse-on relaxation rate constants for the damping factor and occupancy of the two different bath components, respectively, and $(\delta_\mathrm{b})_{\mathrm{F(S)}}$ is the F(S) fraction of the hot bath. $\gamma_\mathrm{p}[n_{\mathrm{c,RO}}]$ and $n_\mathrm{p}[n_{\mathrm{c,RO}}]$ are the steady-state bath values reached at the end of the optical readout pulse. The corresponding rate equations for the hot bath in the pulse-off state are,

$$(\dot{\gamma_{\mathrm{p}}})_{\mathrm{F(S)}}(\tau_{\mathrm{off}}) = -(\zeta_{\gamma_{\mathrm{p}}})_{\mathrm{F(S)}} \left\{(\gamma_{\mathrm{p}})_{\mathrm{F(S)}}(\tau_{\mathrm{off}}) - (\delta_{\mathrm{b}})_{\mathrm{F(S)}}\gamma_{\mathrm{p}}[n_{\mathrm{c,RO}}]\right\}, \tag{6.21}$$

and

$$(\dot{n_{\mathrm{p}}})_{\mathrm{F(S)}}(\tau_{\mathrm{off}}) = -(\zeta_{n_{\mathrm{p}}})_{\mathrm{F(S)}} \left\{(n_{\mathrm{p}})_{\mathrm{F(S)}}(\tau_{\mathrm{off}}) - (\delta_{\mathrm{b}})_{\mathrm{F(S)}}n_{\mathrm{p}}[n_{\mathrm{c,RO}}]\right\}. \tag{6.22}$$

where τ_{off} is the time from the end of the optical pulse, and $(\zeta_{\gamma_{\mathrm{p}}})_{\mathrm{F(S)}}$ and $(\zeta_{\gamma_{\mathrm{p}}})_{\mathrm{F(S)}}$ are the pulse-off relaxation rate constants for the damping factor and occupancy of the two different bath components, respectively.

The model parameters used to fit the specific measured data for the six-shield device (device B) presented in Fig. 6.6 are listed in Table 6.1. Similar bath dynamical parameters are found for all of the measured devices we have studied. Independent of the optical readout pulse power, the fraction of the bath which reacts quickly seems to be consistently close to a value of $(\delta_{\mathrm{b}})_F = 0.65$. The fast component of the bath turns on faster than we can resolve ($\gtrsim$ 50 MHz), while the slow component of the bath turns on with a rate constant of approximately $\theta_S/2\pi = 600$ kHz (for both damping factor and occupancy). The fast component of the bath turns off with an exponential rate constant of $(\zeta_{\gamma_{\mathrm{p}}})_F/2\pi = 150$ kHz for γ_{p} and $(\zeta_{n_{\mathrm{p}}})_F/2\pi = 70$ kHz for n_{p}. Even more slowly, the slow component of the bath turns off with a rate constant of $(\zeta_{\gamma_{\mathrm{p}}})_S/2\pi = 90$ kHz and $(\zeta_{n_{\mathrm{p}}})_S/2\pi = 24$ kHz for the two different bath factors.

Our ability to measure the bare damping rate of the acoustic breathing mode relies on the fact that the hot bath evaporates prior to the actual measurement of the free decay of the breathing mode. This means that the first $\sim 10\ \mu$s of the pulse-off state is dead time in which the dynamics of the breathing mode occupancy is still coupled to that of the hot bath. Crucial to the measurement of a ringdown curve using the red-detuned optical pulse as both a readout signal and an excitation source, is that after this dead time there remain a residual, elevated phonon occupancy of the breathing mode from which the mode can decay. This is clearly the case for the data measured in Fig. 6.6, and is a result of the fact that at this readout power the peak magnitude of γ_{p} (2π(85 kHz)) is still smaller than the fastest decay of the hot bath ($(\zeta_{\gamma_{\mathrm{p}}})_F/2\pi = 150$ kHz), so that the breathing mode occupancy cannot follow that of the fast dynamics of the hot bath. This non-adiabatic quenching leaves the breathing mode with an elevated occupancy after the dead time. At readout powers beyond $n_{\mathrm{c}} = 1000$ this stops being the case, hence our choice of readout pulse powers $n_{\mathrm{c}} \lesssim 600$ in the ringdown measurements.

A few observational comments are warranted. The fact that the hot bath should have faster pulse-on rate constants than pulse-off rate constants might be explained by the fact that there are likely a wide spectrum of phonons which are created by absorption of the optical pulse. This may lead to a hierarchy of phonon baths. Consider for instance a two bath scenario, consisting of a high and a low frequency phonon bath. The high frequency bath is assumed to be directly populated from optical absorption events, while the low frequency bath is predominantly responsible for coupling to the breathing mode of interest. In the high frequency phonon bath, phonons rapidly mix with each other due to the large density of states and mode occupancy. The high frequency phonon bath is also well thermalized to the external substrate through acoustic radiation. Phonons in the low frequency bath are fed from the phonon-phonon scattering processes in the high frequency phonon bath, and are less connected via radiation to the substrate. When the optical pulse is on, the high frequency bath is rapidly populated. The high frequency bath not only acts as a source of phonons for the low frequency bath, but through nonlinear phonon mixing also helps bring it into some quasi-equilibrium temperature. When the optical pulse is turned off, the high frequency bath rapidly decays away, leaving the low frequency bath of phonons to more slowly decay away due to the absence of the phonons in the high frequency bath to mix with. This scenario would also explain the difference in the decay of the low frequency bath γ_{p} damping rate, which depends on the phonon number density, to that of the effective occupancy n_{p}, which is set by the quasi-equilibrium temperature of the bath. The absence of the high frequency bath could greatly slow down the low frequency bath equilibriation rate, and thus the rate of change of the effective bath temperature, while the low frequency bath acoustic coupling to the external substrate will provide a constant decay channel for bath phonons and thus γ_{p}.

We should further note that the dynamical bath parameters reported in Table 6.1 are consistent for devices fabricated from low resistivity SOI. In the case of our high resistivity SOI samples, we have measured devices with a much slower post-read-pulse decay of the hot bath. Hot bath decay times as long as tens of milliseconds have been observed. Although requiring further study, we believe that this very slow decay dynamics of the optical-absorption-induced bath indicate that phonons are not the only parties involved in the optically-induced hot bath, but that the hot bath is likely also composed of much longer lifetime two-level system (TLS) defects. The high resistivity SOI seems to harbor much longer-lived TLS states, possibly due to the reduction of electronic relaxation pathways. Our two-phonon-bath scenario above may in fact be a two-bath scenario consisting of one phonon bath coupled to a longer lived TLS bath. Other evidence for this interpretation is the high values of measured γ_{p} which is more consistent with estimated TLS damping rates (damping due to 3-phonon scattering is shown to be too slow, at least for bath temperatures below 1 K, in sub-Section 5.3.1).

Table 6.1: **Dynamical model parameters of the optical-absorption-induced bath.** These parameters were used to fit the measured phonon occupancy shown in Fig. 6.6 during the entire pulse on period and during the transient initial millisecond after the pulse is turned off. The specific device measured was a six-shield device, device B in Table 4.1, fabricated from low resistivity SOI (ρ = 5-20 Ω-cm).

Parameter	Description	Value	Refs./Notes
$(\delta_{\mathrm{b}})_{\mathrm{F(S)}}$	fast (slow) fractional component of the optically-induced bath	0.65 (0.35)	from model fit
$(\theta_{n_{\mathrm{p}}})_{\mathrm{F(S)}}/2\pi$	n_{p} exponential relaxation rate with optical *pulse on*	$\gtrsim$ 50 MHz (600 kHz)	from model fit
$(\theta_{\gamma_{\mathrm{p}}})_{\mathrm{F(S)}}/2\pi$	γ_{p} exponential relaxation rate with optical *pulse on*	$\gtrsim$ 50 MHz (600 kHz)	from model fit
$(\zeta_{n_{\mathrm{p}}})_{\mathrm{F(S)}}/2\pi$	n_{p} exponential relaxation rate with optical *pulse off*	70 kHz (24 kHz)	from model fit
$(\zeta_{\gamma_{\mathrm{p}}})_{\mathrm{F(S)}}/2\pi$	γ_{p} exponential relaxation rate with optical *pulse off*	150 kHz (90 kHz)	from model fit
$n_{\mathrm{c,RO}}$	readout pulse amplitude	569 photons	
$\gamma_{\mathrm{OM}}/2\pi$	optomechanical back-action rate during *pulse on*	1.4 MHz	measured ind.
n_{p}	steady-state hot bath occupancy for $n_{\mathrm{c,RO}}$ intra-cavity photons	73 phonons	measured ind.
γ_{p}	steady-state hot bath damping rate for $n_{\mathrm{c,RO}}$ intra-cavity photons	85 kHz	measured ind.
τ_{off}	delay time between successive readout pulses	200 μs	
τ_{pulse}	readout pulse length	4 μs	
$n_{\mathrm{m}}^{\mathrm{f}}$	breathing mode occupancy at end (t = 4 μs) of optical readout pulse	4.2 phonons	measured
$n_{\mathrm{m}}^{\mathrm{i}}$	breathing mode occupancy in first measurement bin of readout pulse	13.6 phonons	measured
$\langle n\rangle[0]$	breathing mode occupancy referred back to t = 0 of optical readout pulse	27 phonons	from model fit

6.6 Quantum Cooperativity in Optomechanical System

The utility of cavity optomechanical systems to perform coherent quantum operations between the optical and mechanical degrees-of-freedom is ultimately predicated by their ability to achieve $\langle n \rangle < 1$ and large cooperativity $C \equiv \gamma_{\mathrm{OM}}/\gamma_{\mathrm{b}}$, where $\gamma_{\mathrm{b}} = \gamma_0 + \gamma_{\mathrm{p}}$ is the total coupling rate between the mechanical resonator and its thermal baths. In the example of coherent transfer of photons between optical and superconducting microwave resonators mediated by optomechanical systems [109, 110, 111, 112, 125], the relevant figure of merit is the effective quantum cooperativity $C_{\mathrm{eff}} \equiv C/n_{\mathrm{b}}$, where n_{b} is the effective bath occupancy defined such that $\gamma_{\mathrm{b}} n_{\mathrm{b}} = \gamma_0 n_0 + \gamma_{\mathrm{p}} n_{\mathrm{p}}$ [1]. C_{eff} must be larger than unity in order to achieve low-noise conversion between photons of different energies [102, 110].

Explicitly, the effective cooperativity is

$$C_{\mathrm{eff}} = \frac{\gamma_{\mathrm{OM}}}{\gamma_0(n_0 + 1) + \gamma_{\mathrm{p}}(n_{\mathrm{p}} + 1)}, \tag{6.23}$$

with the $+1$ terms in the denominator arising from spontaneous decay. With the measured absorption-heating bath occupancy and damping rates from previous sections, effective cooperativity can be calculated for the zero-shield and six-shield nanobeam devices, which are plotted in Figure 6.7.

It can be seen from the calculated C_{eff} that it increases together with C first versus n_{c} at low n_{c}, however, at relatively higher optical powers, C_{eff} starts to saturate. This is because $\gamma_{\mathrm{p}} n_{\mathrm{p}} \propto n_{\mathrm{c}}^1$, in the mean time, $\gamma_{\mathrm{OM}} \propto n_{\mathrm{c}}^1$. The quantum effective cooperativity saturates to $C_{\mathrm{eff}} = 0.21$ for six-shield device. In order to achieve $C_{\mathrm{eff}} > 1$ in the presence of continuous-wave pumping, one or more routes can be pursued to increase the ratio of $\gamma_{\mathrm{OM}}/(\gamma_{\mathrm{p}} n_{\mathrm{p}})$, thus C_{eff}.

1. γ_{OM} is directly proportional to the square of vacuum optomechanical coupling rate g_0^2, thus a further optimized design of OMC cavity with higher g_0.

2. γ_{OM} is inversely proportional to optical damping rate $\kappa = \kappa_{\mathrm{i}} + \kappa_{\mathrm{e}}$, thus the loaded optical quality factor can be further increased in order to increase C_{eff}. κ_{e} can be decreased by the optical coupling waveguide design, however, smaller κ_{e} affects data collection efficiency in measurements.

3. Further improvements to the nanofabrication processes of such OMC devices may enable higher intrinsic optical Q-factors κ_{i}.

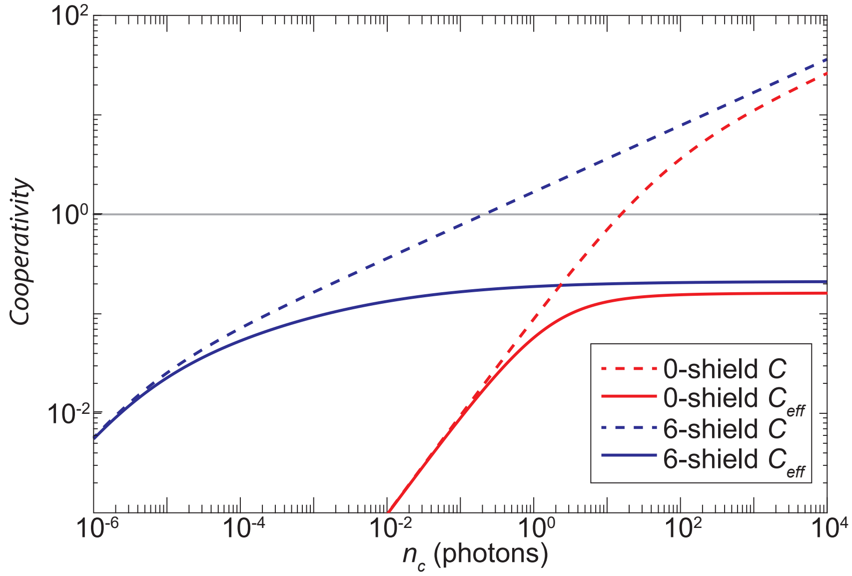

Figure 6.7: **Effective cooperativity in 1D nanobeam OMCs at low temperature.** Calculated bare optomechanical cooperativity C (dotted lines) and quantum effective cooperativity C_{eff} (solid lines) for a zero-shield (red lines, $\gamma_0/2\pi = 14.1$ kHz) and a six-shield (blue lines, $\gamma_0/2\pi = 0.21$ Hz) device. Horizontal gray lines indicate cooperativity of unity. $C, C_{\text{eff}} = 1$.

4. C_{eff} is inversely propotional to $\gamma_{\text{p}} n_{\text{p}}$ at relatively high optical power, decreasing amplitude or scaling rate of $\gamma_{\text{p}} n_{\text{p}}$ is beneficial to C_{eff}.

5. Hot photon bath is generated by optical absorption at the surface of the silicon, thus further improvements to the silicon surface passivation and cleaning potionally decrease hot bath occupancy and damping rate (n_{p} and γ_{p}).

6. Accoding to the Landau-Rumer scattering processes described in Section 6.2, the phonon bath is populated via phonon-assisted relaxation of the surface electronic states, which yields a scaling of the effective bath temperature with the material anharmonicity $A(\omega; \omega_m)$. The bath temperature can potentially be decreased by choosing other substrate materials with lower anharmonicity.

Among all the 6 potential improvements, Quasi-2D OMC devices are clearly a good choice. Quasi-2D planar photonic crystal devices have been shown to exhibit optical Q-factors exceeding 9×10^6 [126]. Photonic crystals in one more dimension instead of index guiding also potentially further confine the optical mode volume thus increases vacuum optomechanical coupling rate g_0. Another major benefit of quasi-2D OMC designs is the increased thermal conductance as mentioned in previous sections and will be also discussed in following sections, which potentially reduces the hot photon bath.

6.7 Measurement of Optical-Absorption-Induced Bath Occupancy in Quasi-2D OMC

With the same proposed microscopic model for the heating and damping illustrated in Fig. 6.1, we performed a series of measurements studying the magnitude and scaling properties of the hot phonon bath occupancy n_p and excess damping rate γ_p in the quasi-2D OMC. In Fig. 6.8, we explore the scaling of n_p versus intracavity photon number n_c. Similarly, to the 1D nanobeam case, a continuous-wave laser pump was tuned to the cavity resonance ($\Delta = 0$), and the sideband-scattered photons at either of the mechanical sidebands were detected at a rate $\Gamma = \eta(\frac{\kappa}{2\omega_\mathrm{m}})^2\gamma_\mathrm{OM}\langle n\rangle$ with the sideband filters aligned, where η is the total optical detection efficiency, κ is the total optical decay rate, and γ_OM is the optomechanical damping rate. The observed count rate is used to extract an equivalent measured mode occupancy ($\langle n\rangle$) as shown in Fig. 6.8. The right-hand axis of Fig. 6.8 gives the effective bath temperature T_p corresponding to the measured occupancy. This measured occupancy is a close approximation to the bath occupancy n_p at power levels where the equivalent bath temperature T_p is much greater than the base bath temperature to which the mode thermalizes, $T_\mathrm{b} = 63$ mK (see Section 3.3).

Unlike in 1D nanobeam OMC, where the coupling waveguide is designed to be evanescently coupled to OMC cavity, the coupling waveguide in quasi-2D devices is designed to be physically connected to one end of the OMC cavity. There are two ways photons may scatter energy into the phonon bath: absorption in the OMC cavity, and absorption outside the OMC cavity in the coupling waveguide and 2D line-defect waveguide. Therefore, n_p can be expressed versus both intracavity photon number n_c and total laser power coupled into coupling waveguide P_in. Intracavity photons n_c have a much larger energetic contribution per photon compared to photons in the waveguide. This is due to the longer photon lifetime within the cavity giving a larger absorption cross-section, and the close proximity of the absorption event near the mechanical resonator.

Via finite-element simulations, this work shows that a ‘weak cavity‘ is formed between the coupling waveguide and the OMC (see Section. 6.11), which was probably the dominant region where cavity photons were absorbed outside of the

OMC cavity. Here the term effective waveguide phonons n_{wg} ($n_{\mathrm{wg}} \propto P_{\mathrm{in}}$) is used to represent the contribution from phonons in the weak cavity, and assumes that the functional form of n_{p} versus n_{c} and n_{wg} are the same, although the heating sources are distinctly independent. The relationship is given by,

$$\begin{aligned} n_{\mathrm{p}}(n_{\mathrm{c}}, P_{\mathrm{in}}) &= n_{\mathrm{p}}(n_{\mathrm{c}} + n_{\mathrm{wg}}) \\ &= n_{\mathrm{p}}(n_{\mathrm{c}} + \beta P_{\mathrm{in}}) \end{aligned} \tag{6.24}$$

where β is a constant that depends on the ratio of n_{c} and n_{wg}, and varies with laser detuning Δ. In order to find the occupancy of the 'hot' bath, the continuous-wave laser pump was tuned to cavity resonance ($\Delta = 0$) where a large portion of incident photons couple into the cavity as intra-cavity photons n_{c}; hence, in this case, the contribution from n_{wg} is ignored. Fitted n_{p} versus n_{c} is plotted in Fig. 6.8, from which we found that n_{p} approximately followed a power-law scaling of $n_{\mathrm{p}} \propto n_{\mathrm{c}}^{0.3}$. This is consistent with the expectation that, as detailed in Section 6.2 and [56], the finite dimensions of the thin-film OMC modify the phonon density of states of the phonon bath at low temperature, giving rise to a quasi-discrete spectrum of bath modes well-approximated by a 2D density of states. Values of n_{p} extracted from 1D OMC devices in Section 6.4 and [56] are also shown as a dashed line in Fig. 6.8. Quasi-2D OMC devices show an improvement by a factor of ~ 7 compared with 1D structures with a same number of intracavity photons n_{c} in both measurement date and numerical simulations (see Section 6.10).

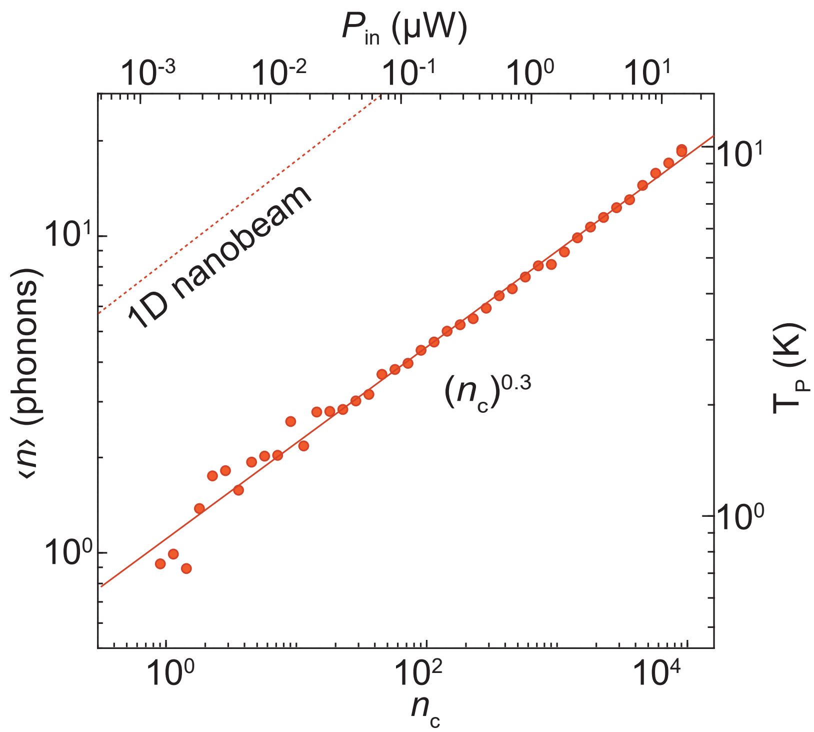

Figure 6.8: **Measured steady-state optical-absorption-induced bath occupancy of quasi-2D OMC.** Plot of n_p versus n_c for quasi-2D eight-shield device. The solid line is a fit to the data giving $n_\mathrm{p} = (1.1) \times n_\mathrm{c}^{0.3}$. Dashed line indicates n_p versus n_c for a 1D nanobeam device for comparison.

6.8 Measurement of Optical-Absorption-Induced Damping in Quasi-2D OMC

A more complete characterization of the 'hot' bath requires a measurement of the bath-induced damping rate γ_p. Different from the measuement methods used in the 1D nanobeam case, to measure this, a spectral measurement of the mechanical response was made at sufficiently large power levels n_c such that the total mechanical linewidth γ is dominated by γ_p rather than by intrinsic frequency jitter or damping due to the DR bath. The damping due to optomechanical back-action γ_OM is minimized by choosing a resonant probe ($\Delta = 0$) such that the total mechanical linewidth extracted from mechanical NPSD in a balanced heterodyne measurement is equal to the sum of the intrinsic linewidth Γ_ϕ and the optical absorption bath-induced damping γ_p. Note that the intrinsic linewidth Γ_ϕ includes spectral diffusion (dephasing) of the mechanical mode, and is distinct from the intrinsic energy decay rate γ_0 (dissipation). Tuning to resonance not only eliminated the optomechanical back-action of the mechanics, but also allowed for efficient loading of the optical cavity. For the device parameters here, an input power of 31 μW generates an average intracavity photon population of about $n_c \sim 1 \times 10^4$. Measured total mechanical linewidth γ is plotted in Fig. 6.9. Although both γ and n_p are assumed to depend on the total intracavity photon number $(n_c + n_{wg})$, a difference in the power laws can be seen upon fitting.

$$\begin{aligned} \Gamma(n_c, P_{in}) &= \Gamma(n_c + n_{wg}) \\ &= \Gamma(n_c + \beta P_{in}) \end{aligned} \tag{6.25}$$

Similar, to n_p fitting, n_{wg} is ignored in this measurement since the laser pump was detuned to cavity resonance where the ratio of P_{in} to n_c is minimized. At lower powers $n_c \sim 10$, the linewidth is expected to be dominated by intrinsic damping and dephasing (combined to yield Γ_ϕ) rather than bath-induced damping, such that γ saturates to Γ_ϕ at lower powers.

The measured and fitted linewidth γ are plotted as well as calculated γ_p against n_c (and P_{in}) in Fig. 6.9. We extract that the bath-induced damping rate γ_p approximately follows a power-law scaling of $\gamma_p \propto n_c^{0.61}$ at lower n_c (P_{in}) and $\gamma_p \propto n_c^{0.29}$ at higher n_c (P_{in}). For lower laser power, this is approximately the same scaling predicted in Section 6.2 and in reference [56] for a 2D density of states model. As going to higher laser power, we can see from the calibration of the temperature found in Fig. 6.8 that the rate goes from being $\propto T^2$ to something $\propto T^1$.

Determining the exact mechanism of the γ_p slow down versus bath temperature (or more directly high n_c and P_{in}) is outside the scope of this article. There are several possible mechanisms for this slow down, from changes in the heat-carrying phonon velocities related to phonon-frequency-dependent scattering in the nanostructure silicon film [127, 128] to thermalization rate of phonons in the hot bath created by optical absorption. Also, we assumed that Landau-Rumar scattering was the cause of coherent energy loss at lower temperatures, which gives a power law $\sim n_c^{2/3}$; however, damping may be dominated by Akhiezer-type dissipation processes above 4K [129].

One possible reason for this crossover relates to the thermal conductance of the nanostructured silicon film, and the transition from a diffusive phonon propagation regime to a ballistic one at higher bath temperature where shorter wavelength phonons predominantly carry the heat and are not as prone to scattering from the patterned surfaces. Phonons relevant to the Landau-Rumar scattering between 20GHz and 100GHz have a wavelength long compared to the small connections in the phononic crystals ($\sim 100nm$), and therefore have a high probability of scattering [122, 128, 130]. However, phonons above 100GHz will not scatter off the 'abrupt phonon junctions' in the phononic crystal, and thus have unity transmission. As temperature increases past 4K, the probability for the higher modes to backscatter becomes negligible, with these modes ultimately determining the thermal conductance. Therefore, we should see a 'slowing down' of the thermal conductance as temperature increases past this threshold. A second possible reason for the crossover is that the assumption of Landau-Rumer scattering is no longer valid. Landau-Rumer scattering is true when the time constant of the phonons within the hot bath are long compared to the inverse frequency of the mechancial mode, $\tau_p\omega_{\mathrm{m}} > 1$, thus ensuring that all phonons other than the damped phonon are within thermal equilibrium. If this condition is not true, then the device operates within the 'Akhiezer regime' [129, 131], where in bulk crystals this gives a damping that goes from $\propto T^4$ down to $\propto T$. Future studies focusing on changes to the critical dimension of the phononic crystal will help elucidate the microscopic origin of this effect. Also, by introducing a thermometer at an appreciable distance from the waveguide and cavity, we may determine the bulk temperature of the hot bath, and not just the part that is relevant for the Landau-Rumer scattering.

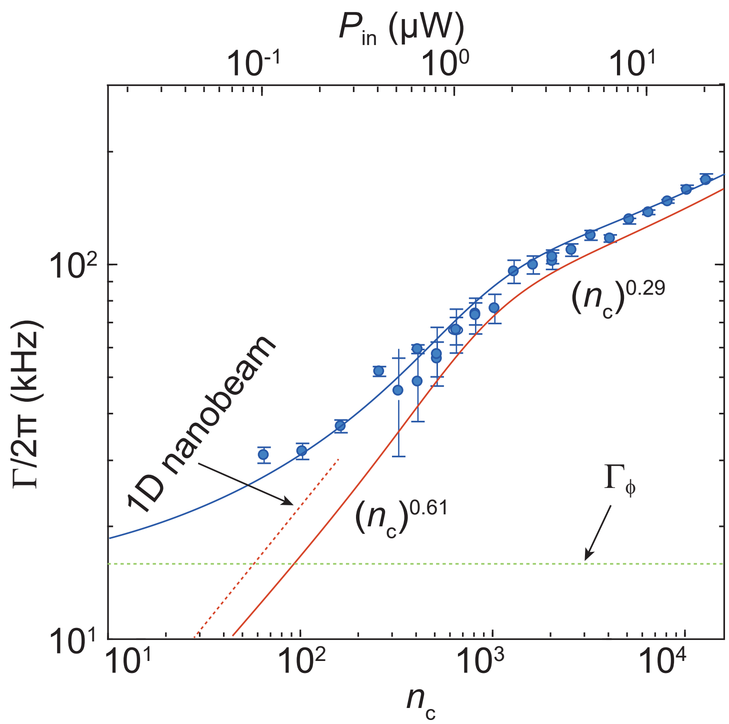

Figure 6.9: **Steady-state total mechanical linewidth of quasi-2D OMC** plot of total mechanical linewidth γ (blue dots) versus n_c for eight-shield device. The blue solid line is a power-law fit to the data: $\Gamma/2\pi = \Gamma_\phi/2\pi + \gamma_p/2\pi = 14.54$ kHz + (1.1 kHz) $\times n_c^{0.61}$ for low n_c regime, $\Gamma/2\pi = 23.91$ kHz + (9.01 kHz) $\times n_c^{0.29}$ for high n_c regime. Red solid line is calculated γ_p, dashed line indicates γ_p versus n_c for a 1D nanobeam device for comparison.

6.9 Quantum Cooperativity in Quasi-2D OMC

The utility of cavity optomechanical systems to perform coherent quantum operations between the optical and mechanical degrees-of-freedom is ultimately predicated by their ability to achieve $\langle n \rangle < 1$ and large cooperativity $C \equiv \gamma_{OM}/\gamma_b$, where $\gamma_b = \gamma_0 + \gamma_p$ is the total coupling rate between the mechanical resonator and its thermal baths. In the coherent transfer of information between quantum fields, the relevant figure-of-merit is the effective quantum cooperativity $C_{eff} \equiv C/n_b$, where n_b is the total effective bath occupancy of both fields. For example, the bi-directional coherent transfer of photons between optical and superconducting microwave circuits mediated by optomechanical systems [102, 110] only become possible if C_{eff} is larger than unity, and where $\gamma_b n_b = \gamma_0 n_0 + \gamma_p n_p$ [1].

A direct measurement of the cooperativity can be made by observing the cooled mechanical occupancy

$$\langle n \rangle = \frac{\gamma_{\mathrm{p}} n_{\mathrm{p}} + \gamma_0 n_0}{\gamma_0 + \gamma_{\mathrm{OM}} + \gamma_{\mathrm{p}}}, \tag{6.26}$$

in the presence of a continuous-wave pump detuned to the red sideband ($\Delta = \omega_{\mathrm{m}}$). Fig. 6.10 shows the results of steady-state mechanical occupancy measurements (blue dots) versus n_{c} and P_{in} in the presence of red-detuned driving. We also plot the predicted steady-state mechanical occupancy using the measurements of γ_{p} and n_{p} from our device with different β values. The red line is prediction of the occupancy for $\beta = 0$.

When measuring steady-state mechanical occupancy, the heating due to optical absorption was much more pronounced than in previous measurements. For the steady state occupancy, the laser pump was detuned to the red sideband ($\Delta = \omega_{\mathrm{m}}$) instead of on resonance ($\Delta = 0$); thus, much higher input laser power was needed in order to generate the same amount of intracavity photons. In Fig. 6.10a, we allow β to be a free parameter to fit $\langle n \rangle$, and plot $\beta = 15$ (blue solid). At lower power, $\gamma_{\mathrm{p}} n_{\mathrm{p}} \propto n_{\mathrm{c}}^{0.91}$ ($\propto P_{\mathrm{in}}^{0.91}$) and $\gamma_{\mathrm{OM}} \propto n_{\mathrm{c}}^{1}$, thus $\langle n \rangle$ is almost flat versus n_{c} and P_{in}. However, fortunately the scaling of the damping rate changes at higher power as mentioned in the previous section, and we gain an advantage by increasing laser power.

We also plot the effective quantum cooperativity Fig. 6.10b using measured hot phonon bath occupancy n_{p} and excess damping rate γ_{p} for both $\beta = 0$ (red) and $\beta = 15$ (blue).

$$C_{\mathrm{eff}} = \frac{\gamma_{\mathrm{OM}}}{\gamma_0(n_0 + 1) + \gamma_{\mathrm{p}}(n_{\mathrm{p}} + 1)}, \tag{6.27}$$

with the +1 terms in the denominator arising from spontaneous decay. These plots indicate that both a mechanical occupancy lower than unity and an effective quantum cooperativity greater than unity are realized under steady-state optical pumping in quasi-2D OMC devices (eight-shield device with $Q_{\mathrm{opt}} = 1.63 \times 10^5$) in high power regime ($P_{\mathrm{in}} > 400\mu W$, $n_{\mathrm{c}} > 900$) even in the presence of extra heating from pump photons absorbed in the weak cavity built in the coupling waveguide.

Looking forward, $\langle n \rangle$ can be further reduced and C_{eff} can be further increased. One potential way to reduce optical-absorption hot phonon bath is to thermally decouple the input coupling waveguide from OMC cavity. By eliminating the parasitic heating from the n_{wg}, we can achieve a C_{eff}, and $\langle n \rangle$ as indicated by the red lines in Fig. 6.10a and b. The back-action damping rate per photon can also benefit from a higher loaded optical quality factor, quasi-2D planar photonic crystal devices have been shown to exhibit intrinsic optical Q-factors exceeding 9 million [126]. In Fig. 6.11, with the measured values of γ_0, g_0, n_p and γ_p, we estimate how much $\langle n \rangle$ and C_eff can be improved at different laser powers (n_c) and Q_opt assuming optical coupling can be designed such that extra heating due to n_wg can be eliminated (For instance, using side-coupling instead of butt-coupling, such that coupling waveguide and OMC cavity are thermally disconnected). Contours of selected C_eff values are also plotted in the same figure. We find with already achieved Q_opt values (zero-shield device with $Q_\mathrm{opt} = 3.90 \times 10^5$), steady-state $\langle n \rangle$ can be maintained under 0.1 and C_eff approaches 5 even at single photon pump levels. If Q_opt can be optimized to 10^6, $\langle n \rangle < 0.02$ and C_eff as large as 44 can be achieved simultaneously at steady-state.

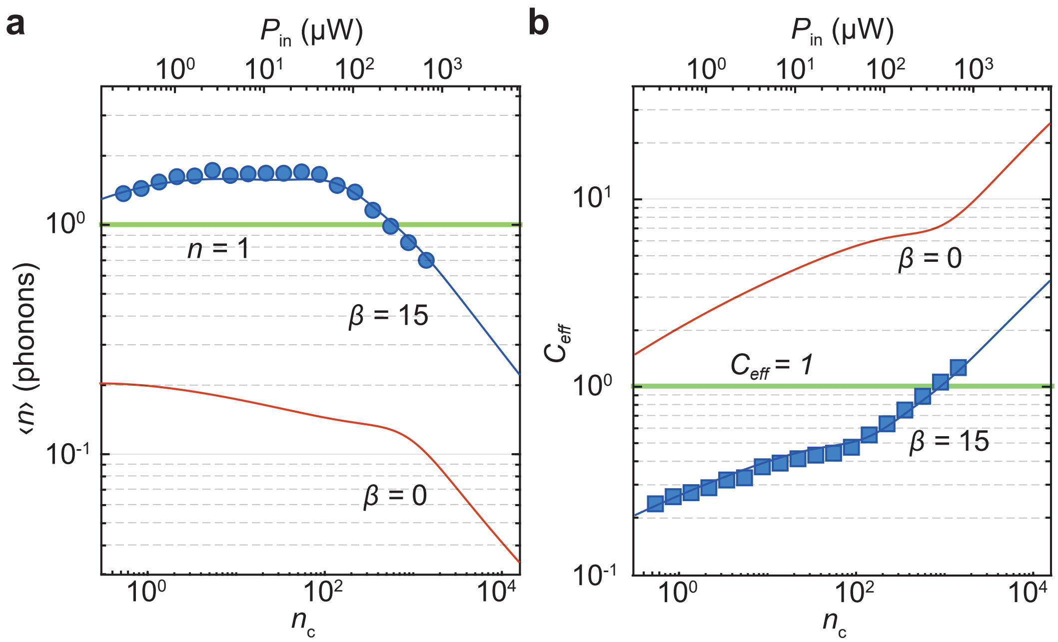

Figure 6.10: **Phonon occupancy and effective quantum cooperativity of quasi-2D OMC. a**, Plot of measured (blue circles) average phonon number, $\langle n \rangle$, in mechanical mode at $\omega_m/2\pi = 10.02$ GHz, versus cooling drive-laser power (in units of intracavity photons, n_c, and optical power coupled into coupling waveguide, P_{in}). Blue solid line is the estimated phonon occupancy from power-law fits of γ_p and n_p, considering optical heating from both n_c and P_{in} with $\beta = 15$, red solid line only considers optical heating from n_c. **b** Plot of quantum cooperativity C_{eff} versus n_c and P_{in} for eight-shield device. The solid blue line is calculated from power-law fits of γ_p and n_p, considering optical heating from both n_c and P_{in} with $\beta = 15$, red solid line only considers optical heating from n_c. The solid blue rectangles are extracted from the measured phonon number in **a**. The solid line is a fit to the data giving $n_p = (1.1) \times n_c^{0.3}$. Dashed line indicates n_p versus n_c for a 1D nanobeam device for comparison.

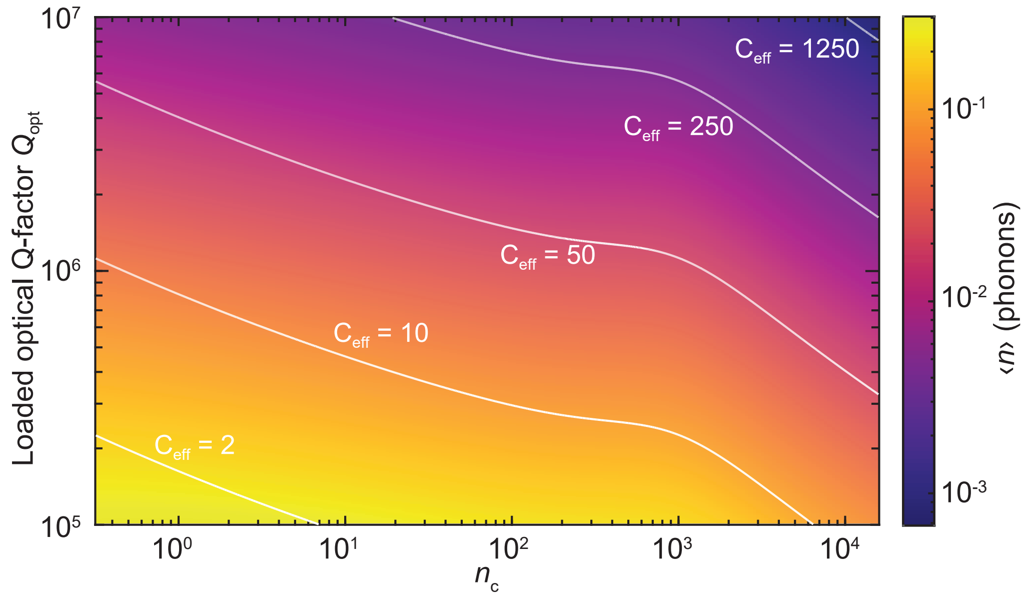

Figure 6.11: **Estimated phonon occupancy and effective quantum cooperativity.** Estimated steady state phonon occupancy $\langle n \rangle$ versus number of intracavity photons and loaded optical Q-factor of quasi-2D OMC devices. The white contours delineate the regions of effective cooperativity C_{eff}.

6.10 Increased Thermal Conductance in Two-Dimensional Cavity

As pointed out in previous sections, quasi-2D OMC devices were measured to have a lower occupancy (n_{p}) within the local hot phonon bath compared to 1D nanobeam OMC devices [56]. This high occupation is due to optical absorption which ultimately heats the high-Q cavity mechanical mode. In the context of this work, the local hot phonon bath at temperature T_{p} is thought to be generated as absorption of photons excited electronic states at $\sim$ eV energy undergo phonon-assisted relaxation processes, emitting high-frequency phonons, which subsequently decay by a cascade of nonlinear multi-phonon processes into a bath of GHz phonons. For the temperature range considered in this work ($T \leq 10$ K), with the acoustic mode of interest at microwave frequencies, the damping and heating of the acoustic mode of interest can be described by the Landau-Rumer theory [68, 122].

Here, we utilize FEM simulations to model the impact of geometry on the thermal conductance of different OMC cavities at millikelvin temperatures. Specifically our approach is as follows. We take previous measurements of a 1D nanobeam OMC cavity and compare it to the results of simulations of a similar 1D OMC cavity geometry with variable material properties. We then find what scaling of the material properties allows us to match experiment to simulation for the 1D OMC cavity. Using these same scaled values of the material properties we then perform simulations of the quasi-2D OMC cavity. Closing the loop, we find that the simulated values of the hot bath temperature are in correspondence with the measured values for the quasi-2D cavity. This would indicate that a simple geometric difference in the connectivity of the 1D and 2D cavities to the external chip bath can explain the lower measured hot bath occupancy for the quasi-2D OMC cavity, validating our original design concept.

Under steady state conditions, the power flow from the hot bath into the DR bath, P_{thm}, is equal to the power flow into the hot bath due to optical absorption. Here, we have implicitly assumed no other sources of heating other than optical absorption and that the hot bath loses energy via coupling to phonons which radiate into the chip bath at the periphery of the device. Also assuming the optical absorption process is linear, we find that the power flow into the hot bath is a fraction η_{abs} of the total input optical power, such that $P_{\text{thm}} = \eta_{\text{abs}} P_{\text{in}} \propto n_{\text{c}}$ (we ignore n_{wg} here for simplicity).

For the temperature range considered in this work (where phonon transport is ballistic), the lattice thermal conductivity scales as a power law of the phonon bath temperature [123, 124]. We thus define the thermal conductance from the center of OMC cavity to the DR bath of both the 1D ($C_{\text{th,1D}}$) and quasi-2D geometries ($C_{\text{th,2D}}$) such that $C_{\text{th}} \propto (T_{\text{p}})^{\alpha}$. The exponent α is equal to the effective number of spatial dimensions d of the geometry. The hot bath is assumed to thermalize at an effective temperature T_{p} and to radiate energy (lattice phonons) into the periphery of the cavity as a black body such that the power lost out of the hot bath goes as $(T_{\text{p}})^{\alpha+1}$. We can thus write a simple model for the thermal conductance between the hot bath and the periphery of the cavity (T_0),

$$P_{\text{thm}} = C_{\text{th}} \Delta T \approx C_{\text{th}} T_{\text{p}}, \tag{6.28}$$

where $\Delta T = T_{\text{p}} - T_0$ and in the range of measured n_{p} ($n_{\text{p}} > 0.5, T_{\text{p}} > 400$ mK) $\Delta T \approx T_{\text{p}}$ since $T_0 \ll T_{\text{p}}$. We define C_{th} as $C_{\text{th}} = \epsilon (T_{\text{p}})^{\alpha}$, where ϵ depends on the geometry of the cavity and its material properties, which allows us to write,

$$P_{\text{thm}} = \epsilon T_{\text{p}}^{\alpha+1} = \eta_{\text{abs}} P_{\text{in}} \propto n_{\text{c}}. \tag{6.29}$$

The power law exponent α in the thermal conductance model is estimated to be $\alpha_0 \approx 2.3$ from the measured data (see Supplementary Figure 6.12). This is consistent with a Si slab of thickness $t = 220$ nm that has an approximately 2D phonon density of states for acoustic modes of frequency in the vicinity of the upper band-edge of the phononic bandgap of the quasi-2D snowflake structure ($\omega/2\pi \gtrsim 10$ GHz).

Assuming a thermal conductivity for the Si slab which is proportional to $(T_{\mathrm{p}})^{\alpha_0}$, FEM simulations were performed on both the 1D nanobeam and the quasi-2D snowflake OMC cavity geometries. As a thermal excitation source we placed a heating source in the center of both OMC cavities with size corresponding to that of the optical mode volume of the cavity mode. The average temperatures within the optical mode volume ($T_{\mathrm{p},(1,2)\mathrm{D}}$) was then calculated versus intra-cavity photons (n_{c}) for the 1D nanobeam cavity. We adjusted the material properties (thermal conductivity and absorption coefficient) in order to match the simulated curve to the measured data of the 1D nanobeam cavity from Ref. [56]. Finally, we used these adjusted material properties to simulate the quasi-2D cavity. All measured and simulated curves are plotted in Fig. 6.12a. We also plot the temperature profile of the 1D and quasi-2D OMC cavities at $n_{\mathrm{c}} = 100$ in Figs. 6.13a and 6.13b, respectively.

By comparing the simulated curves in Supplementary Figure 6.12, we estimate that the thermal conductance of the quasi-2D and 1D structure has a ratio of $\epsilon_{2\mathrm{D}}/\epsilon_{1\mathrm{D}} \approx 42$. For the same optical pump power applied to the 1D and quasi-2D OMC cavities we have that $n_{\mathrm{c},1\mathrm{D}} = n_{\mathrm{c},2\mathrm{D}}$ and $P_{\mathrm{th},1\mathrm{D}} = P_{\mathrm{th},2\mathrm{D}}$. This yields the relation between thermal conductance and acoustic mode occupancy for the two cavity geometries,

$$\epsilon_{1\mathrm{D}} \left(\frac{\hbar \omega_{\mathrm{m},1\mathrm{D}} n_{\mathrm{p},1\mathrm{D}}}{k_B} \right)^{\alpha_0+1} = \epsilon_{2\mathrm{D}} \left(\frac{\hbar \omega_{\mathrm{m},2\mathrm{D}} n_{\mathrm{p},2\mathrm{D}}}{k_B} \right)^{\alpha_0+1}, \tag{6.30}$$

where we have assumed $n_{\mathrm{p}} \approx k_B T_{\mathrm{p}}/\hbar\omega_{\mathrm{m}}$ in rewriting the bath temperatures in each cavity in terms of the bath occupancy at the acoustic cavity mode frequency. Considering that the acoustic mode of the quasi-2D OMC is at frequency $\omega_{\mathrm{m},2\mathrm{D}}/2\pi \approx 10.27$ GHz while that of the 1D resonator is at half this frequency at $\omega_{\mathrm{m},1\mathrm{D}}/2\pi \approx 5$ GHz, we can write for the ratio of the effective bath occupancies in the two cavities,

$$\frac{n_{\mathrm{p},1\mathrm{D}}}{n_{\mathrm{p},2\mathrm{D}}} \approx 2 \left(\frac{\epsilon_{2\mathrm{D}}}{\epsilon_{1\mathrm{D}}} \right)^{1/(\alpha_0+1)} = 6.2. \tag{6.31}$$

This simulated ratio is in good agreement with the measured ratio of the phonon bath occupancy of the 1D nanobeam OMC cavity in Ref. [56] and the quasi-2D

OMC cavity of this work, $n_{p,1D}/n_{p,2D} = 7.94/1.1 \approx 7.2$.

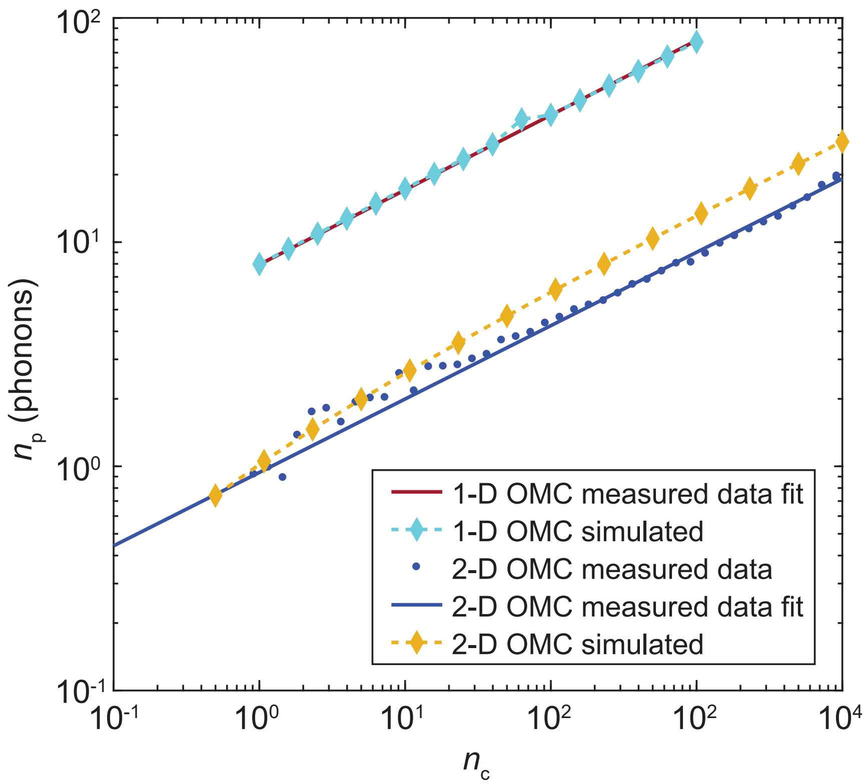

Figure 6.12: **Simulated and measured hot phonon bath occupancy** FEM simulated, measured and fitted n_p of both 1D nanobeam OMC cavity and quasi-2D OMC cavity versus number of intracavity photons n_c. Dashed lines are simulated data and solid lines are fitted curves to measured data. To obtain the material properties used in the simulation, we fit 1D nanobeam measurement data to a phenomenological thermal conductance model described in the text. Same material properties were used in the quasi-2D geometry to generate the simulated curve for the quasi-2D OMC.

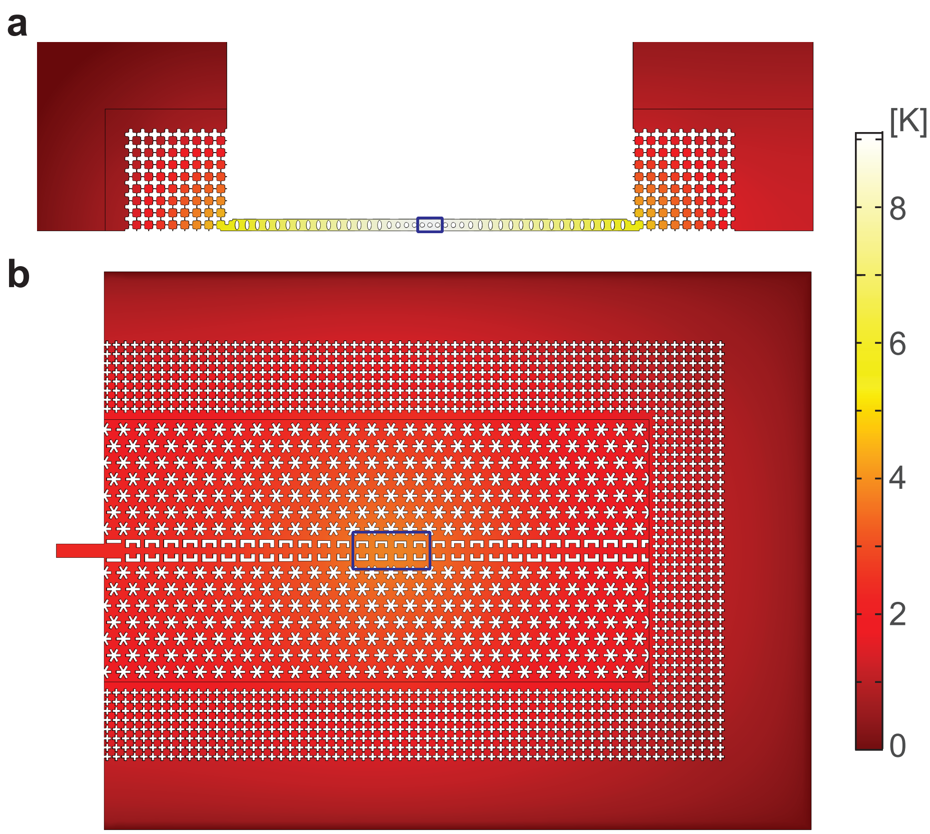

Figure 6.13: **Simulated temperature profile of OMC.** Temperature profile of 1D nanobeam OMC and quasi-2D OMC for n_c = 100 are also plotted in **b** and **c**, respectively. The area indicated by blue boxes in the center of both OMC cavities are the heat source used in FEM simulations, where the sizes the boxes are on the order of optical volume of cavity mode, and total heating power within the boxes volume is P_thm. Size of **a** and **b** are not to scale.

6.11 Modeling Of Extra Heating Contributed by Weak Cavity Formed in Coupling Waveguide

In order to investigate the source of extra optical-absorption heating in these quasi-2D OMC devices, we performed optical FEM simulations on the full device, including the OMC cavity, 1D coupling waveguide and 2D line-defect waveguide. The coupling waveguide in quasi-2D devices was designed to be physically connected to one end of the OMC cavity, instead of evanescently coupled to the OMC cavity as in 1D nanobeam OMC devices [56, 132]. Due to the weak reflectivity of the air-waveguide interface, a ‘weak cavity’ was formed in the waveguides. Thus, there are two major areas of optical absorption found to be contributing to the hot phonon bath: intracavity photons n_c being coupled into OMC cavity and photons being coupled into the weak cavity. The occupation of the bath n_p can depend on both intracavity photon number n_c and total input laser power P_in. Intracavity photons n_c have a much larger energetic contribution per photon compared to photons in the waveguide. This is due to the longer photon lifetime within the cavity giving a larger absorption cross-section, and the close proximity of the absorption event near the mechanical resonator. Here we use the term effective waveguide phonons n_wg ($n_\mathrm{wg} \propto P_\mathrm{in}$) to represent the contribution from photons in the weak cavity.

Simulations were performed using a geometry which was tuned to approximately the same loaded (intrinsic) optical linewidth as the eight-shield device being used for optical absorption bath characterization $(\kappa,\, \kappa_\mathrm{i}) = 2\pi(1.187\ \mathrm{GHz},\, 1.006\ \mathrm{GHz})$. In the case of $\Delta = 0$ GHz as shown in Fig. 6.14a, a large portion of the photons that coupled into the coupling waveguides were eventually coupled into OMC cavity, with the energy of electromagnetic field in the OMC cavity one order-of-magnitude higher than the energy in the weak cavity ($\beta \approx 0$, $n_\mathrm{wg} \approx 0$). However, in the case of $\Delta = 10$ GHz as shown in Fig. 6.14b, a much smaller portion of photons that coupled into coupling waveguides can be eventually coupled into OMC cavity due to the large detuning (optical cavity linewidth $\kappa = 1.187$ GHz), with the energy of electromagnetic field in the OMC cavity only a few percent of the energy in the weak cavity ($\beta \approx 15$). The dominant source of optical absorption is thought to be surface defect states [30, 31], and thus proportional to the energy of the electrical field. Since the nature of parasitic optical absorption in the OMC cavity and weak cavity is the same, the functional form of n_p versus n_c and n_wg were assumed to be the same, even though the heating sources are distinctly independent.

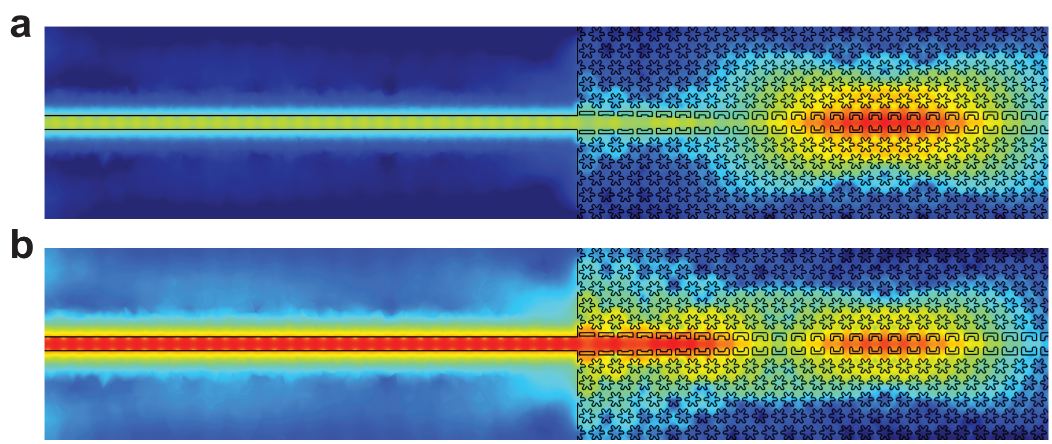

Figure 6.14: **FEM simulated time averaged optical field energy density of quasi-2D OMC cavity with coupling waveguide.** Optical field energy density for **a**, $\Delta = 0$ GHz and **b**, $\Delta = 10$ GHz. Both plots are plotted in logarithm scale and normalized to maximum field density in each simulation.

6.12 Mode Thermalization Measurements

The mode of interest in quasi-2D OMC thermalizes to a base bath temperature T_{b}, which is related to the applied DR temperature T_{f} through the thermal conductance C_{thm} of the structure, as described in section 6.10. This yielded an effective temperature offset between the DR temperature and the bath temperature. To measure this base bath temperature, we used a low-power ($n_{\mathrm{c}} = 9.9$) red-detuned pulsed probe and a device with relatively high mechanical damping $\gamma_0 = 21.8$ kHz (zero-shield device, $Q_{\mathrm{m}} = 4.69 \times 10^5$), so that data integration time was minimized. With relatively high mechanical damping, the mechanical mode quickly thermalized to its base temperature between subsequent incident optical pulses, so that we could use a rapid measurement repetition rate $1/\tau_{\mathrm{per}}$ ($\tau_{\mathrm{per}} = \tau_{\mathrm{pulse}} + \tau_{\mathrm{off}} \gg \gamma_0^{-1}$). The initial mode occupancy during the pulse then approximately corresponded to base bath occupancy n_0. However, after the first several time bins of the pulse when optical absorption starts to heat up the structure, the mechanical mode was heated such that the initial observed occupancy exceeds n_0. We therefore extracted n_0 by fitting the pulse on-state occupancy data to the full dynamical heating and damping model [56], and extrapolated the fit back to the start of pulse to estimate the true bath occupancy n_0.

A fit of bath temperature of quasi-2D OMC is shown in Figure 3.4 in Chapter 3, which yields $T_b = 63$ mK, corresponding to a base mode occupation of $n_0 = 4\times10^{-4}$. Calculated curves for $T_b = 11$ mK (red), 31 mK (yellow), 95 mK (green), 129 mK (cyan) are also plotted for reference.

Chapter 7

APPLICATIONS OF OPTOMECHANICAL CRYSTALS AND ULTRA-HIGH-QUALITY MECHANICAL RESONATORS

By utilizing the advanced methods of nanofabrication and cavity optomechanics, optically-coupled high-frequency mechanical resonators with ultra high mechanical Q, low thermal noise, deep quantum ground state mechanical thermometry and high effective quantum cooperativity has provided a new toolkit to explore quantum acoustodynamics in solid-state materials. It also shows the possibility of creating a hybrid quantum architecture consisting of acoustic and superconducting quantum circuits [77, 78], where the small scale, reduced cross-talk, and ultralong coherence time of quantum acoustic devices may provide significant improvements in connectivity and performance of current quantum hardware. These compact nanomechanical resonators can be viewed as promising candidates to replace the sizable electric microwave cavities. They can serve as a compact high-quality bosonic platform for storing quantum resources and performing ultra-high fidelity in-memory two-qubit gates [133, 134, 135]. They can also be used as a nanomechanical interface between optical photons and microwave electrical signals if combined with piezoelectric material, coherent signal transfer between microwave and optical fields can be achieved by parametric electro-optical coupling using a localized phonon mode.

In this chapter, several applications of optomechanical crystals in hybrid quantum system consisting of acoustic and superconducting quantum circuits, and currently being pursued in Painter's research group are introduced.

7.1 Compact High-Coherence Phonon Quantum Memory for Superconducting Transmon Qubit

Superconducting Josephson junction qubits use microwave signals to control quantum state, and have been widely used in quantum information processing [136, 137, 138, 139, 140, 141]. The transmon qubit has been prevailing among different implementations of the superconducting qubits because its relatively long coherent time (up to ~ 100 μs) and high fabrication reproducibility. The longest coherence time of transmon qubits achieved used 3-D microwave cavities with size of centimeters [142]. This large footprint and limited two-qubit quantum gate fidelity $< 99.9\%$ [141] hinder large scale integration of such superconducting quantum circuit technology which is needed for fault-tolerant quantum computing.

The mechanical resonators with ultra-compact size and ultra-high mechanical quality explored in this work is a promising candidate to replace the sizable electric microwave cavities. They can serve as a high-quality bosonic quantum resources storage and be used to perform ultra-high fidelity in-memory two-qubit gates [133, 134, 135].

Other than probing and controlling mechanical degree freedom with optics, superconducting circuit can be used to couple to mechanical resonators with help of piezoelectric materials. However, piezoelectric materials were found to be mechanically lossy [143, 144, 145], and on-demand swapping quantum state between a qubit and a mechanical resonator is yet to be demonstrated. In this section, a device is proposed which can maintain ultra-high coherence with a mechanical memory cavity, as well as realizing on-demand high-fidelity quantum state transfer between a superconducting transmon qubit and a phononic resonator.

The proposed device contains three subsystems, as illustrated in Fig. 7.1**a** and **c**, a superconducting transmon qubit on suspended Si membrane [146] (red box of Fig. 7.1**c**), a defect phononic crystal cavity on suspended silicon membrane (blue box), and an intermediate hybrid system (green box). These two subsystems are coupled to the intermediate system via pure electric coupling J_q, and pure mechanical piezo-memory coupling J_m, respectively. The intermediate hybrid system contains a tunable electromagnetic resonator (I_em) with frequency ω_em, and a piezoacoustic resonator (I_pa) with frequency ω_pa. I_em and I_pa are strongly coupled with piezoelectric coupling strength J_p.

This hybrid system can be switch between two states, idle-state and swap-state, and switching of theses two states is dependent on whether the intermediate system is hybridized and qubit frequency (ω_q) is tuned to align with the memory cavity frequency (ω_m). In the swap-state, ω_em and ω_pa are tuned to be resonant with each other, and the superpositions of the hybridized microwave resonator mode and the piezoacoustic mode are at frequencies $\omega_\pm = \omega_\text{pa} \pm J_\text{p}$.

The mechanical memory cavity is built based on the ‘cross’ phonoic crystal. A point defect in the 2D phononic crystal is used as a mechanical cavity to localize

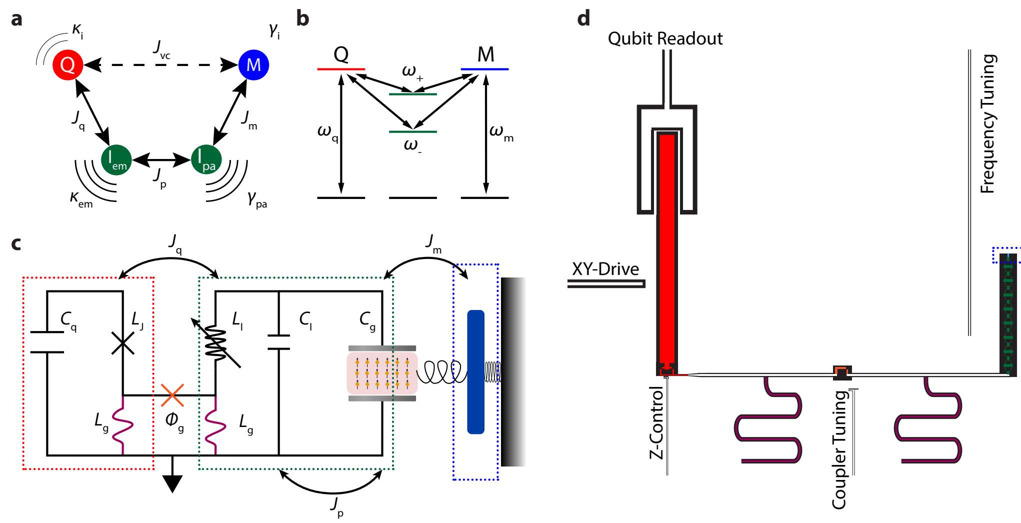

Figure 7.1: **Circuit diagram of phonon quantum memory.** **a**, The virtual coupling model of the proposed system. mode-Q (red), mode-M (blue), and mode-$I_{\text{em,pa}}$ (green) stand for qubit mode, mechanical memory mode, and intermediate electric and piezoacoustic modes. Decay rates of intermediate system (κ_{em} and γ_{pa}), intrinsic decay rate of the qubit (κ_{i}), and intrinsic decay rate memory cavity(γ_{i}) are shown. The acoustic memory mode is assumed to be almost lossless ($\gamma_{\text{i}}/2\pi \sim 1$ Hz) in the system dynamics of interest. **b**, Energy levels of different parts of the hybrid system. **c**, Proposed circuit diagram of the hybrid system. In the red box represents the qubit, the green box represents the high-Q memory resonator and green box represents intermediate system. **d** The illustration (not to scale) of the proposed device layout with different elements colored corresponding to **a**, **b** and **c**.

a mechanical mode [35, 147, 148]. A potential mechanical quality factor around fifty-billion of such cavity leads to a phonon lifetime approximately 1.5 seconds at a refrigerated temperature around 10 mK [56]. A schematic of this mechanical memory cavity and its corresponding mode profile are show in Fig. 7.2.

The piezoacoustic resonator and the memory cavity are located on the same phononic crystal membrane. Nearby mechanical cavities with frequencies around 5 GHz can be coupled through their evanescent mechanical fields. The piezoacoustic resonator needs to be strongly coupled to the tunable electric resonator with a large piezoelectric coupling rate J_{p}, and the piezoacoustic structure should be compact to avoid parasitic mechanical modes coupling to mechanical memory mode and introduce extra mechanical loss. Aluminum Nitride (AlN) is used in this design as it has a relatively low microwave loss tangent ($\tan\delta_{\text{AlN}} \sim 5\times10^{-4}$) [149, 150, 151, 152, 153, 154] and well established nano-fabrication processes [150, 155, 156]. A

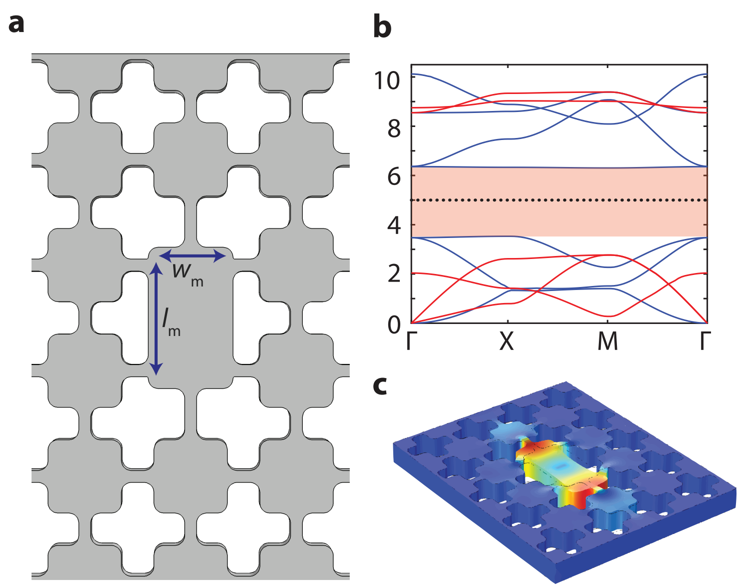

Figure 7.2: **Mechanical memory cavity design.** **a**, The structure of the proposed high-Q acoustic memory cavity which is realized as a phononic defect cavity embedded in a phononic crystal. **b**, The wide microwave bandgap phononic bandstructure of the phononic crystal membrane. The large bandgap in allowed mechanical wave frequency between 4 GHz and 6 GHz is highlighted in orange. The black-dotted line in the middle of the gap corresponds the memory cavity mode frequency $\omega_\mathrm{m}/2\pi \sim 5$ GHz. **d**, Fundamental mode displacement field profile of the memory cavity in **c**.

heavy superconducting metal Molybdenum (Mo) is used as electrodes [150, 155, 156] to better confine acoustic energy in the piezoelectric layer, and Al is used as the metal leads connecting Mo electrodes for ease of fabrication. A schematic of this piezoacoustic resonator together with memory cavity, and their corresponding mode profile are show in Fig. 7.3. Note that the coupling strength between these two resonators can be tuned by perturbing the ‘cross‘ unit cells between them.

As mentioned previously, there are two operation states in this proposed hybrid system, swap-state and idle-state. The swap-state is used to perform a high-fidelity quantum state transfer between qubits and memory cavity. The idle-state is used to preserve ultra-high coherence quantum states that are being swapped into the memory cavity. A virtual coupling scheme is used to perform the swap operation. A diagram showing the energy levels used in the virtual coupling scheme is also plotted in Fig. 7.4. The virtual coupling process can be understood as two quantum channels connecting the qubit with mechanical memory cavity. Each channel is

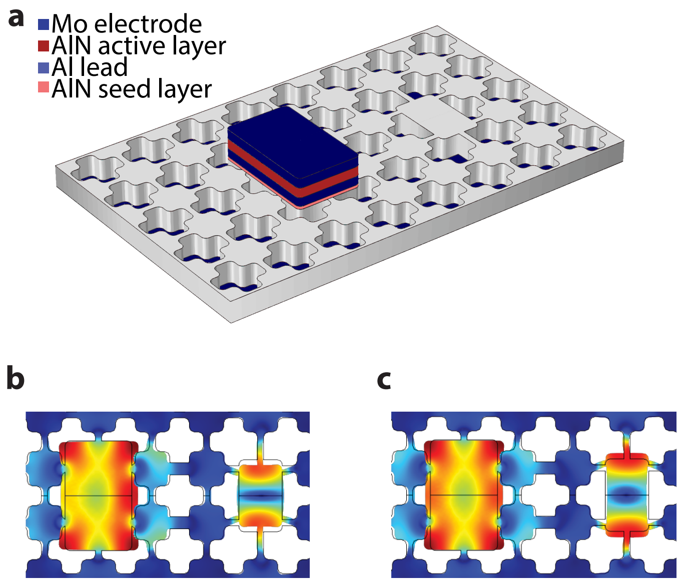

Figure 7.3: **Piezoacoustic resonator design.** **a,** The stack composition of the piezoacoustic resonator. **b** and **c**, Simulated symmetric and anti-symmetric mechanical displacement field profile for coupling modes between piezoacoustic and memory cavity.

formed by a supermode of the intermediate hybrid system which mediates the virtual coupling, coupling rate can be expressed as $J_{\mathrm{vc},\pm} = \pm\frac{J_\mathrm{q}J_\mathrm{m}}{2(\omega_\pm-\omega_\mathrm{m})}$.

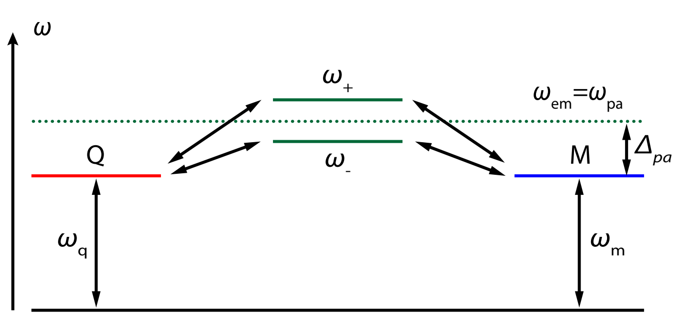

Figure 7.4: **Virtual coupling scheme.** swap-state energy level diagram of the system with $\omega_\mathrm{m}/2\pi \sim 5$ GHz which is about 50 MHz below the lower super-mode of the intermediate system.

On the other hand, for the idle-state, quantum state swap is turned off. A diagram showing the energy levels used in the idle-state is plotted in Fig. 7.5.

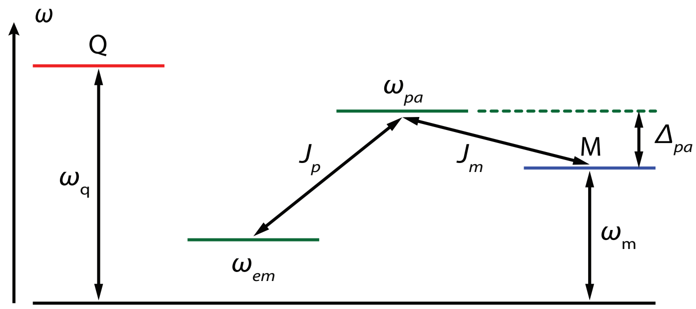

Figure 7.5: **Idle state diagram.** Energy levels of the idle-state. The qubit frequency (ω_q) is far detuned from the memory cavity frequency (ω_m). The tunable electric resonator in the intermediate system is also a far detuned system such that the intermediate system is no longer hybridized. The bare frequency ω_pa is $J_\mathrm{p}/2\pi \simeq 100$ MHz higher than the lower super-mode (ω_-) in the swap-state and the piezoacoustic mode is further detuned from the memory mode by Δ_pa.

The qubit ω_q is tuned to be far detuned from the memory frequency. Electric coupling (J_q) is turned off between the qubit and the intermediate electric resonator. [108, 157, 158]. The tunable electric resonator in the intermediate system is also detuned such that the intermediate system is no longer hybridized. The bare frequency of the piezoacoustic cavity ω_pa is $\simeq 100$ MHz higher than ω_-, and the Δ_pa detunning between the piezoacoustic mode and the memory mode can strongly suppress their coupling to below ~ 100 Hz.

This proposed superconducting circuits and high coherent nano-mechanics hybrid system could enable new research possibilities in compact on-chip quantum memory which can be used for scalable quantum circuits, bosonic quantum error correction, and eventually used for fault-tolerant quantum computing architecture [133, 134, 135]. It also opens a new route to explore the quantum mechanical properties of GHz phonon modes without the parasitic heating from optical probe as mentioned in this work.

7.2 Piezo-Optomechanical Circuits for Quantum-State Transfer from Microwave to Optical Wavelengths

As discussed in the previous section, engineered quantum systems have been rapidly improved in both the performance of individual qubits as well as the number of qubits that are coupled to each other. However, lots of these systems are based on microwave frequency superconducting circuits. Microwave frequency photons are difficult to transmit over long distances, which makes long-distance communication in these superconducting systems very challenging.

On the other hand, optical fibres, which typically have losses below 0.2 dBkm^{-1} at telecommunication wavelengths, as well as close to zero thermal occupancy at room temperature of optical frequency photons, make transmitting quantum information through optical photons an apparent choice. As a result, development of bi-directional transfer of quantum information between microwave and optical photons, a transducer, has been investigated with a number of techniques [108, 109, 110, 111, 112].

A bi-directional microwave to optical transducer must have high quantum efficiency, high fidelity and enough bandwidth. Ideally each input photon should produce one output photon, and the quantum information needs to be maintained in the output photon. Nowadays, the best decoherence times for superconducting qubits are aroud 100 μs, and transducers need enough bandwidth to transmit the information before it losses in the quantum system. Since superconducting quantum circuits usually operate in dilution fridges with base temperatures $\sim$ 10 mK in order to suppress microwave photons, these transducers are also required to be compatible with cryogenic temperature. Several techniques have been investigated as transducers, such as using electro-optic non-linearity materials such as lithium niobate, three level systems, such as rare earth ions, and indirect coupling mediated by a third mode, such as magnetostatic modes or mechanical resonators.

In this section, I will discuss a proposed transducer based on a mechanical resonator being simultaneously coupled to the microwave through piezo-electric coupling, and an optical cavity through optomechanical coupling. A transducer with unity efficiency can be realized with an optomechanical crystal coupled to a microwave circuit. In the rest of this section, I will present the analysis of the proposed optomechanical crystal quantum transducer, and show how it can benefit from large C_{eff}.

7.2.1 Optomechanically Mediated Coupling

Fig.7.6 shows the scheme for the transduction in the proposed piezo-optomechanical transducer. Microwave frequency mechanical mode of the optomechanical crystal is coupled to a tunable superconducting microwave resonator with rate J_{pa}. The

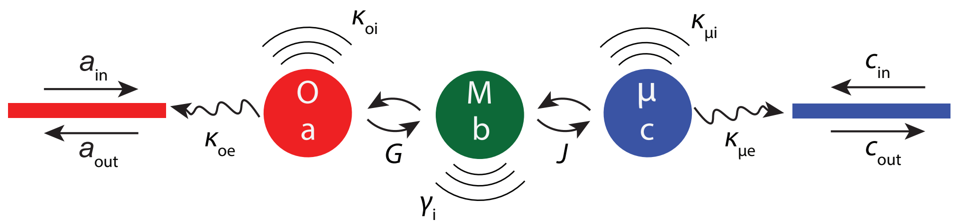

Figure 7.6: **Schematic of transducer.** FEM-simulated mode profile (E_y component of the electric field) of the fundamental optical resonance $\omega_o/2\pi = 194$ THz, with red (blue) corresponding to positive (negative) field amplitude. Simulated displacement profile of fundamental mechanical resonance at $\omega_o/2\pi \approx 5$ GHz. Here, the magnitude of the displacement is represented by color (large displacement in red, zero displacement in blue). Optical cavity mode is coupled to the mechanical mode via the optomechanical coupling. The mechanical mode is strongly hybridized with the mechanical mode piezo-electric material (AlN here) IDE resonator.

optical cavity is coupled to the input fiber with a coupling rate κ_{oe} and it suffers from intrinsic loss to environment with rate κ_{oi}. The superconducting microwave resonator is coupled to a transmission line with rate $\kappa_{\mu e}$ and it has intrinsic loss rate $\kappa_{\mu i}$ to the environment. The intrinsic loss channels will introduce environmental noises ($a^{\mathrm{n}}_{\mathrm{in}}$,$b^{\mathrm{n}}_{\mathrm{in}}$,$c^{\mathrm{n}}_{\mathrm{in}}$) into the system along with signals ($a_{\mathrm{in,out}}$ and $c_{\mathrm{in,out}}$) coupled into the system via external coupling channels to the fiber and superconducting transmission line.

A schematic for the transduction is shown in Fig.7.6. In real implementation, one piezoelectric transducer is strongly hybridized with Si OMC to create acoustic super-modes ($\mathrm{b}^\dagger$). Mode $\mathrm{b}^\dagger$ couples to both the microwave circuit and the optical resonator. FEM simumations of the optical mode and hybridized mechanical mode are plotted in Fig.7.7, a SEM image of fabricated device with fake colors indicating the electrodes are also plotted in Fig.7.8.

The piezo-electric material used here is the same as the quantum memory discussed in the previous section. Reactively sputtered oriented polycrystalline thin films of AlN allows for strong electromechanical coupling via metallic electrodes. The piezo-electro-mechanical transducer is design with pattern aluminum nitride (AlN) on top of pattern Si membrane, such that the mechanical mode is strongly coupled and hybridized with the optomechanical crystal *breathing* mode. The OMC is very similar to the previous discussed High-Q nanobeam OMC devices, where *breathing* mode and a localized optical mode (design to be ~ 1550 nm) are strongly coupled. The OMC was optically probed through an evanescently coupled optical waveguide,

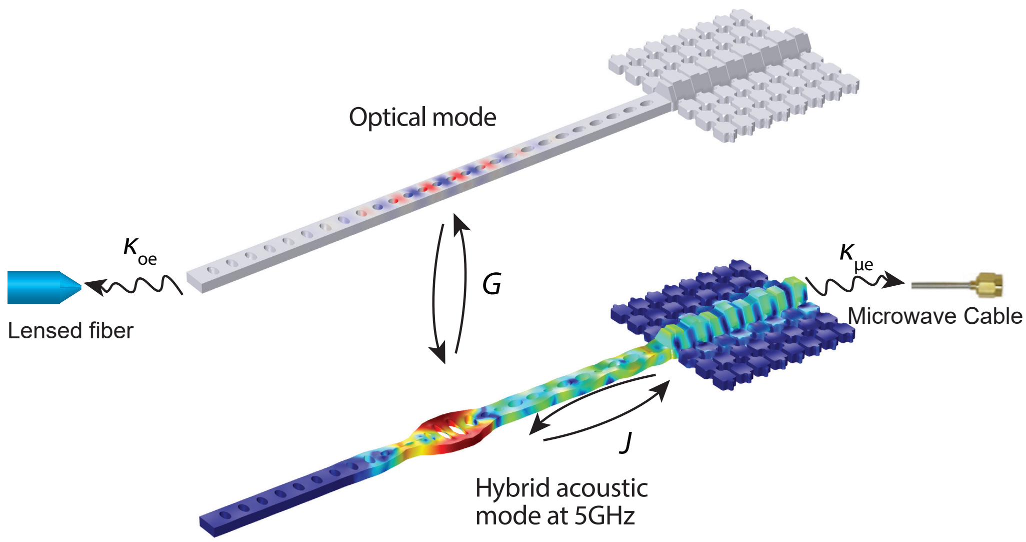

Figure 7.7: **FEM simulation of transducer.** The red mode on the left is the optical cavity mode that is dispersively coupled to the mechanical mode (green) via the optomechanical coupling. The mechanical mode (green) is strongly resonantly coupled to a tunable superconducting microwave resonator/qubit (blue) in a single photon level.

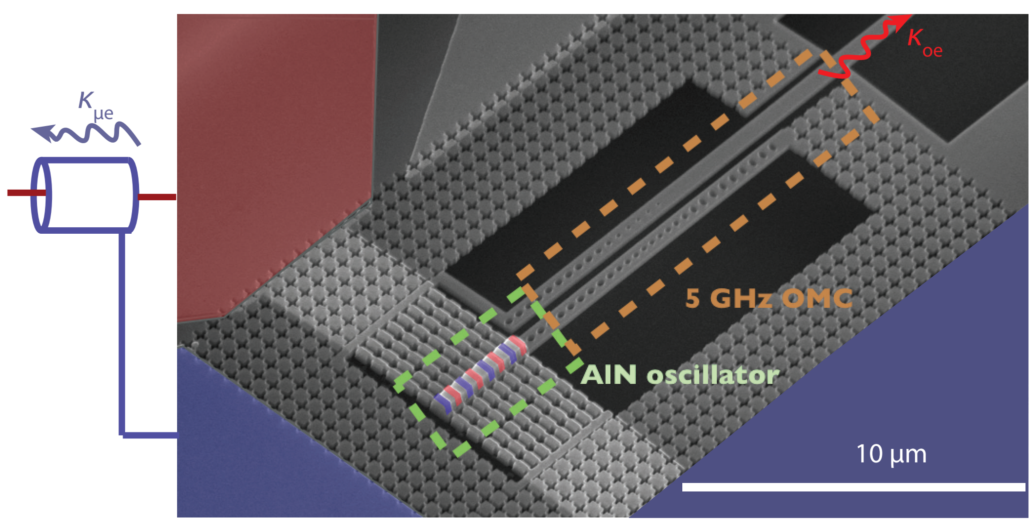

Figure 7.8: **SEM image of fabricated transducer.** Scanning electron micrograph (SEM) of a full piezo-optomechanical transducer silicon-on-insulator (SOI) with IDE eletrods and AlN piezo-electric resonator. A coupling waveguide allows for fiber-to-chip optical coupling as well as side-coupling to nanobeam OMC cavity.

which is End-Fire coupled to lensed fiber. However, in transducer design, one side mirror of the OMC cavity is mechanically less reflective in order to generate strong coupling with the AlN-on-Si piezo-electro-mechanical transducer. AlN-on-Si is patterned to have a periodicity on the scale of mechanical wavelength, the number of mechanical modes in the system are effectively reduced and coupling to the *breathing* mode is increased compared to surface- or bulk-acoustic wave phonons (SAW, BAW) Lamb wave IDTs. Frequency of these devices is designed to be around 5 GHz, which matches that of superconducting qubits, yielding a straightforward integration with these superconducting quantum systems.

The electrodes for IDT are designed to be remote from the optical mode in order to avoid optical photons which can be absorbed by superconducting electrodes leading to microwave decoherence. The electrodes are alternately wired to signal and ground as shown in Fig. 7.8.

A piezo-optomechanical transducer is intrinsically bidirectional because of the symmetry between the optical and microwave fields in the system Hamiltonian (this will be discussed in the following subsection). The intrinsic loss of such a system is comparably low since the optical mode is well confined by optical OMC mirrors, and mechanical modes are further protected by 'cross' acoustic shields as shown in Fig.7.8, which is a necessary condition for high efficiency and low noise operation. The optomechanical coupling rate (G) and electro-mechnical coupling rate (J) of the system are also important factors of transducor performance. In the following subsection, the efficiency and noise of the transducer system are analyzed, and impact of the effective quantum efficiency of the optomechaincal side (C_{eff}) is addressed, which implies that the quasi-2D OMC design can be a potential platform for bi-directional piezo-optomechanical transducers.

7.2.2 Efficiency and Noise Analysis of Bidirectional Microwave to Optical Transducer

The system Hamiltonian for the open quantum system can be written as (7.1)-(7.6).

$$H = H_0 + H_{\text{Drive}} + H_{\text{Signal}} + H_{\text{Noise}} \tag{7.1}$$

$$H_0 = \hbar(\omega_o - \frac{\kappa_o}{2}i)\hat{a}^\dagger\hat{a} + \hbar(\omega_{\text{m}} - \frac{\Gamma}{2}i)\hat{b}^\dagger\hat{b} + \hbar(\omega_\mu - \frac{\kappa_\mu}{2}i)\hat{c}^\dagger\hat{c} \tag{7.2}$$

$$H_{\text{Int}} = \hbar g_0\hat{a}^\dagger\hat{a}(\hat{b}^\dagger + \hat{b}) \tag{7.3}$$

$$H_{\text{Drive}} = -\hbar\sqrt{\kappa_{\text{oe}}}i(\alpha_{\text{in}}^*(t)\hat{a} + \alpha_{\text{in}}(t)\hat{a}^\dagger) \tag{7.4}$$

$$H_{\text{Signal}} = -\hbar\sqrt{\kappa_{\text{oe}}}i(\hat{a}_{\text{in}}^\dagger\hat{a} + \hat{a}_{\text{in}}\hat{a}^\dagger) - \hbar\sqrt{\kappa_{\mu\text{e}}}i(\hat{c}_{\text{in}}^\dagger\hat{c} + \hat{c}_{\text{in}}\hat{c}^\dagger) \tag{7.5}$$

$$H_{\text{Noise}} = -\hbar\sqrt{\kappa_{\text{oi}}}i(\hat{a}_{\text{n}}^\dagger\hat{a} + \hat{a}_{\text{n}}\hat{a}^\dagger) - \hbar\sqrt{\Gamma}i(\hat{b}_{\text{n}}^\dagger\hat{b} + \hat{b}_{\text{n}}\hat{b}^\dagger) - \hbar\sqrt{\kappa_{\mu\text{i}}}i(\hat{c}_{\text{n}}^\dagger\hat{c} + \hat{c}_{\text{n}}\hat{c}^\dagger) \tag{7.6}$$

where $\alpha(t) = \alpha_0\exp(-i\omega_{\text{l}}t)$ is the optical pumping field at ω_{l}. Taking the time dependant unitary transformation to a rotating frame with the driving field shown in $\hat{U} = \exp\left(-i\omega_d\hat{a}^\dagger\hat{a}t\right)$ and then linearizing the Hamiltonian using $\hat{a} = \bar{a} + \delta\hat{a}$ with coherent cavity amplitude $\bar{a}$, we can obtain the standard optomechanical interaction Hamiltonian after rotation-wave-approximation assuming $\Delta_{\text{o}} = \omega_{\text{o}} - \omega_{\text{d}} > 0$

$$H' = H_0' + H_{\text{Signal}}' + H_{\text{Noise}}' \tag{7.7}$$

$$H_0' = \hbar(\Delta_o - \frac{\kappa_o}{2}i)\hat{a}^\dagger\hat{a} + \hbar(\omega_{\text{m}} - \frac{\Gamma}{2}i)\hat{b}^\dagger\hat{b} + \hbar(\omega_\mu - \frac{\kappa_\mu}{2}i)\hat{c}^\dagger\hat{c} \tag{7.8}$$

$$H_{\text{Int}}' = \hbar G(\hat{b}^\dagger\hat{a} + \hat{b}\hat{a}^\dagger) \tag{7.9}$$

$$H_{\text{Signal}}' = -\hbar\sqrt{\kappa_{\text{oe}}}i(\hat{a}_{\text{in}}^\dagger\hat{a} + \hat{a}_{\text{in}}\hat{a}^\dagger) - \hbar\sqrt{\kappa_{\mu\text{e}}}i(\hat{c}_{\text{in}}^\dagger\hat{c} + \hat{c}_{\text{in}}\hat{c}^\dagger) \tag{7.10}$$

$$H_{\text{Noise}}' = -\hbar\sqrt{\kappa_{\text{oi}}}i(\hat{a}_{\text{n}}^\dagger\hat{a} + \hat{a}_{\text{n}}\hat{a}^\dagger) - \hbar\sqrt{\Gamma}i(\hat{b}_{\text{n}}^\dagger\hat{b} + \hat{b}_{\text{n}}\hat{b}^\dagger) - \hbar\sqrt{\kappa_{\mu\text{i}}}i(\hat{c}_{\text{n}}^\dagger\hat{c} + \hat{c}_{\text{n}}\hat{c}^\dagger) \tag{7.11}$$

where we relabelled $\delta\hat{a} \rightarrow \hat{a}$, $\hat{a}_{\text{in}}\exp((i\omega_{\text{d}}t)) \rightarrow \hat{a}_{\text{in}}$, and $\hat{a}_{\text{n}}\exp((i\omega_{\text{d}}t)) \rightarrow \hat{a}_{\text{n}}$. $G = \sqrt{n_c}g_0$ is defined as the optomechanical coupling rate with intracavity photon occupancy $n_{\text{c}} = |\bar{a}|^2$. With relation $\dot{\hat{O}} = \frac{i}{\hbar}\left[H', \hat{O},\right]$, we can derive in time domain,

$$\dot{a} = -i(\Delta_o - \frac{\kappa_o}{2}i)\hat{a} - iG\hat{b} + \sqrt{\kappa_{\text{oe}}}\hat{a}_{\text{in}} + \sqrt{\kappa_{\text{oi}}}\hat{a}_{\text{n}} \tag{7.12}$$

$$\dot{b} = -iG\hat{a} - i(\omega_{\text{m}} - \frac{\Gamma}{2}i)\hat{b} - iJ\hat{c} + \sqrt{\Gamma}\hat{b}_{\text{n}} \tag{7.13}$$

$$\dot{c} = -iJ\hat{b} - i(\omega_\mu - \frac{\kappa_\mu}{2}i)\hat{c} + \sqrt{\kappa_{\mu\text{e}}}\hat{c}_{\text{in}} + \sqrt{\kappa_{\mu\text{i}}}\hat{c}_{\text{n}}. \tag{7.14}$$

Frequency domain equations can be derived using Fourier Transform,

$$-i\omega\tilde{a} = -i(\Delta_o - \frac{\kappa_o}{2}i)\tilde{a} - iG\tilde{b} + \sqrt{\kappa_{\text{oe}}}\tilde{a}_{\text{in}} + \sqrt{\kappa_{\text{oi}}}\tilde{a}_{\text{n}} \tag{7.15}$$

$$-i\omega\tilde{b} = -iG\tilde{a} - i(\omega_{\text{m}} - \frac{\Gamma}{2}i)\tilde{b} - iJ\tilde{c} + \sqrt{\Gamma}\tilde{b}_{\text{n}} \tag{7.16}$$

$$-i\omega\tilde{c} = -iJ\tilde{b} - i(\omega_\mu - \frac{\kappa_\mu}{2}i)\tilde{c} + \sqrt{\kappa_{\mu\text{e}}}\tilde{c}_{\text{in}} + \sqrt{\kappa_{\mu\text{i}}}\tilde{c}_{\text{n}} \tag{7.17}$$

which can be expressed in matrix form:

$$\begin{bmatrix} \Delta_{\mathrm{o}} - \omega - \frac{\kappa_{\mathrm{o}}}{2}i & G & 0 \\ G & \omega_{\mathrm{m}} - \omega - \frac{\Gamma}{2}i & J \\ 0 & J & \omega_\mu - \omega - \frac{\kappa_\mu}{2}i \end{bmatrix} \begin{bmatrix} \tilde{a} \\ \tilde{b} \\ \tilde{c} \end{bmatrix} = -i \begin{bmatrix} \sqrt{\kappa_{\mathrm{oe}}}\tilde{a}_{\mathrm{in}} + \sqrt{\kappa_{\mathrm{oi}}}\tilde{a}_{\mathrm{n}} \\ \sqrt{\Gamma}\tilde{b}_{\mathrm{n}} \\ \sqrt{\kappa_{\mu\mathrm{e}}}\tilde{c}_{\mathrm{in}} + \sqrt{\kappa_{\mu\mathrm{i}}}\tilde{c}_{\mathrm{n}}. \end{bmatrix} \tag{7.18}$$

Inverting the coefficient matrix on the left, we obtain

$$\begin{bmatrix} \tilde{a} \\ \tilde{b} \\ \tilde{c} \end{bmatrix} = -iD[T] \begin{bmatrix} \sqrt{\kappa_{\mathrm{oe}}}\tilde{a}_{\mathrm{in}} + \sqrt{\kappa_{\mathrm{oi}}}\tilde{a}_{\mathrm{n}} \\ \sqrt{\Gamma}\tilde{b}_{\mathrm{n}} \\ \sqrt{\kappa_{\mu\mathrm{e}}}\tilde{c}_{\mathrm{in}} + \sqrt{\kappa_{\mu\mathrm{i}}}\tilde{c}_{\mathrm{n}}, \end{bmatrix} \tag{7.19}$$

where

$$[T] = \begin{bmatrix} (\omega_{\mathrm{m}} - \omega - \frac{\Gamma}{2}i)(\omega_\mu - \omega - \frac{\kappa_\mu}{2}i) - J^2 & -G(\omega_\mu - \omega - \frac{\kappa_\mu}{2}i) & GJ \\ -G(\omega_\mu - \omega - \frac{\kappa_\mu}{2}i) & (\Delta_o - \omega - \frac{\kappa_O}{2}i)(\omega_\mu - \omega - \frac{\kappa_\mu}{2}i) & -J(\Delta_o - \omega - \frac{\kappa_O}{2}i) \\ GJ & -J(\Delta_o - \omega - \frac{\kappa_O}{2}i) & (\Delta_o - \omega - \frac{\kappa_O}{2}i)(\omega_{\mathrm{m}} - \omega - \frac{\Gamma}{2}i). \end{bmatrix} \tag{7.20}$$

$$D = \Bigg((\Delta_o - \omega - \frac{\kappa_o}{2}i)(\omega_{\mathrm{m}} - \omega - \frac{\Gamma}{2}i)(\omega_\mu - \omega - \frac{\kappa_\mu}{2}i) \tag{7.21}$$

$$- G^2(\omega_\mu - \omega - \frac{\kappa_\mu}{2}i) - J^2(\Delta_o - \omega - \frac{\kappa_o}{2}i) \Bigg)^{-1} \tag{7.22}$$

For input signal from microwave transmission line ($\tilde{c}_{\mathrm{in}}$), we can obtain the signal in the optical fiber from the input-output theorem.

$$\tilde{a}_{\mathrm{out}}^{\mathrm{signal}} = D\sqrt{\kappa_{\mathrm{oe}}\kappa_{\mu\mathrm{e}}}GJ\tilde{c}_{\mathrm{in}} \tag{7.23}$$

$$\begin{aligned} \tilde{a}_{\mathrm{out}}^{\mathrm{noise}} = D\Bigg(& \sqrt{\kappa_{\mathrm{oe}}\kappa_{\mathrm{oi}}} \left((\omega_{\mathrm{m}} - \omega - \frac{\Gamma}{2}i)(\omega_\mu - \omega - \frac{\kappa_\mu}{2}i) - J^2 \right) \tilde{a}_{\mathrm{n}} \\ & - \sqrt{\Gamma\kappa_{\mathrm{oe}}}G(\omega_\mu - \omega - \frac{\kappa_\mu}{2}i)\tilde{b}_{\mathrm{n}} + GJ\sqrt{\kappa_{\mu\mathrm{i}}\kappa_{\mathrm{oe}}}\tilde{c}_{\mathrm{n}} \Bigg). \end{aligned} \tag{7.24}$$

A similar analysis can be done for the input signal from the optical fiber ($\tilde{a}_{\mathrm{in}}$). The conversion number efficiency and signal-to-noise ratios for both direction η_{conv} can be shown in (7.25) to (7.27)

$$\eta_{\text{conv}} = \frac{\left\langle \tilde{a}^{\text{signal}\dagger} \tilde{a}^{\text{signal}} \right\rangle}{\left\langle \tilde{c}_{\text{in}}^{\dagger} \tilde{c}_{\text{in}} \right\rangle} = \left| D\sqrt{\kappa_{\text{oe}}\kappa_{\mu\text{e}}} GJ \right|^2 \tag{7.25}$$

$$\begin{aligned} SNR_{\text{o}} &= \frac{\left\langle \tilde{a}^{\text{signal}\dagger} \tilde{a}^{\text{signal}} \right\rangle}{\left\langle \tilde{a}_{\text{out}}^{\text{noise}\dagger} \tilde{a}_{\text{out}}^{\text{noise}} \right\rangle} \\ &= \frac{\kappa_{\mu\text{e}} G^2 J^2}{\frac{\kappa_{\text{oi}} \left| (\omega_{\text{m}} - \omega - \frac{\Gamma}{2} i)(\omega_\mu - \omega - \frac{\kappa_\mu}{2} i) - J^2 \right|^2 \bar{n}_{ob}}{+\Gamma G^2 \left| \omega_\mu - \omega - \frac{\kappa_\mu}{2} i \right|^2 \bar{n}_{mb} + G^2 J^2 \kappa_{\mu\text{i}} \bar{n}_{\mu b}}} \end{aligned} \tag{7.26}$$

$$\begin{aligned} SNR_{\mu} &= \frac{\left\langle \tilde{c}^{\text{signal}\dagger} \tilde{c}^{\text{signal}} \right\rangle}{\left\langle \tilde{c}_{\text{out}}^{\text{noise}\dagger} \tilde{c}_{\text{out}}^{\text{noise}} \right\rangle} \\ &= \frac{\kappa_{\text{oe}} G^2 J^2}{\frac{\kappa_{\mu\text{i}} \left| (\omega_{\text{m}} - \omega - \frac{\Gamma}{2} i)(\omega_{\text{o}} - \omega - \frac{\kappa_{\text{o}}}{2} i) - G^2 \right|^2 \bar{n}_{\mu b}}{+\Gamma J^2 \left| \Delta_o - \omega - \frac{\kappa_o}{2} i \right|^2 \bar{n}_{mb} + G^2 J^2 \kappa_{\text{oi}} \bar{n}_{ob}}} \end{aligned} \tag{7.27}$$

where

$$d = (\Delta_o - \omega - \frac{\kappa_o}{2} i)(\omega_{\text{m}} - \omega - \frac{\Gamma}{2} i)(\omega_\mu - \omega - \frac{\kappa_\mu}{2} i) \tag{7.28}$$

$$- G^2(\omega_\mu - \omega - \frac{\kappa_\mu}{2} i) - J^2(\Delta_o - \omega - \frac{\kappa_o}{2} i) \tag{7.29}$$

$$D = |d|^2 \tag{7.30}$$

$$0 = \frac{\partial D}{\partial \omega} = 2Re\left[\frac{\partial d}{\partial \omega} d^*\right]. \tag{7.31}$$

Note that the denominator of the conversion efficiency can be minimized with respect to the frequency ω by looking for the extrema points of the denominator in (7.30) according to (7.31) with solutions in (7.34) and (7.35) assuming the resonant condition that $\Delta_0 = \omega_{\text{m}} = \omega_\mu$.

$$\zeta = \Big(16G^4 + 32G^2J^2 + 16J^4 - 16G^2\gamma^2 - 16J^2\gamma^2 + \gamma^4$$
$$- 24G^2\gamma\kappa_{\mathrm{o}} - 16G^2\kappa_{\mathrm{o}}^2 + 8J^2\kappa_{\mathrm{o}}^2 - \gamma^2\kappa_{\mathrm{o}}^2$$
$$+ \kappa_{\mathrm{o}}^4 - 24J^2\gamma\kappa_{\mathrm{u}} + 8G^2\kappa_{\mathrm{u}}^2 - 16J^2\kappa_{\mathrm{u}}^2 \tag{7.32}$$
$$- \gamma^2\kappa_{\mathrm{u}}^2 - \kappa\mathrm{o}^2\kappa_{\mathrm{u}}^2 + \kappa_{\mathrm{u}}^4\Big)^{1/2}$$

$$\beta = 8G^2 + 8J^2 - \gamma^2 - \kappa_{\mathrm{o}}^2 - \kappa_{\mathrm{u}}^2 \tag{7.33}$$

$$\omega_{\mu=\pm1,\nu=\pm1} = \omega_{\mathrm{m}} + \mu\frac{\sqrt{\beta+\nu\zeta}}{2\sqrt{3}} \tag{7.34}$$

$$\omega_{\mu=0} = \omega_{\mathrm{m}}. \tag{7.35}$$

For expressions in (7.34), we can notice that typical parameters have $\kappa_{\mathrm{o}} \sim 2\pi\times 1$ GHz, $\kappa_{\mathrm{u}} \sim 2\pi \times 10$ kHz, $\Gamma \sim 2\pi \times 1$ kHz, $\Gamma \sim 2\pi \times 1$ kHz, $J \sim 2\pi \times 10$ MHz, and $G = g_0\sqrt{n_{\mathrm{c}}} \sim 2\pi \times 10$ MHz. These typical parameters lead to $b < 0$. Thus only $\omega_{\mu=\pm1,\nu=1}$ and $\omega_{\mu=0}$ are valid real solutions. It can also be shown that $\omega_{\mu=0}$ leads to a maximal point of D and a local minimal point in (7.25). $\omega_{\mu=\pm1,\nu=1}$ are the maximal points of (7.25).

To highlight the importance of quantum cooperativity for optomechanical and piezoelectric interactions we can further simplify equations for $\mathrm{SNR}_{\mathrm{o}\leftarrow\mu}$ and $\mathrm{SNR}_{\mathrm{o}\rightarrow\mu}$ at the maximum conversion efficiency points,

$$\begin{aligned}\mathrm{SNR}_{\mathrm{o}\leftarrow\mu} &= \frac{\kappa_{\mu\mathrm{e}}J^2}{\gamma A\bar{n}_{\mathrm{mb}}} \\ &= \frac{\kappa_{\mu\mathrm{e}}\kappa_{\mu}}{4A}C_{\mu,\mathrm{m}}^{\mathrm{eff}},\end{aligned} \tag{7.36}$$

$$\begin{aligned}\mathrm{SNR}_{\mathrm{o}\rightarrow\mu} &= \frac{\kappa_{\mathrm{oe}}G^2}{\gamma B\bar{n}_{\mathrm{mb}}} \\ &= \frac{\kappa_{\mathrm{oe}}\kappa_{\mathrm{o}}}{4B}C_{\mathrm{o,m}}^{\mathrm{eff}}\end{aligned} \tag{7.37}$$

where the quantum cooperativities are defined as $C_{\mu,\mathrm{m}}^{\mathrm{eff}} = C_{\mu,\mathrm{m}}/\bar{n}_{\mathrm{mb}}$ and $C_{\mathrm{o,m}}^{\mathrm{eff}} = C_{\mathrm{om}}/\bar{n}_{\mathrm{mb}}$, with standard cooperativities at the microwave and optical ports given as $C_{\mu,\mathrm{m}} = 4J^2/\gamma\kappa_{\mu}$ and $C_{\mathrm{om}} = 4G^2/\gamma\kappa_{\mathrm{o}}$, respectively. In the above equations, $A \equiv \left|\omega_{\mu} - \omega - \frac{\kappa_{\mu}}{2}i\right|^2$ and $B \equiv \left|\Delta_{\mathrm{o}} - \omega - \frac{\kappa_{\mathrm{o}}}{2}i\right|^2$, and we have dropped terms related to $\bar{n}_{\mu\mathrm{b}}$ and $\bar{n}_{\mathrm{ob}}$ since they are very small in the system discussed here (milliKelvin temperatures). We have also neglected spontaneous scattering noise (quantum noise) in the optomechanical interaction [102] due to the very large sideband ratio that we have in our 2D OMC system. From these simple relations we can see the importance of the quantum cooperativity for quantum transduction applications. In order to transduce single photons with SNR greater than unity one needs $C^{\mathrm{eff}}_{\mu,\mathrm{m}}$ and $C^{\mathrm{eff}}_{\mathrm{o,m}}$ to be larger than unity (the pre-coefficients in Eqs. (7.36) and (7.37) are always less than or equal to unity, depending on the level of overcoupling to the optical and microwave external lines).

BIBLIOGRAPHY

[1] M. Aspelmeyer, T.J. Kippenberg, and F. Marquardt. "Cavity optomechanics". In: *Reviews of Modern Physics* 86.4 (2014), pp. 1391–1452 (cit. on pp. xv, 150, 157).

[2] P. Kharel et al. "Ultra-high-Q phononic resonators on-chip at cryogenic temperatures". In: *arXiv* 1 (2018) (cit. on p. xv).

[3] S. Galliou et al. "Extremely Low Loss Phonon-Trapping Cryogenic Acoustic Cavities for Future Physical Experiments". In: *Scientific Reports* 3.2132 (2013), pp. 1–6 (cit. on p. xv).

[4] Jasper Chan. "Laser cooling of an optomechanical crystal resonator to its quantum ground state of motion". PhD thesis. California Institute of Technology, 2012 (cit. on p. 1).

[5] Amir H Safavi-Naeini. "Quantum optomechanics with silicon nanostructures". PhD thesis. California Institute of Technology, 2013 (cit. on p. 1).

[6] Sean Michael Meenehan. *Cavity Optomechanics at Millikelvin Temperatures*. 2015 (cit. on pp. 1, 43).

[7] Markus Aspelmeyer, Tobias J. Kippenberg, and Florian Marquardt. "Cavity optomechanics". In: *Rev. Mod. Phys.* 86 (4 Dec. 2014), pp. 1391–1452 (cit. on pp. 1, 129).

[8] C. K. Law. "Effective Hamiltonian for the radiation in a cavity with a moving mirror and a time-varying dielectric medium". In: *Phys. Rev. A* 49 (Jan. 1994), pp. 433–437 (cit. on p. 3).

[9] Seán M. Meenehan et al. "Pulsed Excitation Dynamics of an Optomechanical Crystal Resonator near Its Quantum Ground State of Motion". In: *Physical Review X* 5.4 (2015), p. 041002. ISSN: 2160-3308. DOI: 10.1103/PhysRevX.5.041002. URL: http://link.aps.org/doi/10.1103/PhysRevX.5.041002 (cit. on pp. 6, 13, 129, 130).

[10] R Riedinger et al. "Non-classical correlations between single photons and phonons from a mechanical oscillator." In: *Nature* 530.7590 (2016), pp. 313–316 (cit. on pp. 6, 13, 129).

[11] Sungkun Hong et al. "Hanbury Brown and Twiss interferometry of single phonons from an optomechanical resonator". In: *Science* 358.6360 (2017), pp. 203–206 (cit. on pp. 6, 13, 129).

[12] Ralf Riedinger et al. "Remote quantum entanglement between two micromechanical oscillators". In: *Nature* 556.7702 (2018), p. 473 (cit. on pp. 6, 13, 129).

[13] Igor Marinkovi ć et al. “Optomechanical Bell Test”. In: *Phys. Rev. Lett.* 121 (22 Nov. 2018), p. 220404. DOI: 10.1103/PhysRevLett.121.220404. URL: https://link.aps.org/doi/10.1103/PhysRevLett.121.220404 (cit. on pp. 6, 13, 129).

[14] R Hanbury Brown, Richard Q Twiss, et al. “Correlation between photons in two coherent beams of light”. In: *Nature* 177.4497 (1956), pp. 27–29 (cit. on pp. 6, 131).

[15] J. Suh et al. “Mechanically Detecting and Avoiding the Quantum Fluctuations of a Microwave Field”. In: *Science* 344 (June 2014), pp. 1262–1265 (cit. on pp. 6, 131).

[16] Gabriel A Peterson et al. “Demonstration of efficient nonreciprocity in a microwave optomechanical circuit”. In: *Physical Review X* 7.3 (2017), p. 031001 (cit. on pp. 6, 129, 131).

[17] Laszlo Daniel Toth et al. “A dissipative quantum reservoir for microwave light using a mechanical oscillator”. In: *Nature Physics* 13.8 (2017), p. 787 (cit. on pp. 6, 131).

[18] Itay Shomroni et al. “Optical backaction-evading measurement of a mechanical oscillator”. In: *Nature communications* 10.1 (2019), p. 2086 (cit. on pp. 6, 130, 131).

[19] David Mason et al. “Continuous force and displacement measurement below the standard quantum limit”. In: *Nature Physics* (2019), p. 1 (cit. on pp. 6, 131).

[20] JD Teufel et al. “Sideband Cooling Micromechanical Motion to the Quantum Ground State”. In: *Nature* 475.7356 (2011), pp. 359–363 (cit. on pp. 6, 129).

[21] E. Verhagen et al. “Quantum-coherent coupling of a mechanical oscillator to an optical cavity mode”. In: *Nature* 482 (2012), pp. 63–67 (cit. on pp. 6, 129).

[22] Massimiliano Rossi et al. “Measurement-based quantum control of mechanical motion”. In: *Nature* 563.7729 (2018), p. 53 (cit. on pp. 6, 129).

[23] Sajeev John. “Strong localization of photons in certain disordered dielectric superlattices”. In: *Physical review letters* 58.23 (1987), p. 2486 (cit. on pp. 7, 129).

[24] Eli Yablonovitch et al. “Extreme selectivity in the lift-off of epitaxial GaAs films”. In: *Appl. Phys. Lett.* 51 (1987), pp. 2222–2224 (cit. on pp. 7, 129).

[25] John David Jackson. *Classical electrodynamics*. 3rd ed. Wiley, 1999. ISBN: 9780471309321 (cit. on p. 7).

[26] C. Cohen-Tannoudji, B. Diu, and F. Laloe. *Quantum Mechanica, Volume I and II*. Wiley, 1991 (cit. on p. 10).

[27] Jasper Chan et al. “Laser cooling of a nanomechanical oscillator into its quantum ground state”. In: *Nature* 478 (2011), pp. 89–92 (cit. on pp. 10–12, 17, 129).

[28] A. Yariv and P. Yeh. *Optical Waves in Crystals*. Wiley-Interscience, 1983 (cit. on p. 10).

[29] Seán M. Meenehan et al. “Silicon optomechanical crystal resonator at millikelvin temperatures”. In: *Phys. Rev. A* 90 (2014), p. 011803 (cit. on pp. 12, 40, 41, 59, 131, 132, 135).

[30] A. Stesmans. “Passivation of P_{bo} amd P_{b1} interface defects in thermal (100) Si/SiO_2 with molecular hydrogen”. In: *App. Phys. Lett.* 68 (1996) (cit. on pp. 13, 129, 131, 166).

[31] M. Borselli et al. “Surface encapsulation for low-loss silicon photonics”. In: *Appl. Phys. Lett.* 91.13 (Sept. 2007), p. 131117 (cit. on pp. 13, 129, 131, 166).

[32] E. Gavartin et al. “Optomechanical Coupling in a Two-Dimensional Photonic Crystal Defect Cavity”. In: *Phys. Rev. Lett.* 106.20 (May 2011), pp. 203902– (cit. on pp. 13, 130, 131).

[33] Amir H. Safavi-Naeini et al. “Two-dimensional phononic-photonic bandgap optomechanical crystal cavity”. In: *Phys. Rev. Lett.* 112 (Apr. 2014), p. 153603 (cit. on pp. 13, 130, 131).

[34] Amir H. Safavi-Naeini and Oskar Painter. “Design of optomechanical cavities and waveguides on a simultaneous bandgap phononic-photonic crystal slab”. In: *Opt. Express* 18.14 (July 2010), pp. 14926–14943 (cit. on pp. 14, 35, 36).

[35] Jasper Chan et al. “Optimized optomechanical crystal cavity with acoustic radiation shield”. In: *Appl. Phys. Lett.* 101.8 (Aug. 2012), p. 081115 (cit. on pp. 14, 17, 36, 69, 70, 74, 75, 82, 171).

[36] Hiroshi Sekoguchi et al. “Photonic crystal nanocavity with a Q-factor of ~ 9 million”. In: *Optics Express* 22.1 (2014), pp. 916–924 (cit. on pp. 17, 18).

[37] COMSOL Multiphysics 3.5, http://www.comsol.com/ (cit. on pp. 17, 35, 44).

[38] Hannes Pfeifer. “Silicon optomechanical crystals for arrays - tunability, disorder and 2D designs for low temperature experiments”. PhD thesis. Jan. 2018 (cit. on p. 17).

[39] Matthew Borselli, Thomas J Johnson, and Oskar Painter. “Measuring the role of surface chemistry in silicon microphotonics”. In: *Applied Physics Letters* 88.13 (2006), p. 131114 (cit. on pp. 18, 22).

[40] Takayuki Takahagi, Hiroyuki Sakaue, and Shoso Shingubara. “Adsorbed water on a silicon wafer surface exposed to atmosphere”. In: *Japanese Journal of Applied Physics* 40.11R (2001), p. 6198 (cit. on p. 18).

[41] S Mizushima. “Determination of the amount of gas adsorption on SiO2/Si (100) surfaces to realize precise mass measurement”. In: *Metrologia* 41.3 (2004), p. 137 (cit. on p. 18).

[42] Hiroyuki Hagino et al. “Effects of fluctuation in air hole radii and positions on optical characteristics in photonic crystal heterostructure nanocavities”. In: *Physical Review B* 79.8 (2009), p. 085112 (cit. on p. 20).

[43] J Chan et al. “Laser cooling of a nanomechanical oscillator into its quantum ground state.” In: *Nature* 478.7367 (2011), p. 89 (cit. on p. 22).

[44] Jasper Chan et al. “Optimized optomechanical crystal cavity with acoustic radiation shield”. In: *Applied Physics Letters* 101.8 (2012), p. 081115 (cit. on p. 22).

[45] Gregory S MacCabe. “Phonon Dynamics and Damping in Three-Dimensional Acoustic Bandgap Cavity-Optomechanical Resonators”. PhD thesis. California Institute of Technology, 2019 (cit. on p. 27).

[46] F. Laermer and A. Schilp. “Method of anisotropically etching silicon”. 5501893. Mar. 1996. URL: `http://www.freepatentsonline.com/5501893.html` (cit. on p. 29).

[47] David K Biegelsen. “Photoelastic tensor of silicon and the volume dependence of the average gap”. In: *Physical Review Letters* 32.21 (1974), p. 1196 (cit. on p. 36).

[48] S Johnson and J Joannopoulos. “Block-iterative frequency-domain methods for Maxwell’s equations in a planewave basis.” In: *Optics express* 8.3 (2001), pp. 173–190. ISSN: 10944087. DOI: `10.1364/OE.8.000173`. URL: `http://ab-initio.mit.edu/wiki/index.php/MIT%7B%5C_%7DPhotonic%7B%5C_%7DBands` (cit. on p. 36).

[49] J. A. Nelder and R. Mead. “A simplex method for function minimization”. In: *The Computer Journal* 7.7 (Jan. 1965), pp. 308–313 (cit. on p. 38).

[50] Justin D. Cohen, Seán M. Meenehan, and Oskar Painter. “Optical coupling to nanoscale optomechanical cavities for near quantum-limited motion transduction”. In: *Opt. Express* 21 (Feb. 2013), pp. 11227–11236. (Visited on 04/09/2013) (cit. on p. 41).

[51] Lumerical Solutions Inc. http://www.lumerical.com/tcad-products/fdtd/ (cit. on p. 42).

[52] Geraint Owen and Paul Rissman. “Proximity effect correction for electron beam lithography by equalization of background dose”. In: *Journal of Applied Physics* 54.6 (1983), pp. 3573–3581 (cit. on p. 46).

[53] Amir H. Safavi-Naeini et al. “Electromagnetically induced transparency and slow light with optomechanics”. In: *Nature* 472 (2011), pp. 69–73 (cit. on pp. 47, 67, 81).

[54] Seán M. Meenehan et al. “Pulsed Excitation Dynamics of an Optomechanical Crystal Resonator near Its Quantum Ground State of Motion”. In: *Phys. Rev. X* 5 (4 Oct. 2015), p. 041002 (cit. on pp. 58, 70, 78).

[55] Justin D Cohen et al. “Phonon counting and intensity interferometry of a nanomechanical resonator”. In: *Nature* 520.7548 (2015), p. 522 (cit. on p. 58).

[56] Gregory S MacCabe et al. “Phononic bandgap nano-acoustic cavity with ultralong phonon lifetime”. In: *arXiv preprint arXiv:1901.04129* (2019) (cit. on pp. 59, 129, 153, 155, 161, 163, 165, 167, 171).

[57] John D. Joannopoulos et al. *Photonic Crystals: Molding the Flow of Light*. 2nd. Princeton University Press, 2008. ISBN: 978-0691124568 (cit. on p. 69).

[58] Sajeev John and Jian Wang. “Quantum optics of localized light in a photonic band gap”. In: *Physical Review B* 43.16 (June 1991), pp. 12772–12789 (cit. on pp. 69, 72).

[59] Martin Maldovan. “Sound and heat revolutions in phononics”. In: *Nature* 503 (Nov. 2013), pp. 209–217. DOI: 10.1038/nature12608 (cit. on p. 69).

[60] Jinwoong Cha, Kun Woo Kim, and Chiara Daraio. “Experimental realization of on-chip topological nanoelectromechanical metamaterials”. In: *Nature* 564 (Dec. 2018), pp. 229–233. DOI: 10.1038/s41586-018-0764-0 (cit. on p. 69).

[61] P.-L. Yu et al. “A phononic bandgap shield for high-Q membrane microresonators”. In: *App. Phys. Lett.* 104 (Jan. 2014), p. 023510 (cit. on p. 69).

[62] A. Barg Y. Tsaturyan, E. S. Polzik, and A. Schliesser. “Ultracoherent nanomechanical resonators via soft clamping and dissipation dilution”. In: *Nature Nanotech.* 12 (June 2017), pp. 776–783. DOI: 10.1038/nnano.2017.101 (cit. on p. 69).

[63] A. H. Ghadimi et al. “Elastic strain engineering for ultralow mechanical dissipation”. In: *Science* 360 (6390 May 2018), pp. 764–768. DOI: 10.1126/science.aar6939 (cit. on pp. 69, 70).

[64] Mahmoud Kalaee et al. “Quantum electromechanics of a hypersonic crystal”. In: *arXiv:1808.04874* (2018) (cit. on p. 69).

[65] R. O. Behunin, F. Intravaia, and P. T. Rakich. “Dimensional transformation of defect-induced noise, dissipation, and nonlinearity”. In: *Phys. Rev. B* 93 (22 June 2016), p. 224110 (cit. on pp. 70, 89).

[66] B. D. Hauer et al. “Two-level system damping in a quasi-one-dimensional optomechanical resonator”. In: *Phys. Rev. B* 98 (Dec. 2018), p. 214303. DOI: 10.1103/PhysRevB.98.214303 (cit. on pp. 70, 89).

[67] L. D. Landau and G. Rumer. “Absorption of sound in solids”. In: *Phys. Z. Sowjetunion* 11.18 (1937) (cit. on pp. 70, 92).

[68] G. P. Srivastava. *The Physics of Phonons*. Taylor & Francis Group, 1990. ISBN: 978-0852741535 (cit. on pp. 70, 92, 93, 95, 98, 99, 132, 135, 161).

[69] W. A. Phillips. “Two-level states in glasses”. In: *Rep. Prog. Phys.* 50 (1987), pp. 1657–1708 (cit. on pp. 70, 89, 105, 108, 109, 121, 123).

[70] Serge Galliou et al. “Extremely Low Loss Phonon-Trapping Cryogenic Acoustic Cavities for Future Physical Experiments”. In: *Scientific Reports* 3 (July 2013), p. 2132. DOI: 10.1038/srep02132 (cit. on p. 70).

[71] K. Rostem, P. J. de Visser, and E. J. Wollack. “Enhanced quasiparticle lifetime in a superconductor by selective blocking of recombination phonons with a phononic crystal”. In: *Phys. Rev. B* 98 (1 July 2018), p. 014522. DOI: 10.1103/PhysRevB.98.014522 (cit. on p. 81).

[72] John M. Martinis and A. Megrant. “UCSB final report for the CSQ program: Review of decoherence and materials physics for superconducting qubits”. In: *arXiv:1410.5793* (Oct. 2014) (cit. on p. 82).

[73] Young-Ik Sohn et al. “Controlling the coherence of a diamond spin qubit through its strain environment”. In: *Nat. Commun.* 9 (1 May 2018), p. 2012. DOI: 10.1038/s41467-018-04340-3 (cit. on p. 82).

[74] Tomás Ramos et al. “Nonlinear Quantum Optomechanics via Individual Intrinsic Two-Level Defects”. In: *Phys. Rev. Lett.* 110 (May 2013), p. 193602. DOI: 10.1103/PhysRevLett.110.193602 (cit. on p. 82).

[75] M. Selim Hanay et al. “Inertial imaging with nanomechanical systems”. In: *Nature Nanotech.* 10 (Mar. 2015), pp. 339–344. DOI: 10.1038/NNANO.2015.32 (cit. on p. 82).

[76] Stefan Nimmrichter, Klaus Hornberger, and Klemens Hammerer. “Optomechanical Sensing of Spontaneous Wave-Function Collapse”. In: *Phys. Rev. Lett.* 113 (2 July 2014), p. 020405. DOI: 10.1103/PhysRevLett.113.020405. URL: https://link.aps.org/doi/10.1103/PhysRevLett.113.020405 (cit. on p. 82).

[77] M. H. Devoret and R. J. Schoelkopf. “Superconducting Circuits for Quantum Information: An Outlook”. In: *Science* 339.6124 (2013), pp. 1169–1174. ISSN: 0036-8075. DOI: 10.1126/science.1231930 (cit. on pp. 82, 169).

[78] Patricio Arrangoiz-Arriola et al. “Coupling a Superconducting Quantum Circuit to a Phononic Crystal Defect Cavity”. In: *Phys. Rev. X* 8 (July 2018), p. 031007. DOI: 10.1103/PhysRevX.8.031007 (cit. on pp. 82, 90, 169).

[79] Mizuho Morita and Tadahiro Ohmi. "Characterization and Control of Native Oxide on Silicon". In: *Jpn. J. Appl. Phys.* 33 (Jan. 1994), pp. 370–374. DOI: 10.1143/JJAP.33.370 (cit. on pp. 88, 120, 123).

[80] Gottlieb S. Oehrlein. "Dry Etching Damage of Silicon: A Review". In: *Materials Science and Engineering: B* 4 (Oct. 1989), pp. 441–450. DOI: 0.1016/0921-5107(89)90284-5 (cit. on pp. 88, 120, 123).

[81] T. O. Woodruff and H. Ehrenreich. "Absorption of Sound in Insulators". In: *Phys. Rev.* 123 (5 Sept. 1961), pp. 1553–1559. DOI: 10.1103/PhysRev.123.1553 (cit. on p. 92).

[82] D. ter Haar. *Collected Papers of L. D. Landau*. 2nd. Elsevier, 2013. ISBN: 9781483152707 (cit. on p. 92).

[83] A. Akhiezer. "On the Absorption of Sound in Solids". In: *J. Phys. (Moscow)* 1 (1 1939), pp. 277–287 (cit. on p. 92).

[84] Ron Lifshitz and M. L. Roukes. "Thermoelastic damping in micro- and nanomechanical systems". In: *Phys. Rev. B* 61.8 (Feb. 2000), pp. 5600–5609 (cit. on p. 92).

[85] Nimrod Moiseyev. *Non-Hermitian Qauntum Mechanics*. Cambridge University Press, 2011. ISBN: 978-0-521-88972-8 (cit. on pp. 92, 96, 104).

[86] M. Field et al. "Measurements of Coulomb blockade with a noninvasive voltage probe". In: *Phys. Rev. Lett.* 70 (9 Mar. 1993), pp. 1311–1314. DOI: 10.1103/PhysRevLett.70.1311. URL: http://link.aps.org/doi/10.1103/PhysRevLett.70.1311 (cit. on p. 96).

[87] Hélène Lefebvre-Brion and Robert W. Field. *The Spectra and Dynamics of Diatomic Molecules: Revised and Enlarged Edition*. Elsevier Academic Press, 2004. ISBN: 978-0-124-41456-3 (cit. on p. 104).

[88] Jiansong Gao. "The Physics of Superconducting Microwave Resonators". PhD thesis. California Institute of Technology, 2008 (cit. on pp. 108, 109, 121).

[89] W. B. Gauster. "Low-Temperature Grüneisen Parameters for Silicon and Aluminum". In: *Phys. Rev. B* 4 (4 Aug. 1971), pp. 1288–1296 (cit. on p. 115).

[90] John J. Hall. "Electronic Effects in the Elastic Constants of n-Type Silicon". In: *Phys. Rev.* 161 (3 Sept. 1967), pp. 756–761. DOI: 10.1103/PhysRev.161.756 (cit. on p. 115).

[91] H. J. McSkimin. "Measurement of Elastic Constants at Low Temperatures by Means of Ultrasonic Waves–Data for Silicon and Germanium Single Crystals, and for Fused Silica". In: *J. Appl. Phys.* 24 (8 Aug. 1953), pp. 988–997. DOI: 10.1063/1.1721449 (cit. on p. 115).

[92] Norikuni Yabumoto et al. “Surface Damage on Si Substrates Caused by Reactive Sputter Etching”. In: *Jpn. J. Appl. Phys.* 20 (5 May 1981), pp. 893–900. DOI: 10.1143/JJAP.20.893 (cit. on pp. 120, 123).

[93] G. S. Oehrlein and J. F. Rembetski. “Plasma-based Dry Etching Techniques in the Silicon Integrated Circuit Technology”. In: *IBM J. Res. Dev.* 36.2 (Mar. 1992), pp. 140–157. ISSN: 0018-8646 (cit. on pp. 120, 123).

[94] Young H. Lee, G. S. Oehrlein, and C. Ransom. “RIE-induced damage and contamination in silicon”. In: *Radiation Effects and Defects in Solids: Incorporating Plasma Science and Plasma Technology* 111-112 (1-2 1989), pp. 221–232. DOI: 10.1080/10420158908212997 (cit. on pp. 120, 123).

[95] M. Morita et al. “Control factor of native oxide growth on silicon in air or in ultrapure water”. In: *Appl. Phys. Lett.* 55 (6 Aug. 1989), p. 562. DOI: 10.1063/1.102435 (cit. on pp. 120, 123).

[96] R. N. Kleiman, G. Agnolet, and D. J. Bishop. “Two-level systems observed in the mechanical properties of single-crystal silicon at low temperatures”. In: *Phys. Rev. Lett.* 59 (18 Nov. 1987), pp. 2079–2082 (cit. on pp. 121, 123).

[97] W. A. Phillips. “Comment on "Two-Level Systems Observed in the Mechanical Properties of Single-Crystal Silicon at Low Temperatures"”. In: *Phys. Rev. Lett.* 61 (22 Nov. 1988), pp. 2632–2632 (cit. on pp. 121, 123).

[98] J. L. Black and B. I. Halperin. “Spectral diffusion, phonon echoes, and saturation recovery in glasses at low temperatures”. In: *Phys. Rev. B* 16 (6 Sept. 1977), pp. 2879–2895. DOI: 10.1103/PhysRevB.16.2879 (cit. on p. 123).

[99] T. J. Kippenberg and K. J. Vahala. “Cavity Optomechanics: Back-Action at the Mesoscale”. In: *Science* 321 (2008), pp. 1172–1176 (cit. on p. 129).

[100] A. A. Clerk et al. “Introduction to quantum noise, measurement, and amplification”. In: *Rev. Mod. Phys.* 82 (2010), pp. 1155–1208 (cit. on pp. 129, 202).

[101] M Selim Hanay et al. “Inertial imaging with nanomechanical systems”. In: *Nature nanotechnology* 10.4 (2015), p. 339 (cit. on p. 129).

[102] Jeff T. Hill et al. “Coherent optical wavelength conversion via cavity optomechanics”. In: *Nature Commun.* 3 (June 2012), p. 1196 (cit. on pp. 129, 130, 150, 157, 183).

[103] Amir H. Safavi-Naeini et al. “Squeezed light from a silicon micromechanical resonator”. In: *Nature* 500 (2013), pp. 185–189 (cit. on p. 129).

[104] Nathan Rafaël Bernier et al. “Nonreciprocal reconfigurable microwave optomechanical circuit”. In: *Nature communications* 8.1 (2017), p. 604 (cit. on p. 129).

[105] M Schmidt et al. “Optomechanical creation of magnetic fields for photons on a lattice”. In: *Optica* 2.7 (2015), pp. 635–641 (cit. on p. 129).

[106] Christian Brendel et al. “Pseudomagnetic fields for sound at the nanoscale”. In: *Proceedings of the National Academy of Sciences* 114.17 (2017), E3390–E3395 (cit. on p. 129).

[107] T. P. Purdy et al. “Strong Optomechanical Squeezing of Light”. In: *Phys. Rev. X* 3 (2013), p. 031012 (cit. on p. 129).

[108] Audrey Bienfait et al. “Phonon-mediated quantum state transfer and remote qubit entanglement”. In: *Science* 364.6438 (2019), pp. 368–371 (cit. on pp. 129, 174, 175).

[109] Joerg Bochmann et al. “Nanomechanical coupling between microwave and optical photons”. In: *Nature Physics* 9 (Nov. 2013), pp. 712–716 (cit. on pp. 129, 131, 150, 175).

[110] R. W. Andrews et al. “Bidirectional and efficient conversion between microwave and optical light”. In: *Nature Physics* 10 (Mar. 2014), pp. 321–326 (cit. on pp. 129–131, 150, 157, 175).

[111] Krishna C Balram et al. “Coherent coupling between radiofrequency, optical and acoustic waves in piezo-optomechanical circuits”. In: *Nature photonics* 10.5 (2016), p. 346 (cit. on pp. 129, 131, 150, 175).

[112] AP Higginbotham et al. “Harnessing electro-optic correlations in an efficient mechanical converter”. In: *Nature Physics* 14.10 (2018), p. 1038 (cit. on pp. 129, 131, 150, 175).

[113] Michael M Sigalas and Eleftherios N Economou. “Elastic and acoustic wave band structure”. In: *Journal of Sound Vibration* 158 (1992), pp. 377–382 (cit. on p. 129).

[114] Manvir S Kushwaha et al. “Acoustic band structure of periodic elastic composites”. In: *Physical review letters* 71.13 (1993), p. 2022 (cit. on p. 129).

[115] Matthew H Matheny. “Enhanced photon-phonon coupling via dimerization in one-dimensional optomechanical crystals”. In: *Applied Physics Letters* 112.25 (2018), p. 253104 (cit. on p. 129).

[116] John Clarke and Frank K Wilhelm. “Superconducting quantum bits”. In: *Nature* 453.7198 (2008), p. 1031 (cit. on p. 129).

[117] Michel H Devoret and Robert J Schoelkopf. “Superconducting circuits for quantum information: an outlook”. In: *Science* 339.6124 (2013), pp. 1169–1174 (cit. on p. 129).

[118] Connor T Hann et al. “Hardware-efficient quantum random access memory with hybrid quantum acoustic systems”. In: *arXiv preprint arXiv:1906.11340* (2019) (cit. on p. 129).

[119] Marek Pechal, Patricio Arrangoiz-Arriola, and Amir H Safavi-Naeini. "Superconducting circuit quantum computing with nanomechanical resonators as storage". In: *Quantum Science and Technology* 4.1 (2018), p. 015006 (cit. on p. 129).

[120] Liu Qiu et al. "High-fidelity laser cooling to the quantum ground state of a silicon nanomechanical oscillator". In: *arXiv preprint arXiv:1903.10242* (2019) (cit. on p. 130).

[121] Amir H. Safavi-Naeini et al. "Optomechanics in an ultrahigh-Q slotted 2D photonic crystal cavity". In: *Appl. Phys. Lett.* 97 (2010), p. 181106 (cit. on p. 130).

[122] P. S. Zyryanov and G. G. Taluts. "On the theory of sound absorption in solids". In: *JETP* 22.6 (June 1966), pp. 1326–1330 (cit. on pp. 132, 156, 161).

[123] M. G. Holland. "Analysis of Lattice Thermal Conductivity". In: *Phys. Rev.* 132 (6 Dec. 1963), pp. 2461–2471. DOI: 10.1103/PhysRev.132.2461 (cit. on pp. 134, 162).

[124] Joseph Callaway. "Model for Lattice Thermal Conductivity at Low Temperatures". In: *Phys. Rev.* 113 (4 Feb. 1959), pp. 1046–1051 (cit. on pp. 134, 162).

[125] K. Stannigel et al. "Optomechanical Transducers for Long-Distance Quantum Communication". In: *Phys. Rev. Lett.* 105 (2010), p. 220501 (cit. on p. 150).

[126] Hiroshi Sekoguchi et al. "Photonic crystal nanocavity with a Q-factor of 9 million". In: *Opt. Express* 22.1 (Jan. 2014), pp. 916–924 (cit. on pp. 151, 159).

[127] Gang Chen. "Particularities of heat conduction in nanostructures". In: *Journal of Nanoparticle Research* 2.2 (2000), pp. 199–204 (cit. on p. 155).

[128] MC Cross and Ron Lifshitz. "Elastic wave transmission at an abrupt junction in a thin plate with application to heat transport and vibrations in mesoscopic systems". In: *Physical Review B* 64.8 (2001), p. 085324 (cit. on pp. 155, 156).

[129] AI Akhiezer. "On the sound absorption in solids". In: *Journal of Physics (USSR)* 1 (1939), p. 277 (cit. on pp. 155, 156).

[130] G. P. Srivastava. *The Physics of Phonons*. Taylor and Francis Group, 1990 (cit. on p. 156).

[131] Ze'ev Lindenfeld, Eli Eisenberg, and Ron Lifshitz. "Phonon-mediated damping of mechanical vibrations in a finite atomic chain coupled to an outer environment". In: *arXiv preprint arXiv:1309.5772* (2013) (cit. on p. 156).

[132] Sean Michael Meenehan. "Cavity Optomechanics at Millikelvin Temperatures". PhD thesis. 2015 (cit. on p. 165).

[133] Wolfgang Pfaff et al. "Controlled release of multiphoton quantum states from a microwave cavity memory". In: *Nature Physics* 13 (June 2017), p. 882 (cit. on pp. 169, 170, 174).

[134] S. Rosenblum et al. "A CNOT gate between multiphoton qubits encoded in two cavities". In: *Nature Communications* 9.1 (Feb. 2018), p. 652. ISSN: 2041-1723 (cit. on pp. 169, 170, 174).

[135] Connor T. Hann et al. "Hardware-efficient quantum random access memory with hybrid quantum acoustic systems". In: *arXiv* (2019). URL: `https://arxiv.org/abs/1906.11340` (cit. on pp. 169, 170, 174).

[136] C. Neill et al. "Ergodic dynamics and thermalization in an isolated quantum system". In: *Nature Physics* 12 (July 2016), p. 1037 (cit. on p. 169).

[137] C. Neill et al. "A blueprint for demonstrating quantum supremacy with superconducting qubits". In: *Science* 360.6385 (2018), pp. 195–199. ISSN: 0036-8075. DOI: `10.1126/science.aao4309` (cit. on p. 169).

[138] P. Roushan et al. "Spectroscopic signatures of localization with interacting photons in superconducting qubits". In: *Science* 358.6367 (2017), pp. 1175–1179. ISSN: 0036-8075. DOI: `10.1126/science.aao1401` (cit. on p. 169).

[139] Nissim Ofek et al. "Extending the lifetime of a quantum bit with error correction in superconducting circuits". In: *Nature* 536 (July 2016), p. 441 (cit. on p. 169).

[140] R. Barends et al. "Digitized adiabatic quantum computing with a superconducting circuit". In: *Nature* 534 (June 2016), p. 222 (cit. on p. 169).

[141] P. Krantz et al. "A quantum engineer's guide to superconducting qubits". In: *Applied Physics Reviews* 6.2 (June 2019), p. 021318. DOI: `10.1063/1.5089550`. URL: `https://doi.org/10.1063/1.5089550` (cit. on pp. 169, 170).

[142] Hanhee Paik et al. "Observation of High Coherence in Josephson Junction Qubits Measured in a Three-Dimensional Circuit QED Architecture". In: *Phys. Rev. Lett.* 107 (24 Dec. 2011), p. 240501. DOI: `10.1103/PhysRevLett.107.240501`. URL: `http://link.aps.org/doi/10.1103/PhysRevLett.107.240501` (cit. on p. 170).

[143] A. D. O'Connell et al. "Quantum ground state and single-phonon control of a mechanical resonator". In: *Nature* 464 (2010), pp. 697–703 (cit. on p. 170).

[144] Yiwen Chu et al. "Quantum acoustics with superconducting qubits". In: *Science* (2017). ISSN: 0036-8075. DOI: `10.1126/science.aao1511` (cit. on p. 170).

[145] A. P. Reed et al. “Faithful conversion of propagating quantum information to mechanical motion”. In: *Nature Physics* 13 (Sept. 2017), p. 1163 (cit. on p. 170).

[146] Andrew J. Keller et al. “Al transmon qubits on silicon-on-insulator for quantum device integration”. In: *Appl. Phys. Lett.* 111 (July 2017), p. 042603. DOI: 10.1063/1.4994661 (cit. on p. 170).

[147] Amir H. Safavi-Naeini and Oskar Painter. “Optomechanical Crystal Devices”. In: *Cavity Optomechanics*. Ed. by Markus Aspelmeyer, Tobias J. Kippenberg, and Florian Marquardt. Quantum Science and Technology. Springer Berlin Heidelberg, 2014, pp. 195–231. ISBN: 978-3-642-55311-0. DOI: 10.1007/978-3-642-55312-7_10 (cit. on p. 171).

[148] Thiago P. Mayer Alegre et al. “Quasi-two-dimensional optomechanical crystals with a complete phononic bandgap”. In: *Opt. Express* 19 (2011), pp. 5658–5669 (cit. on p. 171).

[149] E. Yarar et al. “Low temperature aluminum nitride thin films for sensory applications”. In: *AIP Advances* 6.7 (Dec. 2016), p. 075115. DOI: 10.1063/1.4959895. URL: https://doi.org/10.1063/1.4959895 (cit. on p. 171).

[150] Marc-Alexandre Dubois and Paul Muralt. “Stress and piezoelectric properties of aluminum nitride thin films deposited onto metal electrodes by pulsed direct current reactive sputtering”. In: *Journal of Applied Physics* 89.11 (Dec. 2018), pp. 6389–6395. ISSN: 0021-8979. DOI: 10.1063/1.1359162. URL: https://doi.org/10.1063/1.1359162 (cit. on pp. 171, 172).

[151] Marc-Alexandre Dubois and Paul Muralt. “Properties of aluminum nitride thin films for piezoelectric transducers and microwave filter applications”. In: *Appl. Phys. Lett.* 74.20 (Dec. 2018), pp. 3032–3034. ISSN: 0003-6951. DOI: 10.1063/1.124055. URL: https://doi.org/10.1063/1.124055 (cit. on p. 171).

[152] C. Song et al. “Reducing microwave loss in superconducting resonators due to trapped vortices”. In: *Appl. Phys. Lett.* 95.23, 232501 (2009), p. 232501. DOI: 10.1063/1.3271523. URL: http://link.aip.org/link/?APL/95/232501/1 (cit. on p. 171).

[153] F. Martin et al. “Thickness dependence of the properties of highly c-axis textured AlN thin films”. In: *Journal of Vacuum Science & Technology A* 22.2 (Dec. 2018), pp. 361–365. ISSN: 0734-2101. DOI: 10.1116/1.1649343. URL: https://doi.org/10.1116/1.1649343 (cit. on p. 171).

[154] F. Martin, P. Muralt, and M.-A. Dubois. “Process optimization for the sputter deposition of molybdenum thin films as electrode for AlN thin films”. In: *Journal of Vacuum Science & Technology A* 24.4 (Dec. 2018), pp. 946–952. ISSN: 0734-2101. DOI: 10.1116/1.2201042. URL: https://doi.org/10.1116/1.2201042 (cit. on p. 171).

[155] S. Strite and H. Morkoç. "GaN, AlN, and InN: A review". In: *Journal of Vacuum Science & Technology B: Microelectronics and Nanometer Structures Processing, Measurement, and Phenomena* 10.4 (Dec. 2018), pp. 1237–1266. ISSN: 1071-1023. DOI: 10.1116/1.585897. URL: https://avs.scitation.org/doi/abs/10.1116/1.585897 (cit. on pp. 171, 172).

[156] S. Tadigadapa and K. Mateti. "Piezoelectric MEMS sensors: state-of-the-art and perspectives". In: *Measurement Science and Technology* 20.9 (2009), p. 092001. ISSN: 0957-0233. URL: http://stacks.iop.org/0957-0233/20/i=9/a=092001 (cit. on pp. 171, 172).

[157] Yu Chen et al. "Qubit Architecture with High Coherence and Fast Tunable Coupling". In: *Phys. Rev. Lett.* 113 (22 Nov. 2014), p. 220502. DOI: 10.1103/PhysRevLett.113.220502. URL: https://link.aps.org/doi/10.1103/PhysRevLett.113.220502 (cit. on p. 174).

[158] K. J. Satzinger et al. "Quantum control of surface acoustic wave phonons". In: *arXiv:1804.07308* (Apr. 2018) (cit. on p. 174).

[159] F. Marsili et al. "Detecting single infrared photons with 93% system efficiency". In: *Nature Photon.* 7 (2013), pp. 210–214 (cit. on p. 201).

[160] Jiang Qian et al. "Quantum Signatures of the Optomechanical Instability". In: *Phys. Rev. Lett.* 109.25 (Dec. 2012), p. 253601 (cit. on p. 202).

[161] Andreas Kronwald, Max Ludwig, and Florian Marquardt. "Full photon statistics of a light beam transmitted through an optomechanical system". In: *Phys. Rev. A* 87.1 (Jan. 2013), p. 013847 (cit. on p. 202).

[162] Roy Pike. "Lasers, photon statistics, photon-correlation spectroscopy and subsequent applications". In: *J. Eur. Opt. Soc. - Rapid Publications* 5 (June 2010), 10047S (cit. on p. 202).

Appendix A

POWER SPECTRAL DENSITY OF THE MECHANICAL MODE

A.1 Definition of Fourier Transforms and Power Spectral Density

Definition of Fourier transforms for time-dependent quantum operators and variables throughout this thesis is following,

$$\hat{A}(\omega) = \int_{-\infty}^{\infty} \frac{dt}{\sqrt{2\pi}}\, \hat{A}(t) e^{i\omega t}, \tag{A.1}$$

$$\hat{A}(t) = \int_{-\infty}^{\infty} \frac{d\omega}{\sqrt{2\pi}}\, \hat{A}(\omega) e^{-i\omega t}. \tag{A.2}$$

For the conjugate of $\hat{A}$,

$$\hat{A}^{\dagger}(\omega) = \int_{-\infty}^{\infty} \frac{dt}{\sqrt{2\pi}}\, \hat{A}^{\dagger}(t) e^{i\omega t}, \tag{A.3}$$

Note that this implies the relation $\hat{A}^{\dagger}(\omega) = (\hat{A}(-\omega))^{\dagger}$. The quantum power spectral density of the operator $\hat{A}(t)$ is defined as,

$$S_{\hat{A}\hat{A}}(\omega) = \int_{-\infty}^{\infty} d\tau\; e^{i\omega\tau} \langle \hat{A}^{\dagger}(t+\tau)\hat{A}(t)\rangle \tag{A.4}$$

$$= \int_{-\infty}^{\infty} \frac{d\omega'}{2\pi}\, \langle \hat{A}^{\dagger}(\omega)\hat{A}(\omega')\rangle, \tag{A.5}$$

where $\langle\cdot\rangle$ denotes the quantum expectation value.

A.2 Mechanical Power Spectral Density

Without optomechanical coupling, the spectral density of the mechanical mode only considering thermal phonon bath is,

$$\dot{\hat{b}}(t) = -\left(i\omega_m + \frac{\gamma_i}{2}\right)\hat{b}(t) + \sqrt{\gamma_i}\hat{b}_{\text{in}}(t), \tag{A.6}$$

Same as in the previous section, the spectral density of the mechanical resonator annihilation operator can be computed by transferring A.6 to the frequency domain and use Equ. A.5:

$$S_{\hat{b}\hat{b}}(\omega) = \int_{-\infty}^{\infty} d\omega' \left(\frac{-\sqrt{\gamma_i}}{-i(\omega_m + \omega) + \gamma_i/2}\right)\left(\frac{-\sqrt{\gamma_i}}{i(\omega_m - \omega') + \gamma_i/2}\right)\langle \hat{b}^{\dagger}_{\text{in}}(\omega)\hat{b}_{\text{in}}(\omega')\rangle \tag{A.7}$$

$$= \gamma_i n_{\text{b}} \int_{-\infty}^{\infty} d\omega' \left(\frac{1}{-i(\omega_m + \omega) + \gamma_i/2}\right)\left(\frac{1}{i(\omega_m - \omega') + \gamma_i/2}\right)\delta(\omega + \omega') \tag{A.8}$$

$$= \frac{\gamma_i n_{\text{b}}}{(\omega_m + \omega)^2 + \gamma_i^2/4}. \tag{A.9}$$

For the case with optomechanical coupling, there are $\langle n \rangle$ phonons in the mechanical mode of the optomechanical system, an analogous spectral density functions in terms of the shifted ω_m and total damping rate γcan be defined as,

$$S_{\hat{b}\hat{b}}(\omega; \langle n \rangle) = \frac{\gamma \langle n \rangle}{(\omega_m + \omega)^2 + \gamma/2}, \tag{A.10}$$

Similarly, the corresponding spectral density for the creation operator is found to be

$$S_{\hat{b}^{\dagger}\hat{b}^{\dagger}}(\omega; \langle n \rangle) = \frac{\gamma(\langle n \rangle + 1)}{(\omega_m - \omega)^2 + \gamma/2}. \tag{A.11}$$

Note that these spectral densities can be integrated and phonon number $\langle n \rangle$ can be extracted,

$$\int_{-\infty}^{\infty} \frac{d\omega}{2\pi} S_{\hat{b}\hat{b}}[\omega; \langle n \rangle] = \langle n \rangle, \tag{A.12}$$

$$\int_{-\infty}^{\infty} \frac{d\omega}{2\pi} S_{\hat{b}^{\dagger}\hat{b}^{\dagger}}[\omega; \langle n \rangle] = \langle n \rangle + 1. \tag{A.13}$$

Appendix B

BALANCED HETERODYNE DETECTION

Heterodyne detection measures a photocurrent proportional to the squared field amplitudes incident on a photon detector. In heterodyne detection setups such as shown in Section 3.1.2, a strong local oscillator (L.O.) is used to amplify a signal tone and mixes it into a frequency range which is convenient for detection (usually decided by the bandwidth of photo detectors used).

Balanced heterodyne detection is a method which uses two photon detectors, by subtracting photon currents from two detectors, common mode noise terms coming from the local oscillator can in principle be eliminated. The output field $\hat{a}_{\text{out}}$ from a cavity-optomechanical system is sent to an idealized beam-splitter along with a strong L.O. tone. The difference photocurrent $\hat{I}_{-}(t)$ between the two output port photocurrents is measured.

Defining the time domain *signal* as $\hat{a}(t)$ and the L.O. as $\hat{a}_{\text{LO}}(t)$, where

$$\hat{a}_{\text{LO}}(t) = \alpha_{LO} e^{-i\omega_{\text{LO}} t} + \delta\hat{a}_{\text{LO}}(t), \tag{B.1}$$

$\beta \in \mathbb{C}$ is the square root of the average L.O. photon flux, and $\hat{\delta b}(t)$ is the noise from the L.O. oscillator. We make the substitution $\hat{a}(t) = \tilde{\hat{a}}(t) e^{-i\omega_{\text{LO}} t}$ where $\tilde{\hat{a}}(t)$ is the slowly-varying parts of the relevant fields relative to the L.O.. The difference photocurrent can be written as

$$\hat{I}_{-}(t) \cong i|\alpha_{LO}|\left(e^{-i\phi_{\text{LO}}}\tilde{\hat{a}}(t) - e^{i\phi_{\text{LO}}}\tilde{\hat{a}}^{\dagger}(t)\right). \tag{B.2}$$

The power spectral density of the difference photocurrent of a sideband-resolved system under red-detuned ($\Delta = +\omega_m$) driving as measured on a balanced heterodyne detection setup can be derived as

$$S_{\hat{I}_{-}\hat{I}_{-}}[\omega]\bigg|_{\Delta=+\omega_m} = 2\pi|\alpha_{LO}|^2\left(1 + 2\frac{\kappa_{\text{e}}}{\kappa}\gamma_{\text{OM}}\bar{S}_{\hat{b}\hat{b}}[\omega; n_{\text{b}}]\right), \tag{B.3}$$

where $\bar{S}_{\hat{b}\hat{b}}$ is the power spectral density of $\hat{b}$. Similarly, for the case of blue detuning ($\Delta = -\omega_m$), the power spectral density of difference photocurrent is

$$S_{\hat{I}_-\hat{I}_-}[\omega]\bigg|_{\Delta=-\omega_m} = 2\pi|\alpha_{LO}|^2\left(1 + 2\frac{\kappa_\mathrm{e}}{\kappa}\gamma_\mathrm{OM}\bar{S}_{\hat{b}^\dagger\hat{b}^\dagger}[\omega; n_\mathrm{b}]\right). \tag{B.4}$$

Note that in B.3 and B.4, the efficiency of the optical path and detector are assumed to be unity. These derivations show the principle of measuring the mechanical noise power spectral density base on the intracavity light field detected on a photon detector. The focus of this work is using Balanced Heterodyne Detection for the linewidth of mechanical noise power spectral density (mechanical damping rate), where exact efficiency of Balanced Heterodyne Detection setup is not required.

Appendix C

PHONON COUNTING TECHNIQUE

C.1 Single-Photon Detector

The SPDs used here are amorphous WSi-based superconducting nanowire single-photon detectors developed in collaboration between the Jet Propulsion Laboratory and NIST [159]. The SPDs are designed for a wavelength range $\lambda = 1520-1610$ nm, with maximum count rates as large as 10^7 counts per second (c.p.s.) [159]. The SPDs are mounted on the still stage of the dilution refrigerator at ~ 700 mK. Single-mode optical fibers are passed into the refrigerator through vacuum feedthroughs and coupled to the SPDs via a fiber sleeve attached to each SPD mount. The radio-frequency output of each SPD is amplified by a cold-amplifier mounted on the 50 K stage of the dilution refrigerator as well as a room-temperature amplifier, then read out by a triggered PicoQuant PicoHarp 300 time-correlated single photon counting module. After filtering out the long wavelength blackbody radiation inside the DR through a bandpass filter and isolating the input optical fiber from environmental light sources at room temperature, we observed SPD dark count rates as low as ~ 1 (c.p.s.) and a SPD quantum efficiency $\eta_{\mathrm{SPD}} \simeq 60\%$ (see Figure. C.1).

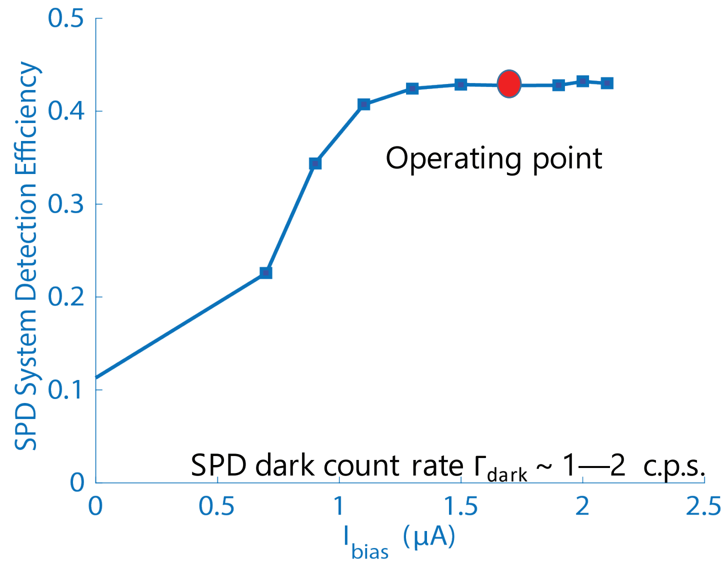

Figure C.1: **Single-photon detector calibration curve.** Efficiency calibrations for an SPD used in this work, plotted against the D.C. bias current applied through the nanowire. At high bias current ($I_{\text{bias}} \gtrsim 2.5\ \mu$A), the SPD switches into a normal state and its response is no longer linear. We operate in the saturated region of the curve, where the linear efficiency η_{SPD} of the SPD is not sensitive to small fluctuations in bias current. Here η includes all losses from the input fiber to the dilution fridge to the SPD. Note that through fiber-coiling techniques, black-body radiation isolation, and minimization of stray light entering the optical path, we are able to operate the SPDs with ultra-low intrinsic dark-count rates around 1 to 2 c.p.s.

C.2 Phonon Counting

Other than heterodyne detection of a quantum mechanical system coupled to optical or electrical field [100], probing the quantum dynamics of the coupled optomechanical system by photon counting is particularly suitable for optomechanical systems [160, 161]. This kind of intensity interferometry technique has been widely used in measurements of particle and molecular motion in materials [162].

In our experiments, we have a high-Q, GHz-frequency mechanical resonator coupling to an optical nanocavity. Phonon-photon coupling is enhanced and we collect the scattered photons into a preferred optical mode to study the dynamics of mechinical renonator. By counting the photons collected on a single-photon-detector, we are effectively counting phonons in the mechanical resonator. In this section, the basics of phonon counting is briefly introduced for red-detuned ($\Delta = +\omega_m$) driving case in a sideband-resolved optomechincal system.

With the driving laser parked at red-detuned frequency, the optical field amplitudes in the frequency domain is

$$\hat{a}(\omega) = \frac{-iG(\hat{b}^\dagger(\omega) + \hat{b}(\omega)) + \sqrt{\kappa_e}\hat{a}_{in}(\omega) + \sqrt{\kappa_i}\hat{a}_i(\omega)}{i(\Delta - \omega) + \kappa/2}, \tag{C.1}$$

$$\hat{b}(\omega) = \frac{\sqrt{\gamma_i}\hat{b}_{in}(\omega) - iG(\hat{a}(\omega) + \hat{a}^\dagger(\omega))}{i(\omega_m - \omega) + \gamma_i/2}. \tag{C.2}$$

The scattered photons to the optical cavity frequency by mechanical resonance is then filtered out by band-pass filters with the bandwidth much smaller then the optical cavity linewidth, where the filtering can be expressed by following the transmission function:

$$\mathrm{F_f}(\omega; \omega_f) = \frac{\kappa_f/2}{i(\omega - \omega_f) + \kappa_f/2}, \tag{C.3}$$

where κ_f is the bandwidth of the filter and ω_f is the center frequency of the filter. in order to filter out the scattered photons mentioned above, filter center frequency is set to $\omega_f = \omega_m$.

$$\hat{a}_{filt}(\omega)\Big|_{\Delta=+\omega_m} = \mathrm{F_f}(\omega; \omega_m)\hat{a}(\omega)\Big|_{\Delta=+\omega_m}. \tag{C.4}$$

The photon count rate detected on SPD after the filter is

$$\begin{aligned}\Gamma(t) &= \langle \hat{a}^\dagger_{filt}(t)\Big|_{\Delta=+\omega_m} \hat{a}_{filt}(t)\Big|_{\Delta=+\omega_m}\rangle \\ &= \frac{1}{2\pi}\int_{-\infty}^{\infty} d\omega \int_{-\infty}^{\infty} d\omega' e^{i(\omega+\omega')t}\langle \hat{a}^\dagger_{filt}(\omega)\hat{a}_{filt}(\omega')\rangle.\end{aligned} \tag{C.5}$$

Here, we ignore the vacuum noise terms $\hat{a}_{in}$ and $\hat{a}_i$, and count-rate can be expressed as

$$\Gamma(t) = \frac{1}{2\pi}\left(|\mathrm{F_f}(0;\omega_m)|^2|\alpha_{out}|^2 + \frac{\kappa_e}{\kappa}\gamma_{OM}\int_{-\infty}^{\infty} d\omega\ |\mathrm{F_f}(\omega;\omega_m)|^2 S_{\hat{b}\hat{b}}[\omega;\langle n\rangle]\right) \tag{C.6}$$

$$= \frac{1}{2\pi}\left(|\mathrm{F_f}(0;\omega_m)|^2|\alpha_{out}|^2 + \frac{\kappa_e}{\kappa}\gamma_{OM}\langle n\rangle\right) \tag{C.7}$$

$$\approx Atten|\alpha_{out}|^2 + \frac{\kappa_e}{\kappa}\gamma_{OM}\langle n\rangle, \tag{C.8}$$

where $F_f(\omega_m; \omega_m) = 1$ in Equation C.8, since filter bandwidth is much larger than mechanical linewidth. $Atten \equiv |F_f(0; \omega_m)|^2/(2\pi)$ in the attenuation factor of the driving frequency laser set by the filter.

Assuming $Atten$ is very small and accounting for the noise terms (rejection of pump photon by filtering, *pump noise* photon count rate $\Gamma_{\text{pump}} = \eta A|\alpha_{\text{out}}|^2 + \Gamma_{\text{noise}}$, where detection efficiency η models the optical losses in the detection optical path.), the real scattered signal photon count rate is directly proportional to $\langle n \rangle$, therefore, by counting photons on a single-photon-detector, we can equivalently count phonons in the mechanical resonator.

The final measured count rate single-photon-detector also includes a dark-count rate Γ_{dark}, which describes both dark counts of the single-photon-detector as well as counts arising from stray radiation (e.g. due to thermal blackbody radiation inside the fridge to the filters inside the fridge or directly to single-photon-detector). Finally, for red- and blue-detuning, the total measured output photon count rate is

$$\Gamma(\Delta = \pm\omega_{\text{m}}) = \Gamma_{\text{DCR}} + \Gamma_{\text{pump}} + \Gamma_{\text{SB},0}(\langle n \rangle + \frac{1}{2}(1 \mp 1)), \tag{C.9}$$

where the $\langle n \rangle \longrightarrow \langle n \rangle + 1$ for blue detuning comes from integral of $S_{\hat{b}^\dagger \hat{b}^\dagger}[\omega; \langle n \rangle]$. $\Gamma_{\text{SB},0} \equiv \eta \frac{\kappa_{\text{e}}}{\kappa} \gamma_{\text{OM}}$ is defined as the count rate per phonon.

C.2.1 Noise in Phonon Counting

The noise (in units of mechanical occupation quanta) in phonon counting can be characterized by dividing the total noise floor by the per-phonon count rate:

$$n_{\text{NEP}} = \frac{\Gamma_{\text{DCR}} + \Gamma_{\text{pump}}}{\Gamma_{\text{SB},0}}. \tag{C.10}$$

Substituting $\gamma_{\text{OM}} = 4g_0^2 n_{\text{c}}/\kappa$, and $\Gamma_{\text{SB},0} = \eta|\gamma_{\text{OM}}|$, this yields

$$n_{\text{NEP}}(n_{\text{c}}) = \frac{\kappa^2 \Gamma_{\text{dark}}}{4\eta\kappa_{\text{e}} g_0^2 n_{\text{c}}} + A\left(\frac{\kappa\omega_m}{2\kappa_{\text{e}} g_0}\right)^2. \tag{C.11}$$

From the above equation, we can see that large cavity-enhanced optomechanical coupling g_0 is critical for both low power sensitivity, which is limited by detector dark counts, and the high power sensitivity, which is limited by pump bleed-through.

INDEX